Analytic Theory of Cross-Polarization Dynamics in Quadrupolar Spins

A Thesis Submitted

in Partial Fulfilment of the Requirements

for the Degree of

DOCTOR OF PHILOSOPHY

by

Ekta

(2018CYZ0003)



DEPARTMENT OF CHEMISTRY INDIAN INSTITUTE OF TECHNOLOGY ROPAR

February, 2025

Ekta: Analytic Theory of Cross-Polarization Dynamics in Quadrupolar Spins Copyright ©YYYY, Indian Institute of Technology Ropar All Rights Reserved

Dedicated to my mother and family

Declaration of Originality

I hereby declare that the work which is being presented in the thesis entitled **Analytic** Theory of Cross-Polarization Dynamics in Quadrupolar Spins has been solely authored by me. It presents the result of my own independent investigation/research conducted during the time period from July 2018 to August 2024 under the supervision of Dr. Manoj Kumar Pandey, Assistant professor at the Indian Institute of Technology Ropar. To the best of my knowledge, it is an original work, both in terms of research content and narrative, and has not been submitted or accepted elsewhere, in part or in full, for the award of any degree, diploma, fellowship, associateship, or similar title of any university or institution. Further, due credit has been attributed to the relevant state-of-the-art and collaborations (if any) with appropriate citations and acknowledgments, in line with established ethical norms and practices. I also declare that any idea/data/fact/source stated in my thesis has not been fabricated/ falsified/ misrepresented. All the principles of academic honesty and integrity have been followed. I fully understand that if the thesis is found to be unoriginal, fabricated, or plagiarized, the Institute reserves the right to withdraw the thesis from its archive and revoke the associated Degree conferred. Additionally, the Institute also reserves the right to appraise all concerned sections of society of the matter for their information and necessary action (if any). If accepted, I hereby consent for my thesis to be available online in the Institute's Open Access repository, inter-library loan, and the title and abstract to be made available to outside organizations.

Signature

Name: Ekta

Entry Number: 2018CYZ0003

Program: PhD

Department: Chemistry

Indian Institute of Technology Ropar

Rupnagar, Punjab 140001

Date: 27^{th} February, 2025

Acknowledgement

I would like to express my gratitude to all those who have supported me over the course of my doctoral degree. I would like to convey my sincere appreciation to my PhD supervisor, Dr. Manoj Kumar Pandey, for his unwavering encouragement, advice, and support throughout my PhD journey. His constant words of motivation and inspiration profoundly influenced my PhD journey, providing me with the strength to persevere through challenges, particularly during moments of research setbacks and paper rejections. I am deeply moved by his research enthusiasm and his dedicated efforts to make valuable contributions to the scientific community. I'll always cherish these qualities and strive to cultivate them in my life. I express my gratitude to my doctoral committee members: Prof. Rajendra Srivastava (Chairperson), Prof. T. J. Dhilip Kumar, Dr. Sudipta Kumar Sinha and Dr. Partha Sharathi Dutta for their valuable input and support over the course of my research. Their contributions during my doctoral studies have facilitated my development as a researcher and enabled the completion of my thesis. I would like to extend my heartfelt gratitude to IIT Ropar for fellowship, research facilities as well as for addressing my other requests. I express my deepest gratitude to all my lab members of Magnetic Resonance Lab, IIT Ropar (Ketan Rohilla, Yayatika Bhardwaj and Neelam Sehrawat) for fostering a collaborative laboratory atmosphere and for their invaluable assistance. I would also like to thank M.Sc. students (Anjali Rajora, Sumit Kumar, Vivek Gupta, Pallavi Pandey, Gyan Singh Meena) for creating a joyful laboratory environment each year. As someone not well-versed in computer programming, my friend **Apoorv Kushwaha** has been a great help in program-related issues. I would like to thank Prof. Ramesh Ramachandran and his research group at IISER Mohali for fruitful discussions and all the support with this work.

My friends have always been an important part of the circle of my life. I would like to extend my heartfelt gratitude to my friends (Anu Janngal, Rajdeep Lehnga, Suman Lakhotia, Anmol Punia, Vivek Yadav, Kuldeep Goyal, Sanchit Chhabra, Navneet Mishra, Arpit Mishra and Yayatika Bhardwaj) for always bringing laughter into my life and taken good care of my overly emotional behavior.

I am fortunate to have a large family that has always encouraged me and my choices, including pursuing a PhD. I will forever be grateful to My Family. I am especially grateful to my mother (Dropati Jaria) for always believing in me and celebrating and taking pride in my successes, no matter how small or big. For this, I am eternally thankful. I am immensely thankful to everyone who has contributed to the completion of this PhD thesis. Above all, I am thankful to my ishta Shiv Ji and my family's ishta devata Hanuman Ji for the strength, endurance and, perseverance, protection they have bestowed upon me.

Certificate

This is to certify that the thesis entitled Analytic Theory of Cross-Polarization Dynamics in Quadrupolar Spins, submitted by Ekta (2018CYZ0003) for the award of the degree of Doctor of Philosophy of Indian Institute of Technology Ropar, is a record of bonafide research work carried out under my guidance and supervision. To the best of my knowledge and belief, the work presented in this thesis is original and has not been submitted, either in part or full, for the award of any other degree, diploma, fellowship, associateship or similar title of any university or institution.

In my opinion, the thesis has reached the standard fulfilling the requirements of the regulations relating to the Degree.

Signature of the Supervisor

Name: Dr. Manoj Kumar Pandey

Manof.

Department: Chemistry

Indian Institute of Technology Ropar

Rupnagar, Punjab 140001 Date: 27^{th} February, 2025

Lay Summary

Cross-polarization experiment is a routinely employed experimental technique for sensitivity enhancement of the dilute/insensitive spins in the solid-state NMR spectroscopy. This double resonance experiment is based on the polarization from the abundant to less abundant nuclei mediated through heteronuclear dipolar couplings. Understanding the mechanism of the cross-polarization transfer dynamics in quadrupolar spins (I>1/2) has remained an open problem in the field of solid-state NMR spectroscopy. This is primarily due to the complexity in the description of the analytic theory due to the presence of multiple energy levels, a non-commuting set of operators in the interaction Hamiltonian and the strength of the quadrupolar coupling constant. In this thesis, an operator-based analytic theory is presented to describe the spin dynamics of the cross-polarization experiment involving quadrupolar spins. Utilizing the concept of the "Effective-field" method an effective CP Hamiltonian is derived, which accurately predicts the spin dynamics across all the quadrupolar coupling regimes. The effective-field formalism is shown to converge faster with the requirement of a minimal number of unitary transformations in contrast to conventional perturbative approaches. Results emerging form the analytic theory are rigorously compared and validated with more exact numerical simulations for a wide range of the experimental parameters. The CP signal expressions derived in this thesis are capable of identifying all the possible modes of the polarization transfer pathways and their interplay in deciphering the overall CP efficiency in isotropic and anisotropic solids.

Abstract

Cross-polarization (CP) method forms the building block in the design of multi-dimensional experiments in solid-state nuclear magnetic resonance (NMR) CP between spin-1/2 systems is a routine experimental method for sensitivity enhancement of insensitive spins in solid samples. It involves the transfer of polarization from the highly abundant spins to the less abundant (insensitive) spins. CP is mediated through heteronuclear dipolar coupling spin interactions by simultaneous irradiation of radio-frequency (RF) fields on both spins. The polarization transfer efficiency is maximized when the RF amplitudes on both nuclei are matched, a condition that is referred to as the Hartmann-Hahn (HH) energy level matching condition for static or non-rotating solids. While the mechanism of polarization transfer dynamics during CP process is well understood through various theoretical frameworks for spin-1/2 systems, a straightforward extension of the CP experiment involving quadrupolar spins $(S > 1/2; {}^{2}D,$ ⁶Li, ¹⁴N, ²³Na, ³⁵Cl, etc.) remains elusive. This is primarily due to the magnitude of the quadrupolar interaction (ranging from a few kHz to MHz), which in general is much higher than the magnitude of other internal spin interactions and the amplitude of the available RF fields that result in poor polarization transfer efficiency. This has acted as a roadblock for the optimal implementation of CP-based experimental methods involving quadrupolar spins and forms the motivation behind the thesis. From a theoretical perspective, the presence of multiple energy-levels/transitions and non-commuting set of operators in the interaction Hamiltonian along with the strength of quadrupolar coupling complicate the unified description of the spin dynamics. Previously, the theoretical descriptions of the CP were reported either using the average Hamiltonian theory (AHT) or Floquet theory. In both approaches the doubly rotating frame Hamiltonian is described in the quadrupolar interaction frame leading to time-dependent Hamiltonians. Depending on the strength of quadrupolar interaction, the Hamiltonian in the quadrupolar interaction frame requires perturbation corrections up to several orders of magnitude. Nevertheless, such descriptions are of limited utility in describing the CP dynamics across all the quadrupolar coupling regimes both for single crystal (single crystallite orientation with respect to the applied Zeeman field) as well as powder samples wherein quadrupolar frequencies are distributed over a wide range of crystallite orientations. In contrast to the existing theoretical models, in this thesis we attempt to provide an alternate description of the CP dynamics described using effective Hamiltonians that are derived from rotation operators based on the "effective-field" approach. Our effective-field approach results in faster convergence with improved accuracy in comparison to the existing theoretical frameworks. We have identified all the CP matching conditions in terms of the single-transition operators and also highlighted their role in deciphering the mechanism of CP transfer dynamics in non-rotating solids. We have presented a unified description of the CP dynamics involving quadrupolar spins through a single mathematical framework that is valid both for single crystal as well as powder samples across all the quadrupolar coupling regimes. The results emerging from the analytic theory are verified with numerical simulations over a wide range of experimental parameters. We believe that the analytic theory presented in this thesis would provide necessary impetus for better understanding of the CP experiments involving quadrupolar spins and could be a guiding tool for designing new experimental strategies.

Keywords: Cross-polarization; quadrupolar spin; Hartmann-Hahn condition; effective-field method; effective Hamiltonian; density matrix.

Contents

D	eclar	ation		iv
A	ckno	wledge	ement	\mathbf{v}
\mathbf{C}	ertifi	cate		vi
La	ay Su	ımmar	y	vii
A	bstra	ıct		viii
$\mathbf{L}_{\mathbf{i}}$	ist of	Symb	ols	xiv
1	Inti	oduct	ion	1
	1.1	Introd	luction	1
	1.2	Objec	tives and scope of the thesis	5
	1.3	Funda	amentals of NMR	6
		1.3.1	Nuclear spin interactions in NMR	6
		1.3.2	Secular approximation	13
		1.3.3	Time-Evolution of the spin-system	15
	1.4	Conce	ept of the "Effective Hamiltonian"	18
		1.4.1	Derivation of the effective Hamiltonian: Perturbation-based method	19
		1.4.2	Derivation of the effective Hamiltonian : "Effective-field" based	
			$method \dots \dots$	21
	1.5	Organ	ization of the thesis	25
2		•	nd Methodology: An effective-field approach to understand	
	\mathbf{the}		anism of cross-polarization dynamics between spin-1/2 systems	
	2.1	Theor	y and Methodology	26
		2.1.1	Derivation of the effective CP Hamiltonian	27
		2.1.2	Time-evolution of the spin-system	29
		2.1.3	Calculation of the CP Signal	30
		2.1.4	Evaluation of the Hartmann-Hahn (HH) CP matching conditions	31
	2.2		ts and discussion	32
		2.2.1	Description of the CP dynamics under on-resonance S -spin irradiation	
		2.2.2	Description of the CP dynamics under off-resonance S -spin irradiation	
		2.2.3	State-picture representation of the CP spin dynamics	42

Contents

	2.3	Concl	usions	51
3		-	theory of cross-polarization (CP) dynamics between spin- $1/2$ l nuclei	53
	3.1	_		54
	0.1	3.1.1	Derivation of the effective CP Hamiltonians via the effective-field	01
		0.1.1		55
		3.1.2	Time-evolution of the spin-system during the CP mixing period	59
		3.1.3		60
		3.1.4		60
	3.2			61
		3.2.1	Description of CP dynamics in a single-crystal (with specific orientation α_Q and $\beta_Q = 0^{\circ}$)	
		3.2.2	Description of CP dynamics in a single-crystal (with general	69
		3.2.3	Description of the CP dynamics in a powder sample	
		3.2.4	Extraction of the dipolar coupling parameters from the CP lineshapes	
	3.3	Concl	usions	
4		resona Theor	y	81 82
		4.1.1	Derivation of the effective CP Hamiltonians via the effective-field method	83
		4.1.2	Time-evolution of the spin-system	89
		4.1.3	Detection of the S -spin polarization: CP Signal calculation	92
		4.1.4	Insights into the Hartmann-Hahn CP matching conditions	93
	4.2	Result	s and discussion	95
		4.2.1	Description of CP spin-dynamics under the second-order quadrupolar coupling interaction	95
		4.2.2	State-picture representation of the CP dynamics a single-crystal sample	ഹ
	4.3	Concl	usions	
5	Ana	alytic t	theory of cross-polarization (CP) dynamics between spin- $1/2$	
	and	spin-3	3/2 nuclei 1	14
	5.1	Theor	y and Methodology	.15
		5.1.1	Derivation of the effective CP Hamiltonian	.15
		5.1.2	Time-evolution of the spin-system during the CP mixing period 1	.21
		5.1.3	Detection of the S -spin polarization	.23
		5.1.4	Insights into the Hartmann-Hahn CP matching conditions 1	.24
	5.2	Result	s and discussion	26

xii Contents

	5.2.1	Description of CP dynamics in a single-crystal (with specific orientation α_Q and $\beta_Q = 0^{\circ}$)	197
	5.2.2	Description of CP dynamics in a single-crystal (with general	
		orientation α_Q and $\beta_Q \neq 0^{\circ}$)	
	5.2.3	Description of the CP dynamics in a powder sample	
	5.2.4	Extraction of the dipolar coupling parameters from the CP lineshapes	
5.3	3 Concli	usions	148
6 Sı	ummary	and Conclusions	150
	A	Theory and Methodology: An effective-field approach to understand	
		the mechanism of cross-polarization dynamics between spin- $1/2$	
		systems	150
	В	Analytic theory of cross-polarization (CP) dynamics between	
		spin-1/2 and spin-1 nuclei	151
	\mathbf{C}	Understanding the role of second-order quadrupolar coupling and	
		off-resonance effects in CP dynamics	151
	D	Analytic theory of cross-polarization (CP) dynamics between	
		spin-1/2 and spin-3/2 nuclei	152
Refe	rences		154
Appe	endix		168
Appe	endix A		168
Α.	.1 Matrix	x representation of the basis states and spin-operators for the $S=1$	
	spin-sy	ystem	168
Appe	endix B		170
В.	.1 Matrix	x representation of the product basis states and spin-operators for the	
	I=1	/2 and $S = 1/2$ coupled spin-system	170
Appo	endix C		172
С.	.1 Matrix	x representation of the product basis states and spin-operators for the	
	I = 1	/2 and $S=1$ coupled spin-system	172
С.	.2 Descri	aption of CP spin dynamics based on existing reports	172
Appe	endix D		181
		cients in the calculation of the density matrix in TQ_{16} , SQ_{34} , DQ_{15} ,	-0-
2.		DQ_{26} and ZQ_{35} subspaces	182
Δ nn.	endix E		188
		x representation of the basis states and spin-operators for the $S=$	100
₽.		oin-system	188

	•••
Contents	X111
0016601663	AII

E.2	E.2 Matrix representation of the product basis states and spin-operators for the	
	I=1/2 and $S=3/2$ coupled spin-system	3
Public	eations 188	3

List of Symbols

 $\hat{S}_x, \hat{S}_y, \hat{S}_z$ Spin-angular momentum components for nuclear spin S

 (α, β, γ) Euler angles of rotation

 $\gamma_{I/S}$ Gyromagnetic ratios of nuclear spin I/S

Zeeman interaction Hamiltonian

 μ Nuclear magnetic moment

 ω_0 Larmor precession frequency

 $\omega_{1S/1I} = 2\pi\nu_{1S/1I}$ RF amplitude for nuclear spin S/I

 ω_d Heteronuclear dipolar coupling frequency

 ω_{eff} Effective frequency

 ω_Q Quadrupolar coupling frequency

 $\omega_O^{(1)}$ First-order quadrupolar frequency

 $\omega_O^{(2)}$ Second-order quadrupolar frequency

 Ω_S S-spin offset

 θ_m Magic angle

NMR active isotope of Carbon-13 (I=1/2)

NMR active isotope of Nitrogen-14 (I=1)

NMR active isotope of Nitrogen-15 (I=1/2)

NMR active isotope of Sodium-23 (I=3/2)

 C_Q Quadrupole coupling constant

 $D_{mm'}^{l}(\alpha, \beta, \gamma)$ Wigner rotation matrix

I/S Spin-quantum number

Q Quadrupole moment

 \mathbf{r}_{ij} Internuclear distance between nuclear spins i and j

 \mathbf{R}_{m}^{l} Spatial tensor with rank l and component m

S(t) Signal expression

List of Symbols

T^l_m	Spherical tensor with rank l and component m
$\hat{ ho}(0)$	Density matrix at time instant $t = 0$
$\hat{ ho}(t)$	Density matrix at time instant t
\hat{H}_{CP}	CP Hamiltonian
\hat{H}_D	Heteronuclear dipolar coupling Hamiltonian
\hat{H}_{eff}	Effective Hamiltonian
$\hat{H}_Q^{(1)}$	First-order quadrupolar coupling Hamiltonian
$\hat{H}_Q^{(2)}$	First-order quadrupolar coupling Hamiltonian
\hat{H}_{RF}	RF interaction Hamiltonian
$\hat{I}_x,\hat{I}_y,\hat{I}_z$	Spin-angular momentum components for nuclear spin ${\cal I}$
\hat{S}^{ij}_{lpha}	Single-transition operator between energy state $ i\rangle$ and $ j\rangle$ where $\alpha=x,y,z$
$\hat{U}(\mathrm{t})$	Unitary transformation function
\hbar	$h/2\pi$
$^{1}\mathrm{H}$	NMR active isotope of Proton $(I=1/2)$
AHT	Average Hamiltonian theory
CP	Cross-polarization
CT	Central transition
CW	Continuous-wave
DQ	Double-quantum
EFG	Electric-field gradient
FQ	Four-quantum
FT	Fourier Transform
h	Planck constant
HH	Hartmann-Hahn
LAB	Laboratory axis frame
MAS	Magic Angle Spinning
MolAS	Molecular axis system

xvi List of Symbols

NMR Nuclear Magnetic Resonance

PAS Principal axis system

RF radio-frequency

SQ Single-quantum

ssNMR Solid-state nuclear magnetic resonance

ST Satellite transition

TLS Two-level system

TQ Triple-quantum

ZQ Zero-quantum

Chapter 1

Introduction

1.1 Introduction

Following the discovery by Felix Bloch and Edward Mills Purcell in 1946 [1,2], Nuclear Magnetic Resonance (NMR) spectroscopy has become an indispensable tool for structural characterization of chemical compounds in solution and solid states. The heart of NMR spectroscopy lies in the various internal (magnetic and electric) interactions present in the system, which collectively rise as a source of structural constraints in the form of chemical environment, internuclear distances, torsional angles, etc., and dynamics at an atomic level. NMR spectroscopy has gained popularity among other types of spectroscopic methods due to its ability to tailor these internal interactions through spin and/or space manipulations, allowing determination of the structural constraints of interest. Despite the presence of similar nuclear spin interactions in solution and solid-state samples, the solid samples exhibit broad and featureless spectra due to the restricted mobility of molecules. The rapid tumbling motion in the solution sample produces well-resolved and sharp resonances rendered by the spatial averaging of the orientation-dependent (anisotropic) interactions. The low resolution and sensitivity in solid-state NMR is caused by anisotropic broadening. Additional challenges come from the poor signal-to-noise (S/N) ratio of the NMR spectra [3,4] due to lower gyromagnetic ratio and natural abundance. Except ¹H and ¹⁹F, all nuclear spins suffer from the poor S/N or sensitivity issue due to their low natural abundance and/or gyromagnetic ratio; therefore, all NMR active nuclei are classified as abundant spin (¹H and ¹⁹F) and dilute or less-abundance spins (e.g., ²H, ¹³C, ^{15/14}N, ²³Na, etc.). Due to high natural abundance and widespread occurrence in the majority of the organic and inorganic compounds, the ¹H NMR has attracted a great deal of attention in the NMR spectroscopy. However, the stronger ¹H-¹H homo-nuclear dipolar coupling network coupled with its small chemical shift range, made one-dimensional (1D) ¹H NMR analysis almost impossible for slightly larger molecules due to poor resolution and sensitivity. Discoveries of the Magic Angle Spinning (MAS) by E. R. Andrew et. al. [5] and Lowe et. al. [6] in 1953 and Fourier Transform (FT) NMR by R.R. Ernst [7] had a significant influence on the hardware and technological advancements of the NMR spectroscopy tailored towards improved resolution and sensitivity. These advancements have increased flexibility in the design and development of new pulse sequences, therefore opening the door to a wide range of samples to be studied through the solution and solid-state NMR. The magic angle spinning (MAS) technique has been the major thrust towards multisite resolution and sensitivity enhancement of solid-state NMR spectra by

averaging the orientation-dependent interactions. The solid sample is rapidly spun in a rotor inclined at the magic angle $\theta_m = 54.736^{\circ}$, with respect to the Zeeman magnetic field, which mimics the tumbling motion of solution samples, but at the cost of inducing periodic time-dependence [8] to the interaction Hamiltonian. Improved resolution and sensitivity rendered due to MAS has resulted in increased interest in observing dilute spins like ¹³C and ¹⁵N, etc. Due to their large chemical shift dispersion and smaller homo-nuclear dipolar coupling network, even at slow MAS (range) we may accomplish the desired resolution by averaging anisotropic interactions. Nevertheless, the poor sensitivity remained a major concern for observing such dilute spins, as MAS alone may not provide the desired sensitivity [9]. Although isotopic enrichment can alleviate the problem of their lower natural abundance, however only at a high cost and with the requirement of large sample volume. To this end, most of the developments in the solid-state NMR spectroscopy have been focused on improving the sensitivity without compromising the structural The polarization transfer-based experiments, such as cross-polarization information. (CP) [10], insensitive nuclei enhanced by polarization transfer (INEPT) [11], nuclear Overhauser effects (NOE) [12], dynamic nuclear polarization transfer (DNP) [13, 14], etc. have been the best-suited choice for enhancing the sensitivity of the dilute spins. These experiments are based on the fact that in solids, the dilute spins lie in close or spatial proximity of the abundant spin (mostly ¹H) and are connected via a heteronuclear dipolar coupling interaction which is exploited to transfer the large polarization of abundant spins to less abundant spin. One such experiment in solids is the double-resonance cross-polarization (CP) experiment introduced in 1962 by Hartmann and Hahn, [10] (also referred to as the Hartmann-Hahn CP). Since its inception, CP has become an integral building block of solid-state nuclear magnetic resonance (ssNMR) experiments for observing less sensitive nuclei. The CP [10, 15-17] between highly abundant nuclei I =1/2 (e.g., ¹H with high gyromagnetic ratio) and less abundant (insensitive) nuclei S =1/2 (e.g., ¹³C, ¹⁵N, ²⁹Si, etc., with low gyromagnetic ratio) spins is a routinely employed experimental method for signal enhancement of insensitive nuclei in solid samples. The polarization transfer is mediated through the heteronuclear dipolar coupling interaction by simultaneous irradiation of radio-frequency (RF) fields (spin-locking) applied on both nuclei [18]. The polarization transfer is maximized when the RF amplitudes on both nuclei are matched, a condition that is referred to as the Hartmann-Hahn (HH) energy level matching condition ($\omega_{1I} = \pm \omega_{1S}$) for static (non-rotating) samples [10, 17]. For spinning samples, the magic angle (MAS) averages the heteronuclear dipolar coupling, which is the medium of polarization transfer. In this regard, Schaefer et. al. [19] showed that simultaneous RF irradiation interfere with the spinning frequency at the rotor period, and the heteronuclear dipolar coupling can be reintroduced. Under sample spinning, the HH conditions are modified and the polarization transfer is maximized only when the difference in the RF amplitudes on both spins is equal to the multiples of the spinning frequency ($\omega_{1I} = m\omega_r \pm \omega_{1S}$) and the strength of the heteronuclear dipolar coupling is much smaller than the spinning frequency [17, 19–28]. Since then, the CPMAS experiment combined with heteronuclear decoupling has become a standard technique for the excitation of dilute spins [29–31]. Apart from the sensitivity enhancement, the CP-based transfer is also used to probe internuclear dipolar connectives, rigidity and mobility of the sample dynamics and spectral editing in multi-dimensional experiments [32–37]. Due to the wider applications of cross-polarization experiments, the technique forms the building block of around 80-90% of the solid-state nuclear magnetic resonance (NMR) experiments. In the literature, many variants of CP exist for spin-1/2 systems such as continuous-wave (CW), amplitude-modulated RAMP-CP [22] and adiabatic CP [38], frequency-modulated broadband BRAIN-CP [39], Lee-Goldberg (LG)-CP [40], etc. From a theoretical perspective, the underlying spin dynamics of CP transfer between spin-1/2 nuclei is well understood and documented in the literature [25, 26, 41–43].

Although CP-based polarization transfer among spin-1/2 systems (between I = 1/2 and S=1/2) is a routinely employed experimental technique [17, 19, 23, 24], its applicability to quadrupolar spins (S > 1/2) remains less straightforward and less intuitive [16, 44–49]. From a practical aspect, the polarization transfer among spins in the CP experiment is established through appropriate matching of the radio frequency (RF) fields employed on the spins of interest. Since the amplitude of the RF fields employed in the CP experiments are much higher (magnitude-wise) than the magnitude of the internal spin interactions (such as chemical shift, dipolar coupling interactions, etc.), the optimal implementation of the CP experiment is well-established and described within the existing theoretical frameworks. Nevertheless, a straightforward extension of the theory of CP dynamics involving quadrupolar spins $(S > 1/2; {}^{2}D, {}^{6}Li, {}^{14}N, {}^{23}Na, {}^{35}Cl, etc.)$ is less straightforward and less intuitive for both static as well as spinning samples [45, 47–50, 50–62]. The quadrupolar nuclei (S > 1/2) constitute around 75% of all NMR active nuclei [16,63] and are present in the majority of organic, biomolecular, and inorganic compounds [64–68]. Furthermore, due to their non-spherical nuclear charge distribution, the presence of quadrupolar interaction provides an additional structural constraint, namely the electronic environment. A detailed description of the quadrupolar coupling interaction is provided in the next section. Quadrupolar nuclei suffer from poor sensitivity and resolution due to their lower gyromagnetic ratio and/or natural abundance, and the presence of high electric quadrupolar coupling strength (kHz to MHz range). With the currently available RF irradiation strengths, the direct excitation of quadrupolar nuclei for getting structural constraints and spectral assignments is always challenging. To overcome this issue, in the last few decades, many different excitation schemes have been developed to improve their excitation efficiency and sensitivity [69,70]. Among quadrupolar nuclei, the half-integral nuclei (S = 3/2, 5/2, 7/2, etc.) have the presence of single-quantum central transition (CT), which is first-order quadrupolar coupling devoid, therefore have better excitation efficiency and resolution [71–76]. Nevertheless, the central transitions (CT) are broadened by the higher-order (kHz) quadrupolar effects [77]. These higher-order broadenings can be scaled down by the MAS and high magnetic fields but cannot be completely averaged out [78]. In contrast the integral spins (S = 1, 3, etc.) lack the first-order quadrupolar devoid central

transitions and therefore remained less explored nuclei [79–81]. Even after nearly seven decades of NMR, poor sensitivity and resolution remained the main roadblock in the quadrupolar NMR. Despite CP being an established technique of sensitivity enhancements for spin-1/2 nuclei, its applicability to quadrupolar nuclei remains less straightforward and less intuitive. In CP experiments involving quadrupolar nuclei, the magnitude of the quadrupolar interaction (ranging from a few kHz to MHz) in general is much higher than the magnitude of other internal spin interactions and the amplitude of the available RF fields [16, 44, 71, 82, 83]. Consequently, identifying the exact HH matching conditions essential for the optimal implementation of CP experiment is often fraught with difficulty [84]. Besides, the presence of multiple energy levels/transitions lead to inefficient spin-locking and therefore poor CP transfer efficiency [85–89]. Depending on the strength of quadrupolar interaction, the Zeeman energy levels are modified to different orders of magnitudes during the simultaneous RF irradiation and result in several CP matching conditions that complicate the unified theoretical description of the CP dynamics. The periodic modulation of the energy level matching caused by MAS further complicates the spin-locking process. Although, on the theoretical front, a handful of research work associated with the quadrupolar CP spin-dynamics is available in the literature [45–49,54,81,90–94], a comprehensive description of the CP matching conditions over a wide range of quadrupolar coupling constants has remained challenging. This limitation has remained a major roadblock in the design and development of CP-based experimental methods for quadrupolar spins [58,59,62,82,95–101] and forms the motivation behind the thesis.

From a theoretical perspective, the presence of the dominant quadrupolar interactions has often been the main hindrance in analytic descriptions [69, 83, 102] of the spin dynamics in quadrupolar CP experiments. To this end, descriptions in the quadrupolar interaction frames were proposed for describing the spin dynamics. In combination with Average Hamiltonian theory (AHT) [3, 90, 103] and in some cases with Floquet theory [93,104–109], semi-analytical methods have also emerged for describing experiments involving quadrupolar spins, both in non-rotating (static) and rotating solids. In the initial description proposed by Vega and coworkers [45,47], the CP dynamics was described in systems with larger quadrupolar interactions based on effective Hamiltonians derived using the fictitious spin-1/2 operator formalism [17, 110-113]. Nevertheless, such descriptions were of limited utility in quantifying the CP profiles in powder samples due to the distribution of quadrupolar coupling frequencies. In a subsequent development, Ernst and coworkers [90] presented an alternate description of the CP experiment that was specific to cases where the quadrupolar coupling constant was on par with the amplitude of the radio-frequency field employed on the quadrupolar spin. However, their approach was restricted only to the special case mentioned above and was of limited utility in addressing the dynamics in powder samples. In an alternate formulation, Pratum and Klein [91] predicted the presence of additional matching conditions and derived approximate Hamiltonians that could qualitatively explain the CP matching conditions observed in experiments. Nevertheless, a comprehensive analytic description of the CP dynamics over a wide range of experimentally relevant parameters has always been challenging, even for static samples. To address this issue, in this thesis, we attempt an alternate approach to describe the CP dynamics consistent with experimental observations. In contrast to perturbative methods employed in the quadrupolar interaction frame, the CP dynamics is described through effective Hamiltonians derived from rotation operators based on the "effective-field" approach [70, 80, 109, 114, 115]. The proposed analytic framework based on the effective-field approach offers faster convergence and presents an attractive framework for describing the underlying spin dynamics in both isotropic and anisotropic solids. Accordingly, the CP matching conditions observed are described in terms of the transition operators associated with a given system [114,115]. With this objective in mind, an analytic theory based on the concept of effective Hamiltonian is proposed to offer a detailed description of the CP spin dynamic involving quadrupolar spins. A brief outline of the thesis is given in the next section.

1.2 Objectives and scope of the thesis

In order to improve the efficiency of polarization transfer in quadrupolar spins, developing an operator-based analytic theory is vital. The theoretical descriptions should be equally valid in describing the CP dynamics in all the quadrupolar coupling regimes, both for single crystal (single crystallite orientation with respect to the applied Zeeman field) as well as powder samples wherein quadrupolar coupling frequencies are distributed over a wide range of crystallite orientations. Besides, the analytic theory of CP dynamics described in a coupled spin operator basis through a single mathematical framework is not available. In contrast to the existing theoretical models, we attempt to provide an alternate description of the CP dynamics using effective Hamiltonians derived from rotation operators based on the "effective-field" approach [115–117]. We show that the effective-field approach adopted in the thesis for describing the CP dynamics results in a faster convergence with improved accuracy.

The thesis is based on the following three objectives:

- To present an operator-based analytic theory of CP dynamics between spin-1/2 (I) and spin-1 (S) systems using the effective-field method under S-spin on-resonance irradiation and the first-order quadrupolar coupling Hamiltonian.
- To understand the role of the second-order quadrupolar coupling and the S-spin off-resonance irradiation in the CP dynamics between spin-1/2 and spin-1 systems.
- To use the effective-field approach for describing the CP dynamics between spin-1/2 (I) and spin-3/2 (S) systems.

In the section below, we have provided a brief description of the nuclear spin interactions and the density operator approach to study the time-evolution of the spin-system under the effective NMR interaction Hamiltonian.

1.3 Fundamentals of NMR

1.3.1 Nuclear spin interactions in NMR

NMR spectroscopy relies on non-zero spin angular momentum (represented as I) property of the nuclear spin. Like mass, size and charge, nuclear spin angular momentum is a fundamental/intrinsic property of an atom/nucleus. However, unlike mass and size, spin angular momentum has no classical analog and therefore requires quantum-mechanical description of the nuclear spin interaction. The nuclear spin angular momentum can be correlated with the nuclear magnetic moment μ as $\mu = \hbar \gamma I$, where γ is the gyromagnetic ratio. Therefore, the presence of nuclear spin angular momentum gives rise to a tiny magnetic field/moment (\approx n Tesla) around the nucleus, which is directed along/opposite to the direction of spin angular momentum depending on the sign of the gyromagnetic ratio. Classically, when these tiny magnets are placed inside a strong static magnetic field (B_0) try to align themselves along the direction of the static magnetic field and start precession around the static field due to torque with the frequency termed as Larmor precession frequency ($\omega_0 = -\gamma B_0$) [16,44]. Under thermal equilibrium, this process results in a minimum energy state and a net nuclear bulk magnetization is generated. In a real system, the NMR sample consists of an ensemble/collection of nuclear spins, each spin with its own tiny magnetic field interacting with other nuclear spins or with an external magnetic field present around the nucleus. Therefore, the interaction in NMR can be broadly classified as internal and external interactions, with a detailed explanation provided in the following section.

A. External Interactions:

The external interactions are classified as the interactions between the magnetic field of the nuclear spin and the externally applied magnetic fields like the Zeeman field and electromagnetic wave (radio-frequency field).

AI. Zeeman Interaction:

Any nuclear spin with spin quantum number I possesses 2I+1 energy levels. In the absence of an external magnetic field, these energy levels are equally populated, *i.e.*, the total energy difference will be zero under the effect of thermal processes. However, as soon as the external field (B_0) is switched on, the total energy of the system will undergo a redistribution creating a net energy difference. This interaction between the magnetic moment of the nuclear spin and magnetic field is termed as the Zeeman interaction [118, 119] and the Hamiltonian for this interaction is given as

$$\hat{H}_z = -\sum_i \mu_i . B_0 = -\sum_i \hbar \gamma_i \hat{I}_{iz} . B_0 = \sum_i \hbar \omega_{0i} \hat{I}_{iz};$$
 (1.1)

where the Zeeman field (B_0) is applied along a fixed direction (z-axis). Here $\omega_{0i}(=-\gamma_i B_0)$ and γ_i are the Larmor precession frequency and gyromagnetic ratio of nuclear spin i, respectively. $\hbar = h/2\pi$, where h is the Planck's constant. This is the strongest interaction in NMR and all other interactions act as perturbations to the Zeeman interaction. It has a timescale of $(t_c = 2\pi/\omega_{0i})$ nanosecond. Therefore, any other process should have a longer time scale than the Zeeman interaction to be observed. The Zeeman energy level for I = 1/2, 1 and 3/2 spin systems are shown in Figure 1.1.

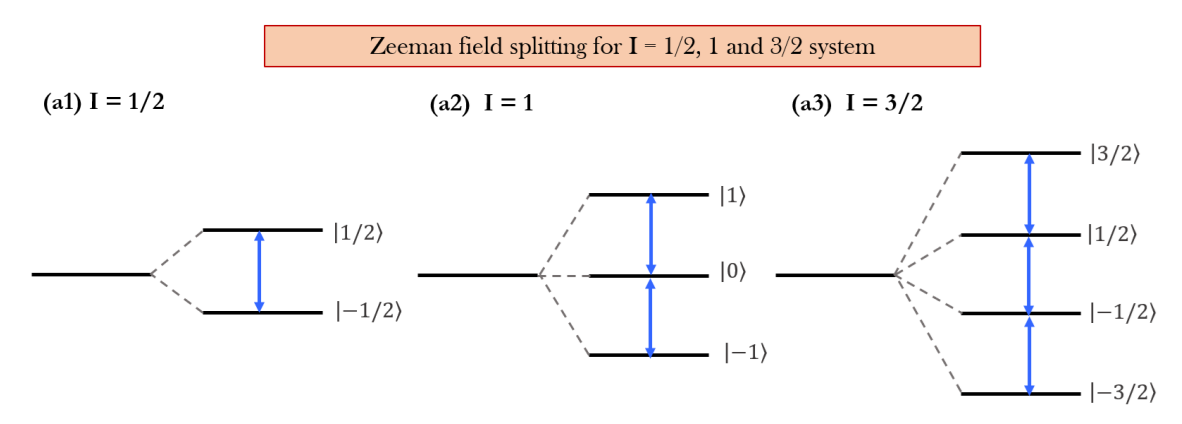


Figure 1.1: Schematic representation of the Zeeman energy levels for the I = 1/2, 1 and 3/2 spin systems

AII. Radio-frequency (RF) field interaction:

The purpose of the Zeeman interaction is to generate a population difference between the Zeeman energy levels. However, in order to observe this population difference, an oscillatory/rotating radio-frequency field is applied in the perpendicular direction (x/y) to the Zeeman field (z), which acts as a time-dependent perturbation and causes an oscillatory population exchange between the ground and excited states [120]. Once the radio-frequency field is turned off, the system tries to regain its original equilibrium state by releasing this energy resulting in an NMR signal in terms of free induction decay (FID). The interaction Hamiltonian for this interaction is given as

$$\hat{H}_{RF} = -\mu_i \cdot B_{RF}(t)\hat{x}$$

$$= -2\hbar\gamma_i B_1(t)\cos(\omega_{RF}t + \phi)\hat{I}_x$$
(1.2)

where $B_{RF}(t) = 2B_1(t)\cos(\omega_{RF}t + \phi)$.

$$\hat{H}_{RF} = 2\hbar\omega_{1i}(t)\cos(\omega_{RF}t + \phi)\hat{I}_x; \quad \omega_{1i}(t) = -\gamma_i B_1(t). \tag{1.3}$$

Here $B_1(t)$ and $\omega_{1i}(t)$ represent the amplitude and nutation frequency of the radio-frequency field, respectively, which could be time-independent or dependent and (ω_{RF}, ϕ) represent the frequency and phase of the RF field, respectively. In NMR language, the term $\omega_{1i}(t)$ is referred to to as the amplitude of the radio-frequency field and this terminology is used throughout this thesis. \hat{I}_x is the spin-operator pointing in the direction

of the applied B_1 field. The direction of the applied RF field can be altered by changing the phase of the RF pulse.

B. Internal Interactions:

Below a brief mathematical description of all the internal NMR interactions is given.

BI. Chemical shielding interaction:

It is the indirect interaction between the magnetic moment of the nucleus (μ_i) with the Zeeman field (B_0) mediated through the surrounding electron clouds. The electrons due to their orbital and spin-angular momentum possess a magnetic field which due to their negative sign of the gyromagnetic ratio generally opposes the magnetic field of the nuclear spin (induced field); hence the nuclear spin gets shielded from the applied Zeeman field and termed as chemical shielding interaction [3]. This difference in the local magnetic field experienced by the nuclear spin is different from the actual magnetic field applied as given below:

$$\hat{B}_{ind} = \hat{\sigma}.\hat{B}_0. \tag{1.4}$$

Here $\hat{\sigma}$ is the chemical shielding tensor, which contains the information about the electronic environment like isotropy, anisotropy, degree of asymmetry and the orientation of electrons with respect to the nucleus and the Zeeman field. The Hamiltonian for this induced interaction is given as

$$\hat{H}_{ind} = -\hbar \sum_{i} \mu_{i} \cdot \hat{\hat{\sigma}} \cdot \hat{B}_{0}. \tag{1.5}$$

The local magnetic field experienced by the nuclear spin in the presence of the surrounding electrons is given by

$$\hat{B}_{local} = \hat{B}_0 - \hat{B}_{ind}
= \hat{B}_0 - \hat{\sigma} \cdot \hat{B}_0.$$
(1.6)

The Hamiltonian for the chemical shift is given as

$$\hat{H}_{chemical shift} = -\hbar \sum_{i} \mu_{i}.\hat{B}_{loc,i} = -\hbar \sum_{i} \gamma_{i}\hat{I}_{iz}.(\mathbb{I} - \hat{\sigma}).\hat{B}_{0}. \tag{1.7}$$

This acts as a fingerprint of the local electronic environment in the NMR spectrum.

BII. J-coupling interaction:

Like chemical shielding interaction, the electronic clouds can establish indirect interaction between two or more magnetically inequivalent nuclei, and this interaction is termed as the scalar or J-coupling [121]. It arises due to the coupling of the angular momentum of two individual nuclei. The Hamiltonian for this interaction is given as

$$\hat{H}_J = h \sum_{i,j} \hat{I}_i . \hat{\hat{J}} . \hat{I}_j. \tag{1.8}$$

Here \hat{J} is the second-rank J-coupling tensor and (i,j) refer to the two nuclei involved in the coupling. In this coupling, the angular momenta of two nuclei couples due to the presence of electron clouds; it is independent of their orientation or internuclear distance and hence is labeled as a scalar or J-coupling. This interaction occurs via bonding electrons; therefore, its strength falls dramatically with an increase in bond distance and is usually studied to understand the chemical bonding between the nuclei. The magnitude of this interaction is smaller than any other internal interactions present, therefore, it is usually ignored in solid-state NMR.

BIII. Dipolar coupling interaction:

A nuclear spin acts as a tiny magnetic dipole, therefore, it can interact with other magnetic dipoles without any external mediation. This through-space interaction between nuclear spins is termed as dipole-dipole interaction. Unlike J-coupling, this is a vector coupling interaction that depends on the orientation of the involved spins with respect to the magnetic field. The Hamiltonian for this interaction is given as

$$\hat{H}_D = \frac{\gamma_i \gamma_j \hbar^2}{r_{ij}^3} \sum_{i,j} \hat{I}_i \cdot \hat{\hat{D}} \cdot \hat{I}_j \tag{1.9}$$

where \hat{D} is the dipolar coupling tensor, which like any other NMR interaction, is a second-rank tensor and r_{ij} is the internuclear distance between nuclear spins i and j. This interaction could occur between any magnetically active nuclear spins; therefore, it is classified as homo (like spin-pair) and heteronuclear (different spin-pair) dipolar interactions.

BIV. Electric quadrupolar coupling interaction:

The structure of the nucleus is influenced by the distribution of nucleons within the nucleus, which in turn affects the total spin angular momentum and is the central property of interest in NMR spectroscopy. The charge distribution of the nucleus with total charge "Ze" (Z is the atomic number or total number of protons and e is the charge on a single proton) is described in terms of the nuclear charge density (ρ) per unit volume inside the nucleus [16,122,123]. Classically, the electrostatic interaction energy of the nuclear charge with the electric potential V around the nucleus is given by the following Eq.,

$$E = \int \rho(r)V(r)d\tau \tag{1.10}$$

where $\rho(r)$ corresponds to the nuclear charge density per unit volume (see Figure 1.2 for a pictorial representation) and the electric potential V(r) arises due to the non-uniform distribution of electrons and surrounding nuclei. The electric potential around the nucleus can be presented in terms of multipole expansion around the center of mass of the nucleus.

$$E = \int \rho(r) \Big\{ V(0) + \sum_{i} x_{i} \Big(\frac{\partial V}{\partial x_{i}} \Big)_{r=0}(r) + \frac{1}{2!} \sum_{i,j} x_{i} x_{j} \Big(\frac{\partial^{2} V}{\partial x_{i} x_{j}} \Big)_{r=0} + \dots \Big\} d\tau$$

$$= V(0) \int \rho(r) d\tau + \sum_{i} \Big(\frac{\partial V}{\partial x_{i}} \Big)_{r=0} \int x_{i} \rho(r) d\tau + \frac{1}{2!} \sum_{i,j} \Big(\frac{\partial^{2} V}{\partial x_{i} x_{j}} \Big)_{r=0} \int x_{i} x_{j} \rho(r) d\tau + \dots$$

$$(1.11)$$

where

 $\int \rho(r)d\tau = Ze$ is the electric monopole and corresponds to the total nuclear charge, $\int x_i \rho(r)d\tau = P_i$ is the electric dipole moment and it is a vector quantity and $\int x_i x_j \rho(r)d\tau = Q_{ij}$ is the electric quadrupole moment and is a second-rank tensor. The above Eq. is re-written as

$$E = ZeV(0) + \sum_{i} E_{i}P_{i} + \frac{1}{2!} \sum_{i,j} \left(\frac{\partial E_{i}}{\partial x_{j}}\right)_{r=0} Q_{ij} + \dots$$
 (1.12)

In the above Eq., $V_i = \frac{\partial V}{\partial x_i} = E_i$ and $V_{ij} = \frac{\partial^2 V}{\partial x_i x_j} = \frac{\partial E_i}{\partial x_j}$ correspond to the electric field and electric field gradient (EFG) tensor components, respectively.

The first term in Eq. (1.12) represents pure electrostatic potential energy, which does not result in any NMR energy level shift, while the second term represents the interaction between the nuclear electric dipole moment and electric field around the nucleus, which is usually parity forbidden because it moves the center of mass of the nucleus. However, the third term in Eq. (1.12) can be finite and it is referred to as quadrupolar coupling interaction. This interaction represents the coupling of the quadrupole moment (Q) of the nucleus with the electric field gradient (EFG) present around the nucleus. Higher-order multipole expansion terms are generally not finite in NMR spectroscopy.

$$E_Q = \frac{1}{2} \sum_{i,j} V_{ij} Q_{ij}. \tag{1.13}$$

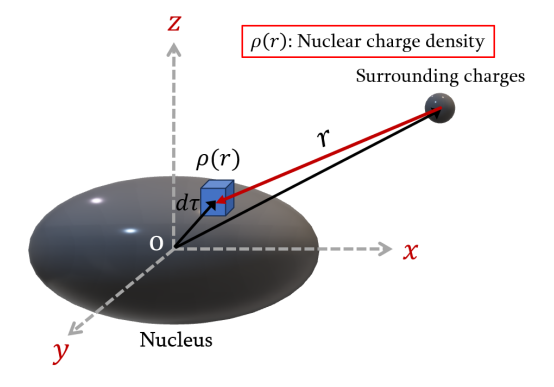


Figure 1.2: Electrostatic interaction between the nucleus and the electric potential V (due to surrounding charges) in the center of mass (O) fixed Cartesian co-ordinate system. Here $d\tau$ is the volume element inside the nucleus with the nuclear charge density $\rho(r)$ at distance r from the surrounding charge.

It is always convenient to define a principal axis system (PAS) of the potential V where all the off-diagonal terms of the EFG are zero, i.e. $\sum_{i,j} V_{ij} = 0$ if $i \neq j$; hence electric quadrupolar interaction is traceless. For mathematical convenience, it will prove beneficial to define Q_{ij} as:

$$Q'_{ij} = \int (3x_i x_i - \delta_{ij} r^2) \rho d\tau. \tag{1.14}$$

Substituting this in the Eq. (1.13) results

$$E_Q = \frac{1}{6} \sum_{i,j} V_{ij} Q'_{ij}. \tag{1.15}$$

The above Eq. represents the quadrupolar interaction energy in terms of classical moments, which needs to be transformed into its quantum-mechanical equivalent, *i.e.*, the Hamiltonian and quadrupolar spin operators for infusing the spin-angular momentum concept.

$$\hat{H}_Q = \frac{1}{6} \sum_{i,j} V_{ij} \hat{Q}'_{ij}. \tag{1.16}$$

Here the quadrupolar moment operator seems to be a function of all the nucleon's positions, which becomes a tedious many-body problem. However, in NMR transitions, we are only interested in the change in the nuclear spin angular momentum states. Using the Wigner-Eckart theorem [16, 124, 125] and the Clebsch-Gordan coefficients [126, 127], the matrix elements of the quadrupole operators can be represented as

$$\langle I, m | \hat{Q}'_{ij} | I, m' \rangle = C \langle I, m | \frac{3}{2} (\hat{I}_i \hat{I}_j + \hat{I}_j \hat{I}_i) - \delta_{ij} \hat{I}_{ij}^2 | I, m' \rangle$$
 (1.17)

where $C = \frac{eQ}{6I(2I-1)}$ and Q is the quadrupole moment of the nucleus. For nuclei with spherical charge distribution, the spin angular momentum become I = 1/2 and therefore, the higher-order expansion reduces to zero and the nuclei result in purely magnetic interaction in NMR [Eq. (1.17)]. However, nuclei with non-spherical nuclear charge distribution consists of non-zero higher-order terms in the multipole expansion and possesses quadrupolar moment [Eq. (1.17)]. Employing Eqs. (1.16) and (1.17), the quadrupolar coupling Hamiltonian is re-expressed as

$$\hat{H}_Q = \frac{eQ}{6I(2I-1)} \sum_{i,j} V_{ij} \left\{ \frac{3}{2} (\hat{I}_i \hat{I}_j + \hat{I}_j \hat{I}_i) - \delta_{ij} \hat{I}_{ij}^2 \right\}.$$
 (1.18)

or

$$\hat{H}_{Q} = \frac{eQ}{4I(2I-1)} \left[\sqrt{\frac{2}{3}} V_{0}(3\hat{I}_{z}^{2} - \hat{I}^{2}) - V_{+1}(\hat{I}_{-}\hat{I}_{z} + \hat{I}_{z}\hat{I}_{-}) + V_{-1}(\hat{I}_{+}\hat{I}_{z} + \hat{I}_{z}\hat{I}_{+}) + V_{+2}\hat{I}_{-}^{2} + V_{-2}\hat{I}_{+}^{2} \right]$$

$$(1.19)$$

where the components of the EFG tensor are given as

$$\begin{split} V_0 &= \sqrt{3/2} V_{zz}; \\ V_{+1} &= -V_{zx} - i V_{zy}; \\ V_{-1} &= V_{zx} - i V_{zy}; \\ V_{+2} &= \frac{1}{2} (V_{xx} - V_{yy}) + i V_{xy}; \\ V_{-2} &= \frac{1}{2} (V_{xx} - V_{yy}) - i V_{xy}. \end{split}$$

For a simplified representation, we consider the principal axis system (PAS) representation $(V_{ij} = 0 \ \forall \ i \neq j)$ of the above Hamiltonian where the EFG tensor is traceless $(V_{xx} + V_{yy} + V_{zz} = 0)$; hence the above Hamiltonian is reduced to a much simpler form.

$$\hat{H}_Q(PAS) = \frac{eQ}{4I(2I-1)} \Big[V_{zz} (3\hat{I}_z^2 - \hat{I}^2) + (V_{xx} - V_{yy})(\hat{I}_x^2 - \hat{I}_y^2) \Big]. \tag{1.20}$$

The above expression is re-expressed in terms of $V_{zz} = eq$ (magnitude of the largest components of the EFG tensor) and degree of asymmetry in the quadrupolar coupling tensor $\eta_Q = \frac{V_{xx} - V_{yy}}{V_{zz}}$.

$$\hat{H}_Q(PAS) = \frac{\hbar\omega_Q}{6} \left[(3\hat{I}_z^2 - \hat{I}^2) + \frac{\eta_Q}{2} (\hat{I}_+^2 - \hat{I}_-^2) \right],\tag{1.21}$$

where
$$C_Q = \frac{e^2 Qq}{\hbar}$$
 and $\omega_Q = \frac{3C_Q}{2I(2I-1)}$.

To achieve a more comprehensive mathematical description, the quadrupolar PAS Hamiltonian is transformed in the laboratory (LAB) frame defined by the Zeeman interaction. For simplified calculation, the quadrupolar PAS Hamiltonian is re-written in the tensorial representation as given below:

$$\hat{H}_Q(PAS) = \sum_{l=0}^{2} \sum_{m=-l,\neq 0}^{l} (-1)^m R_{-m}^l(PAS) T_m^l$$
(1.22)

where $R_{-m}^l(PAS)$ and T_m^l represent the spatial and spin parts of the quadrupolar Hamiltonian in the PAS system. The PAS quadrupolar interaction Hamiltonian is transformed into the LAB frame through a molecular axis system (MolAS) as given below:

$$\hat{H}_{Q}(LAB) = \sum_{l=0}^{2} \sum_{m=-l,\neq 0}^{l} (-1)^{m} R_{-m}^{l}(LAB) T_{m}^{l}$$

$$= \sum_{l=0}^{2} \sum_{m,m',m''=-l,\neq 0}^{l} (-1)^{m} R_{-m}^{l}(PAS) D_{mm'}^{l}(\alpha_{PM},\beta_{PM},\gamma_{PM})$$

$$\times D_{m'm''}^{l}(\alpha_{ML},\beta_{ML},\gamma_{ML}) T_{m}^{l},$$
(1.23)

where $D_{mm'}^l(\alpha_{PM}, \beta_{PM}, \gamma_{PM})$ and $D_{m'm''}^l(\alpha_{ML}, \beta_{ML}, \gamma_{ML})$ represent the Wigner matrices [124] from PAS to MolAS and MolAS to LAB frame transformations, respectively. In the case of single-crystal samples, the PAS and MolAS frames coincide.

1.3.2 Secular approximation

In NMR, the total Hamiltonian is given by the sum of all interactions (external + internal) acting in the spin system. Below, a representative Hamiltonian comprising all the interactions mentioned in the previous section is given:

$$\hat{H}_{total} = \underbrace{\hat{H}_Z + \hat{H}_{RF}}_{External} + \underbrace{\hat{H}_{CS} + \hat{H}_J + \hat{H}_D + \hat{H}_Q}_{Internal}$$
(1.24)

The size of various interactions follows the order, $||\hat{H}_Z|| >> ||\hat{H}_Q|| > ||\hat{H}_{RF}|| > ||\hat{H}_D|| \approx ||\hat{H}_{CS}|| > ||\hat{H}_J||$. The magnitude of the Zeeman interaction surpasses all the interactions present in the spin system, and all the remaining interactions act as perturbations to the Zeeman Hamiltonian. Therefore, NMR spectrum calculation involves diagonalization of the above Hamiltonian [Eq. (1.24)] employing various perturbative methods. A mathematically convenient method equivalent to a perturbative-based approach is to transform the total Hamiltonian into the Zeeman interaction frame, which removes the effect of Zeeman interaction, thereby facilitating the measurement of small internal interactions. The resulting Hamiltonian after the Zeeman interaction frame transformation is given below:

$$\hat{H}_{total}^{I}(t) = \hat{U}(t)\hat{H}_{total}\hat{U}(t)^{\dagger}$$
(1.25)

where $\hat{U}(t) = \exp\left\{-\frac{i}{\hbar} \hat{H}_Z t\right\} = \exp\{-i\omega_0 t \hat{I}_z\}$ is the required transformation operator/function. The above rotating frame transformation induces periodic time-dependency into the overall Hamiltonian with periodicity $\tau_0 = 2\pi/\omega_0$. However, considering the explicit form of the interaction Hamiltonian, it is evident that a portion of the interaction Hamiltonians (except the quadrupolar interaction) commute with the transformation function $\hat{U}(t)$ or \hat{I}_z operator and therefore remain time-independent (secular) on the Zeeman time-scale as given below:

$$\hat{H}_{total}^{I}(t) = \hat{H}_{total}^{I,secular}(t) + \hat{H}_{total}^{I,non-secular}(t); [\hat{H}_{total}^{I,secular}(t), \hat{I}_{z}] = 0.$$

$$(1.26)$$

Under secular approximation, the non-secular terms of the interaction Hamiltonians are ignored. This truncation of the Hamiltonian is equivalent to the first-order perturbation approximation. All the non-secular terms will result in higher-order energy shifts, which are generally insignificant in NMR. Under secular approximation, various internal interaction Hamiltonians are presented below:

$$\hat{H}_{CS} = \sum_{i} \hbar \omega_{i,CS} \hat{I}_{iz}$$
 for chemical shift interaction, (1.27)

$$\hat{H}_D^{hetero} = \sum_{i,j} \hbar \omega_{ij,D}^{hetero} \hat{I}_{iz} \hat{S}_{jz} \text{ for heteronuclear dipolar interaction,}$$
 (1.28)

and

$$\hat{H}_D^{homo} = \sum_{i,j} \hbar \omega_{ij,D}^{homo} (3\hat{I}_{iz}\hat{I}_{jz} - \hat{I}_i.\hat{I}_j) \text{ for homonuclear dipolar interaction.}$$
 (1.29)

Here the coefficients $\omega_{i,CS}$, $\omega_{ij,D}^{hetero}$ and $\omega_{ij,D}^{homo}$ are frequency components which include Wigner function for principal axis frame to laboratory axis frame transformation. However, the secular approximation does not always holds good for quadrupolar nuclei due to the large magnitude of the associated quadrupolar interaction. As this thesis is focused on the quadrupolar nuclei, therefore it is rational to give a detailed account of the quadrupolar Hamiltonian in the Zeeman interaction frame. As described previously, the transformation function $\hat{U}(t)$ [Eq. (1.25)] transforms the laboratory frame quadrupolar coupling Hamiltonian [Eq. (1.23)] into the Zeeman interaction frame as follows:

$$\hat{H}_{Q}^{I}(LAB;t) = exp(-i\omega_{0}t\hat{I}_{z})\hat{H}_{Q}(LAB)exp(i\omega_{0}t\hat{I}_{z})$$

$$= \hbar \sum_{l=0}^{2} \sum_{m=-l,\neq 0}^{l} (-1)^{m} R_{-m}^{l}(LAB)T_{m}^{l}exp(-im\omega_{0}t)$$
(1.30)

where the transformed Hamiltonian becomes time-dependent with the period $\tau_0 = 2\pi/\omega_0$. Using Average Hamiltonian theory [3, 20, 103, 128] (AHT), the quadrupolar Hamiltonian evaluated up to the second order of the perturbation correction is given as

$$\hat{H}_Q(LAB) \approx \hat{H}_Q^{(1)}(LAB) + \hat{H}_Q^{(2)}(LAB),$$
 (1.31)

where

$$\hat{H}_Q^{(1)}(LAB) = \frac{1}{\tau_0} \int_0^{\tau_0} \hat{H}_Q^I(t')dt' = \hbar R_0^2(LAB)T_0^2, \tag{1.32}$$

$$\begin{split} \hat{H}_{Q}^{(2)}(LAB) &= \frac{-\hbar}{2\tau_{0}} \int_{0}^{\tau_{0}} dt'' \int_{0}^{t''} [\hat{H}_{Q}^{I}(t''), \hat{H}_{Q}^{I}(t')] dt' \\ &= \frac{-\hbar}{2\omega_{0}} \left[R_{0}^{2}(LAB) R_{1}^{2}(LAB) [T_{0}^{2}, T_{1}^{2}] - R_{0}^{2}(LAB) R_{-1}^{2}(LAB) [T_{0}^{2}, T_{-1}^{2}] \right. \\ &+ R_{1}^{2}(LAB) R_{-1}^{2}(LAB) [T_{-1}^{2}, T_{1}^{2}] + \frac{1}{2} \left\{ R_{0}^{2}(LAB) R_{-2}^{2}(LAB) [T_{0}^{2}, T_{2}^{2}] \right. \\ &- R_{0}^{2}(LAB) R_{2}^{2}(LAB) [T_{0}^{2}, T_{-2}^{2}] - R_{2}^{2}(LAB) R_{-2}^{2}(LAB) [T_{-2}^{2}, T_{2}^{2}] \right\} \right]. \end{split}$$

$$(1.33)$$

The second-order quadrupolar coupling Hamiltonian for spin-1 systems may be simplified to a more concise form:

$$\hat{H}_{Q}^{(2)}(LAB) = \frac{-1}{2\omega_0} \left[R_1^2(LAB)R_{-1}^2(LAB)[T_{-1}^2, T_1^2] - R_2^2(LAB)R_{-2}^2(LAB)[T_{-2}^2, T_2^2] \right]. \tag{1.34}$$

The aforementioned quadrupolar Hamiltonians are reformulated in the spin-operator representation as

$$\hat{H}_Q^{(1)}(LAB) = \frac{\hbar\omega_Q^{(1)}}{6}(3\hat{S}_z^2 - \hat{S}^2),\tag{1.35}$$

and

$$\hat{H}_Q^{(2)}(LAB) = \hbar \omega_Q^{(2)} \hat{S}_z, \tag{1.36}$$

where $\omega_Q^{(1)}=\sqrt{6}R_0^2(LAB)$ and $\omega_Q^{(2)}=\frac{-1}{2\omega_0}\Big[R_1^2(LAB)R_{-1}^2(LAB)-R_2^2(LAB)R_{-2}^2(LAB)\Big]$ are the first and second-order quadrupolar coupling frequencies, respectively.

1.3.3 Time-Evolution of the spin-system

The quantum mechanical description of any experimental phenomenon requires studying or observing the change in the state of the system as a response to any external or internal perturbations acting on the system. In particular, any spectroscopic measurements involve studying either the emission or absorption of the energy by the system and consequently, generating corresponding energy spectrum. Depending on the state and nature of the system, the standard operational process involves the solution of the time-dependent Schrödinger equation or the quantum-Liouville equation. The time-dependent Schrödinger equation becomes a useful tool for describing the dynamics in systems with the pure state (a single wave function for the whole system) and is given below:

$$i\hbar \frac{\partial |\psi(t)\rangle}{\partial t} = \hat{H}(t) |\psi(t)\rangle$$
 (1.37)

where $|\psi(t)\rangle$ represents the state of the system at some instance t. The standard solution of Eq. (1.37) is written as

$$|\psi(t)\rangle = \underbrace{T\exp\left\{-\frac{i}{\hbar}\int_{0}^{t}\hat{H}(t')dt'\right\}}_{\text{Evolution-operator: }\hat{U}(t)}|\psi(0)\rangle. \tag{1.38}$$

Here $|\psi(0)\rangle$ is the initial state at t=0 and T is the Dyson time-ordering operator. Given that the state of any quantum-mechanical system is not known prior to the measurements, it is a common practice to express the state as a linear combination of the complete set of basis states, $|\phi\rangle_i$.

$$|\psi(t)\rangle = \sum_{i=1}^{n} C_i(t) |\phi\rangle_i$$
 (1.39)

where $C_i(t)$ are complex coefficients. These coefficients are essential for calculating the transition probability amplitudes for any time-dependent process. Subsequently, the expectation value of any observable of the interest $(\hat{O};$ mathematical equivalent of any physical quantity) can be calculated using the expression given below:

$$\langle \hat{O}(t) \rangle = \frac{\langle \psi(t) | \hat{O} | \psi(t) \rangle}{\langle \psi(t) | \psi(t) \rangle}.$$
 (1.40)

Although, the Schrödinger method is a standard approach for dealing with a quantum mechanical process, however, its utility is limited for bulk measurements, as in case of NMR spectroscopy. For the bulk sample, a single wave function cannot describe the

state of the whole spin-system (the system is said to have mixed states). Consequently, Eq. (1.38) necessitates handling the wave function for individual spins, followed by summation over the entire sample volume/ensemble. From a theoretical perspective, the Schrödinger method appears impractical and inadequate for bulk measurements. To overcome the challenge, the concept of density operator was invoked. In the density operator formulation, the state of individual spins is replaced by a more generalized state of the entire ensemble, denoted by $\rho(t)$ [129, 130]. Mathematically, $\rho(t)$ is defined as an average over the whole ensemble as given below:

$$\rho(t) = \overline{|\psi_j(t)\rangle\langle\psi_j(t)|} = \sum_{j=1}^{N} P_j |\psi_j(t)\rangle\langle\psi_j(t)|.$$
 (1.41)

The density operator is constructed in the basis $|\phi_i\rangle$ as described below:

$$\rho(t) = \sum_{j=1}^{N} P_j \sum_{i=1}^{n} \sum_{k=1}^{n} C_i(t) C_k^*(t) |\phi_i\rangle \langle \phi_k|$$

$$= \sum_{i=1}^{n} \sum_{k=1}^{n} \overline{C_i(t) C_k^*(t)} |\phi_i\rangle \langle \phi_k|$$

$$= \sum_{i=1}^{n} \sum_{k=1}^{n} \rho_{ik}(t) |\phi_i\rangle \langle \phi_k|.$$
(1.42)

In above Eq., $\rho_{ik}(t) = \overline{C_i(t)C_k^*(t)}$ represents the matrix element of the density operator between basis states $|\phi_i\rangle$ and $|\phi_k\rangle$. The diagonal elements $\rho_{ii}(t) = \overline{C_i(t)C_i^*(t)}$ represent the populations and the off-diagonal elements $\rho_{ik}(t) = \overline{C_i(t)C_k^*(t)}$ represent the coherence between involved basis states. The coherence order can be calculated by the difference between the magnetic quantum number of the involved basis states, i.e., $M_{ij} = m_i - m_j$, where M_{ij} can be any positive or negative integer. Based on this expression a coherence or transition matrix can be generated which will highlight the number and nature (quantum of transition) of possible transitions in a spin-system.

Substituting, Eq. (1.42) into Eq. (1.37), we obtain the time-evolution of the density matrix as described below:

$$i\hbar \frac{\partial \hat{\rho}(t)}{\partial t} = [\hat{H}(t), \hat{\rho}(t)].$$
 (1.43)

The above equation is famously known as the quantum-Liouville equation or Liouville-von Newmann equation. This equation is an operator equivalent of the time-dependent Schrödinger equation shown in Eq. (1.37).

The formal solution to the above equation is given below:

$$\hat{\rho}(t) = T \exp\left\{-\frac{i}{\hbar} \int_0^t \hat{H}(t')dt'\right\} \hat{\rho}(0) \exp\left\{\frac{i}{\hbar} \int_0^t \hat{H}(t')dt'\right\}$$
(1.44)

where $\hat{\rho}(0)$ is the initial density matrix at t = 0 and $\exp\left\{-\frac{i}{\hbar}\int_0^t \hat{H}(t')dt'\right\}$ represents the time-evolution operator, $\hat{U}(t)$. The explicit form of the density matrix at any instance t

will depend on the Hamiltonian operator $[\hat{H}(t)]$ acting on the spin-system. In contrast to Eq. (1.40), the expectation value of an observable for any physical quantity can be calculated by following Eq.,

$$\langle \hat{O}(t) \rangle = \operatorname{Trace}(\hat{O}.\hat{\rho}(t)).$$
 (1.45)

This standard operating procedure is utilized for evaluation of spin-dynamics of any NMR experiments regardless of the numerical or theoretical methodology employed. In the numerical methods, the exponential operator in Eq. (1.44) is solved by considering an infinitesimally small time-step where the Hamiltonian is treated as time-independent. For instance, SIMPSON [131, 132] (A General Simulation Program for Solid-State NMR Spectroscopy) a numerical simulation software utilizes this method. A pictorial representation of this process is shown in Figure 1.3. While numerical methods yield accurate results, they are of lesser utility in offering detailed insights into the spin dynamics of any quantum-mechanical process. In order to achieve a thorough understanding of the role of various interactions and coherences in deciphering the spin-dynamics requires a detailed analytic derivation of Eq. (1.44). The theoretical derivation of this equation involves explicit calculation of the time-evolution operator $[\hat{U}(t)]$ which gets complicated when

- the Hamiltonian is time-dependent: $\int_0^t \hat{H}(t')dt' \neq \hat{H}t$.
- the Hamiltonian consists of the non-commuting set of operators: $[\hat{H}(t_1), \hat{H}(t_2)] \neq 0$.

To overcome the above difficulties in the time-evolution of the spin-system, the effective Hamiltonians are derived. By the connotation "effective Hamiltonian," we mean an approximate Hamiltonian which is time-independent, more diagonal, and contains all the necessary information of the full Hamiltonian. Such an effective Hamiltonian simplifies the study of the spin dynamics of any complex NMR experiments. A conventional way to obtain the effective Hamiltonian is to use perturbation-based expansions, which may

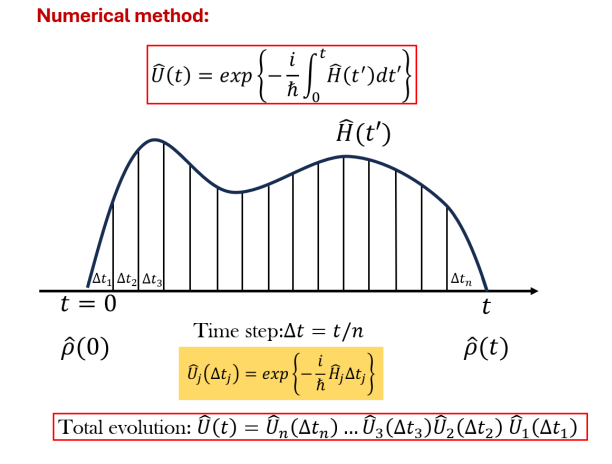


Figure 1.3: Pictorial representation of the numerical method for computation of the time-evolution operator.

involve a number of perturbation corrections to get a convergent solution. However, such methods lose their generality when it comes to the quadrupolar system. This is mainly due to two factors: (a) The large size of the quadrupolar interaction necessitates quadrupolar interaction frame transformation of the Hamiltonian, which renders time-dependency into the system, and (b) it requires many-orders of the perturbation corrections, which complicates the derivation of the effective Hamiltonian. In the following section, we have emphasized the complexity associated with the quadrupolar spins using a single spin-1 model system framework. An alternate approach known as the "effective-field" method is presented to obtain an effective Hamiltonian without invoking a large number of perturbation corrections, as discussed in the literature.

1.4 Concept of the "Effective Hamiltonian"

To clarify the notion of the effective Hamiltonian, we investigated the spin dynamics for a simplified single-spin system S=1 under on-resonance RF irradiation. The rotating frame Hamiltonian for such a system is given as:

$$\hat{H}_S = \hat{H}_{RF} + \hat{H}_Q^{(1)}$$

$$= \hbar \omega_{1S} \hat{S}_x + \frac{\hbar \omega_Q^{(1)}}{6} (3\hat{S}_z^2 - \hat{S}^2).$$
(1.46)

In the above equation, ω_{1S} and $\omega_{Q}^{(1)}$ represent the RF amplitude and first-order quadrupolar coupling frequency [Eq. (1.35)], respectively. As discussed previously, the derivation of the spin dynamics requires a solution of the Liouville-von Newmann equation as given below:

$$\hat{\rho}(t) = \exp\left\{-\frac{i}{\hbar}\hat{H}_S t\right\} \hat{\rho}(0) \exp\left\{\frac{i}{\hbar}\hat{H}_S t\right\}$$
(1.47)

where $\hat{\rho}(0)$ is the initial density matrix $(\hat{\rho}(0) = \hat{S}_z)$. Here the solution of the Eq. (1.47) becomes complex due to the non-commuting RF and quadrupolar coupling terms i.e., $[\hat{S}_x, (3\hat{S}_z^2 - \hat{S}^2)] \neq 0$. A brute-force method for finding the solution of Eq. (1.47) through the Baker-Campbell-Hausdorff (BCH) expansion [133, 134].

$$\hat{\rho}(t) = \hat{S}_z - \frac{it}{\hbar} [\hat{H}_S, \hat{S}_z] + \frac{1}{2!} \left(\frac{it}{\hbar}\right)^2 [\hat{H}_S, [\hat{H}_S, \hat{S}_z]] + \frac{1}{3!} \left(\frac{it}{\hbar}\right)^3 [\hat{H}_S, [\hat{H}_S, [\hat{H}_S, \hat{S}_z]]] + \dots (1.48)$$

Substituting the Hamiltonian operator based on Eq. (1.46), the above Eq. becomes

$$\hat{\rho}(t) = \hat{S}_z - \underbrace{\omega_{1S}t\hat{S}_y}_{\text{First commutator}} - \underbrace{\frac{1}{2!} \left\{ \omega_{1S}^2 t^2 \hat{S}_z - \frac{\omega_Q^{(1)} \omega_{1S}}{2} t^2 (\hat{S}_z \hat{S}_x + \hat{S}_x \hat{S}_z) \right\}}_{\text{Second commutator}} - \underbrace{\frac{1}{3!} \left\{ \omega_{1S}^3 t^3 \hat{S}_y - \frac{\omega_Q^{(1)} \omega_{1S}^2}{2} t^3 (\hat{S}_x \hat{S}_y + \hat{S}_y \hat{S}_x) + \frac{(\omega_Q^{(1)})^2 \omega_{1S}}{12} t^3 (\hat{S}_z^2 \hat{S}_y + 2\hat{S}_z \hat{S}_y \hat{S}_z + \hat{S}_y \hat{S}_z^2) \right\}}_{\text{Third commutator}}$$

 $+ \dots$ (1.49)

Subsequent evaluation of the higher-order commutators is expected to become more complicated. Given that $\omega_Q^{(1)} >> \omega_{1S}$, it can be concluded that the approximated solution (up to to the first few terms) will not converge. Thus, the theoretical method based on the explicit calculation of the BCH expansion [Eq. (1.49)] using the exact Hamiltonian [Eq. (1.46)] does not provide closed form solutions, is computationally less efficient, and generally relies on numerical evaluation. While the numerical approaches yield accurate results, their utility in elucidating the nuances of the spin dynamics is limited. To achieve a deeper insight into the spin physics, the development of analytic theory becomes essential which primarily relies on the diagonalization of the underlying Hamiltonian to produce a more complete and computationally efficient "Effective Hamiltonian" (\hat{H}_{eff}). Under the effective Hamiltonian (\hat{H}_{eff}), the spin-dynamics of the NMR experiments is described by the following Eq.,

$$\hat{\rho}_{eff}(t) = \exp\left\{-\frac{i}{\hbar}\hat{H}_{eff}t\right\}\hat{\rho}_{eff}(0)\exp\left\{\frac{i}{\hbar}\hat{H}_{eff}t\right\}$$
(1.50)

where $\hat{\rho}_{eff}(0)$ and $\hat{\rho}_{eff}(t)$ represent the density matrices initial (t=0) and final t times, respectively, in the same frame of reference as effective Hamiltonian, \hat{H}_{eff} . This equation will be employed throughout this thesis to evaluate the CP spin-dynamics.

1.4.1 Derivation of the effective Hamiltonian: Perturbation-based method

To facilitate the implementation of the perturbation procedure, the Hamiltonian in Eq. (1.46) is re-expressed as zero-order (\hat{H}_0) and perturbing Hamiltonian (\hat{H}_1) .

$$\hat{H}_S = \hat{H}_{RF} + \hat{H}_Q^{(1)} = \underbrace{\hbar\omega_{1S}\hat{S}_x}_{\hat{H}_0} + \underbrace{\frac{\hbar\omega_Q^{(1)}}{6}(3\hat{S}_z^2 - \hat{S}^2)}_{\hat{H}_1}.$$
 (1.51)

Since we are interested primarily in studying the influence of the radio-frequency pulse (i.e., \hat{S}_x) on the spin-system, the quadrupolar interaction (i.e., \hat{S}_z) acts as a perturbation. As shown in the previous section, due to the anisotropic nature of the first-order quadrupolar coupling interaction, there will be a distribution of quadrupolar coupling frequencies

 $\omega_Q^{(1)}$ for the samples with multiple-crystallite orientations. For a simplified analogy, we can consider PAS coincident with the MolAS. In this case the quadrupolar PAS angles $[\Omega_{PR} \equiv \Omega_{MR} = (\alpha_Q, \beta_Q, \gamma_Q)]$ will define the crystallite orientations. Based on the relative magnitudes of these interactions, the three different coupling regimes $\omega_{1S} >> \omega_Q^{(1)}$ (weak coupling regime), $\omega_{1S} \approx \omega_Q^{(1)}$ (intermediate coupling regime) and $\omega_{1S} << \omega_Q^{(1)}$ (strong coupling regime) are possible.

Weak coupling regime: If the condition $\omega_{1S} >> \omega_Q^{(1)}$ is satisfied, the effective Hamiltonian can be approximated to the RF irradiation term as shown below:

$$\hat{H}_{eff,S} \approx \hat{H}_{RF} = \omega_{1S} \hat{S}_x . \tag{1.52}$$

In this coupling regime, the spin system under RF irradiation behaves like a spin-1/2 system. The time-evolution of the spin system is solely determined by the RF irradiation term as described below:

$$\hat{\rho}(t) = \exp\left\{-\frac{i}{\hbar}\omega_{1S}\hat{S}_x t\right\} \hat{\rho}(0) \exp\left\{\frac{i}{\hbar}\omega_{1S}\hat{S}_x t\right\}$$
(1.53)

where $\hat{\rho}(0) = \hat{S}_z$ in the present context.

In anisotropic solids, this condition is met for crystallite orientations near $\beta_Q = 54.736^{\circ}$, regardless of the value of C_Q . In such cases we observe better excitation efficiencies, similar to that seen in the spin-1/2 systems. In the case of powder samples, which is the statistically weighted ensemble of all possible crystallite orientations. This weak coupling condition will be satisfied for a smaller portion of crystallite orientations; however, in general, we have $\omega_{1S} \approx \omega_Q^{(1)}$ or $\omega_{1S} << \omega_Q^{(1)}$.

Strong coupling regime: To address a stronger quadrupolar coupling system ($\omega_{1S} << \omega_Q^{(1)}$), a common approach is to utilize the quadrupolar interaction frame transformation which involves the transformation function $\hat{U}'(t) = \exp\left\{-\frac{i}{\hbar}\hat{H}_Q^{(1)}t\right\}$:

$$\tilde{\hat{H}}_{S}(t) = \exp\left\{-\frac{i}{\hbar}\hat{H}_{Q}^{(1)}t\right\}(\hat{H}_{RF} + \hat{H}_{Q}^{(1)})\exp\left\{\frac{i}{\hbar}\hat{H}_{Q}^{(1)}t\right\}
= \tilde{\hat{H}}_{RF}(t).$$
(1.54)

The time-evolution of the spin system in the quadrupolar interaction frame is given:

$$\tilde{\hat{\rho}}(t) = \exp\left\{-\frac{i}{\hbar} \int_0^t \tilde{\hat{H}}_{RF}(t')dt'\right\} \hat{\rho}_{eff}(0) \exp\left\{\frac{i}{\hbar} \int_0^t \tilde{\hat{H}}_{RF}(t')dt'\right\}$$
(1.55)

where the effect of the much stronger quadrupolar interaction is nullified. However, as a consequence of this interaction frame transformation, the RF irradiation becomes time-dependent with a period defined by the quadrupolar coupling strength. Conventional ways to treat such time-dependent Hamiltonians are:

- (1) Average Hamiltonian theory (AHT)
- (2) Floquet theory and contact transformation method.

The AHT [3,20] provides a time-averaged Hamiltonian at a fixed cycle time $(t_c = 2\pi/\omega_Q^{(1)})$;

in this case), and as a result, it lacks description of the spin-dynamics in between cycle times. Also in the regime $\omega_{1S} \approx \omega_Q^{(1)}$ the convergent solution requires a large number of perturbation corrections which are tedious to evaluate [70]. Such descriptions are of lesser utility for powder samples described as statistical distribution of different crystallite orientations. Since each crystallite is associated with a fixed $\omega_O^{(1)}$ dependence while performing interaction frame transformation, hence different crystallites cannot be evaluated simultaneously at a single instant of time. This issue is addressed by utilizing Floquet-based perturbative methods [104-109], which do not operate at the cycle time, but only at the cost of evaluating many order perturbation corrections to the zero-order Hamiltonian [69, 70]. Consequently, the process of obtaining the effective Hamiltonian and the time evolution of the spin system becomes quite cumbersome. Additionally, the effective Hamiltonians derived in different coupling regimes might not provide accurate results in anisotropic samples. To overcome these challenges and achieve a faster convergence, this thesis is based on an alternate method to derive effective Hamiltonians by utilizing the concept of the "effective-field". In this approach through a set of unitary transformations, magnetization associated with a particular interaction is maximized along a suitable direction/axis. This process is computationally efficient and provides more convergent solutions which are equally valid for isotropic and anisotropic solids.

1.4.2 Derivation of the effective Hamiltonian: "Effective-field" based method

In this section we have shown the utility of the effective-field approach to evaluate the efficiency of the double-quantum transition in the S=1 spin-system. To simplify the description, the Hamiltonian in Eq. (1.51) is re-expressed in terms of the single-transition operators [45, 110, 112, 113] as given below:

$$\hat{H}_S = \sqrt{2}\omega_{1S}[\hat{S}_x^{12} + \hat{S}_x^{23}] + \frac{\omega_Q^{(1)}}{3}[\hat{S}_z^{12} - \hat{S}_z^{23}]. \tag{1.56}$$

The superscript (i, j) in the operators \hat{S}_{α}^{ij} ($\alpha = x, y, z$) represents the the Zeeman basis states the S = 1 system and are defined according to the energy level diagram depicted in Figure 1.4(a). The populations and coherences in the S = 1 spin system are illustrated in the transition matrix shown in Figure 1.4(b). The single-transition operators are defined as follows:

$$\hat{S}_{x}^{ij} = \frac{1}{2} [|i\rangle \langle j| + |j\rangle \langle i|], \quad \hat{S}_{y}^{ij} = \frac{1}{2i} [|i\rangle \langle j| - |j\rangle \langle i|], \quad \hat{S}_{z}^{ij} = \frac{1}{2} [|i\rangle \langle i| - |j\rangle \langle j|]. \tag{1.57}$$

The matrix representations of the Cartesian and single-transition operators are given in Table A.2 and A.3 in Appendix-A. In the effective-field method, each interaction (say, λ) in the Hamiltonian is considered as a field that has a specific direction (interaction operator, \hat{S}_{λ}) and the strength of the field is indicated by the interaction frequency (ω_{λ}) .

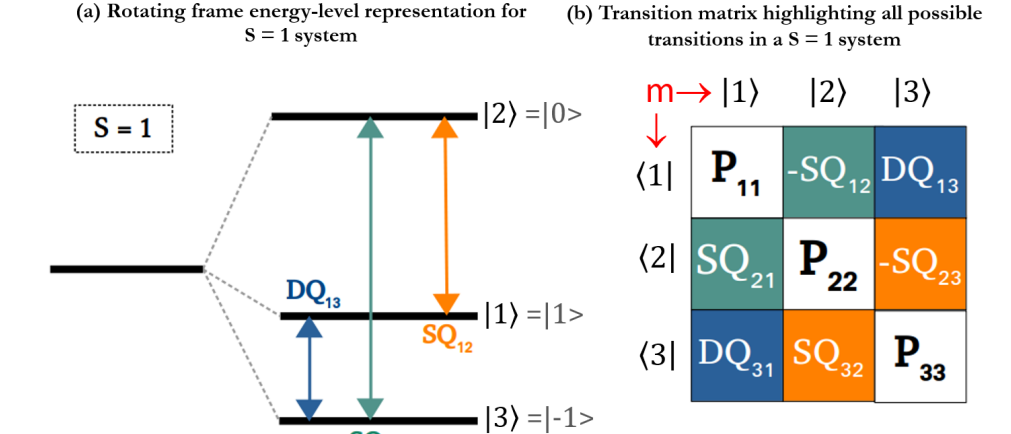


Figure 1.4: (a) Schematic depiction of the energy level diagram in the S=1 spin system. The spin states $|1\rangle$, $|2\rangle$ and $|3\rangle$ are representative of the the Zeeman basis states $(|m_S\rangle)$ $|1\rangle$, $|0\rangle$ and $|-1\rangle$, respectively. (b) Transition matrix representation of the populations and coherences in the S=1 spin system. The diagonal elements depict the populations (of the states $|m_S\rangle$) and are represented through ' P_{ii} '. The off-diagonal elements depict the coherences (between the states $|m_S\rangle$, $|m_S'\rangle$) and are represented as double-quantum (DQ₁₃: $|+1\rangle \leftrightarrow |-1\rangle$), single-quantum (SQ₁₂: $|-1\rangle \leftrightarrow |0\rangle$ and SQ₂₃: $|1\rangle \leftrightarrow |0\rangle$).

The pictorial representation of the fields for the S-spin Hamiltonian [Eq. (1.46)] is given in Figure 1.5(a). Through an initial unitary transformation $\hat{U}_1 = \exp\left\{-\frac{i\theta_1}{\sqrt{2}}\left[-\hat{S}_y^{12} + \hat{S}_y^{23}\right]\right\}$ [115, 116], the S-spin Hamiltonian is transformed and is given below:

$$\hat{H}_{S} = \hat{U}_{1} \hat{H}_{S} \hat{U}_{1}^{\dagger}
= \sqrt{2} \Big(\omega_{1S} \cos \theta_{1} - \frac{\omega_{Q}^{(1)}}{4} \sin \theta_{1} \Big) [\hat{S}_{x}^{12} + \hat{S}_{x}^{23}] + \Big\{ \omega_{1S} \sin \theta_{1} + \frac{\omega_{Q}^{(1)}}{4} \Big(\frac{1}{3} + \cos \theta_{1} \Big) \Big\} [\hat{S}_{z}^{12} - \hat{S}_{z}^{23}]
+ \Big\{ \omega_{1S} \sin \theta_{1} + \omega_{Q}^{(1)} \Big(\frac{\cos \theta_{1} - 1}{4} \Big) \Big\} [\hat{S}_{x}^{13}].$$
(1.58)

The angle $\theta_1 \left(\tan \theta_1 = \frac{4\omega_{1S}}{\omega_Q^{(1)}} \right)$ is selected to ensure the compensation of the SQ operators $(\hat{S}_x^{12} + \hat{S}_x^{23})$ in \hat{H}_S . Accordingly, the Hamiltonian after the first transformation takes on the following form:

$$\tilde{\hat{H}}_S = \left(\frac{\omega_e - \omega_Q^{(1)}}{4}\right) \left[\hat{S}_x^{13}\right] + \left(\frac{3\omega_e + \omega_Q^{(1)}}{12}\right) \left[\hat{S}_z^{12} - \hat{S}_z^{23}\right]. \tag{1.59}$$

The term $\omega_e \left(= \sqrt{(\omega_Q^{(1)})^2 + 16\omega_{1S}^2} \right)$ represents the effective-field experienced by the S-spin *i.e.*, it has contributions from the RF field as well as the quadrupolar interaction (refer to Figure 1.5(b)). As described above, the Hamiltonian after the first transformation comprises operators \hat{S}_x^{13} corresponding to the double-quantum transitions $\left[DQ_S \left(1 \leftrightarrow 3 \right) \right]$. To further simplify the description, the above Hamiltonian is transformed using the unitary transformation $\hat{U}_2 = \exp \left\{ i \frac{\pi}{2} \left[\hat{S}_y^{13} \right] \right\}$ such that the

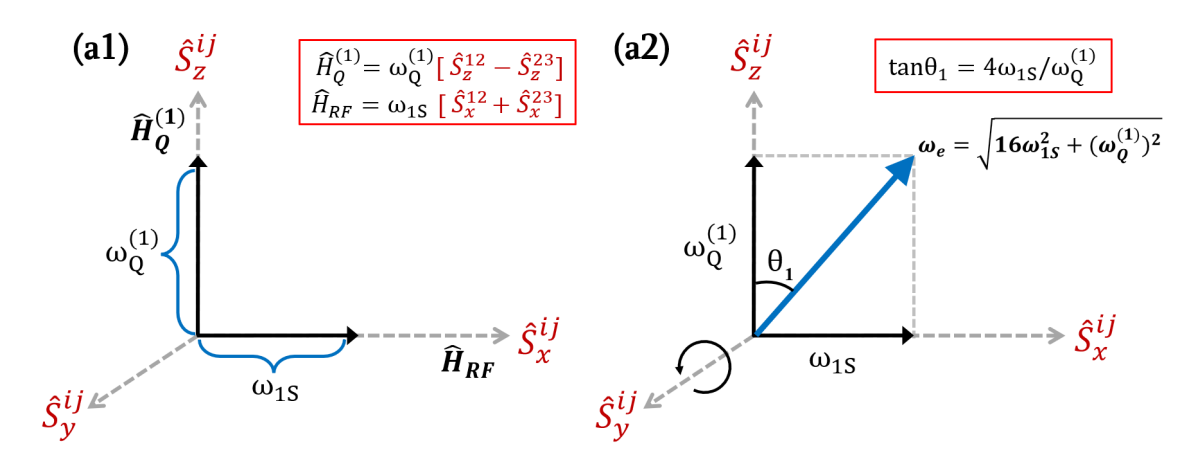


Figure 1.5: (a1) Pictorial representation of the fields due to the RF irradiation and the first-order quadrupolar coupling interactions. In the field representation, the spin operator and frequency terms define the direction and magnitude of the field, respectively. (a2) Schematic depiction of the effective-field experienced by the S-spin due to contributions from the RF irradiation and the first-order quadrupolar coupling interaction.

Hamiltonian is diagonal in the chosen coupled basis.

$$\hat{H}_{eff,S} = \hat{U}_2 \hat{H}_S \hat{U}_2^{\dagger}$$

$$= \left(\frac{\omega_e - \omega_Q^{(1)}}{4}\right) \left[\hat{S}_z^{13}\right] + \left(\frac{3\omega_e + \omega_Q^{(1)}}{12}\right) \left[\hat{S}_z^{12} - \hat{S}_z^{23}\right]. \tag{1.60}$$

The time-evolution of the spin system is described as follows:

$$\hat{\rho}_{eff}(t) = \exp\left\{-\frac{i}{\hbar}\hat{H}_{eff,S}t\right\}\hat{\rho}_{eff}(0)\exp\left\{\frac{i}{\hbar}\hat{H}_{eff,S}t\right\}^{\dagger}$$

$$= 2\cos\theta_1/2\left[\left[\hat{S}_z^{13}\right]\cos\left(\frac{\omega_e + \omega_Q^{(1)}}{4}t\right) + \left[\hat{S}_y^{13}\right]\sin\left(\frac{\omega_e + \omega_Q^{(1)}}{4}t\right)\right]$$

$$-\sqrt{2}\sin\theta_1/2\left[\left[\hat{S}_x^{12} - \hat{S}_x^{23}\right]\cos\left(\frac{\omega_e}{4}t\right) + \left[\hat{S}_y^{12} - \hat{S}_y^{23}\right]\sin\left(\frac{\omega_e}{4}t\right)\right].$$
(1.61)

For a consistent description, the detection operator for each observable is also transformed with the same set of transformations $\hat{U}_1\hat{U}_2$. Accordingly, the excitation efficiency of the DQ₁₃ transition is the expectation value of the observable $\langle \hat{S}^{13}_{+}(t) \rangle$ and is evaluated using the standard procedure outlined below.

$$S(t)_{13} = \langle \hat{S}^{13}_{+}(t) \rangle = Trace\{\hat{S}^{13}_{eff,+}\hat{\rho}_{eff}(t)\}$$
 (1.62)

where

$$\hat{S}_{eff,+}^{13} = 2\hat{S}_{+}^{13}\cos\theta_1/2 + (\hat{S}_z^{12} - \hat{S}_z^{23})\frac{(\cos\theta_1 - 1)}{4} - \sqrt{2}(\hat{S}_{+}^{12} + \hat{S}_{+}^{23})\sin\theta_1/2.$$
 (1.63)

The signal expression for double-quantum detection is given below:

$$S(t)_{13} = \frac{i}{2} \left[(1 + \cos \theta_1) \sin \left(\frac{\omega_e - \omega_Q^{(1)}}{4} t \right) + (1 - \cos \theta_1) \sin \left(\frac{\omega_e + \omega_Q^{(1)}}{4} t \right) \right]. \tag{1.64}$$

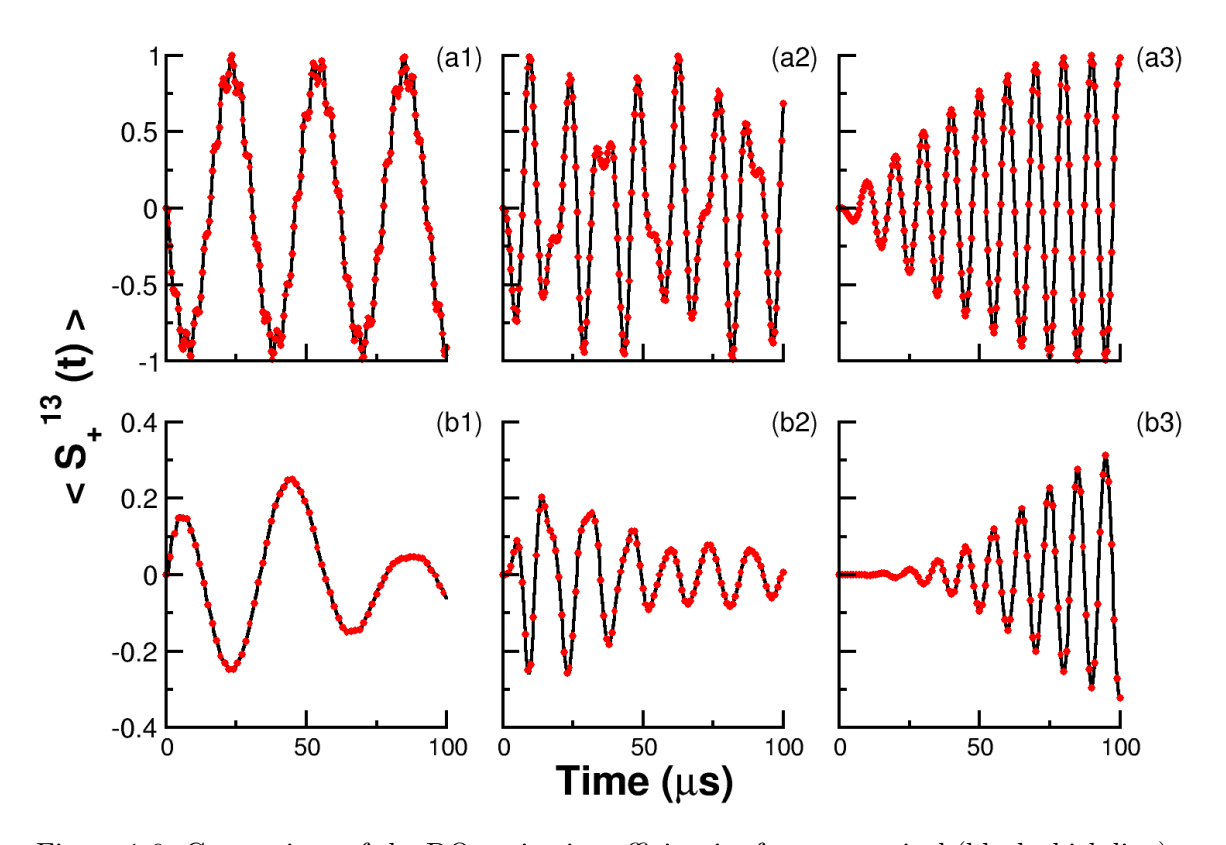


Figure 1.6: Comparison of the DQ excitation efficiencies from numerical (black thick line) and analytic simulations (red solid dots) based on Eq. (1.64) for single-crystal (a1-a3) and powder (b1-b3) samples. The following simulation parameters were used: $C_Q = 1.0$ MHz (a1-b1), 200 kHz (a2-b2) and 20 kHz (a3-b3), asymmetry $\eta_Q = 0.1$, quadrupolar coupling PAS angles (α_Q , β_Q , $\gamma_Q = 30^\circ$, 40° , 60°) and RF parameters: $\nu_{1S} = 50$ kHz. The powder simulations were performed using 4180 orientations (i.e., zcw4180) of α and β .

To substantiate the validity of the effective Hamiltonian [Eq. (1.60)] derived using the concept of "effective-field", the analytic simulations based on the Eq. (1.64) were compared with the more exact numerical simulations using SIMPSON software. As depicted in Figure 1.6, the analytic simulations are in good agreement across all quadrupolar coupling regimes for both isotropic (single-crystal) and anisotropic (powder) solids. In contrast to the conventional Floquet and AHT-based methods, the effective-field formalism provided a faster convergence with a minimal number of unitary transformations. In this thesis, the proposed effective field-based analytic framework is extended to describe the spin dynamics of the cross-polarization experiments between spin-1/2 and quadrupolar spins ($S=1,\,3/2$). A brief outline of the thesis is presented in the following section.

1.5 Organization of the thesis

In this thesis, an operator-based analytic theory is presented to describe the mechanism of the standard cross-polarization experiment in a more complex quadrupolar system. For the development of an efficient CP pulse sequence, it is essential to have a quantitative description of the underlying spin dynamics in CP experiments. With this objective, an analytic framework based on the effective Hamiltonian is presented to provide a unified description of the quadrupolar CP dynamics in both isotropic and anisotropic solids. Chapter 2 will focus on basic theory and methodology adopted in the thesis to describe the spin-dynamics of cross-polarization experiments in non-rotating single-crystal and powder samples. In particular, this chapter will contain a description of the operator-based analytic theory of CP experiments involving much simpler spin-1/2 systems (I = 1/2and S=1/2). A detailed description of the CP dynamics will be provided through effective Hamiltonians derived using the rotation operators-based effective-field approach. In Chapter 3, employing the effective-field based analytic framework, the spin-dynamics of cross-polarization experiment will be outlined for I=1/2 to a more complex S=1quadrupolar nuclei under on-resonance RF irradiation [116]. In contrast to other existing theoretical studies, the polarization transfer among spins is quantified and individual contributions emerging from all plausible CP matching conditions are evaluated. Chapter 4 will discuss the mechanism of cross-polarization between I = 1/2 to S = 1 in the presence of second-order quadrupolar interaction and S-spin off-resonance RF irradiation [117]. Multiple insights emerging out from this study will be highlighted through a single mathematical framework derived using the effective-field approach. In Chapter 5 the proposed analytic framework will be extended to describe the CP transfer dynamics in I = 1/2 to S = 3/2 under static condition [135]. All the results of the thesis will be summarized and future directions will be provided in **Chapter 6**.

Chapter 2

Theory and Methodology:
An effective-field approach to
understand the mechanism
of cross-polarization dynamics
between spin-1/2 systems

In this chapter of the thesis, an alternate operator-based analytic theory utilizing the concept of the "effective-field" is introduced to describe the spin dynamics of the cross-polarization experiment between spin-1/2 systems. A simpler spin-1/2 model framework is used to develop the theoretical method that will serve as a test bud for describing the CP dynamics in a more complex quadrupolar systems.

2.1 Theory and Methodology

The basic pulse sequence for the continuous-wave cross-polarization experiment is depicted in Figure 2.1(a). We have considered an isolated two spin-1/2 (I=1/2 and S=1/2) model system [Figure 2.1(b)] to describe the CP dynamics. The doubly rotating frame CP Hamiltonian for such a system is given as

$$\hat{H}_{CP} = \omega_{1I}\hat{I}_x + \Omega_S\hat{S}_z + \omega_{1S}\hat{S}_x + 2\omega_d\hat{I}_z\hat{S}_z, \quad \hbar = 1.$$
 (2.1)

In the above equation, ω_{1I} and ω_{1S} represent the radio-frequency (RF) amplitudes for I and S spins, respectively. The symbol Ω_S represents the off-resonance irradiation on the S-spin, while on-resonance irradiation is considered on the I-spin channel. The term $\omega_d \left(= \frac{\mu_o}{4\pi} \frac{\gamma_I \gamma_S}{r_{IS}^3} \frac{(3\cos^2\beta_d - 1)}{2} \right)$ represents the dipolar coupling (I-S) frequency, r_{IS} the internuclear distance between I and S-spin pair, and β_d is the orientation of the dipolar vector with respect to the applied Zeeman magnetic field. A detailed description of the above CP Hamiltonian can be found in the literature [4, 16, 44].

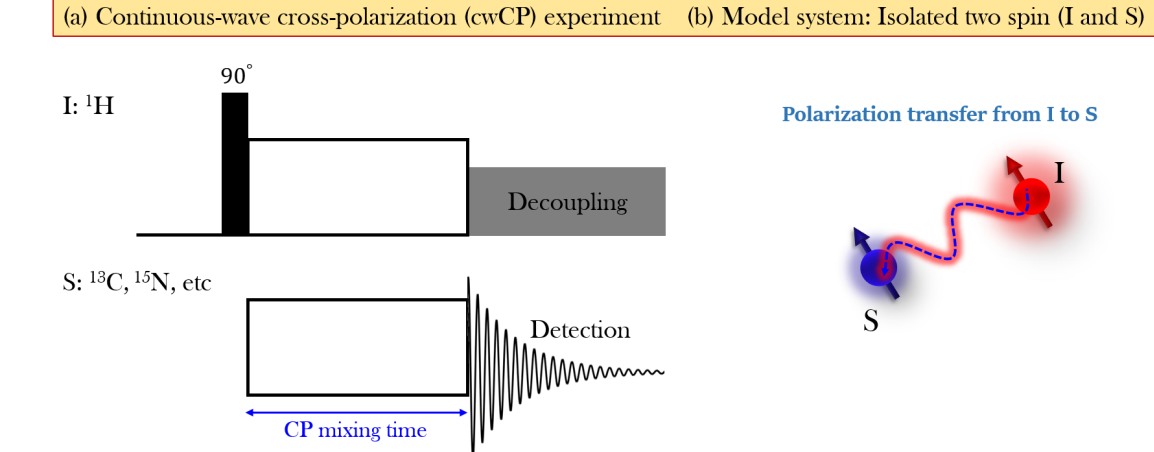


Figure 2.1: Schematic representation of the (a) continuous-wave (cw) cross-polarization pulse-sequence and (b) an isolated two spins (I and S) model system.

2.1.1 Derivation of the effective CP Hamiltonian

For operational convenience during the diagonalization process, the above Hamiltonian [Eq. (2.1)] is re-expressed in terms of the single-transition operators (*incoupledbasis*) [110–112] as given below:

$$\hat{H}_{CP} = \omega_{1I}(\hat{S}_x^{13} + \hat{S}_x^{24}) + \Omega_S(\hat{S}_z^{12} + \hat{S}_z^{34}) + \omega_{1S}(\hat{S}_x^{12} + \hat{S}_x^{34}) + \omega_d(\hat{S}_z^{12} - \hat{S}_z^{34}). \tag{2.2}$$

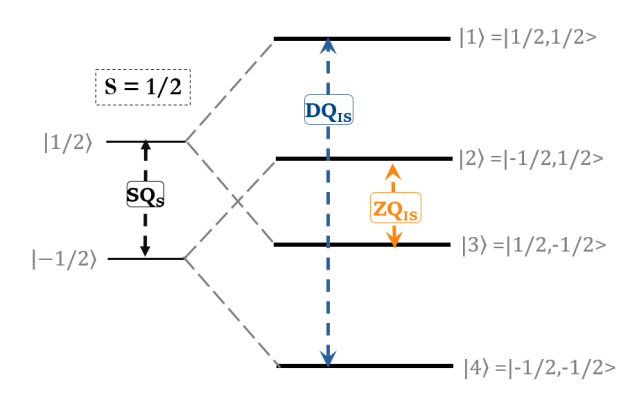
A schematic description of the populations and coherences observed in a coupled spin-pair (I=1/2 and S=1/2) is given in Figure 2.2(b). The matrix representations of the above spin-operators are provided in Table B.1 (refer to Appendix-B). In general, for an efficient CP process, we have $\omega_{1I/1S}>\omega_d$. In order to reduce the off-diagonalities due to stronger RF irradiation terms, we employed double-titled rotating frame transformation $\hat{U}_1\hat{U}_2=\exp\left\{i\theta_1(\hat{S}_y^{13}+\hat{S}_y^{24})\right\}\exp\left\{i\theta_2(\hat{S}_y^{12}+\hat{S}_y^{34})\right\}$ and the resulting Hamiltonian is given as,

$$\tilde{\hat{H}}_{CP} = \omega_{1I} \left[\hat{S}_z^{13} + \hat{S}_z^{24} \right] + \omega_{e,S} \left[\hat{S}_z^{12} + \hat{S}_z^{34} \right] + \underbrace{\omega_d \cos \theta_2 \left[\hat{S}_x^{14} \right]}_{DQ_{14}} + \underbrace{\omega_d \cos \theta_2 \left[\hat{S}_x^{23} \right]}_{ZQ_{23}} - \underbrace{\omega_d \sin \theta_2 \left[\hat{S}_x^{13} - \hat{S}_x^{24} \right]}_{SQ_{d,I}}$$

Heteronuclear dipolar coupling Hamiltonian

where, $\omega_{eS} = \sqrt{\Omega_S^2 + \omega_{1S}^2}$ and angles θ_1 and θ_1 are given as $\theta_1 = \frac{\pi}{2}$ and $\theta_2 = \tan^{-1} \frac{\Omega_S}{\omega_{1S}}$. The dipolar transitions are categorized according to the total change in the S and I-spin quantum numbers in transitions involved. For instance, $\{1,4\}/\{2,3\}$ are labeled as double and zero-quantum (DQ₁₄ and ZQ₂₃, respectively) dipolar transitions. The last term in the dipolar coupling Hamiltonian *i.e.*, $SQ_{d,I}$ operator involves single-quantum I-spin dipolar transitions which does not result in an independent CP transfer mode like DQ₁₄/ZQ₂₃ transitions but rather provides a pathway to account for the loss in the magnetization of I-spin. In the existing literature reports, these $SQ_{d,I}$ dipolar transitions are usually

(a) S = 1/2 and I = 1/2 coupled basis states and two spin flip/flop (dipolar) transitions



(b) Transition matrix highlighting all possible transitions in a coupled system

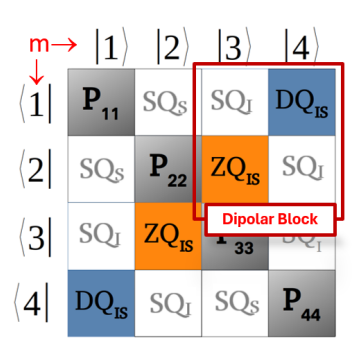


Figure 2.2: (a) Schematic depiction of the energy level diagram in a coupled two-spin (I = 1/2 and S = 1/2) system. The spin states $|1\rangle$, $|2\rangle$, $|3\rangle$ and $|4\rangle$ are representative of the product basis states $(|m_I, m_S\rangle) |1/2, 1/2\rangle$, $|1/2, -1/2\rangle$, $|-1/2, 1/2\rangle$ and $|-1/2, -1/2\rangle$, respectively. (b) Transition matrix representation of the populations and coherences in the coupled two-spin (I and S) system. The diagonal elements depict the populations (of the states $|m_I, m_S\rangle$) and are represented through ' P_{ii} '. The coherences wherein both spins change their states are represented as the double-quantum (DQ_{IS}) and zero-quantum (ZQ_{IS}) . The coherences where only the state of S-spin changes are represented by SQ_I , while coherences where only the state of I-spin changes are represented by SQ_I .

ignored under the assumption $\Omega_S << \omega_{1S}$ [29, 41, 136]. However, as shown later in this chapter, such an approximation does not always hold good. To offer a consistent and comprehensive analytic description that is valid across all the coupling regimes ($\Omega_S << \omega_{1S}$, $\Omega_S \approx \omega_{1S}$ and $\Omega_S > \omega_{1S}$), we decided to retain the $SQ_{d,I}$ dipolar transitions as well in further descriptions. For this purpose, the unitary transformation $\hat{U}_3 = \exp\left\{i\theta_3(\hat{S}_y^{13} - \hat{S}_y^{24})\right\}$ is utilized to evaluate the effective-field or nutation frequencies for I-spin transitions (SQ_I (ω_{1I}) and $SQ_{d,I}$) as follows:

$$\tilde{\hat{H}}_{CP} = \omega_{e,I} \left[\hat{S}_z^{13} + \hat{S}_z^{24} \right] + \omega_{e,S} \left[\hat{S}_z^{12} + \hat{S}_z^{34} \right] + \underbrace{\omega_d \cos \theta_2 \sin \theta_3 \left[\hat{S}_x^{14} \right]}_{DQ_{14}} + \underbrace{\omega_d \cos \theta_2 \sin \theta_3 \left[\hat{S}_x^{23} \right]}_{ZQ_{23}}$$
(2.4)

where, $\omega_{e,I} = \sqrt{\omega_{1I}^2 + (2\omega_d\Omega_S/\omega_{e,S})^2}$ and $\tan\theta_3 = \frac{\omega_{1I}\omega_{e,S}}{2\omega_d\Omega_S}$. To accomplish the dipolar coupling mediated Hartmann-Hahn CP conditions, the S and I-spin Hamiltonians are rearranged using the relation $\hat{S}_z^{ik} = \hat{S}_z^{ij} + \hat{S}_z^{jk}$ leading to the following equation

$$\tilde{\hat{H}}_{CP} = \Sigma [\hat{S}_z^{14}] + \omega_d^{14,23} [\hat{S}_x^{14}] + \Delta [\hat{S}_z^{23}] + \omega_d^{14,23} [\hat{S}_x^{23}]$$
 (2.5)

where, $\Sigma = \omega_{e,I} + \omega_{e,S}$, $\Delta = \omega_{e,I} - \omega_{e,S}$ and $\omega_d^{14,23} = \omega_d \cos \theta_2 \sin \theta_3$. In Eq. (2.5), the CP Hamiltonian is the sum of longitudinal/diagonal (\hat{S}_z^{ij}) and transverse/off-diagonal (\hat{S}_x^{ij}) components in two independent subspaces (DQ₁₄ and ZQ₂₃). The CP Hamiltonian [Eq. (2.5)] is further diagonalized by employing the rotation operators $\hat{U}_4 = \hat{U}_4^{(14)} \hat{U}_4^{(23)} = \exp\left\{i\left(\frac{\pi}{2} - \theta_{14}\right)[\hat{S}_y^{14}]\right\} \exp\left\{i\left(\frac{\pi}{2} - \theta_{23}\right)[\hat{S}_y^{23}]\right\}$. The angles θ_{14} and θ_{23} are chosen such

that the effective fields in individual subspaces are quantized along their respective z-axes $\left(\tan\theta_{14} = \frac{\Sigma}{\omega_d^{14,23}}, \ \tan\theta_{23} = \frac{\Delta}{\omega_d^{14,23}}\right)$. The pictorial representations of these transformations are given in Figure 2.3. Subsequently, the resulting effective CP Hamiltonian is given as

$$\hat{H}_{eff} = \omega_{eff}^{14} [\hat{S}_z^{14}] + \omega_{eff}^{23} [\hat{S}_z^{23}]$$
(2.6)

where, $\omega_{eff}^{14} = \sqrt{\Sigma^2 + (\omega_d^{14,23})^2}$ and $\omega_{eff}^{23} = \sqrt{\Delta^2 + (\omega_d^{14,23})^2}$. In this analytic framework, the effective CP Hamiltonian is a sum of two independent effective CP fields, namely DQ₁₄ and ZQ₂₃ effective-fields.

Effective fields in the Double-quantum (DQ₁₄) and Zero-quantum (ZQ₂₃) subspaces:

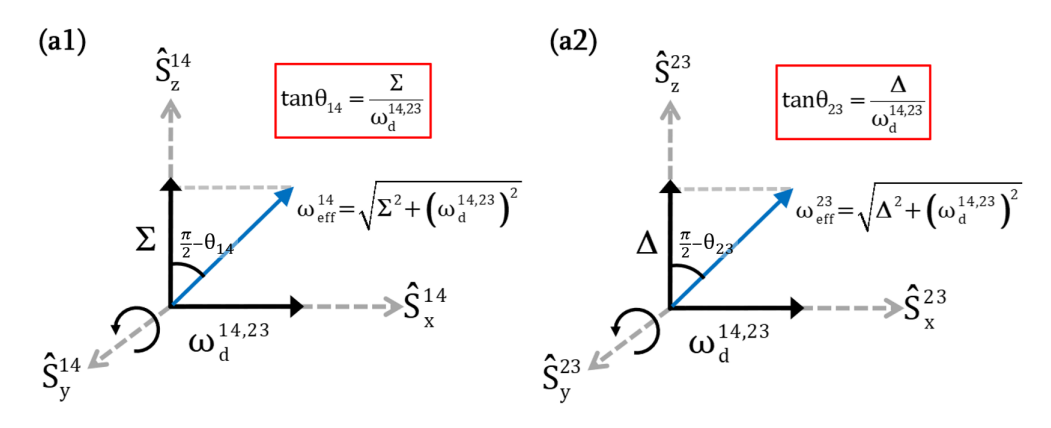


Figure 2.3: Pictorial representation of the unitary transformations $\hat{U}_4^{(14)}$ and $\hat{U}_4^{(23)}$ while diagonalization of the CP Hamiltonian in the double-quantum (DQ₁₄) (a1) and zero-quantum (ZQ₂₃) (a2) subspaces, respectively.

2.1.2 Time-evolution of the spin-system

To describe the time evolution of the spin system during the CP mixing (spin-locking/contact) period (t), the solution of the Liouville-von Neumann equation [Eq. (1.44)] described in the previous chapter is employed.

$$\hat{\rho}(t) = \exp\{-\frac{i}{\hbar}\hat{H}_{CP}t\}\hat{\rho}(0)\exp\{\frac{i}{\hbar}\hat{H}_{CP}t\}$$
(2.7)

where, $\hat{\rho}(0) = \hat{I}_x$ represents the initial density operator. For a consistent description, the initial density operator is also transformed using the same set of unitary transformations involved in the derivation of the effective CP Hamiltonian [Eq. (2.6)]. Employing the unitary transformations $\hat{U}_1\hat{U}_2\hat{U}_3\hat{U}_4$, the initial density matrix is transformed as

$$\hat{\rho}_{eff}(0) = \sin \theta_2 \left[\hat{S}_z^{14} \sin \theta_{14} - \hat{S}_x^{14} \cos \theta_{14} \right] + \sin \theta_2 \left[\hat{S}_z^{23} \sin \theta_{23} - \hat{S}_x^{23} \cos \theta_{23} \right] - \cos \theta_2 \left[(\hat{S}_x^{13} - \hat{S}_x^{24}) \sin \left(\frac{\theta_{14} + \theta_{23}}{2} \right) - (\hat{S}_x^{12} + \hat{S}_x^{34}) \cos \left(\frac{\theta_{14} + \theta_{23}}{2} \right) \right].$$
(2.8)

The time evolution of the spin-system under the effective CP Hamiltonian [Eq. (2.6)] is given as

$$\begin{split} \hat{\rho}_{eff}(t) &= \exp\left\{-i\hat{H}_{eff}t/\hbar\right\}\hat{\rho}_{eff}(0) \exp\left\{i\hat{H}_{eff}t/\hbar\right\} \\ &= \sin\theta_2 \left[\hat{S}_z^{14} \sin\theta_{14} - \cos\theta_{14} \left\{\hat{S}_x^{14} \cos\omega_{eff}^{14}t + \hat{S}_y^{14} \sin\omega_{eff}^{14}t\right\} \right. \\ &\quad \left. + \hat{S}_z^{23} \sin\theta_{23} - \cos\theta_{23} \left\{\hat{S}_x^{23} \cos\omega_{eff}^{23}t + \hat{S}_y^{23} \sin\omega_{eff}^{23}t\right\}\right] \\ &\quad \left. - \cos\theta_2 \sin\left(\frac{\theta_{14} + \theta_{23}}{2}\right) \left[(\hat{S}_x^{13} - \hat{S}_x^{24}) \cos\left(\frac{\omega_{eff}^{23} - \omega_{eff}^{14}}{2}t\right) + (\hat{S}_y^{13} - \hat{S}_y^{24}) \sin\left(\frac{\omega_{eff}^{23} - \omega_{eff}^{14}}{2}t\right)\right] \\ &\quad \left. + \cos\theta_2 \cos\left(\frac{\theta_{14} + \theta_{23}}{2}\right) \left[(\hat{S}_x^{12} + \hat{S}_x^{34}) \cos\left(\frac{\omega_{eff}^{23} + \omega_{eff}^{14}}{2}t\right) - (\hat{S}_y^{12} + \hat{S}_y^{34}) \sin\left(\frac{\omega_{eff}^{23} + \omega_{eff}^{14}}{2}t\right)\right]. \end{split}$$

2.1.3 Calculation of the CP Signal

To evaluate the polarization transfer from spin I to spin S, the expectation value of the observable S-spin $<\hat{S}_x(t)>$ or the CP signal is derived using the following expression:

$$S(t) = \langle \hat{S}_x(t) \rangle = Trace[\hat{S}_{eff,x}.\hat{\rho}_{eff}(t)]$$
(2.10)

where, $\hat{S}_{eff,x}$ represents the detection operator in the same frame of reference as the effective Hamiltonian [Eq. (2.6)]. Using the standard operation procedure, the final CP signal expression is given as

$$S(t) = \frac{\omega_{1I}}{\omega_{e,I}} \frac{\omega_{1S}}{\omega_{e,S}} \left[\underbrace{\left\{ \frac{\omega_{1S}}{\omega_{e,I}} \frac{\omega_{d}}{\omega_{e,I}} \sin \theta_{14} \cos \theta_{14} - \cos^{2} \theta_{14} \right\} \sin^{2} \frac{\omega_{eff}^{14}}{2} t}_{\text{Double-quantum}} + \underbrace{\left\{ -\frac{\omega_{1S}}{\omega_{e,I}} \frac{\omega_{d}}{\omega_{e,I}} \sin \theta_{23} \cos \theta_{23} + \cos^{2} \theta_{23} \right\} \sin^{2} \frac{\omega_{eff}^{23}}{2} t}_{\text{Zero-quantum}} - \underbrace{\frac{2\omega_{1S}\Omega_{S}}{\omega_{e,I}\omega_{e,S}} \cos \left(\frac{\theta_{23} - \theta_{14}}{2} \right) \sin \left(\frac{\theta_{23} - \theta_{14}}{2} \right) \left\{ \cos \left(\frac{\omega_{eff}^{23} - \omega_{eff}^{14}}{2} t \right) - \cos \left(\frac{\omega_{eff}^{23} + \omega_{eff}^{14}}{2} t \right) \right\}}_{\text{Interference term}} \right].$$

Besides, the loss in the *I*-spin magnetization can be evaluated by the expectation value of the \hat{I}_x operator ($\langle \hat{I}_x(t) \rangle$) given below:

$$S(t)_{I} = \frac{1}{2} \left[2 \sin^{2} \theta_{3} \underbrace{-2 \sin^{2} \theta_{3} \cos^{2} \theta_{14} \sin^{2} \frac{\omega_{eff}^{14}}{2} t}_{\text{Double-quantum}} - \underbrace{2 \sin^{2} \theta_{3} \cos^{2} \theta_{23} \sin^{2} \frac{\omega_{eff}^{23}}{2} t}_{\text{Zero-quantum}} + \cos^{2} \theta_{3} \cos \left(\frac{\omega_{eff}^{23} - \omega_{eff}^{14}}{2} t \right) \right].$$
Interference term

The final CP signal expression [Eq. (2.11)] has contributions from the double-quantum

 (DQ_{14}) and zero-quantum (ZQ_{23}) CP transfer modes, along with an interference term arising from the DQ_{14} and ZQ_{23} CP modes. The pure DQ_{14}/ZQ_{23} CP transfer modes in the CP signal have manifestation of the absorptive $(\cos^2\theta_{ij})$ and dispersive $(\cos\theta_{ij}\sin\theta_{ij})$ components. To the best of our knowledge, the interference and dispersion terms resulting purely from the S-spin off-resonance irradiation in the description of CP spin dynamics between spin-1/2 systems have not been discussed in the existing literature. The CP transfer could be maximized through any of the possible CP modes by adjusting the RF field amplitudes employed on I and S-spin channels; known as the Hartmann-Hahn (HH) matching conditions as described below.

2.1.4 Evaluation of the Hartmann-Hahn (HH) CP matching conditions

• ZQ₂₃ CP matching condition:

Setting $\Delta = 0 \implies \omega_{e,I} = \omega_{e,S}$.

Under the exact ZQ_{23} CP matching condition, the resulting signal expression is given as

$$S(t) = \frac{\omega_{1I}\omega_{1S}}{\omega_{e,I}\omega_{e,S}} \left[\underbrace{\sin^2 \frac{\omega_d^{14,23}}{2} t}_{\text{Zero-quantum}} + \underbrace{\left\{ \frac{\omega_{1S}}{\omega_{e,I}} \frac{\omega_d}{\omega_{e,I}} \sin \theta_{14} \cos \theta_{14} - \cos^2 \theta_{14} \right\} \sin^2 \frac{\omega_{eff}^{14}}{2} t}_{\text{High-frequency DQ term}} + \text{High-frequency interference term} \right].$$

$$(2.13)$$

Exact setting of the ZQ₂₃ HH CP matching condition will not only optimize the polarization transfer through ZQ₂₃ CP modes but also make other modes of CP transfer high-frequency terms that are less relevant for the polarization transfer. It is important to note that $\omega_{e,I}$ (= $\sqrt{\omega_{1I}^2 + (2\omega_d\Omega_S/\omega_{e,S})^2}$) exhibits dipolar coupling dependence under off-resonance S-spin irradiation. Consequently, the HH CP matching condition will vary based on the strength and orientation of the heteronuclear dipolar coupling. These effects become operationally significant while extracting the dipolar coupling parameters from the CP lineshape with improved accuracy.

• DQ₁₄ CP matching condition:

Setting $\Sigma = 0 \implies \omega_{e,I} = -\omega_{e,S}$.

Under exact DQ_{14} CP matching condition, the CP signal expression is given as follows:

$$S(t) = \frac{\omega_{1I}\omega_{1S}}{\omega_{e,I}\omega_{e,S}} \left[\underbrace{-\sin^2 \frac{\omega_d^{14,23}}{2} t}_{\text{Double-quantum}} + \underbrace{\left\{ -\frac{\omega_{1S}}{\omega_{e,I}} \frac{\omega_d}{\omega_{e,I}} \sin \theta_{23} \cos \theta_{23} + \cos^2 \theta_{23} \right\} \sin^2 \frac{\omega_{eff}^{23}}{2} t}_{\text{High-frequency ZQ term}} + \text{interference term} \right].$$

$$(2.14)$$

The DQ_{14} signal expression is just the 180° phase-shifted version of the ZQ_{23} signal expression. Therefore, both the CP matching conditions are expected to show similar CP dynamics for static samples.

• Interference of the \mathbf{DQ}_{14} and \mathbf{ZQ}_{23} term:

$$\omega_{eff}^{14} = \pm \omega_{eff}^{23} \implies \omega_{1I} = 0.$$

This condition is not like any normal HH CP matching condition. Still, it represents a condition where only the I-spin loses the polarization without transferring to the S-spin. Therefore, such conditions should be avoided while setting the CP conditions.

Under on-resonance S-spin irradiation, i.e. $\Omega_S = 0$, the above CP signal reduces to a much simpler form as given below:

$$S(t) = \left[\underbrace{-\cos^2 \theta_{14} \sin^2 \frac{\omega_{eff}^{14}}{2} t}_{\text{Double-quantum}} + \underbrace{\cos^2 \theta_{23} \sin^2 \frac{\omega_{eff}^{23}}{2} t}_{\text{Zero-quantum}}\right]. \tag{2.15}$$

The final CP signal expression [Eq. (2.15)] has contributions from the double-quantum (14) and zero-quantum (23) CP transfer modes which are individually optimized to evaluate the HH CP matching conditions shown in Table 2.1.

Table 2.1: The expression and transitions associated with various HH CP matching conditions for the CP transfer between I = 1/2 and S = 1/2 spin systems.

CP matching conditions and associated transitions	off-resonance S -spin irradiation	on-resonance S -spin irradiation
Double-quantum (DQ ₁₄) $ 1/2, 1/2\rangle \leftrightarrow -1/2, -1/2\rangle$	$\omega_{e,I} = -\omega_{e,S}$	$\omega_{1I} = -\omega_{1S}$
Zero-quantum (ZQ ₂₃) $ -1/2, 1/2\rangle \leftrightarrow 1/2, -1/2\rangle$	$\omega_{e,I} = \omega_{e,S}$	$\omega_{1I} = \omega_{1S}$

2.2 Results and discussion

To test the validity of our proposed analytic theory of the CP dynamics in an isolated two spin I=1/2 and S=1/2 model framework, we carried out a comparison between the CP efficiency profiles generated using computer simulation based on Eq. (2.11) and the more exact numerical simulation program, SIMPSON [131]. All the simulations were generated considering the $I={}^{1}{\rm H}$ and $S={}^{15}{\rm N}$ model system; although the proposed analytical framework is equally applicable for any I=1/2 and S=1/2 spin system. The simulation parameters: internuclear distance $(r_{IS}=1.05~{\rm \AA})$, contact time = 2.0 ms and RF irradiation amplitude ν_{1S} ($\omega_{IS}/2\pi=50~{\rm kHz})$ on the S-spin channel, are used unless specified. For a pedagogical description, we begin by discussing the CP spin dynamics for on-resonance S-spin irradiation followed by off-resonance irradiations.

The state-picture representation is offered in Section 2.3.3 as an alternative formalism to describe the underlying CP spin dynamics in spin-1/2 systems.

2.2.1 Description of the CP dynamics under on-resonance S-spin irradiation

In the simulations depicted in Figure 2.4, the CP efficiency is plotted as a function of 1 H RF amplitude at constant mixing/contact time ($\tau_{c} = 2.0 \, ms$) for single-crystal (panels a1-a2) and powder (panels b1-b2) samples. As illustrated in Figure 2.4, the analytic simulations based on Eq. (2.15) are in excellent agreement with those obtained from numerical simulations for both single-crystal and powder samples. Therefore, validates our theoretical model framework. To analyze the similarities and differences between the ZQ₂₃ and DQ₁₄ CP conditions, the CP efficiency profiles are generated under each CP condition (panels a1-b1: ZQ₂₃ CP condition and panels a2-b2: DQ₁₄ CP condition). The CP efficiency profile for the DQ₁₄ CP condition is generated by shifting the phase of the

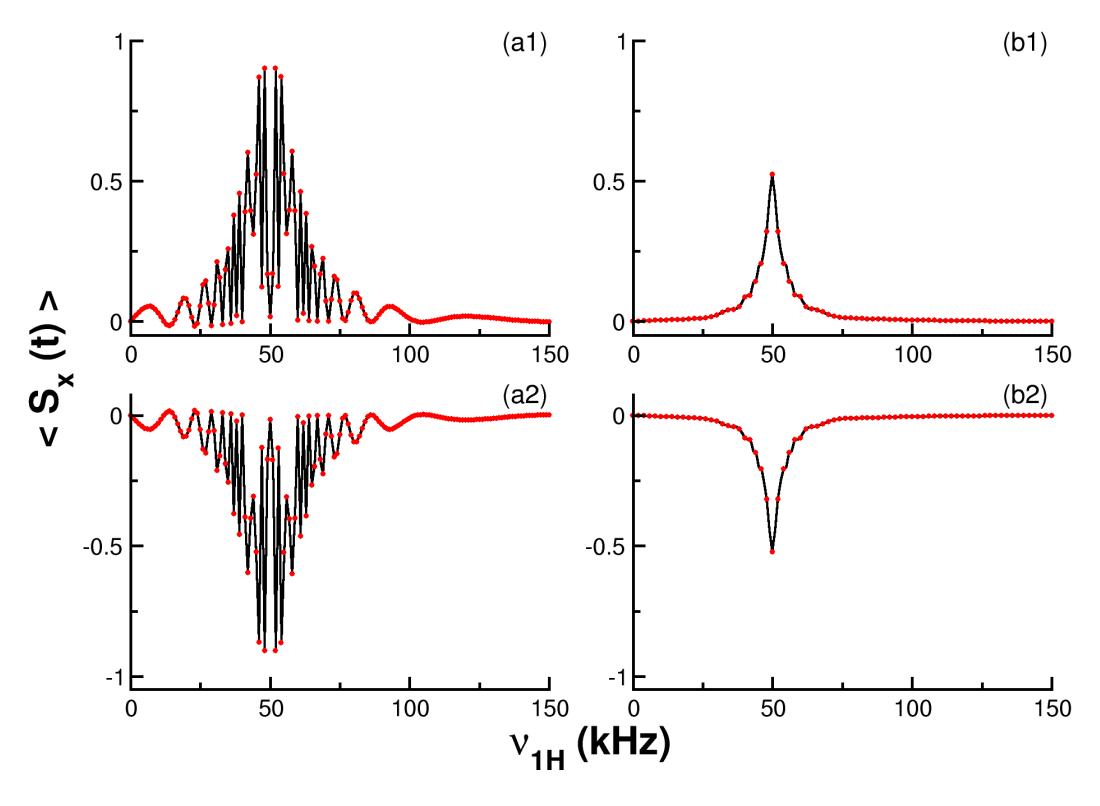


Figure 2.4: In the CP simulations depicted, the polarization build-up on the S-spin (due to transfer from the I-spin) is monitored as a function of the ¹H RF amplitude for single-crystal (a1-a2) and powder (b1-b2) samples. The following parameters were employed in the simulations: Dipolar coupling parameters (internuclear distance $r_{IS} = 1.05$ Å and dipolar PAS angle $\beta_d = 0^{\circ}$ and dipolar PAS angle $\beta_d = 0^{\circ}$), RF parameters $\nu_{1S} = 50$ kHz (a1-b1) and $\nu_{1S} = -50$ kHz (by shifting the phase of the I-spin by 180°) (a2-b2) under on-resonance irradiation for both I and S-spins and the mixing time during the CP experiment was held constant (2 ms). The SIMPSON simulations (black curve) are fitted with the analytic signal expressions $ZQ_{23}+DQ_{14}$ (red solid circle) [Eq. (2.15)]. The powder simulations were performed using 4180 orientations of α and β angles (zcw4180).

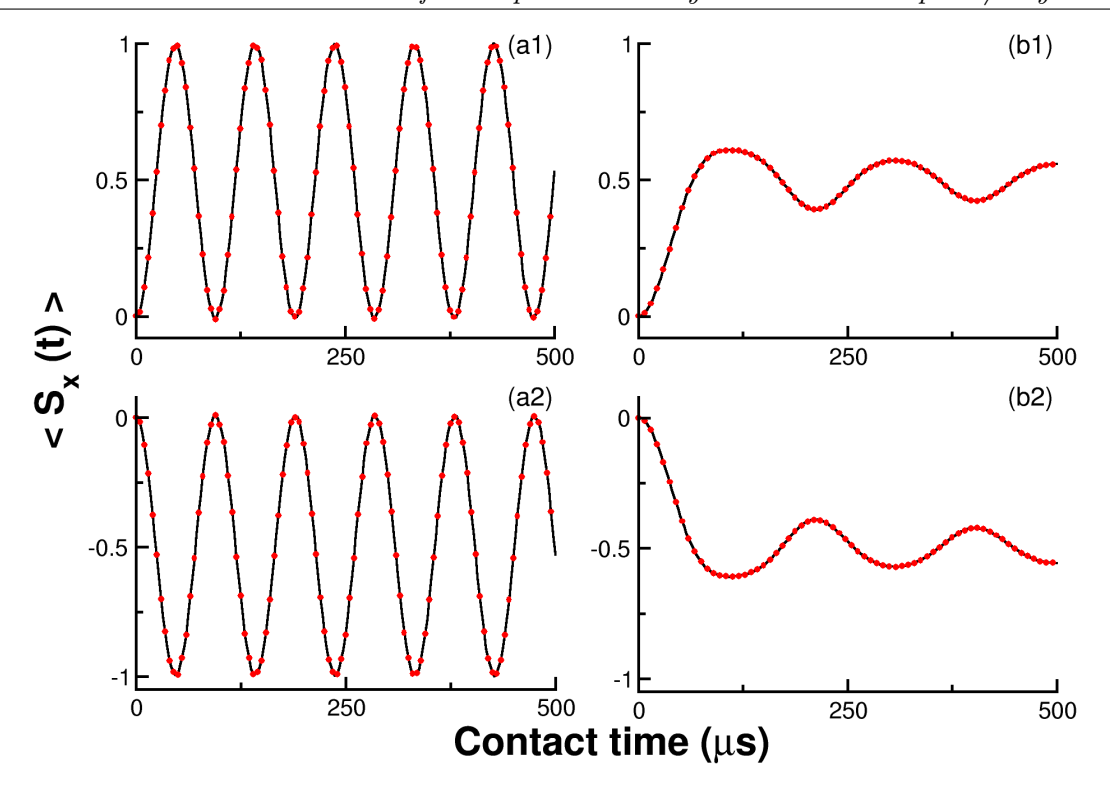


Figure 2.5: In the CP simulations depicted, the polarization build-up on the S-spin (due to transfer from the I-spin) is monitored as a function of the contact time under constant RF amplitudes on both the spins for single-crystal (a1-a2) and powder (b1-b2) samples. The following parameters were employed in the simulations: Dipolar coupling parameters (internuclear distance $r_{IS} = 1.05$ Å and dipolar PAS angle $\beta_d = 0^{\circ}$), RF parameters ZQ₂₃ CP condition ($\nu_{1H} = 50$ kHz and $\nu_{1S} = 50$ kHz) in panels (a1-b1) and DQ₁₄ CP condition ($\nu_{1H} = 50$ kHz and $\nu_{1S} = -50$ kHz; shifting the phase of the I-spin by 180°) in panels (a2-b2) under on-resonance irradiation. The SIMPSON simulations (black curve) are fitted with the analytic signal expressions ZQ₂₃+DQ₁₄ (red solid circle) [Eq. (2.15)]. The powder simulations were performed by considering the zcw4180 crystallite orientations.

I-spin RF irradiation by 180°. Due to the similarity in the DQ₁₄ and ZQ₂₃ CP efficiency profiles, henceforth, we have plotted the CP efficiency profiles from the ZQ₂₃ CP condition. In the case of a single-crystal sample, the RF-domain CP efficiency profiles are symmetrically placed around exact HH CP matching conditions ($\nu_{1H} = \nu_{1S} = 50 \text{ kHz}$). The exactness of the proposed analytic theory is also validated through the time-domain simulations in Figure 2.5 (panels a1-a2). The powder averaging expression [4,137] for the CP signal [Eq. (2.15)] is given as

$$\overline{S(t)} = \frac{1}{8\pi^2} \int_0^{2\pi} d\alpha_{ML} \int_0^{\pi} d\beta_{ML} \sin\beta_{ML} \int_0^{2\pi} d\gamma_{ML} S(\alpha_{ML}, \beta_{ML}, \gamma_{ML}; t). \tag{2.16}$$

Here $(\alpha_{ML}, \beta_{ML}, \gamma_{ML})$ represents the powder orientation, and $\sin \beta_{ML}$ is the weighting factor which is maximum for the orientation in the plane perpendicular to the Zeeman magnetic field. In the case of powder samples, the statistical distributions of crystallite orientations (shown in Eq. (2.16), interfere to result in averaged CP behavior. Due to this reason, the overall width of the CP resonance is reduced in Figure 2.4 (panels b1-b2),

and the time-domain simulations show a slower polarization build-up [Figure 2.5 (panels b1-b2)] in comparison with the single-crystal sample.

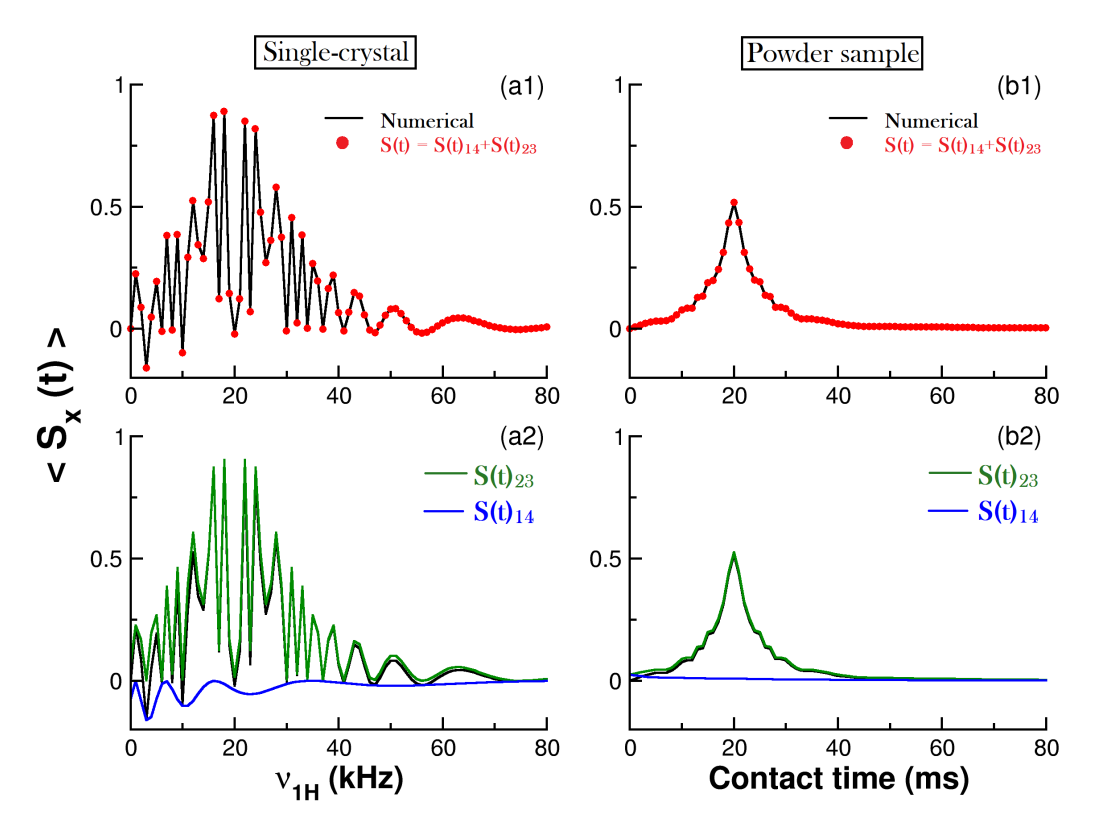


Figure 2.6: In the CP simulations depicted, the polarization build-up on the S-spin (due to transfer from the I-spin) is monitored as a function of the ¹H RF amplitude for single-crystal and powder samples in panels (a1-a2) and (b1-b2), respectively. The following parameters were employed in the simulations: Dipolar coupling parameters (internuclear distance $r_{IS} = 1.05$ Å and dipolar PAS angle $\beta_d = 0^{\circ}$), RF parameters (internuclear distance r_{IS} = 1.05 Å and dipolar PAS angle $\beta_d = 0^{\circ}$), RF parameters $\nu_{1S} = 20$ kHz under on-resonance irradiation for both I and S-spins and the mixing time during the CP experiment was held constant (say $t_{mix} = 2$ ms). The SIMPSON simulations (black curve) are fitted with the analytic signal expressions ZQ_{23} +DQ₁₄ (red solid circle), ZQ_{23} (green curve) and DQ₁₄ (blue curve) [Eq. (2.15)]. The powder simulations were performed by considering the zcw4180 crystallite orientations.

These simulations are carried out at fixed S-spin RF amplitude, which is in the weak coupling regime i.e., $\omega_d \ll \omega_{1S}$ [24,138]. Figure 2.6 depicts the CP efficiency profiles in the $\omega_d \approx \omega_{1S}$ coupling regimes for single-crystal and powder samples. Details of the simulation parameters can be found in the figure caption. In this coupling regime, the results emerging from the analytic theory match perfectly well with the numerical simulations. In particular, the CP resonance becomes slightly unsymmetric with a negative CP efficiency towards lower I-spin RF amplitudes. To understand the origin of observations, we evaluated the individual signal contributions from the two CP conditions [Eq. (2.15)] for both single-crystal and powder samples. For the ZQ₂₃ CP matching condition, the dominant contribution to the polarization transfer arises from the contributions from the ZQ₂₃ CP signal expression, while a finite contribution comes from the otherwise high-frequency phase-shifted DQ₁₄ signal component. This indicates

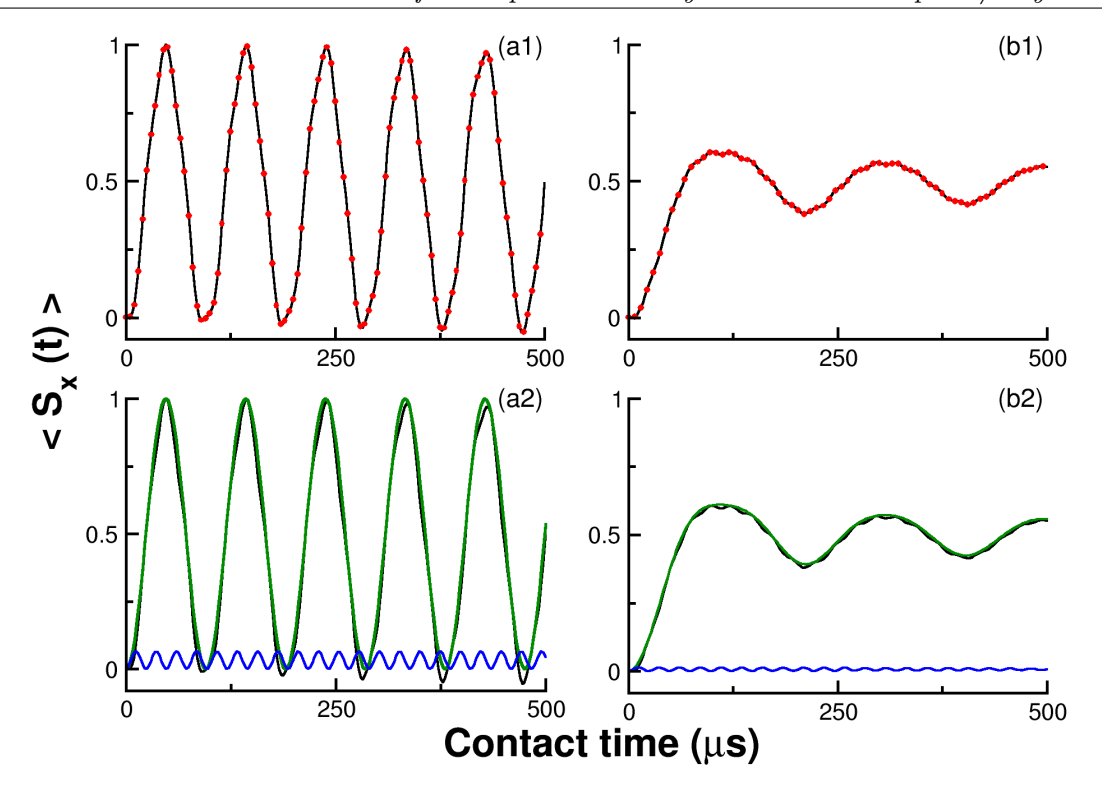


Figure 2.7: In the CP simulations depicted, the polarization build-up on the S-spin (due to transfer from the I-spin) is monitored as a function of the contact time under constant RF amplitudes (ZQ₂₃ CP condition) on both the spins single-crystal and powder samples in panels (a1-a2) and (b1-b2), respectively. The following parameters were employed in the simulations: Dipolar coupling parameters (internuclear distance $r_{IS} = 1.05$ Å and dipolar PAS angle $\beta_d = 0^{\circ}$), RF parameters $\nu_{1H} = 20$ kHz and $\nu_{1S} = 20$ kHz under on-resonance irradiation for both I and S-spins. The SIMPSON simulations (black curve) are fitted with the analytic signal expressions ZQ₂₃+DQ₁₄ (red solid circle), ZQ₂₃ (green curve) and DQ₁₄ (blue curve) [Eq. (2.15)]. The powder simulations were performed by considering the zcw4180 crystallite orientations.

that the spin-locking is not perfectly unidirectional in the ZQ₂₃ subspace as expected. Rather, the polarization leaks in the high-frequency DQ₁₄ subspace, in the strong coupling regime. This behavior could be attributed to the competing nature of the ZQ₂₃ and DQ₁₄ matching conditions *i.e.*, the prefactor $\left\{\frac{(\omega_d^{14,23})^2}{\Sigma^2 + (\omega_d^{14,23})^2}\right\}$ in the DQ₁₄ condition becomes comparable to the prefactor in $\left\{\frac{(\omega_d^{14,23})^2}{\Delta^2 + (\omega_d^{14,23})^2}\right\}$ in the ZQ₂₃ matching condition [Eq. (2.15)] at lower *I*-spin RF amplitudes. These observations are also well-corroborated in the time-domain simulations, where the oscillations deviate from a perfect sinusoidal behavior due to mixing of the DQ₁₄ CP efficiency for both single-crystal as well as powder samples (Figure 2.7).

From an experimental standpoint, it is advantageous to provide a concise analytic description of the evaluation of the dipolar coupling parameter through CP lineshape [137, 139]. To extract the dipolar coupling parameters from the CP experiment, the CP efficiency is monitored as a function of the mixing time, and the resulting data is Fourier

transformed (FT) to get the frequency-domain CP spectrum as shown below.

Depending on the nature of the CP matching conditions, the corresponding time-domain signal, $S(t)_{ij}$ is Fourier transformed to obtain the frequency-domain CP signal expression $[S(\omega)_{ij}]$,

$$S(\omega)_{ij} = C_{ij} \int_{-\infty}^{\infty} \sin^2\left(\frac{\omega_{eff}^{ij}}{2}t\right) e^{-i\omega t} dt$$

$$= \frac{C_{ij}}{2} \int_{-\infty}^{\infty} \left(1 - \cos\omega_{eff}^{ij}t\right) e^{-i\omega t} dt$$
(2.17)

where (ij) refer to 14 (DQ) and 23 (ZQ) matching conditions, and the constants C_{ij} are: $C_{14} = -\left(\frac{\omega_d^{14,23}}{\omega_{eff}^{14}}\right)^2$ and $C_{23} = \left(\frac{\omega_d^{14,23}}{\omega_{eff}^{23}}\right)^2$. Using the integral definition of the Dirac delta function, the Fourier-transformed CP signal expression is given as

$$S(\omega)_{ij} = C_{ij}\pi \left[\delta(\omega) - \frac{1}{2} \left\{\delta(\omega - \omega_{eff}^{ij}) + \delta(\omega + \omega_{eff}^{ij})\right\}\right]. \tag{2.18}$$

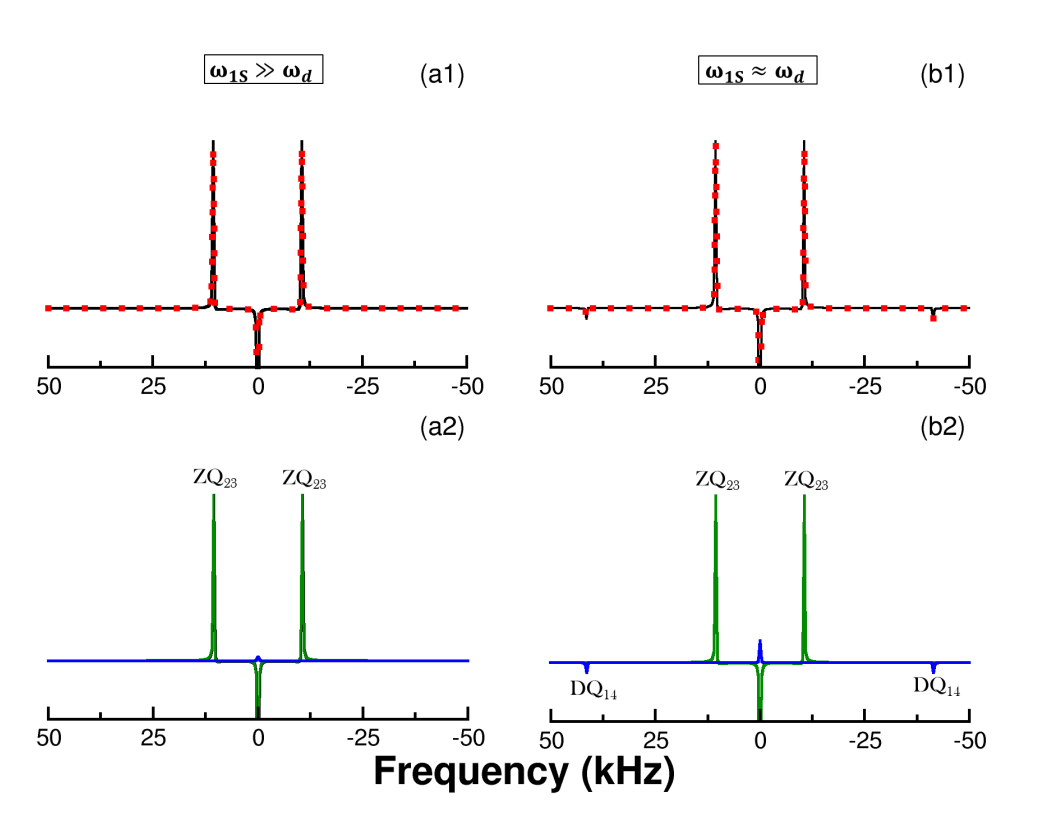


Figure 2.8: The Fourier transform of the variable contact time CP signal for the exact ZQ₂₃ CP matching condition for a single-crystal sample in different coupling regimes. The time-domain simulations were performed using a total contact time = 2.5 ms. The following parameters were employed in the simulations: Dipolar coupling parameters (internuclear distance $r_{IS}=1.05$ Å and dipolar PAS angle $\beta_d=0^\circ$), RF parameters (internuclear distance $r_{IS}=1.05$ Å and dipolar PAS angle $\beta_d=0^\circ$), RF parameters $\omega_d<<\omega_{1S}$ ($\nu_{1H}=50$ kHz and $\nu_{1S}=50$ kHz) in panels (a1-a2) and $\omega_d\approx\omega_{1S}$ ($\nu_{1H}=20$ kHz and $\nu_{1S}=20$ kHz) in panels (b1-b2) under on-resonance irradiation for both I and S-spins. The SIMPSON simulations (black curve) are fitted with the analytic signal expressions ZQ₂₃+DQ₁₄ (red solid square), ZQ₂₃ (green curve) and DQ₁₄ (blue curve) [Eq. (2.15)].

Under the exact ZQ_{23}/DQ_{14} CP matching condition, the above equation reduces to the form given below:

$$S(\omega)_{ij} = C_{ij}\pi \left[\underbrace{\delta(\omega)}_{\text{Zero-frequency}} - \frac{1}{2} \left\{ \underbrace{\delta(\omega - \omega_d^{14,23}) + \delta(\omega + \omega_d^{14,23})}_{\text{Purely dipolar splitting } (2\omega_d)} \right\} \right]. \tag{2.19}$$

The ZQ_{23}/DQ_{14} frequency-domain signal expressions [Eq. (2.19)] for the single-crystal sample displays three distinct singularities. The zero frequency ($\omega = 0$) peak appears due to the non-oscillatory component of the time-domain signal expression and the remaining two appear at the conjugate symmetric transition frequencies ($\omega = -\omega_{eff}^{ij}$ and $\omega = \omega_{eff}^{ij}$; ij = 14/23) resulting from the oscillatory components of the time-domain On setting the exact HH matching conditions, the separation signal expression. between the two symmetric singularities provides information about the dipolar coupling strength. The more intense central peak is inverse phase-related with the two conjugate symmetric singularities. As a consequence, the central peak does not interfere with the symmetric singularities, a feature that is essential for extracting dipolar coupling strengths, particularly for weakly coupled systems. Figure 2.8 demonstrates the CP spectrum generated using the Fourier transform of the time-domain simulations for a single-crystal sample. These simulations are conducted in two different coupling regimes $(\omega_d < \omega_{1S} \text{ and } \omega_d \approx \omega_{1S} \text{ in panels a1-a2 and b1-b2, respectively})$ at fixed dipolar coupling strength, and the radio frequency (RF) amplitudes are adjusted for the ZQ₂₃ CP condition. Clearly, the separation between the CP singularities will be a characteristic of the dipolar coupling constant and is similar for both CP lineshapes. However, the CP lineshape in the strong coupling limit ($\omega_d \approx \omega_{1S}$) [panels (b1-b2)] is associated with the high-frequency components from the phase-shifted DQ_{14} CP condition. In the ideal scenario presented in this thesis, these unwanted distortions will not interfere with the dipolar coupling evaluation because of the inverse phase relations. The CP lineshapes in the case powder sample are shown in Figure 2.9. For the powder sample, the interference from various weighted powder orientations (sin β_{ML} ; β_{ML} is the powder angle from MolAS to Laboratory frame and $\sin \beta_{ML}$ represents the probability of that particular orientation) leads to a CP lineshape with well-defined singularities (Pake-doublet). The key difference from a regular peak doublet is the presence of central zero-frequency peaks. The distance between the singularities will be a direct measure of the dipolar coupling strength (Figure 2.9). Contrary to the single-crystal sample, the magnitude of the DQ_{14} high-frequency components are relatively smaller in the powder sample. This is attributed to the orientation dependence heteronuclear dipolar coupling frequency (see Appendix Figure B.1), the condition ($\omega_d \approx \omega_{1S}$) is satisfied for a very small fraction of orientations which have a very smaller statistical probability $(\sin \beta_{ML})$ in the overall powdered behavior. We feel such a contribution might have a significant impact while considering the CSA contribution in the CP dynamics.

2.2.2 Description of the CP dynamics under off-resonance S-spin irradiation

The off-resonance irradiation effects are unavoidable considering the large spectral widths of the dilute spins and are known to significantly alter the CP spin dynamics in spin-1/2 systems [140]. Figure 2.10 depicts the CP efficiency profiles with a variation of the ¹H RF field in different coupling regimes $\Omega_S << \omega_{1S}$, $\Omega_S \approx \omega_{1S}$ and $\Omega_S > \omega_{1S}$ for single-crystal as well as powder samples. The analytic simulations based on Eq. (2.11) are in excellent agreement with those obtained from numerical simulation for both single-crystal as well as powder samples across various coupling regimes. Therefore, it validates our theoretical model framework. The off-resonance irradiation deteriorates the overall CP efficiency and CP resonance becomes highly distorted and asymmetrical. To understand the origin of these distortions, we evaluated the individual contributions from the ZQ₂₃, DQ₁₄ and interference terms in Eq. (2.11) (panels a2-c2). Across all coupling regimes, the overall CP transfer is dominated by the ZQ₂₃ CP condition and finite contributions are observed

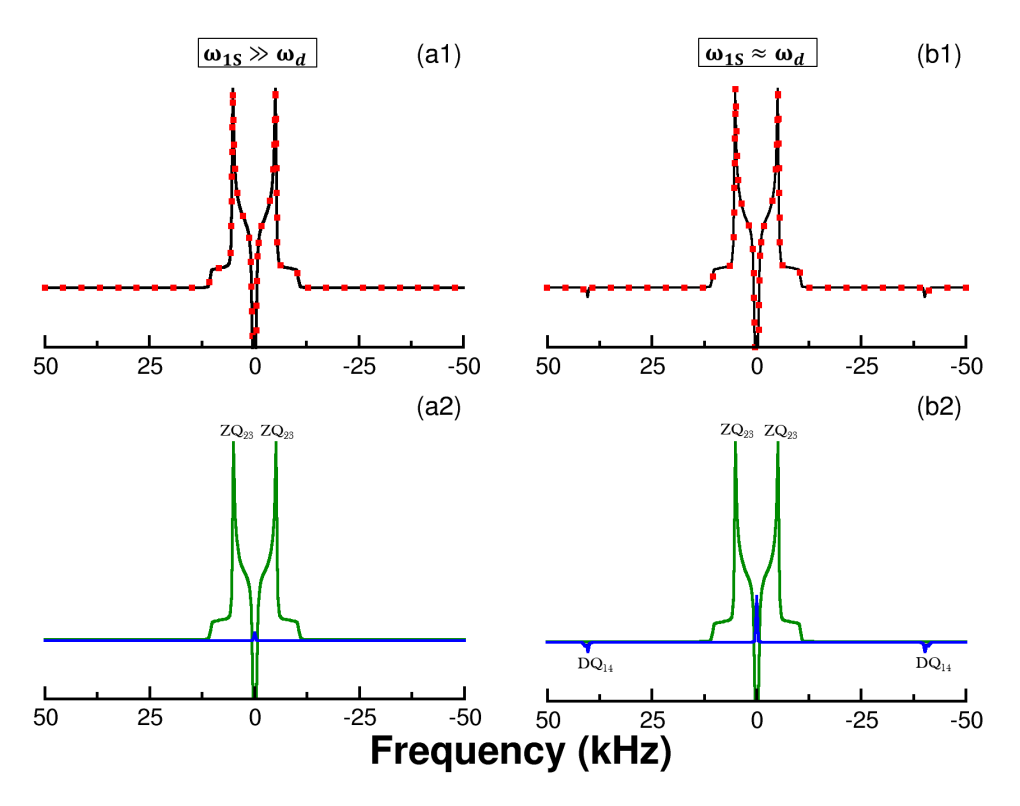


Figure 2.9: The Fourier transform of the variable contact time CP signal for the exact ZQ₂₃ CP matching condition for powder sample in different coupling regimes. The time-domain simulations were performed using a total contact time = 2.5 ms. The following parameters were employed in the simulations: Dipolar coupling parameters (internuclear distance $r_{IS} = 1.05$ Å and dipolar PAS angle $\beta_d = 0^{\circ}$), RF parameters $\omega_d << \omega_{1S}$ ($\nu_{1H} = 50$ kHz and $\nu_{1S} = 50$ kHz) in panels (a1-a2) and $\omega_d \approx \omega_{1S}$ ($\nu_{1H} = 20$ kHz and $\nu_{1S} = 20$ kHz) in panels (b1-b2) under on-resonance irradiation for both I and S-spins. The SIMPSON simulations (black curve) are fitted with the analytic signal expressions ZQ₂₃+DQ₁₄ (red solid square), ZQ₂₃ (green curve) and DQ₁₄ (blue curve) [Eq. (2.15)]. The powder simulations were performed by considering the zcw4180 crystallite orientations.

from the otherwise high-frequency DQ₁₄ CP condition and interference terms. Besides, both ZQ₂₃ and DQ₂₃ CP conditions have absorptive $(\cos^2\theta_{ij})$ and dispersive $(\sin\theta_{ij}\cos\theta_{ij})$ polarization pathways [Eq. (2.11)] which introduce distortions in overall CP resonance. These distortions (dispersive components) are purely based on the single-quantum I-spin dipolar transitions (SQ_{d,I}). This argument is further supported by simulations carried out with and without the inclusion of these SQ_{d,I} dipolar transitions (Figure 2.11). Apart from the distortions, these SQ_{d,I} dipolar transitions induce a dipolar-dependent shift in the position of the HH CP matching conditions, and the degree of shift is prominent in the $\Omega_S > \omega_{1S}$ coupling regime which decreases towards the weaker coupling regime ($\Omega_S << \omega_{1S}$) (Figure 2.12). These factors, along with inefficient spin-locking $\left(\text{scaling factor} = \frac{\omega_{1I}\omega_{1S}}{\omega_{e,I}\omega_{e,S}}\right)$ results in lowering of the CP intensity as well as the widths of CP resonance in the strong coupling regime ($\Omega_S > \omega_{1S}$). As the overall CP resonance narrows, the CP transfer will become less tolerant to any mismatch in the HH CP condition and RF inhomogeneities. Therefore, stronger RF irradiations are required to compensate

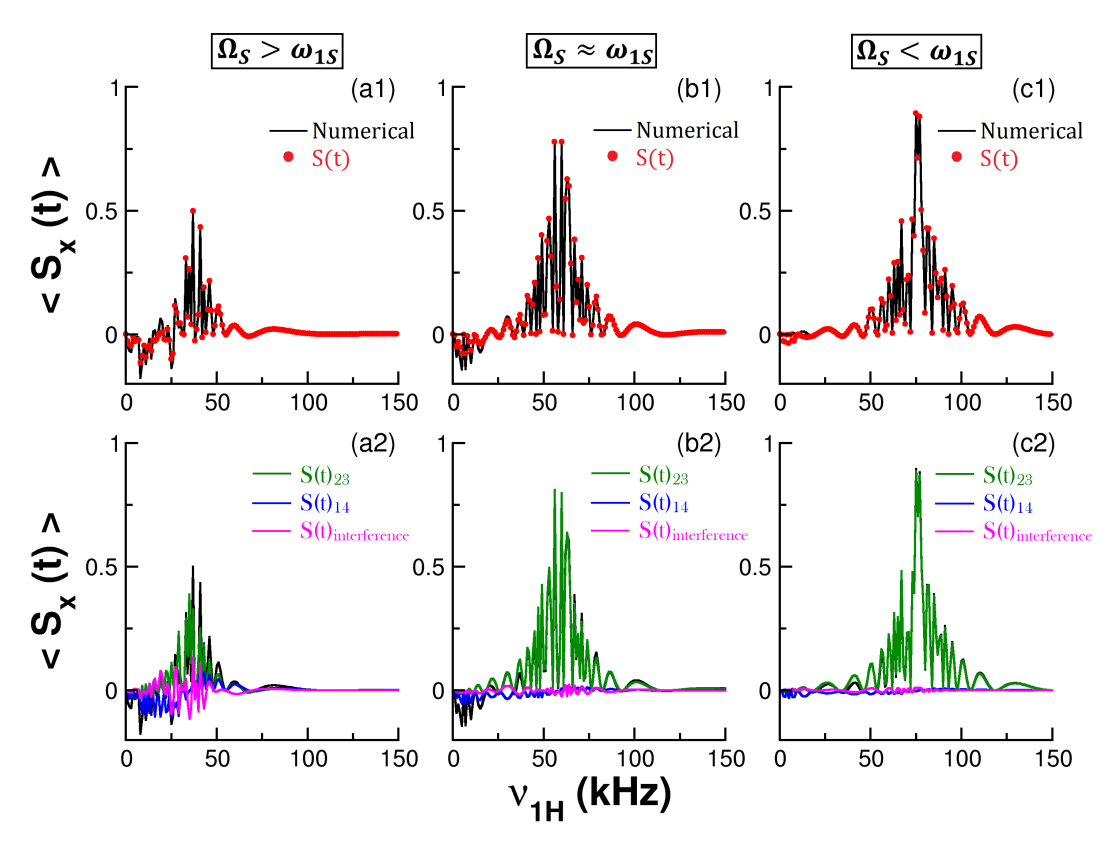


Figure 2.10: In the CP simulations depicted, the polarization build-up on the S-spin (due to transfer from the I-spin) is monitored in a single-crystal sample as a function of the RF field employed on the I-spin. The following parameters were employed in the simulations: Dipolar coupling parameters (internuclear distance $r_{IS} = 1.05$ Å and dipolar PAS angle $\beta_d = 0^{\circ}$), RF parameters $\nu_{1S} = 20$ kHz (a1-a2); $\nu_{1S} = 50$ kHz (b1-b2) and $\nu_{1S} = 70$ kHz (c1-c2) under the S-spin off-resonance irradiation $\Omega_S = 30$ kHz. The SIMPSON simulations (black curve) are fitted with the analytic signal expressions ZQ₂₃+DQ₁₄ (red solid circle), ZQ₂₃ (green curve), DQ₁₄ (blue curve) and interference term (magenta curve) [Eq. (2.11)].

for the off-resonance irradiations, which strongly affect the widths of CP resonances as suggested by the plot of the effective dipolar coupling constant ($\omega_d^{14,23}$) vs the S-spin off-resonance irradiation in Figure 2.12. Similar CP dynamics are manifested for powder samples (Figure 2.13). Due to powder interference from various crystallite orientations, the degree of contribution from the high-frequency components in the CP signal decreases. From these simulations, we conclude that CP transfer in spin-1/2 systems is not always unidirectional for both single-crystal and powder samples, and experimentally it may not always be possible to avoid such undesired conditions. The time-domain signal will always be associated with multiple frequency modulations like that observed for on-resonance irradiation in the regime of stronger dipolar couplings i.e., $\omega_d \approx \omega_{1S}$. Such time-domain simulations are shown in Figures 2.14 and 2.15 under various irradiation strengths.

As described in the previous section, these distortion and high-frequency components will be clearly visible in the frequency domain CP spectrum. Hence, the FT spectrum essential for dipolar coupling parameter estimation will be distorted and associated

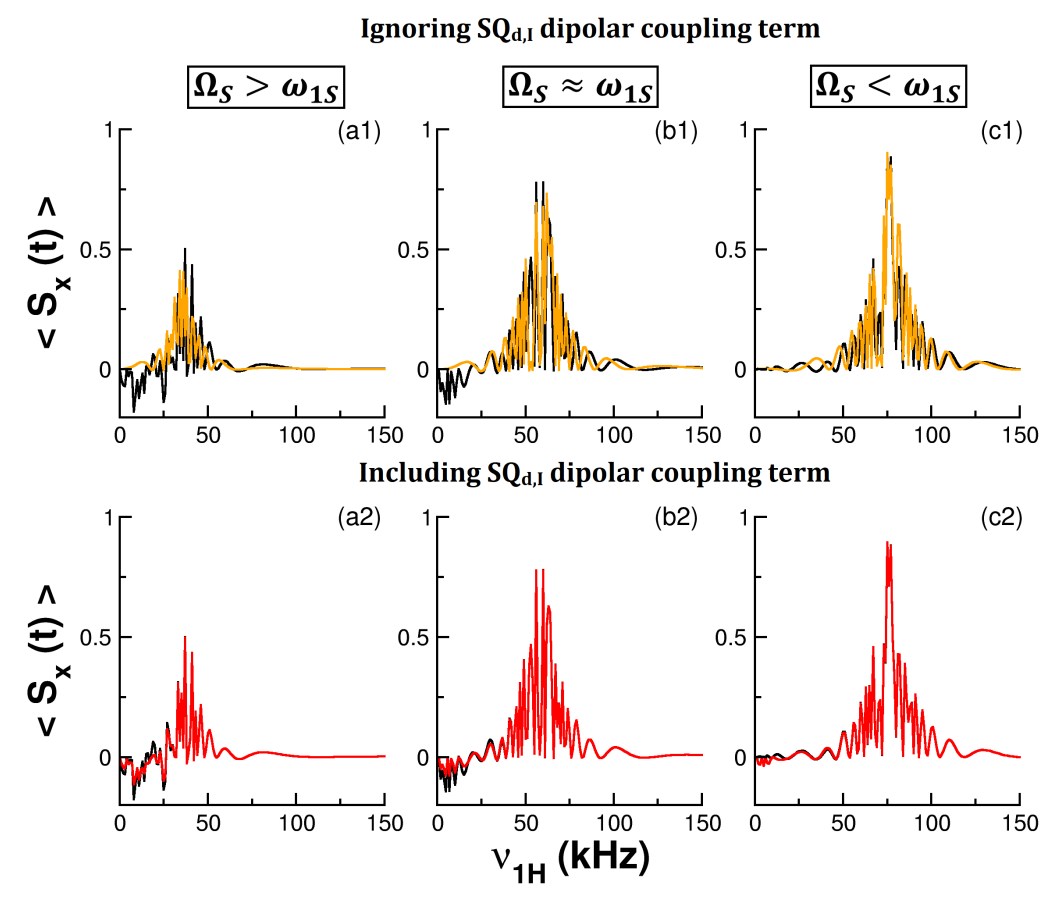


Figure 2.11: In the CP simulations depicted, the polarization build-up on the S-spin (due to transfer from the I-spin) is monitored in a single-crystal sample sample as a function of the RF field employed on the I-spin. The following parameters were employed in the simulations: Dipolar coupling parameters (internuclear distance $r_{IS} = 1.05$ Å and dipolar PAS angle $\beta_d = 0^{\circ}$), RF parameters $\nu_{1S} = 20$ kHz (a1-a2); $\nu_{1S} = 50$ kHz (b1-b2) and $\nu_{1S} = 70$ kHz (c1-c2) under the S-spin off-resonance irradiation $\Omega_S = 30$ kHz. The SIMPSON simulations (black curve) are fitted with the analytic signal expressions in absence (orange curve) and in presence (red curve) of the SQ_{d,I} term in Eq. (2.11).

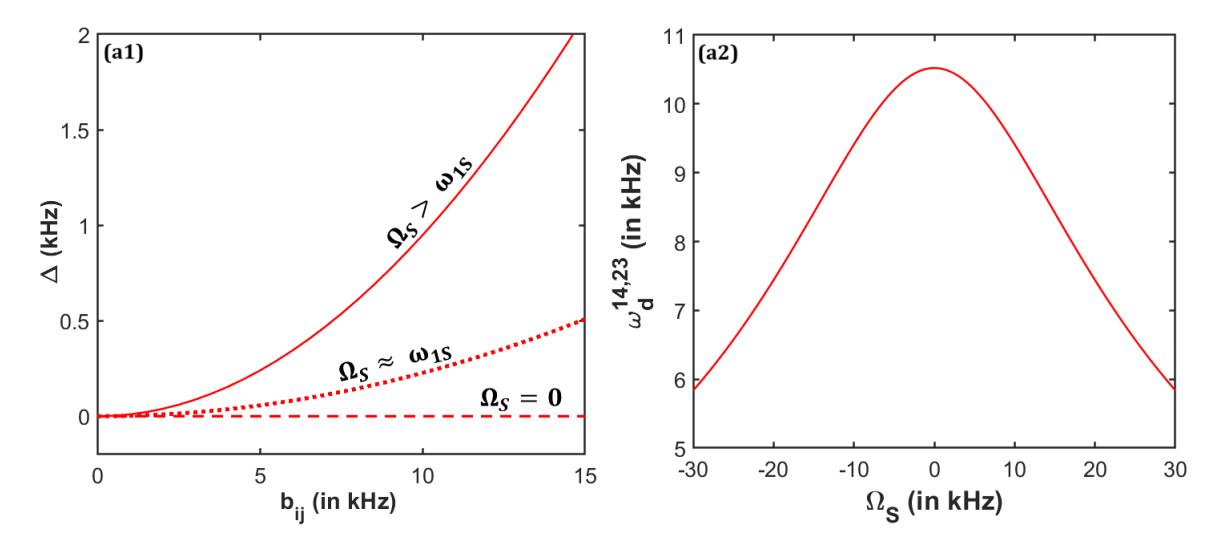


Figure 2.12: (a1) The effect of dipolar coupling strength on the ZQ_{23} CP matching condition under three different S-spin off-resonance irradiation strengths. (a2) Variation of the effective dipolar coupling constant as a function of the S-spin off-resonance irradiation strength.

with the extra frequency components. Moreover, the effective dipolar coupling constant $(\omega_d^{14,23})$ will also have RF amplitudes and off-resonance dependent scaling factor; thus, the distance between the CP singularities will be different in different coupling regimes [Figure 2.16]. The separation between the singularities will be minimum in $\Omega_S < \omega_{1S}$ (weaker coupling regime) (panels a1-a2) and maximum in $\Omega_S > \omega_{1S}$ (stronger coupling regime) (panels c1-c2). Additionally, to calculate the CP lineshape, we need to set the exact HH CP matching condition and any mis-setting will alter the modulation frequency $\sqrt{\delta^2 + (\omega_d^{14,23})^2}$ where δ is the degree of mis-setting. Another important error comes from the effect of dipolar dependent shifts while setting HH CP matching conditions (Figure 2.12). Hence, the proposed analytic theory will be beneficial in the quantitative analysis of the origin of various distortions and unwanted frequency components in the resulting CP spectrum. Moreover, the effective-field based analytic theory has provided unique insights into the CP spin dynamics, such as non-unidirectional spin-locking behavior, dipolar dependent shifts, and the presence of interference terms for isotropic and anisotropic solids. The proposed theory can be easily expanded to include the effects of chemical-shift anisotropy (CSA) for both I and S-spins. This extension may allow a quantitative understanding of the selective and non-selective excitation of the CSA orientations under different RF and off-resonance irradiation strengths. However, any inference drawn based on the above discussion will require a detailed experimental and theoretical study, which is beyond the scope of the current work.

2.2.3 State-picture representation of the CP spin dynamics

The observed behavior of CP transfer in operator-based theory can also be correlated with the energy eigen-level diagram obtained by analytic theory (section 2.1.1) and numerical diagonalization of the CP Hamiltonian shown in Figures 2.17 and 2.18. In the energy-level

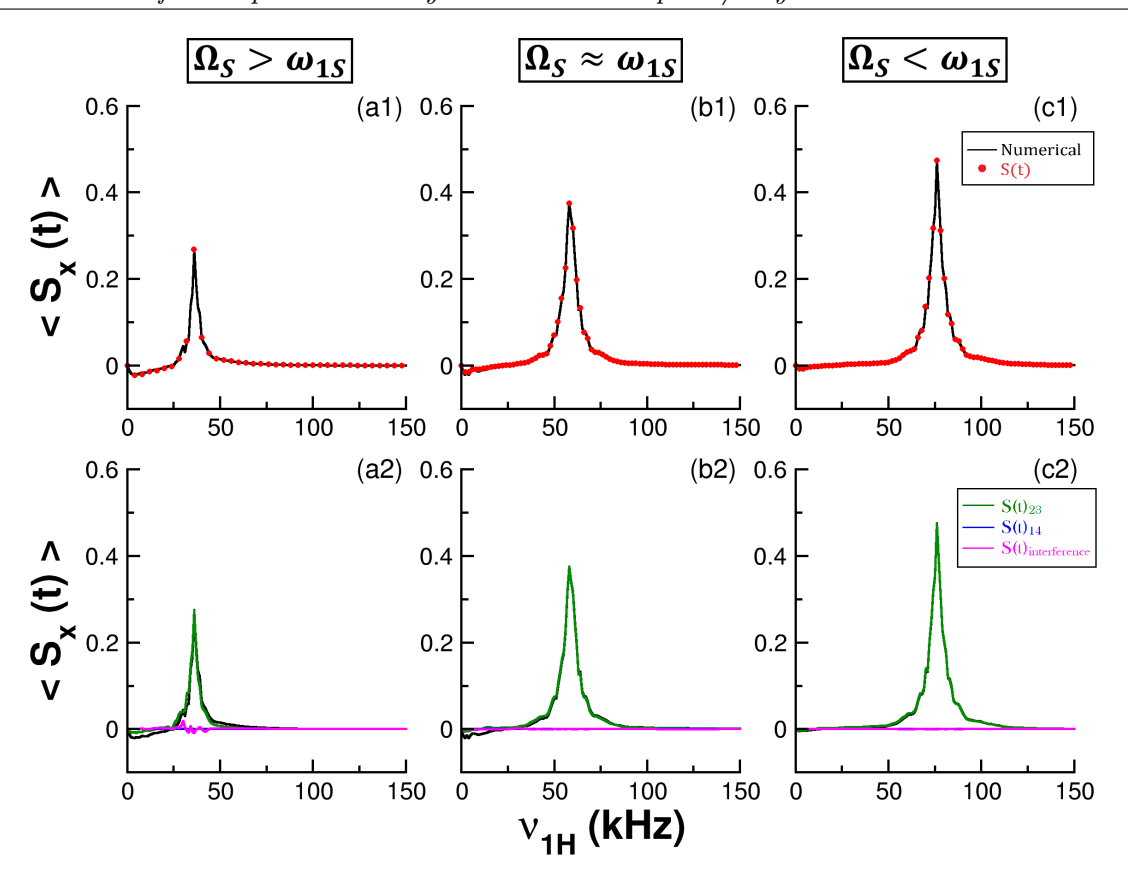


Figure 2.13: In the CP simulations depicted, the polarization build-up on the S-spin (due to transfer from the I-spin) is monitored in the powder sample as a function of the RF field employed on the I-spin. The following parameters were employed in the simulations: Dipolar coupling parameters (internuclear distance $r_{IS} = 1.05$ Å and dipolar PAS angle $\beta_d = 0^{\circ}$), RF parameters $\nu_{1S} = 20$ kHz (a1-a2); $\nu_{1S} = 50$ kHz (b1-b2) and $\nu_{1S} = 70$ kHz (c1-c2) under the S-spin off-resonance irradiation $\Omega_S = 30$ kHz. The SIMPSON simulations (black curve) are fitted with the analytic signal expressions $ZQ_{23}+DQ_{14}$ (red solid circle), ZQ_{23} (green curve), DQ_{14} (blue curve) and interference term (magenta curve) [Eq. (2.11)]. The powder simulations were performed by considering the zcw4180 crystallite orientations.

diagram, the regions of various avoided crossings are referred to as the HH CP matching conditions. In the presence and absence of S-spin off-resonance irradiations, we observed two such avoided crossings, which are in line with the HH matching conditions expressions given in Table 2.1 and corroborate extremely well with the CP resonances observed in Figures 2.4, 2.6 and 2.10 for the single-crystal sample.

To understand the origin of these avoided crossings, it is important to consider the CP Hamiltonian [Eq. (2.5)] presented in the previous theory section. The matrix representation of the above Hamiltonian is given as

$$\tilde{\hat{H}}_{CP} = \frac{1}{2} \begin{bmatrix}
\Sigma & 0 & 0 & \omega_d^{14,23} \\
0 & \Delta & \omega_d^{14,23} & 0 \\
0 & \omega_d^{14,23} & -\Delta & 0 \\
\omega_d^{14,23} & 0 & 0 & -\Sigma.
\end{bmatrix}$$
(2.20)

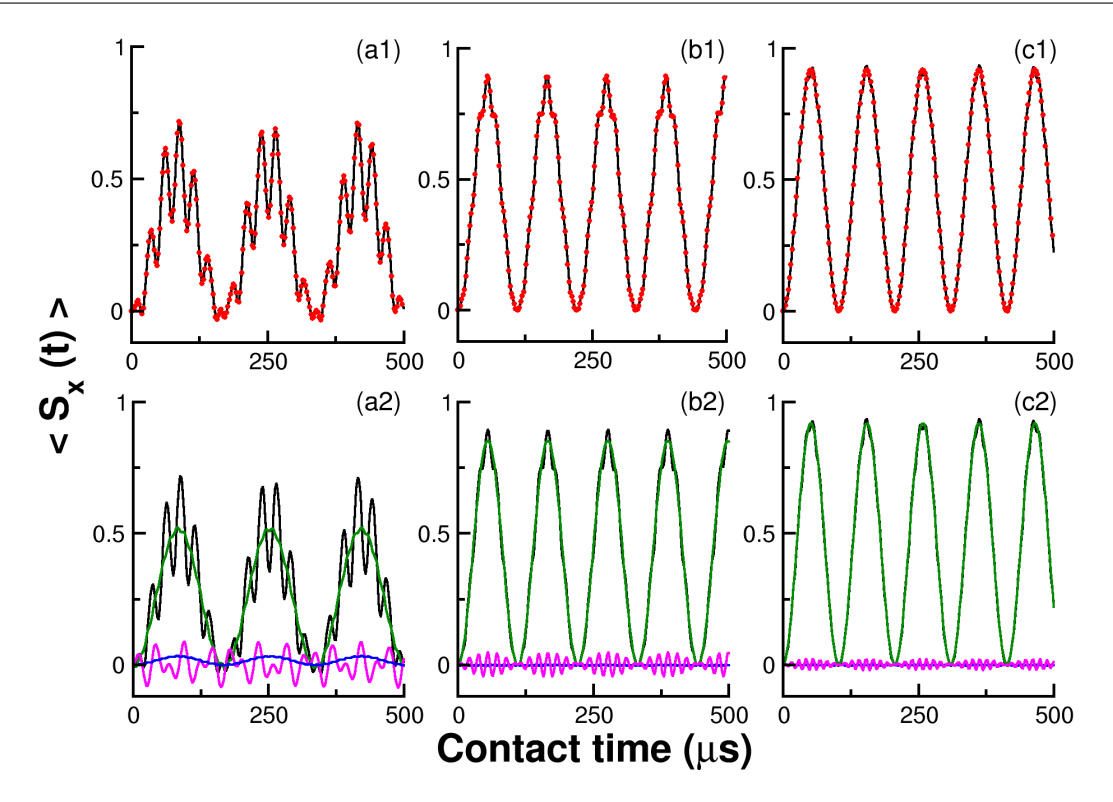


Figure 2.14: In the CP simulations depicted, the polarization build-up on the S-spin (due to transfer from the I-spin) is monitored in single-crystal as a function of the contact time under constant RF amplitudes adjusted for the ZQ₂₃ CP condition. The following parameters were employed in the simulations: Dipolar coupling parameters (internuclear distance $r_{IS} = 1.05$ Å and dipolar PAS angle $\beta_d = 0^{\circ}$), RF parameters $\nu_{1H} = 36.05$ kHz and $\nu_{1S} = 20$ kHz (a1-a2); $\nu_{1H} = 56.3$ kHz and $\nu_{1S} = 50$ kHz (b1-b2) and $\nu_{1H} = 76.35$ kHz and $\nu_{1S} = 70$ kHz (c1-c2) under the S-spin off-resonance irradiation $\Omega_S = 30$ kHz. The SIMPSON simulations (black curve) are fitted with the analytic signal expressions ZQ₂₃+DQ₁₄ (red solid circle), ZQ₂₃ (green curve), DQ₁₄ (blue curve) and interference term (magenta curve) [Eq. (2.11)].

For better visualization, the above Hamiltonian is separately written in two coupled subspaces in accordance with Figure 2.2.

$$\tilde{\hat{H}}_{CP} = \tilde{\hat{H}}_{CP}^{(14)} + \tilde{\hat{H}}_{CP}^{(23)}
= \frac{1}{2} \begin{bmatrix} \Sigma & \omega_d^{14,23} \\ \omega_d^{14,23} & -\Sigma \end{bmatrix}_{|1\rangle,|4\rangle} + \frac{1}{2} \begin{bmatrix} \Delta & \omega_d^{14,23} \\ \omega_d^{14,23} & -\Delta \end{bmatrix}_{|2\rangle,|3\rangle}.$$
(2.21)

As shown in above Eq. (2.21), the CP Hamiltonian in each subspace is independent of each other and is associated with longitudinal (constituted by the RF and off-resonance irradiation part) and transverse (effective dipolar coupling part) components, which correspond to the energy (position of avoided crossing/HH CP matching condition) and driving field/potential, respectively. In mathematical terms, the energy transfer in each subspace is analogous to a two-level system (TLS). The pictorial mathematical depiction of the CP Hamiltonian within each subspace during on or off-resonance S-spin irradiations

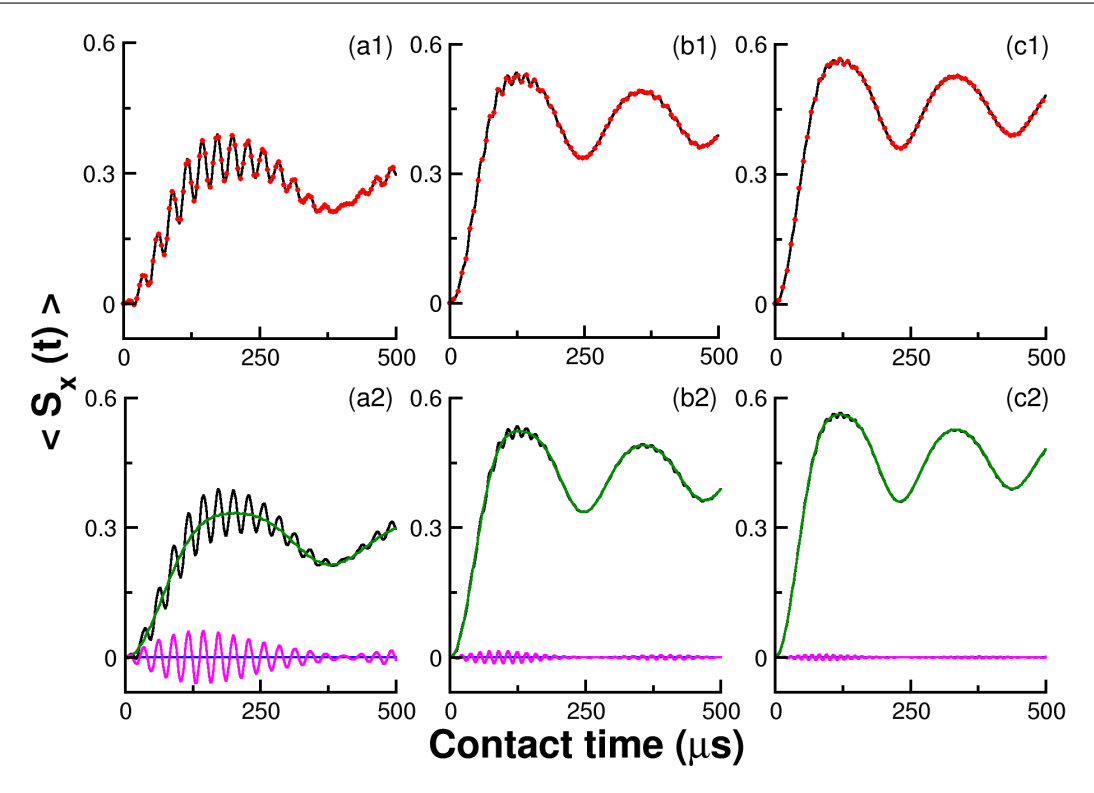


Figure 2.15: In the CP simulations depicted, the polarization build-up on the S-spin (due to transfer from the I-spin) is monitored in powder sample as a function of the contact time under constant RF amplitudes adjusted for ZQ₂₃ CP condition. The following parameters were employed in the simulations: Dipolar coupling parameters (internuclear distance $r_{IS} = 1.05$ Å and dipolar PAS angle $\beta_d = 0^{\circ}$), RF parameters $\nu_{1H} = 36.05$ kHz and $\nu_{1S} = 20$ kHz (a1-a2); $\nu_{1H} = 56.3$ kHz and $\nu_{1S} = 50$ kHz (b1-b2) and $\nu_{1H} = 76.35$ kHz and $\nu_{1S} = 70$ kHz (c1-c2) under the off-resonance irradiation strength $\Omega_S = 30$ kHz. The SIMPSON simulations (black curve) are fitted with the analytic signal expressions ZQ₂₃+DQ₁₄ (red solid circle), ZQ₂₃ (green curve), DQ₁₄ (blue curve) and interference term (magenta curve) [Eq. (2.11)]. The powder simulations were performed by considering the zcw4180 crystallite orientations.

is presented below

$$\hat{H}_{ij} = \underbrace{E_{ij}\hat{S}_z^{ij}}_{\hat{H}_{ij}^0} + \underbrace{\omega_d^{ij}\hat{S}_x^{ij}}_{\hat{D}_{ij}} \tag{2.22}$$

where, \hat{H}_{ij}^0 acts as diagonal term and \hat{D}_{ij} is the perturbation. Here the states $|i\rangle$ and $|j\rangle$ will be linear combinations of the Zeeman basis vectors which are defined by the unitary transitions involved in the analytic theory section $(\hat{U}_1\hat{U}_2\hat{U}_3)$. The matrix representation of the above Hamiltonian is given as

$$\hat{H}_{ij} = \frac{1}{2} \begin{bmatrix} E_{ii} & \omega_d^{ij} \\ \omega_d^{ij} & -E_{jj} \end{bmatrix}$$
 (2.23)

where, $E_{ii/jj}$ is a linear function of the *I*-spin RF amplitude [for exact relation see coeffs. for Σ and Δ in Eq. (2.5)]. We define the energy difference between diabatic states $\Delta_{ij} = E_{ii} - E_{jj}$. The perturbative term (ω_d^{ij}) is only effective when the energy difference between

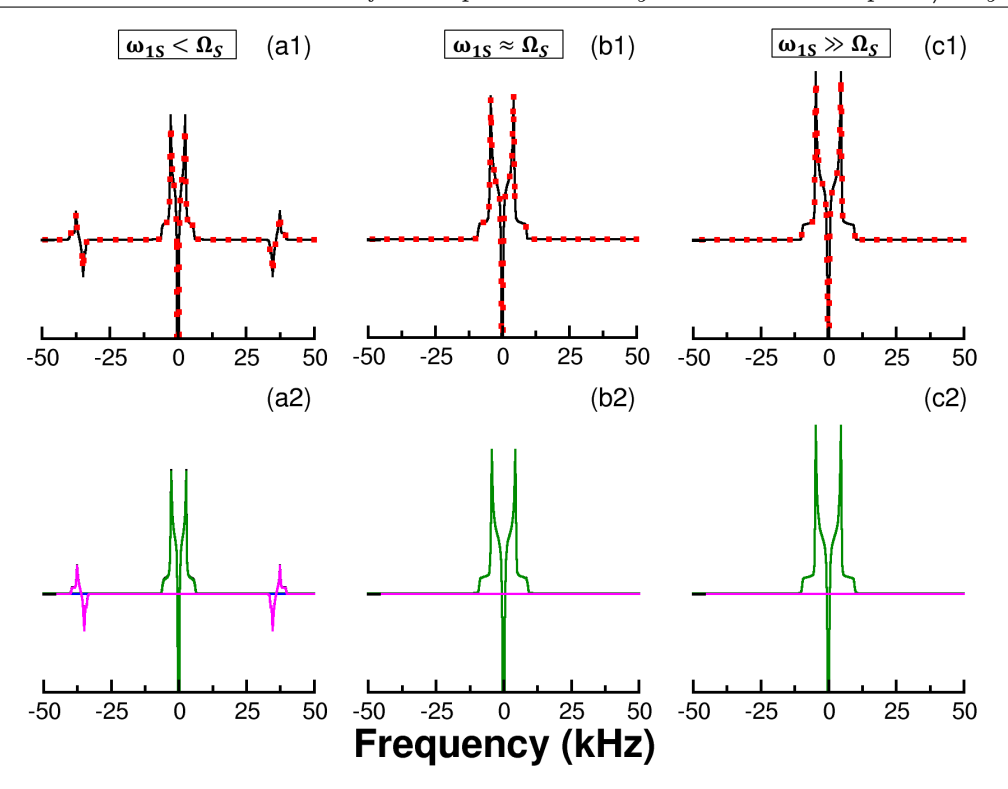


Figure 2.16: The Fourier transform of the variable contact time CP signal for the exact ZQ₂₃ CP matching condition for powder sample in different coupling regimes. The time-domain simulations were performed using a total contact time = 2.5 ms. The following parameters were employed in the simulations: Dipolar coupling parameters (internuclear distance $r_{IS} = 1.05$ Å and dipolar PAS angle $\beta_d = 0^{\circ}$), RF parameters $\nu_{1H} = 36.05$ kHz and $\nu_{1S} = 20$ kHz (a1-a2); $\nu_{1H} = 56.3$ kHz and $\nu_{1S} = 50$ kHz (b1-b2) and $\nu_{1H} = 76.35$ kHz and $\nu_{1S} = 70$ kHz (c1-c2) under the S-spin off-resonance irradiation $\Omega_S = 30$ kHz. The SIMPSON simulations (black curve) are fitted with the analytic signal expressions ZQ₂₃+DQ₁₄ (red solid square), ZQ₂₃ (green curve) and DQ₁₄ (blue curve) [Eq. (2.15)]. The separation of between the CP singularities ($2\nu_d^{14,23}$) are given in panels a1-a2, b1-b2 and c1-c2 are 18.6, 28.7 and 30.82 kHz. The powder simulations were performed by considering the zcw4180 crystallite orientations.

involved states $|i\rangle$ and $|j\rangle$ (Δ_{ij}) becomes smaller or comparable to the strength of the perturbation ($\Delta_{ij} \approx \omega_d^{ij}$). To solve this problem, it is necessary to perform the analytical diagonalization of the Hamiltonian mentioned earlier, which is already demonstrated in the theory section.

$$\hat{H}_{ij}^{E} = \frac{1}{2} \begin{bmatrix} \mathbb{E}_{i} & 0\\ 0 & -\mathbb{E}_{j} \end{bmatrix}$$
 (2.24)

where, $\mathbb{E}_{i/j} = \pm \sqrt{\Delta_{ij}^2 + (\omega_d^{ij})^2}$. The transformation involved in this diagonalization process simplifies the evaluation of the eigenbasis (adiabatic basis) states. The adiabatic basis states are linear combinations of the involved Zeeman basis states (diabatic basis). The adiabatic basis states are given as

$$|i'\rangle = \sin \theta_{ij} |i\rangle + \cos \theta_{ij} |j\rangle \text{ and } |j'\rangle = -\sin \theta_{ij} |i\rangle + \cos \theta_{ij} |j\rangle$$
 (2.25)

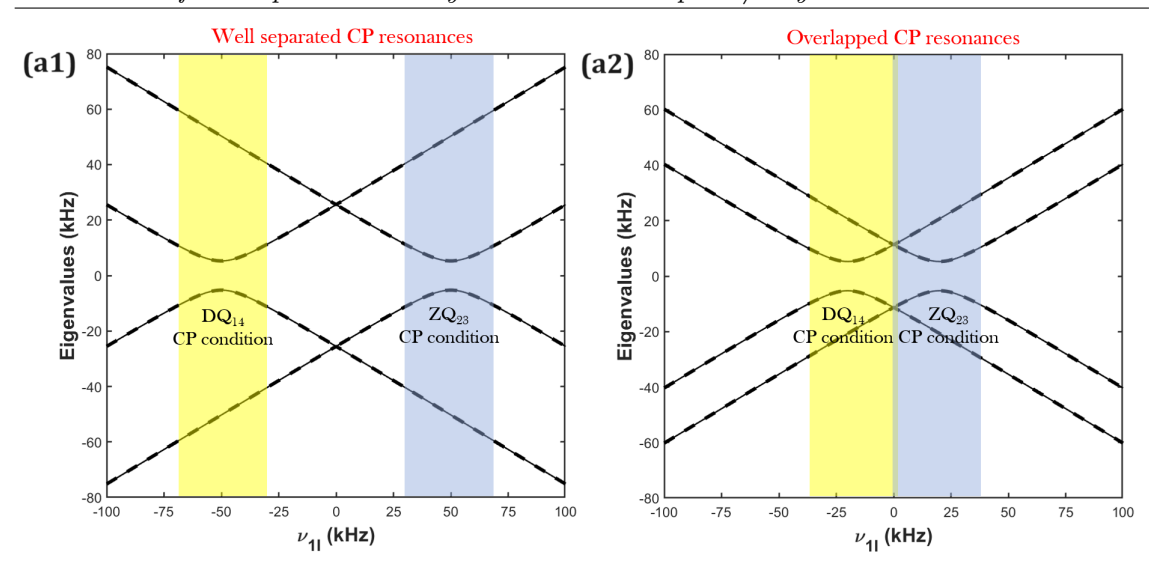


Figure 2.17: The eigenenergy level plot as a function of ¹H RF amplitude for a single-crystal sample. The following parameters were employed in the simulations: Dipolar coupling parameters (internuclear distance $r_{IS} = 1.05$ Å and dipolar PAS angle $\beta_d = 0^{\circ}$), RF parameters $\nu_{1S} = 50$ kHz (a1) and $\nu_{1S} = 20$ kHz (a2) under on-resonance irradiation. The numerical diagonalized eigenvalues (dashed curve) are fitted with the analytic diagonalized eigenvalues (solid curve) [Eq. (2.6)]. The region of avoided crossings are referred to as the HH CP matching conditions and are labelled in accordance with the CP efficiency profiles in Figures 2.4 and 2.6.

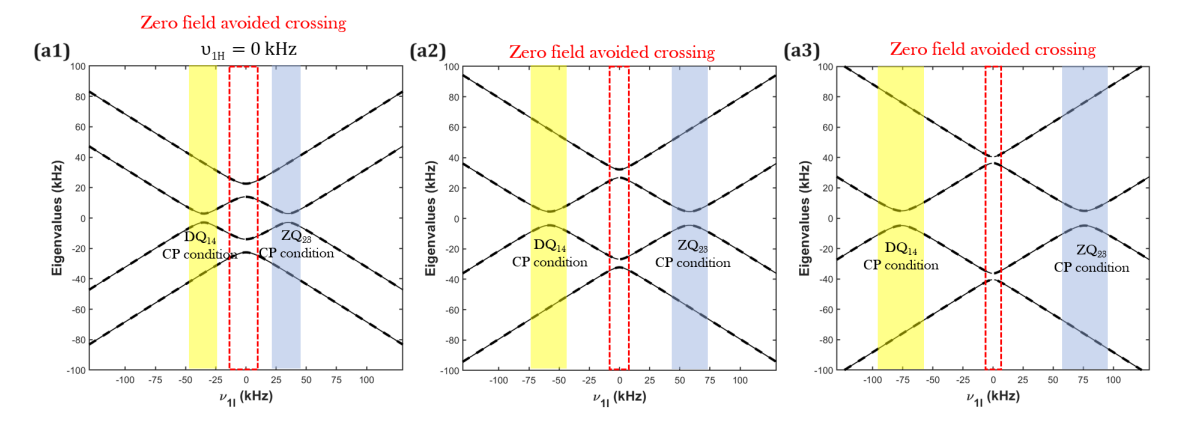


Figure 2.18: The eigen energy level plots as a function of ^{1}H RF amplitude for a single-crystal sample. The following parameters were employed in the simulations: Dipolar coupling parameters (internuclear distance $r_{IS}=1.05$ Å and dipolar PAS angle $\beta_{d}=0^{\circ}$), RF parameters $\nu_{1S}=20$ kHz (a1), $\nu_{1S}=50$ kHz (a2) and $\nu_{1S}=70$ kHz (a3) under the S-spin off- resonance irradiation $\Omega_{1S}=30$ kHz. The numerical diagonalized eigenvalues (dashed curve) are fitted with the analytic diagonalized eigenvalues (solid curve) [Eq. (2.6)]. The regions of avoided crossings are referred to as the HH CP matching conditions and are labelled in accordance with the CP efficiency profiles in Figure 2.10. The avoided crossing at zero ^{1}H RF amplitude ($\nu_{1H}=0$ kHz) are due to presence of single-quantum I-spin dipolar transitions (SQ_{d,I}).

where, $\tan \theta_{ij} = \frac{\Delta_{ij}}{\omega_d^{ij}}$ acts as a mixing angle between the original diabatic basis. The energy level representation in this TLS is shown in Figure 2.19 with variation in ¹H RF amplitude. In the absence of the perturbation ω_d^{ij} or $(\Delta_{ij} >> \omega_d^{ij})$, the energies of the

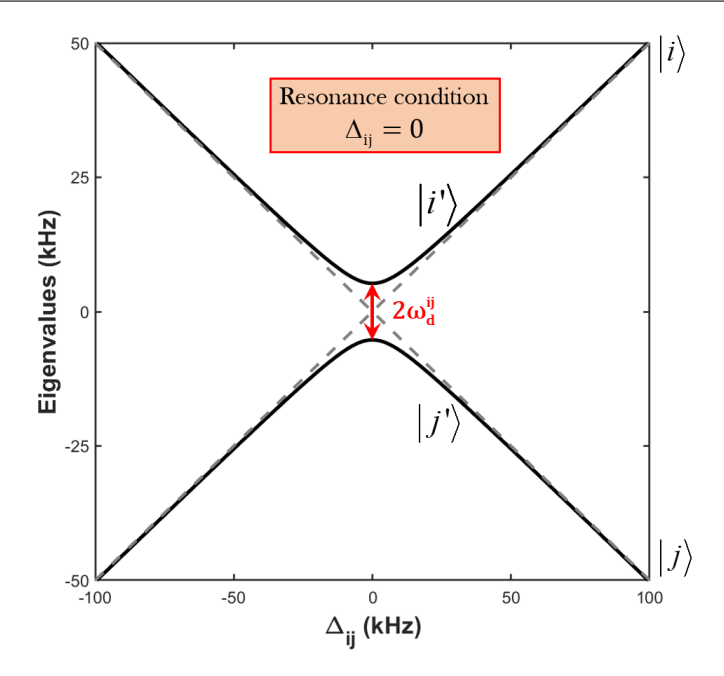


Figure 2.19: The eigen energy level plot as a function of Δ_{ij} in a two-level system (TLS). The simulations are performed using the perturbation strength $\omega_d^{ij} = 0$ kHz (gray dashed lines) and 10.52 kHz (black solid lines). The minimum in the region of avoided crossing is the resonance condition, where the energy difference between two states becomes zero in the absence of any external perturbation.

eigenstates exactly follow a linear variation with respect to $^1\mathrm{H}$ RF amplitude and become equal at the condition $\Delta_{ij}=0$; at this resonance condition we observe an exact level crossing. On the other hand, when the perturbation is active, the energy states exhibit a linear slope (ω_{1I}) in the region $\Delta_{ij}>>\omega_d^{ij}$. As soon as system enters in $\Delta_{ij}\approx\omega_d^{ij}$ region, the energy eigen states shifts from the linear to a quadratic trajectory as given by the Eq. (2.24) $\mathbb{E}_{i/j}=\pm\sqrt{\Delta_{ij}^2+(\omega_d^{ij})^2}\approx\left\{\Delta_{ij}+\frac{1}{\Delta_{ij}}(2\omega_d^{ij})^2\right\}$. In this case, the adiabatic states never cross, but rather acquire a minimum at a certain RF condition $(\Delta_{ij}=0)$ and this resonance condition is termed as Hartmann-Hahn matching condition in the CP process. Exactly, near resonance i.e., $\Delta_{ij}=0$, the energy of the system is given by $2\omega_d^{ij}$ at the mixing angle $\theta_{ij}=\frac{\pi}{4}$ and we observe a level repulsion or avoided crossing (LAC). In other words, at this condition two diabatic states perfectly mix and result in perfect adiabatic states which can efficiently lead to CP transfer via maximum population exchange. This population exchange can be calculated by the mixing coefficient in the adiabatic states or with the density operator calculation shown through Eq. (2.9). However, the process of coherent spin-mixing can be illustrated by plotting the time-evolution of the coherence terms in the density matrix expressions under various LAC [Eq. (2.9)].

The population transfer in the TLS can occur via the adiabatic pathway, where the population smoothly follows the energy eigen states without undergoing any transition or can result in a sudden jump (non-adiabatic transition) across the energy difference. The pathway of the population exchange is determined by the Landua-Zener expression (LZ) [141, 142], which states that the rate of change of the energy difference and the

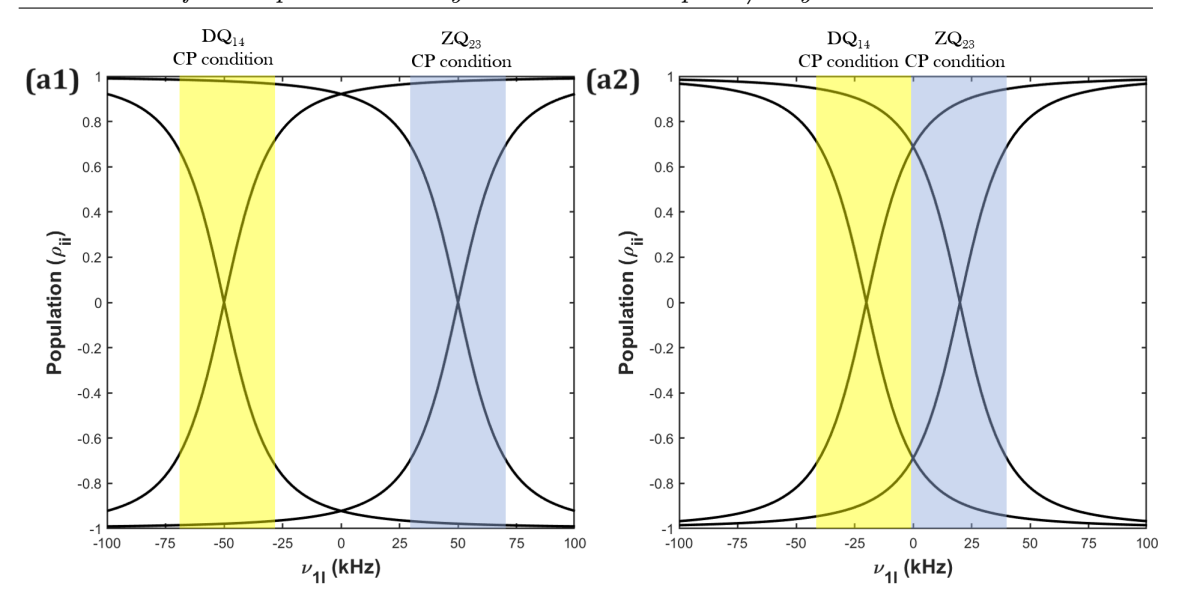


Figure 2.20: The population exchange dynamics for different HH CP matching conditions as a function of ^{1}H RF amplitude for a single-crystal sample. The population coefficients for different HH matching conditions are calculated based on the final density matrix calculation as given in Eq. (2.9) and are given as DQ₁₄ (ρ_{11} , ρ_{44}): (sin² θ_{14} , -sin² θ_{14}) and ZQ₂₃ (ρ_{22} , ρ_{33}): (sin² θ_{23} , -sin² θ_{23}). The area between each avoided crossings can be correlated with the width of each CP resonance observed in Figures 2.4 and 2.6. All simulation parameters are exactly the same as used in Figure 2.17.

strength of the perturbation acting in the system actively plays a role in deciding the mixing pathways. In the above representation, the probability of the LZ transition is given as

$$P_{i \to j}^{nad} = exp \left\{ \frac{2(\omega_d^{ij})^2}{d\Delta_{ij}/dt} \right\}$$
 (2.26)

while the probability of adiabatic transition is given as

$$P_{i \to j}^{ad} = 1 - exp \left\{ \frac{2(\omega_d^{ij})^2}{d\Delta_{ij}/dt} \right\}.$$
 (2.27)

The dynamics in the system is driven by the presence of perturbation (effective dipolar coupling), therefore it acts as a natural/internal time-period of the system ($\tau_i = \frac{2\pi}{\omega_{ij}^{ij}}$), while the ¹H RF amplitude acts as external tuning parameter ($\tau_e = \frac{2\pi}{\omega_{1H}}$). In case $\tau_e >> \tau_i$, the system evolves adiabatically through the energy gap ($P_{i\to j}^{ad} \approx 1$), otherwise it can make non-adiabatic transition. Hence, it is the energy difference across the LAC that determines the nature of dynamics. In the case of a weaker coupled system (drive-frequency < Rabi frequency, *i.e.*, energy difference), the probability of the non-adiabatic transition increases, however it decreases rapidly away from the resonance condition. In a strongly coupled system, the probability of the non-adiabatic transitions decreases and we observe a broad CP resonance.

Having established the mechanism of the LAC or HH-condition, we now focus on the different avoided crossings observed in Figures 2.17 and 2.18 for a single-crystal sample.

We observed that the ZQ_{23} and DQ_{14} HH CP matching conditions are just phase-shifted versions of each other and the DQ₁₄ transfer is experimentally achieved by setting the phase of either I or S-spins RF-field by 180° . The area under the avoided crossing is a direct manifestation of the strength of the perturbation (effective dipolar coupling i.e., $\omega_d^{14,23}$) acting between the states involved in CP transfer. Under on-resonance irradiation, the area enclosed by the curves are constant in different coupling regimes (Figure 2.17). However, the regions of the avoided crossings overlap for the ZQ₂₃ and DQ₁₄ HH CP conditions in the stronger coupling regime ($\omega_d \approx \omega_{1S}$). Hence, in the region of overlapping both the CP conditions (ZQ_{23} and DQ_{14}) are simultaneously satisfied and this effect is similar to the effect of non-unidirectionality of the spin-locking field in Figure 2.6. The degree of overlapping can be quantitatively evaluated using the population exchange diagram. The population exchange at various LACs are shown in Figure 2.20 where the population is plotted by selecting the coefficients of all Zeeman states in the final density matrix in Eq. (2.9) (see Figure caption for more information). In the population diagram (panel a1), clearly $|1\rangle/|4\rangle$ and $|2\rangle/|3\rangle$ exchange their populations (i.e., population difference becomes zero $\hat{\rho}_{ii} - \hat{\rho}_{jj} = 0$) at exact HH CP matching condition which correlates well with the Figures 2.4 and 2.6 and point towards an adiabatic transfer. The population exchange trajectories for the DQ_{14} and ZQ_{23} CP conditions in the strong coupling regime clearly demonstrates the effect of the overlapping CP resonances. From an operational standpoint, it is important to mention that despite the overlapping of the CP resonances, CP transfer in DQ_{14} and ZQ_{23} subspaces are independent process and still can be explained using TLS problem. As the strength of the S-spin off-resonance irradiation increases, the CP resonances shift towards increasing ¹H RF amplitudes, and the area decreases monotonically. The strength of the effective dipolar coupling constant $(\omega_d^{14,23})$ is directly correlated with the nature of transition at the exact HH CP matching condition (sudden or adiabatic transfer). As the strength of the off-resonance irradiation increases, the probability of the non-adiabatic (sudden jump) increases. Additionally, the avoided crossings observed at $\nu_{1H}=0$ kHz corresponds to the pure single-quantum I-spin dipolar transitions ($SQ_{d,I}$). It should also be noted that a significant loss in the I-spin polarization (refer to $\langle \tilde{I}_x(t) \rangle$) detection in Figure 2.21) is observed during the transfer process while the gain in the S-spin polarization is minimal. This is primarily due to the involvement of $\hat{I}_x^{ij}\hat{S}_z$ transition operators in the polarization transfer process.

At zero-field avoided crossing ($\nu_{1H}=0$ kHz), we don't observe any significant population exchange (Figure 2.22), again highlighting the presence of pure $SQ_{d,I}$ I-spin dipolar transitions. Nevertheless, the population exchange dynamics observed in panels a2-a3 for the stronger off-resonance irradiations demonstrate a behavioral shift from adiabatic to sudden transitions. Besides, the area enclosed in between two population curves directly signifies the width of the overall CP transfer as observed in Figures 2.20 and 2.22. It is important to note that the aforementioned observations are based on the parameters used while generating the simulations, and the nature of CP dynamics may change by selecting other parameters set.

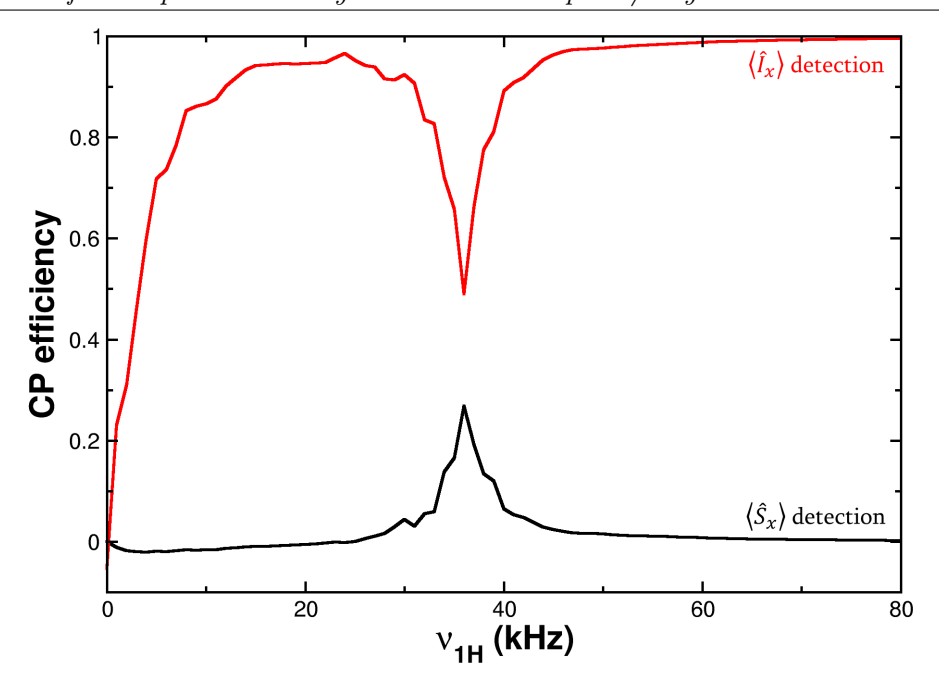


Figure 2.21: In the CP simulations (SIMPSON) depicted, the polarization build-up on the S-spin (black curve) and loss on the I-spin (red curve) is monitored simultaneously in the powder sample as a function of the RF field employed on the I-spin. The following parameters were employed in the simulations: Dipolar coupling parameters (internuclear distance $r_{IS} = 1.05$ Å and dipolar PAS angle $\beta_d = 0^{\circ}$), RF parameters $\nu_{1S} = 20$ kHz under the S-spin off-resonance irradiation $\Omega_S = 30$ kHz. The powder simulations were performed by considering the zcw4180 crystallite orientations.

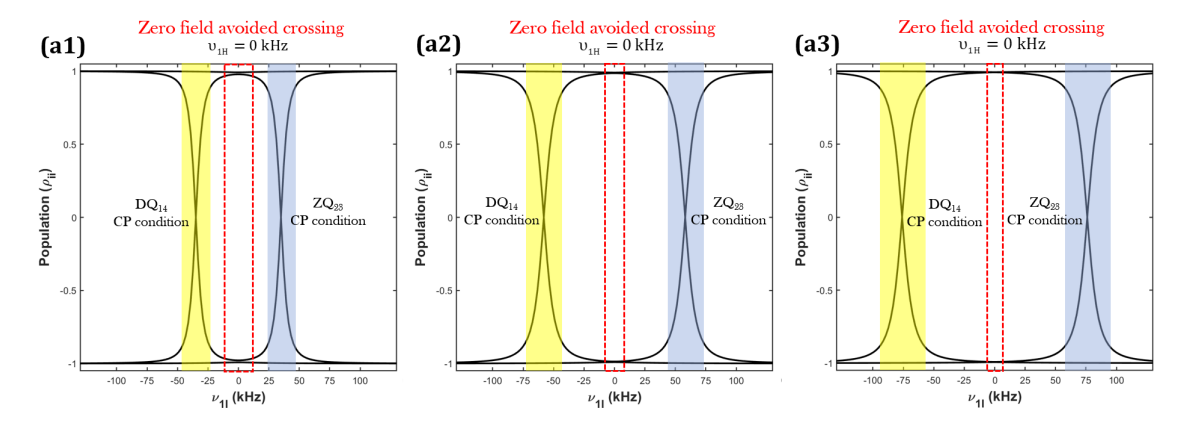


Figure 2.22: The population exchange dynamics for different HH CP matching conditions as a function of ^{1}H RF amplitude for a single-crystal sample. The population coefficients for different HH matching conditions are calculated based on the final density matrix calculation as given in Eq. (2.9) and are given as DQ₁₄ (ρ_{11} , ρ_{44}): (sin² θ_{14} , -sin² θ_{14}) and ZQ₂₃ (ρ_{22} , ρ_{33}): (sin² θ_{23} , -sin² θ_{23}). The area between each avoided crossings can be correlated with the width of each CP resonances observed in Figure 2.10. All simulation parameters are exactly the same as used in Figure 2.18.

2.3 Conclusions

In summary, the effective-field approach presented in this chapter is well suited for describing the CP spin dynamics between the I = 1/2 (¹H) and S = 1/2 spin

systems. The analytic theory perfectly reproduces the literature findings and offers an in-depth understanding of CP dynamics behavior subjected to on and off-resonance S-spin irradiations. Unlike previous studies, the proposed operator-based analytic theory provides a unified description of the CP spin dynamics that is valid across all coupling regimes. Moreover, the proposed effective field-based theory introduces the concept of a non-unidirectional spin-locking field, dipolar-dependent shifts, dispersion, and interference effects, which are unique to the proposed effective field-based theory. As an alternative to the operator-based analytic framework, a thorough state-picture representation is provided to describe the CP spin dynamics.

Chapter 3

Analytic theory of cross-polarization (CP) dynamics between spin-1/2 and spin-1 nuclei

In the previous chapter, we discussed the usefulness of the effective-field approach in the theoretical description of the CP experiment in spin-1/2 systems. We extend the proposed operator-based analytic theory in a more complex quadrupolar sample with spin-quantum number S=1. The presence of dominant quadrupolar interaction frequently poses significant challenges in the analytical description of spin dynamics [69,83,102,143–147]. This led to the descriptions of spin-dynamics involving quadrupolar spins in the quadrupolar interaction frame or more commonly known as the quadrupolar jolting frame [148, 149]. This transformation rendered the time-dependency of the interaction Hamiltonian, which further requires application of sophisticated analytic treatments. Utilizing the Average Hamiltonian theory (AHT) [3, 90, 103] and in some cases with the Floquet theory [93, 104–109], semi-analytical methods have also emerged for describing experiments involving quadrupolar spins, both in non-rotating (static) and rotating solids. In the initial description put forth by Vega and coworkers [45] using the effective Hamiltonian approach the CP dynamics was described in systems with larger quadrupolar interactions (i.e., $\omega_Q >> \omega_{1S}$). However, these descriptions are not useful for quantifying the CP efficiency profiles in powder samples primarily due to the distribution of quadrupolar coupling frequencies. Later, Ernst and coworkers [90] provided an alternate description of the CP dynamics based on the AHT, however the experimental validation of the proposed analytic treatment was provided only in the intermediate coupling regime (i.e. $\omega_Q \approx \omega_{1S}$). Pratum and Klein [91] proposed an alternate formulation, which could quantitatively explain the origin of multiple CP matching conditions observed in experiments. Nonetheless, a comprehensive analytic description of the CP dynamics over a wide range of experimentally relevant parameters has remained elusive. For the sake of clarity and completeness, a brief account of the results obtained from the Hamiltonians proposed by Pratum and Klein is discussed in Appendix C (refer to section C.2). To address this issue, we propose an alternate analytic formalism to describe the CP dynamics which is consistent with experimental observations. Unlike the conventional perturbative methods in the quadrupolar interaction frame, the CP dynamics is described by the effective Hamiltonians derived using rotation operators based

on the "effective-field" approach [70, 80, 109, 114, 115]. The proposed analytic framework based on the effective-field approach offers faster convergence and presents an attractive tool for describing the underlying spin dynamics in both isotropic and anisotropic solids. Accordingly, the CP matching conditions observed are described in terms of the transition operators associated with a given system [114, 115].

3.1 Theory and Methodology

To outline the basic operational aspects of the CP experiment, we begin with a model two-spin (say I = 1/2 and S = 1) Hamiltonian. In an appropriate interaction frame, the Hamiltonian of such a system under on-resonance irradiation (on the spins I and S) is represented by the following equation:

$$\hat{H} = \underbrace{\omega_{1S}(\cos\phi_{S}\hat{S}_{x} + \sin\phi_{S}\hat{S}_{y})}_{\hat{H}_{S}^{RF}} + \underbrace{\frac{\omega_{Q}^{(1)}(\alpha_{Q}, \beta_{Q})}{6}(3\hat{S}_{z}^{2} - \hat{S}^{2})}_{\hat{H}_{S}^{Q}} + \underbrace{\omega_{1I}(\cos\phi_{I}\hat{I}_{x} + \sin\phi_{I}\hat{I}_{y})}_{\hat{H}_{I}^{RF}} + \underbrace{2\omega_{d}\hat{I}_{z}\hat{S}_{z};}_{\hat{H}_{IS}^{D}}, \quad \hbar = 1.$$

$$(3.1)$$

In the above equation, $\omega_{II}(\omega_{1S})$ and $\phi_{I}(\phi_{S})$ represent the RF amplitude and phase on I(S) spin. \hat{H}_{S}^{Q} is the first-order quadrupolar Hamiltonian for the S-spin. The quadrupolar interaction is often expressed in terms of quadrupolar coupling frequency $(\omega_{Q}^{(1)})$ and quadrupolar coupling constant (C_{Q}) . A detailed description of the quadrupolar Hamiltonian can be found in Chapter 1. The term ω_{d} (= $\frac{\mu_{o}}{4\pi} \frac{\hbar \gamma_{I} \gamma_{S}}{r_{IS}^{3}} \frac{(3\cos^{2}\beta_{d}-1)}{2}$; γ_{I} and γ_{S}) represents the dipolar coupling (I-S) frequency, r_{IS} is the internuclear distance between I and S-spin pair, and β_{d} is the orientation of dipolar vector with respect to the applied Zeeman magnetic field (z-direction). The matrix representation of the various spin operators in Eq. (3.1) both I and S-spins) can be found in Appendix C. When the phases of the RF fields employed on the two spins are set to zero $(i.e., \phi_{S} = \phi_{I} = 0^{\circ})$, the above Hamiltonian [Eq. (3.1)] reduces to a compact form given below:

$$\hat{H}_{CP} = \omega_{1S}\hat{S}_x + \frac{\omega_Q^{(1)}(\alpha_Q, \beta_Q)}{6}(3\hat{S}_z^2 - \hat{S}^2) + \omega_{1I}\hat{I}_x + 2\omega_d\hat{I}_z\hat{S}_z.$$
(3.2)

The discussion that follows is equally valid in both single-crystal and powder samples.

3.1.1 Derivation of the effective CP Hamiltonians via the effective-field method

To simplify the description, the above Hamiltonian is re-expressed in terms of the single-transition operators [17,110–113] as given below:

$$\hat{H}_{CP} = \underbrace{\sqrt{2}\omega_{1S}[\hat{S}_{x}^{12} + \hat{S}_{x}^{23} + \hat{S}_{x}^{45} + \hat{S}_{x}^{56}]}_{\hat{H}_{S}^{RF}} + \underbrace{\frac{\omega_{Q}^{(1)}}{3}[\hat{S}_{z}^{12} - \hat{S}_{z}^{23} + \hat{S}_{z}^{45} - \hat{S}_{z}^{56}]}_{\hat{H}_{S}^{Q}} + \underbrace{\omega_{1I}[\hat{S}_{x}^{14} + \hat{S}_{x}^{25} + \hat{S}_{x}^{36}]}_{\hat{H}_{I}^{RF}} + \underbrace{2\omega_{d}[\hat{S}_{z}^{13} - \hat{S}_{z}^{46}]}_{\hat{H}_{IS}^{D}}.$$

$$(3.3)$$

The superscript (i, j) in the operators \hat{S}_{α}^{ij} $(\alpha = x, y, z)$ represents the spin-states in a coupled system and are defined according to the energy level diagram depicted in Figure 3.1(a). Accordingly, the operators have the following definitions:

(a) S = 1 and I = 1/2 coupled basis states and two spin flip/flop (dipolar) transitions

S = 1 |1) | TQ | |3) | SQ | |4) | SQ | |6) | 5)

(b) Transition matrix highlighting all possible transitions in a coupled system

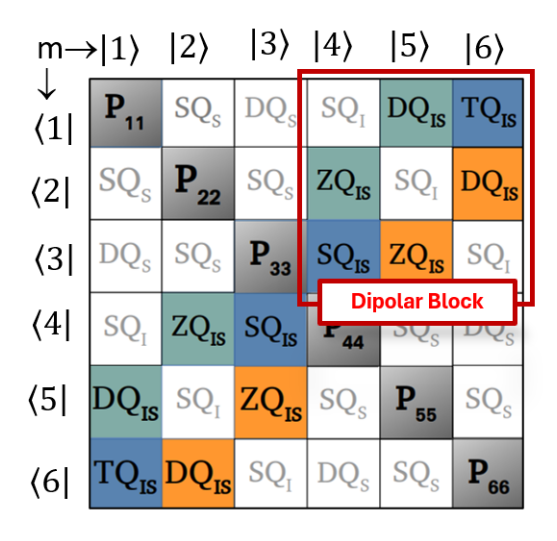


Figure 3.1: (a) Schematic depiction of the energy level diagram in a coupled two-spin (I = 1/2 and S = 1) system. The spin states $|1\rangle$, $|2\rangle$, $|3\rangle$, $|4\rangle$, $|5\rangle$ and $|6\rangle$ are representative of the product basis states ($|m_I, m_S\rangle$) $|1/2, 1\rangle$, $|1/2, 0\rangle$, $|1/2, -1\rangle$, $|-1/2, 1\rangle$, $|-1/2, 0\rangle$ and $|-1/2, -1\rangle$, respectively. (b) Matrix representation of the populations and coherences in the coupled two-spin (I and S) system. The diagonal elements depict the populations (of the states $|m_I, m_S\rangle$) and are represented through ' P_{ii} '. The coherences wherein both spins change their states are represented as the triple-quantum (TQ_{IS}), double-quantum (DQ_{IS}), single-quantum (SQ_{IS}), and zero-quantum (SQ_{IS}). The coherences where only the state of S-spin changes are represented by DQ_S and SQ_S , while, coherences where only the state of I-spin changes are represented by, SQ_I . The blue-colored (TQ_{IS}/SQ_{IS}) coherences involve double-quantum transitions associated with the S-spin ($|+1\rangle \leftrightarrow |-1\rangle$), while orange and green-colored (DQ_{IS}/ZQ_{IS}) coherences involve single-quantum transitions associated with S-spin, SQ_S ($|-1\rangle \leftrightarrow |0\rangle$) and ($|0\rangle \leftrightarrow |+1\rangle$).

$$\hat{S}_{x}^{ij} = \frac{1}{2} [|i\rangle \langle j| + |j\rangle \langle i|], \quad \hat{S}_{y}^{ij} = \frac{1}{2i} [|i\rangle \langle j| - |j\rangle \langle i|], \quad \hat{S}_{z}^{ij} = \frac{1}{2} [|i\rangle \langle i| - |j\rangle \langle j|]. \tag{3.4}$$

A schematic description of the populations and coherences observed in a coupled spin-pair (I=1/2 and S=1) is given in Figure 3.1(b). The matrix representation of the various spin-operator and their product Zeeman basis is given in Appendix C. To derive insights into the CP spin dynamics and facilitate analytic description, the Hamiltonian [Eq. (3.3)] is divided into three parts:

- 1. Hamiltonian for the S-spin system $(\hat{H}_S = \hat{H}_S^{RF} + \hat{H}_S^Q)$
- 2. Hamiltonian for the *I*-spin system (\hat{H}_{I}^{RF})
- 3. Hamiltonian for the *I-S* spin pair (\hat{H}_{IS}^D)

Subsequently, employing unitary transformations, the Hamiltonians are diagonalized using the procedure outlined below.

A: Derivation of effective Hamiltonian for the S-spin system

A detailed procedure of the derivation of the effective S-spin Hamiltonian in the single-spin Zeeman basis is outlined in section 1.4 (Chapter 1). To avoid repetition, the complete description of the diagonalization process is cautiously omitted. The diagonalization of S-spin Hamiltonian is accomplished via two-step unitary transformations $\hat{U}_1 = \exp\left\{-\frac{i\theta_1}{\sqrt{2}}\left[-\hat{S}_y^{12} + \hat{S}_y^{23} - \hat{S}_y^{45} + \hat{S}_y^{56}\right]\right\}$ and $\hat{U}_2 = \exp\left\{i\frac{\pi}{2}\left[\hat{S}_y^{13} + \hat{S}_y^{46}\right]\right\}$. The resulting S-spin effective Hamiltonian is given below:

$$\tilde{\hat{H}}_{S} = \hat{U}_{2}\hat{U}_{1}\hat{H}_{S}\hat{U}_{1}^{\dagger}\hat{U}_{2}^{\dagger} = \left(\frac{\omega_{e} - \omega_{Q}^{(1)}}{4}\right)\left[\hat{S}_{z}^{13} + \hat{S}_{z}^{46}\right] + \left(\frac{3\omega_{e} + \omega_{Q}^{(1)}}{12}\right)\left[\hat{S}_{z}^{12} - \hat{S}_{z}^{23} + \hat{S}_{z}^{45} - \hat{S}_{z}^{56}\right]$$
(3.5)

where, $\omega_e = \sqrt{(\omega_Q^{(1)})^2 + 16\omega_{1S}^2}$ and $\tan \theta_1 = 4\omega_{1S}/\omega_Q^{(1)}$. The effectiveness of the S-spin effective Hamiltonian is evaluated in the preceding section 1.4 and is demonstrated to offer the convergent solutions to the spin-dynamics for isotropic and anisotropic solids.

B: Derivation of effective Hamiltonian for the *I*-spin system

In a similar way, employing the unitary transformation $\hat{U}_3 = \exp\left\{i\frac{\pi}{2}\left[\hat{S}_y^{14} + \hat{S}_y^{25} + \hat{S}_y^{36}\right]\right\}$, the Hamiltonian for the *I*-spin is transformed such that it is diagonal in the chosen basis.

$$\tilde{\hat{H}}_{I}^{RF} = \hat{U}_{3}\hat{H}_{I}^{RF}\hat{U}_{3}^{\dagger} = \omega_{1I} [\hat{S}_{z}^{14} + \hat{S}_{z}^{25} + \hat{S}_{z}^{36}]. \tag{3.6}$$

As the operators involved in the unitary transformations, \hat{U}_1 and \hat{U}_2 commute with the *I*-spin Hamiltonian, the above form of the Hamiltonian remains invariant under the transformations employed on the *S*-spin.

C: Derivation of effective Hamiltonian for the I-S spin pair

To have a consistent description, the dipolar coupling Hamiltonian (\hat{H}_{IS}) is also transformed by the same set of unitary transformations employed on the S and I-spin Hamiltonians.

$$\hat{\tilde{H}}_{IS}^{D} = \hat{U}_{3}\hat{U}_{2}\hat{U}_{1}\hat{H}_{IS}^{D}\hat{U}_{1}^{\dagger}\hat{U}_{2}^{\dagger}\hat{U}_{3}^{\dagger} = 2\omega_{d} \left\{ \left[\hat{S}_{x}^{16} + \hat{S}_{x}^{34} \right] \cos\theta_{1}/2 - \left[\hat{S}_{x}^{26} + \hat{S}_{x}^{35} \right] \sin\theta_{1}/2 \right\}.$$
(3.7)

As illustrated above, in contrast to the single spin Hamiltonians [(refer to Eqs. (3.5) and (3.6)], the transformed dipolar coupling Hamiltonian is off-diagonal in the chosen basis system. Combining the transformed Hamiltonians, $\hat{\tilde{H}}_S$, $\hat{\tilde{H}}_I^{RF}$ and $\hat{\tilde{H}}_{IS}^D$, the complete Hamiltonian describing the CP dynamics is represented by the following equation:

$$\tilde{\hat{H}} = \tilde{\hat{H}}_S + \tilde{\hat{H}}_I + \tilde{\hat{H}}_{IS}^D
= \left(\frac{\omega_e - \omega_Q^{(1)}}{4}\right) \left[\hat{S}_z^{13} + \hat{S}_z^{46}\right] + \left(\frac{3\omega_e + \omega_Q^{(1)}}{12}\right) \left[\hat{S}_z^{12} - \hat{S}_z^{23} + \hat{S}_z^{45} - \hat{S}_z^{56}\right] + \omega_{1I} \left[\hat{S}_z^{14} + \hat{S}_z^{25} + \hat{S}_z^{36}\right]
+ 2\omega_d \cos\theta_1 / 2 \left[\hat{S}_x^{16} + \hat{S}_x^{34}\right] - 2\omega_d \sin\theta_1 / 2 \left[\hat{S}_x^{26} + \hat{S}_x^{35}\right].$$
(3.8)

As described above, the CP Hamiltonian in its present form is highly off-diagonal (mainly due to the dipolar coupling) and is of lesser utility in further descriptions of the spin dynamics. To address this issue, the transformed single spin Hamiltonians are re-expressed in terms of the operators employed in the description of the dipolar coupling Hamiltonian through the relation $\hat{S}_z^{ik} = \hat{S}_z^{ij} + \hat{S}_z^{jk}$ between the single-transition operators as given below:

$$\tilde{\hat{H}} = \underbrace{\sum_{16} \left[\hat{S}_{z}^{16} \right] + \omega_{d}^{16,34} \left[\hat{S}_{x}^{16} \right]}_{\tilde{\tilde{H}}_{16}} + \underbrace{\Delta_{34} \left[\hat{S}_{z}^{34} \right] + \omega_{d}^{16,34} \left[\hat{S}_{x}^{34} \right]}_{\tilde{\tilde{H}}_{34}} + \underbrace{\sum_{35} \left[\hat{S}_{z}^{35} \right] + \omega_{d}^{26,35} \left[\hat{S}_{x}^{35} \right]}_{\tilde{\tilde{H}}_{35}} + \underbrace{\Delta_{26} \left[\hat{S}_{z}^{26} \right] + \omega_{d}^{26,35} \left[\hat{S}_{x}^{26} \right]}_{\tilde{\tilde{H}}_{26}} - \underbrace{\omega_{Q}^{(1)} \left[\hat{S}_{z}^{12} - \hat{S}_{z}^{23} + \hat{S}_{z}^{45} - \hat{S}_{z}^{56} \right]}_{\text{residual terms}}. \tag{3.9}$$

The coefficients in the above equation have the following definitions: $\Sigma_{16} = \left\{\frac{4\omega_{1I} + (\omega_e - \omega_Q^{(1)})}{4}\right\}$, $\Delta_{34} = \left\{\frac{4\omega_{1I} - (\omega_e - \omega_Q^{(1)})}{4}\right\}$, $\Sigma_{35} = \left\{\frac{4\omega_{1I} + (\omega_e + \omega_Q^{(1)})}{4}\right\}$, $\Delta_{26} = \left\{\frac{4\omega_{1I} - (\omega_e + \omega_Q^{(1)})}{4}\right\}$, and the effective dipolar coupling constants are $\omega_d^{16,34} = 2\omega_d \cos \theta_1/2$ and $\omega_d^{26,35} = -2\omega_d \sin \theta_1/2$.

Accordingly, in the new representation, the CP Hamiltonian comprises contribution emerging from the four transitions (that involve flipping of both spins) present in the coupled system [refer to Figure 3.1(a)]. The term $\hat{\tilde{H}}_{16}$ is representative of the triple-quantum (TQ₁₆) transition $(|1/2,1\rangle \leftrightarrow |-1/2,-1\rangle)$, while $\hat{\tilde{H}}_{34}$ is representative of

the single-quantum (SQ₃₄) transition $\left(|1/2,-1\rangle\leftrightarrow|-1/2,1\rangle\right)$. In a similar vein, the term $\tilde{\tilde{H}}_{35}$ is representative of the zero-quantum (ZQ₃₅) transition $\left(|-1/2,-1\rangle\leftrightarrow|1/2,0\rangle\right)$, while $\tilde{\tilde{H}}_{26}$ is representative of the double-quantum (DQ₂₆) transition $\left(|1/2,-1\rangle\leftrightarrow|-1/2,0\rangle\right)$ in a coupled spin basis. It is important to note that the magnitude of the effective dipolar coupling is different in TQ₁₆/SQ₃₄ and ZQ₃₅/DQ₂₆ sets of transitions. Since polarization transfer amongst spins entails simultaneous flipping of the spin states of both the spins involved, the contribution from the residual terms in the above Hamiltonian [Eq. (3.9)] are of lesser significance and are ignored in further calculations.

$$\tilde{\tilde{H}} = \tilde{\tilde{H}}_{16} + \tilde{\tilde{H}}_{34} + \tilde{\tilde{H}}_{35} + \tilde{\tilde{\tilde{H}}}_{26}$$

$$= \underbrace{\sum_{16} \left[\hat{S}_{z}^{16} \right] + \omega_{d}^{16,34} \left[\hat{S}_{x}^{16} \right]}_{\tilde{\tilde{H}}_{16}} + \underbrace{\Delta_{34} \left[\hat{S}_{z}^{34} \right] + \omega_{d}^{16,34} \left[\hat{S}_{x}^{34} \right]}_{\tilde{\tilde{\tilde{H}}}_{34}} + \underbrace{\sum_{35} \left[\hat{S}_{z}^{35} \right] + \omega_{d}^{26,35} \left[\hat{S}_{x}^{35} \right]}_{\tilde{\tilde{\tilde{H}}}_{35}} + \underbrace{\Delta_{26} \left[\hat{S}_{z}^{26} \right] + \omega_{d}^{26,35} \left[\hat{S}_{x}^{26} \right]}_{\tilde{\tilde{H}}_{26}}. \tag{3.10}$$

Unlike other existing reports in the literature [45, 91], it is important to note that the Hamiltonian in Eq. (3.10) contains all the modes of CP transfer within a single framework. This forms the major highlight of the present study and will be substantiated in the following sections. For comparative purposes, the analytic description of the spin dynamics emerging from previously reported Hamiltonians is summarized in Appendix C (refer to section C.2). As illustrated in Eq. (3.10), the CP Hamiltonian in the effective-field framework reduces to the sum of transverse (\hat{S}_x^{ij}) and longitudinal (\hat{S}_z^{ij}) operators in each subspace (see Figure 3.2). Subsequently, employing the rotation operators, the Hamiltonians in the respective sub-spaces are diagonalized through rotation operators (analogous to the spin-1/2) defined below:

$$\hat{U}_{4}^{16} = \exp\left\{i\left(\frac{\pi}{2} - \theta_{4}^{16}\right)\left[\hat{S}_{y}^{16}\right]\right\}, \quad \hat{U}_{4}^{34} = \exp\left\{i\left(\frac{\pi}{2} - \theta_{4}^{34}\right)\left[\hat{S}_{y}^{34}\right]\right\}, \quad \hat{U}_{4}^{35} = \exp\left\{i\left(\frac{\pi}{2} - \theta_{4}^{35}\right)\left[\hat{S}_{y}^{35}\right]\right\},$$
and
$$\hat{U}_{4}^{26} = \exp\left\{i\left(\frac{\pi}{2} - \theta_{4}^{26}\right)\left[\hat{S}_{y}^{26}\right]\right\}.$$
(3.11)

The angles θ_4^{16} , θ_4^{34} , θ_4^{35} and θ_4^{26} are chosen such that the effective-fields in individual subspaces are quantized along the z-axes: $\tan\theta_4^{16} = \frac{\Sigma_{16}}{\omega_d^{16,34}}$, $\tan\theta_4^{34} = \frac{\Delta_{34}}{\omega_d^{16,34}}$, $\tan\theta_4^{35} = \frac{\Sigma_{35}}{\omega_d^{26,35}}$, and $\tan\theta_4^{26} = \frac{\Delta_{26}}{\omega_d^{26,35}}$. The pictorial representations of these transformations are given in Figure 3.2(a1)-(a4). Subsequently, the effective Hamiltonian depicting the CP dynamics is represented by the following equation.

$$\begin{split} \hat{H}_{eff} &= \hat{H}_{eff,16} + \hat{H}_{eff,34} + \hat{H}_{eff,35} + \hat{H}_{eff,26} \\ &= \hat{U}_{4}^{16} \hat{H}_{16} \hat{U}_{4}^{16\dagger} + \hat{U}_{4}^{34} \hat{H}_{34} \hat{U}_{4}^{34\dagger} + \hat{U}_{4}^{35} \hat{H}_{35} \hat{U}_{4}^{35\dagger} + \hat{U}_{4}^{26} \hat{H}_{26} \hat{U}_{4}^{26\dagger} \\ &= \omega_{eff}^{(16)} \left[\hat{S}_{z}^{16} \right] + \omega_{eff}^{(34)} \left[\hat{S}_{z}^{34} \right] + \omega_{eff}^{(35)} \left[\hat{S}_{z}^{35} \right] + \omega_{eff}^{(26)} \left[\hat{S}_{z}^{26} \right] \end{split}$$
(3.12)

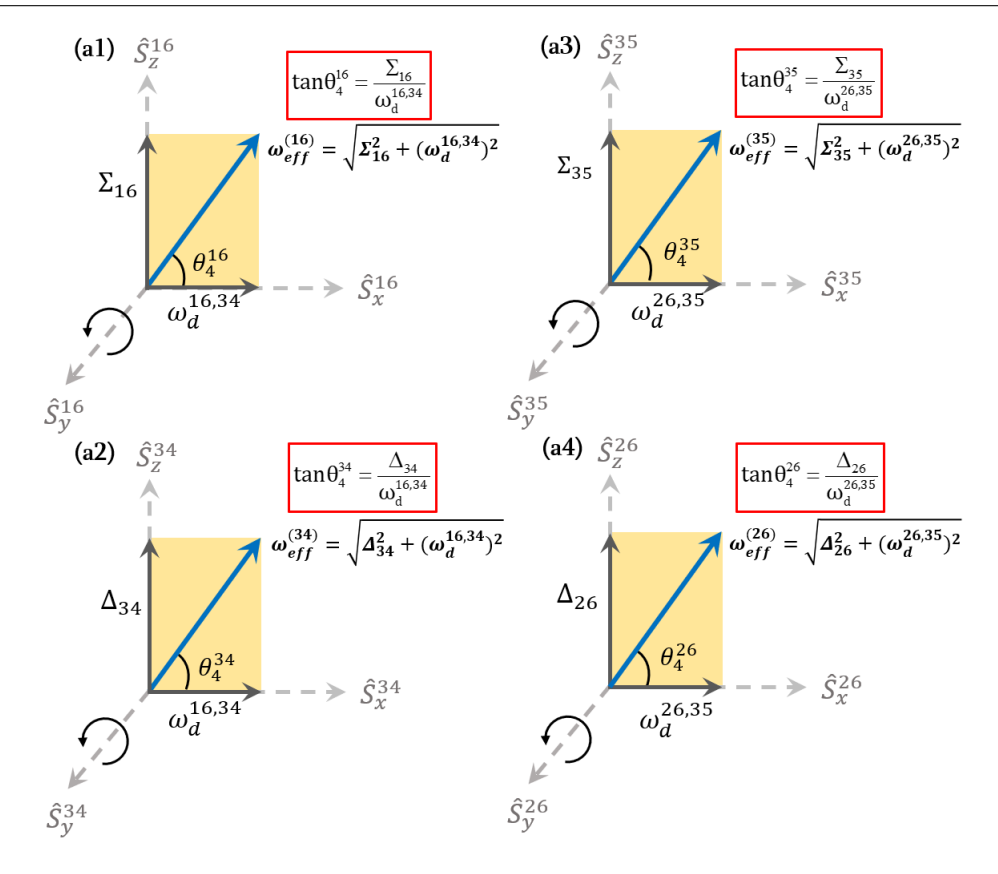


Figure 3.2: Schematic representation of the "effective-fields" experienced in the TQ₁₆ (a1), SQ_{34} (a2), ZQ_{35} (a3), and DQ_{26} (a4) sub-spaces.

where,
$$\omega_{eff}^{(16)} = \sqrt{\Sigma_{16}^2 + (\omega_d^{16,34})^2}$$
, $\omega_{eff}^{(34)} = \sqrt{\Delta_{34}^2 + (\omega_d^{16,34})^2}$, $\omega_{eff}^{(35)} = \sqrt{\Sigma_{35}^2 + (\omega_d^{26,35})^2}$ and $\omega_{eff}^{(26)} = \sqrt{\Delta_{26}^2 + (\omega_d^{26,35})^2}$.

3.1.2 Time-evolution of the spin-system during the CP mixing period

The time-evolution of spin-system is described using the standard operational process [Eq. (1.44)]. The initial density operator: $\hat{\rho}(0) = \hat{I}_x$. For a consistent description, the initial density operator is transformed using the same set of unitary transformations on the Sand I-spins.

$$\hat{\tilde{\rho}}(0) = \hat{U}_{3}\hat{U}_{2}\hat{U}_{1}\hat{\rho}(0)\hat{U}_{1}^{\dagger}\hat{U}_{2}^{\dagger}\hat{U}_{3}^{\dagger}
= \underbrace{\left[\hat{S}_{z}^{16}\right]}_{\hat{\rho}_{16}(0)} + \underbrace{\left[\hat{S}_{z}^{34}\right]}_{\hat{\rho}_{34}(0)} + \underbrace{\left[\hat{S}_{z}^{35}\right]}_{\hat{\rho}_{35}(0)} + \underbrace{\left[\hat{S}_{z}^{26}\right]}_{\hat{\rho}_{26}(0)} - \left[\hat{S}_{z}^{36}\right].$$
(3.13)

Subsequently, ignoring the residual contributions from the operator $[\hat{S}_z^{36}]$, the density operator at time 't' is calculated using the effective Hamiltonians [Eq. (3.12)] in respective sub-spaces as given below:

$$\hat{\rho}_{eff}^{(16)}(t) = \exp\left\{-i\hat{H}_{eff,16}t\right\} \hat{U}_{4}^{16}\hat{\rho}_{16}(0)\hat{U}_{4}^{16\dagger} \exp\left\{i\hat{H}_{eff,16}t\right\}$$

$$= \left[\hat{S}_{z}^{16}\right] \sin\theta_{4}^{16} - \left\{\left[\hat{S}_{x}^{16}\right] \cos\omega_{eff}^{(16)}t + \left[\hat{S}_{y}^{16}\right] \sin\omega_{eff}^{(16)}t\right\} \cos\theta_{4}^{16},$$
(3.14)

$$\hat{\rho}_{eff}^{(34)}(t) = \exp\left\{-i\hat{H}_{eff,34}t\right\} \hat{U}_{4}^{34} \hat{\rho}_{34}(0) \hat{U}_{4}^{34\dagger} \exp\left\{i\hat{H}_{eff,34}t\right\}
= \left[\hat{S}_{z}^{34}\right] \sin\theta_{4}^{34} - \left\{\left[\hat{S}_{x}^{34}\right] \cos\omega_{eff}^{(34)}t + \left[\hat{S}_{y}^{34}\right] \sin\omega_{eff}^{(34)}t\right\} \cos\theta_{4}^{34},$$
(3.15)

$$\begin{split} \hat{\rho}_{eff}^{(35)}(t) &= \exp\left\{-i\hat{H}_{eff,35}t\right\} \hat{U}_{4}^{35}\hat{\rho}_{35}(0)\hat{U}_{4}^{35\dagger} \exp\left\{i\hat{H}_{eff,35}t\right\} \\ &= \left[\hat{S}_{z}^{35}\right]\sin\theta_{4}^{35} - \left\{\left[\hat{S}_{x}^{35}\right]\cos\omega_{eff}^{(35)}t + \left[\hat{S}_{y}^{35}\right]\sin\omega_{eff}^{(35)}t\right\}\cos\theta_{4}^{35}, \end{split} \tag{3.16}$$

$$\begin{split} \hat{\rho}_{eff}^{(26)}(t) &= \exp\left\{-i\hat{H}_{eff,26}t\right\} \hat{U}_{4}^{26} \hat{\rho}_{26}(0) \hat{U}_{4}^{26\dagger} \exp\left\{i\hat{H}_{eff,26}t\right\} \\ &= \left[\hat{S}_{z}^{26}\right] \sin\theta_{4}^{26} - \left\{\left[\hat{S}_{x}^{26}\right] \cos\omega_{eff}^{(26)}t + \left[\hat{S}_{y}^{26}\right] \sin\omega_{eff}^{(26)}t\right\} \cos\theta_{4}^{26}. \end{split} \tag{3.17}$$

3.1.3 Detection of the S-spin polarization

For a consistent description, the detection operator is also transformed with the same set of transformations. In the present context, polarization transfer from spin I to spin S is calculated. Accordingly, the expectation value of the observable $\langle \hat{S}_x(t) \rangle$ is derived employing Eqs. (3.14)-(3.17),

$$S(t) = \langle \hat{S}_x(t) \rangle = Trace\{\hat{S}_{eff,x}.\hat{\rho}_{eff}(t)\}$$
(3.18)

where, $\hat{\rho}_{eff}(t) = \hat{\rho}_{eff}^{(16)}(t) + \hat{\rho}_{eff}^{(34)}(t) + \hat{\rho}_{eff}^{(35)}(t) + \hat{\rho}_{eff}^{(26)}(t)$. Accordingly, the final signal expression has separate contributions from the TQ₁₆, SQ₃₄, ZQ₃₅, and DQ₂₆ sub-spaces as given below:

$$S(t) = \langle \hat{S}_{eff,x}(t) \rangle_{16} + \langle \hat{S}_{eff,x}(t) \rangle_{34} + \langle \hat{S}_{eff,x}(t) \rangle_{35} + \langle \hat{S}_{eff,x}(t) \rangle_{26}$$

$$= \frac{4\omega_{1S}}{\omega_{e}} \left[\underbrace{-\frac{(\omega_{d}^{16,34})^{2}}{\Sigma_{16}^{2} + (\omega_{d}^{16,34})^{2}} \sin^{2} \frac{\sqrt{\Sigma_{16}^{2} + (\omega_{d}^{16,34})^{2}}}{2}}_{TQ_{16}} t + \underbrace{\frac{(\omega_{d}^{16,34})^{2}}{\Delta_{34}^{2} + (\omega_{d}^{16,34})^{2}} \sin^{2} \frac{\sqrt{\Delta_{34}^{2} + (\omega_{d}^{16,34})^{2}}}{2}}_{SQ_{34}} t - \underbrace{\underbrace{\frac{(\omega_{d}^{26,35})^{2}}{\Sigma_{35}^{2} + (\omega_{d}^{26,35})^{2}} \sin^{2} \frac{\sqrt{\Sigma_{35}^{2} + (\omega_{d}^{26,35})^{2}}}{2}}_{ZQ_{35}} t + \underbrace{\underbrace{\frac{(\omega_{d}^{26,35})^{2}}{\Delta_{26}^{2} + (\omega_{d}^{26,35})^{2}} \sin^{2} \frac{\sqrt{\Delta_{26}^{2} + (\omega_{d}^{26,35})^{2}}}{2}}_{DQ_{26}} t \right]}_{DQ_{26}}$$

$$(3.19)$$

As described above, the final signal expression has contributions from all the four possible CP transfer modes and is significantly different from those derived based on existing reports in the literature (refer to section C.2 in Appendix C).

3.1.4 Insights into the Hartmann-Hahn CP matching conditions

Based on the analytic expression [Eq. (3.19)], the CP signal could in principle be maximized by optimizing one of the four matching conditions as discussed below. When the amplitude of the RF field on I-spin is adjusted to one of the matching conditions the corresponding signal expression gets maximized and results in simplified expressions as follows:

• Single-quantum SQ₃₄ CP matching condition:

$$\Delta_{34} = 0 \implies \omega_{1I} = \frac{1}{4} (\omega_e - \omega_Q^{(1)}).$$

$$S(t) = \underbrace{\frac{4\omega_{1S}}{\omega_{e}} \sin^{2} \frac{\omega_{d}^{16,34}}{2} t}_{S(t)_{34}} + \underbrace{S(t)_{16} + S(t)_{26} + S(t)_{35}}_{\text{high-frequency terms}}.$$
 (3.20)

In the scenario, where the high-frequency terms can be ignored, the overall signal can be approximated to the SQ_{34} signal expression as given below:

$$S(t) \approx \underbrace{\frac{4\omega_{1S}}{\omega_e} \sin^2 \frac{\omega_d^{16,34}}{2} t}_{S(t)_{34}}.$$
 (3.21)

This behavior could also be displayed at other HH CP conditions as well.

• Triple-quantum TQ₁₆ matching condition: $\Sigma_{16} = 0 \implies \omega_{1I} = -\frac{1}{4}(\omega_e - \omega_Q^{(1)}).$

$$\Sigma_{16} = 0 \implies \omega_{1I} = -\frac{1}{4}(\omega_e - \omega_Q^{(1)}).$$

$$S(t) = \underbrace{-\frac{4\omega_{1S}}{\omega_e} \sin^2 \frac{\omega_d^{16,34}}{2} t}_{S(t)_{16}} + \underbrace{S(t)_{34} + S(t)_{26} + S(t)_{35}}_{\text{high-frequency terms}}.$$
 (3.22)

• Double-quantum
$$\mathbf{DQ}_{26}$$
 matching condition: $\Delta_{26} = 0 \implies \omega_{1I} = \frac{1}{4}(\omega_e + \omega_Q^{(1)}).$

$$S(t) = \underbrace{\frac{4\omega_{1S}}{\omega_{e}} \sin^{2} \frac{\omega_{d}^{26,35}}{2}}_{S(t)_{26}} t 2t + \underbrace{S(t)_{16} + S(t)_{34} + S(t)_{35}}_{\text{high-frequency terms}}.$$
 (3.23)

• Zero-quantum ZQ₃₅ matching condition:
$$\Sigma_{35} = 0 \implies \omega_{1I} = -\frac{1}{4}(\omega_e + \omega_Q^{(1)}).$$

$$S(t) = \underbrace{\frac{-4\omega_{1S}}{\omega_e} \sin^2 \frac{\omega_d^{26,35}}{2} t}_{S(t)_{35}} t 2t + \underbrace{S(t)_{16} + S(t)_{34} + S(t)_{26}}_{\text{high-frequency terms}}.$$
 (3.24)

As illustrated, the signal expressions for the TQ_{16} (and ZQ_{35}) are phase-shifted to those obtained from the corresponding SQ₃₄ (and DQ₂₆) CP matching conditions and could play an important role in the CP dynamics.

3.2 Results and discussion

To test the validity of the proposed analytic framework, polarization transfer from spin I=1/2 (say, ¹H and $\gamma_{^1H}=26.752\times 10^7$ rad s⁻¹T⁻¹) to S=1 (say, ¹⁴N and $\gamma_{^{14}N}=1$ $1.9331\times10^7~{\rm rad~s^{-1}T^{-1}})$ at proton Larmor frequency 600 MHz was examined over a wide

Table 3.1: The expression and transitions associated with various HH CP matching conditions for the CP transfer between I = 1/2 and S = 1/2 spin systems

CP matching conditions and associated transitions	$\omega_Q^{(1)} eq 0$	$\omega_Q^{(1)}=0$
Single-quantum (SQ ₃₄) $ 1/2, -1\rangle \leftrightarrow -1/2, 1\rangle$	$4\omega_I = (\omega_e - \omega_Q^{(1)})$	$\omega_{1I} = \omega_{1S}$
Triple-quantum (TQ ₁₆) $ -1/2, -1\rangle \leftrightarrow 1/2, 1\rangle$	$4\omega_I = -(\omega_e - \omega_Q^{(1)})$	$\omega_{1I} = -\omega_{1S}$
Double-quantum (DQ ₂₆) $ 1/2, -1\rangle \leftrightarrow -1/2, 0\rangle$	$4\omega_I = (\omega_e + \omega_Q^{(1)})$	$\omega_{1I} = \omega_{1S}$
Zero-quantum (ZQ ₃₅) $ -1/2, -1\rangle \leftrightarrow 1/2, 0\rangle$	$4\omega_I = -(\omega_e + \omega_Q^{(1)})$	$\omega_{1I} = -\omega_{1S}$

range of experimentally relevant parameters. The discussion presented below is equally valid for any set of spin-1/2 and spin-1 systems. For pedagogical purposes, the dynamics of polarization transfer in single-crystal and powder samples are examined separately. To explicate the interplay between the quadrupolar coupling constant and the amplitude of the RF field employed on the I-spin, the discussion is split into three regimes in the present study: Regime-I ($C_Q = 20 \text{ kHz}$, Weak), Regime-II ($C_Q = 200 \text{ kHz}$, Intermediate) and Regime-III ($C_Q = 1.0 \text{ MHz}$, Strong).

3.2.1 Description of CP dynamics in a single-crystal (with specific orientation α_Q and $\beta_Q = 0^{\circ}$)

3.2.1.1 Regime-I ($C_Q = 20 \text{ kHz}, \text{ Weak}$)

In the simulations depicted in Figure 3.3, polarization transfer from I=1/2 to S=1 is monitored as a function of the RF amplitude on the I-spin under constant mixing time employing a constant RF field on the quadrupolar spin, S. The simulations in solid black lines are derived from the numerical method based on SIMPSON (a software package for simulating NMR experiments) [131] and are employed to test the validity of the analytic theory. All other relevant simulation parameters are given in the Figure captions. To explicate the contributions from the four CP matching conditions predicted by the analytic theory, we begin with analytic simulations based on Eq. (3.19). As illustrated (refer to panel a1 in Figure 3.3), the analytic simulations based on Eq. (3.19) are in excellent agreement to those obtained from SIMPSON.

To explicate the role of the individual contributions emerging from the four CP matching conditions, additional analytic simulations were also explored. Accordingly, in the simulations illustrated along the second row, the contributions emerging from the single-quantum (SQ_{34}), triple-quantum (TQ_{16}) matching conditions and their sum ($SQ_{34}+TQ_{16}$) are depicted. In a similar vein, the contributions emerging from the double-quantum (DQ_{26}), zero-quantum (ZQ_{35}) matching conditions and their sum ($DQ_{26}+ZQ_{35}$) are depicted in the third row. As illustrated, the individual analytic

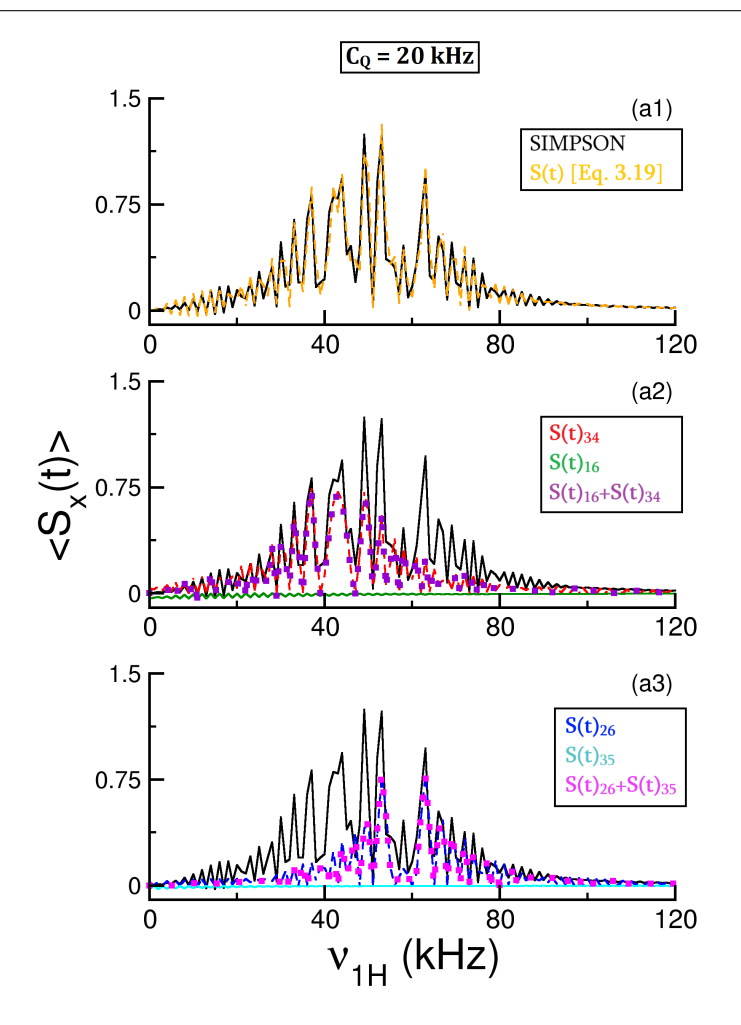


Figure 3.3: In the CP simulations depicted, the polarization build-up on the S-spin (due to transfer from the I-spin) is monitored in a single-crystal as a function of the RF field employed on the I-spin. The numerical simulations (based on SIMPSON) are represented by solid black lines. The following parameters were employed in the simulations: Quadrupolar parameters ($C_Q = 20 \text{ kHz}, \eta_Q = 0$, quadrupolar coupling PAS angles α_Q and $\beta_Q = 0^\circ$) and Dipolar parameters (internuclear distance $r_{IS} = 1.05$ Å and dipolar PAS angle $\beta_d = 0^{\circ}$ and dipolar PAS angle $\beta_d = 0^{\circ}$). A constant RF amplitude of $\nu_{1S} = 50$ kHz was employed on the quadrupole, S-spin, and the mixing time during the CP experiment was held constant (say $t_{mix} = 0.5$ ms). In panel (a1) the analytic simulations comprise contributions from all the four CP matching conditions $(SQ_{34}+TQ_{16}+DQ_{26}+ZQ_{35})$ and is represented in orange color. In panel (a2) the analytic simulations based on the contributions from the SQ_{34} (red dashed curve), TQ_{16} (green color), and SQ₃₄+TQ₁₆ (indigo color square) CP conditions are depicted. In panel (a3) the analytic simulations based on the contributions from the DQ_{26} (blue dashed curve), ZQ₃₅ (cyan color) and DQ₂₆+ZQ₃₅ (magenta color square) CP conditions are depicted.

simulations based on the two sets of CP matching conditions: SQ₃₄+TQ₁₆ (second row) or DQ₂₆+ZQ₃₅ (third row) are inaccurate when compared to those obtained from SIMPSON. Additionally, in the weak-coupling regime, the dominant contribution to the polarization transfer arises from the contributions from the SQ₃₄ and DQ₂₆ matching conditions that overlap to result in a single-broad CP resonance. These observations are also well-corroborated through additional simulations depicted in Figure 3.4 wherein, the

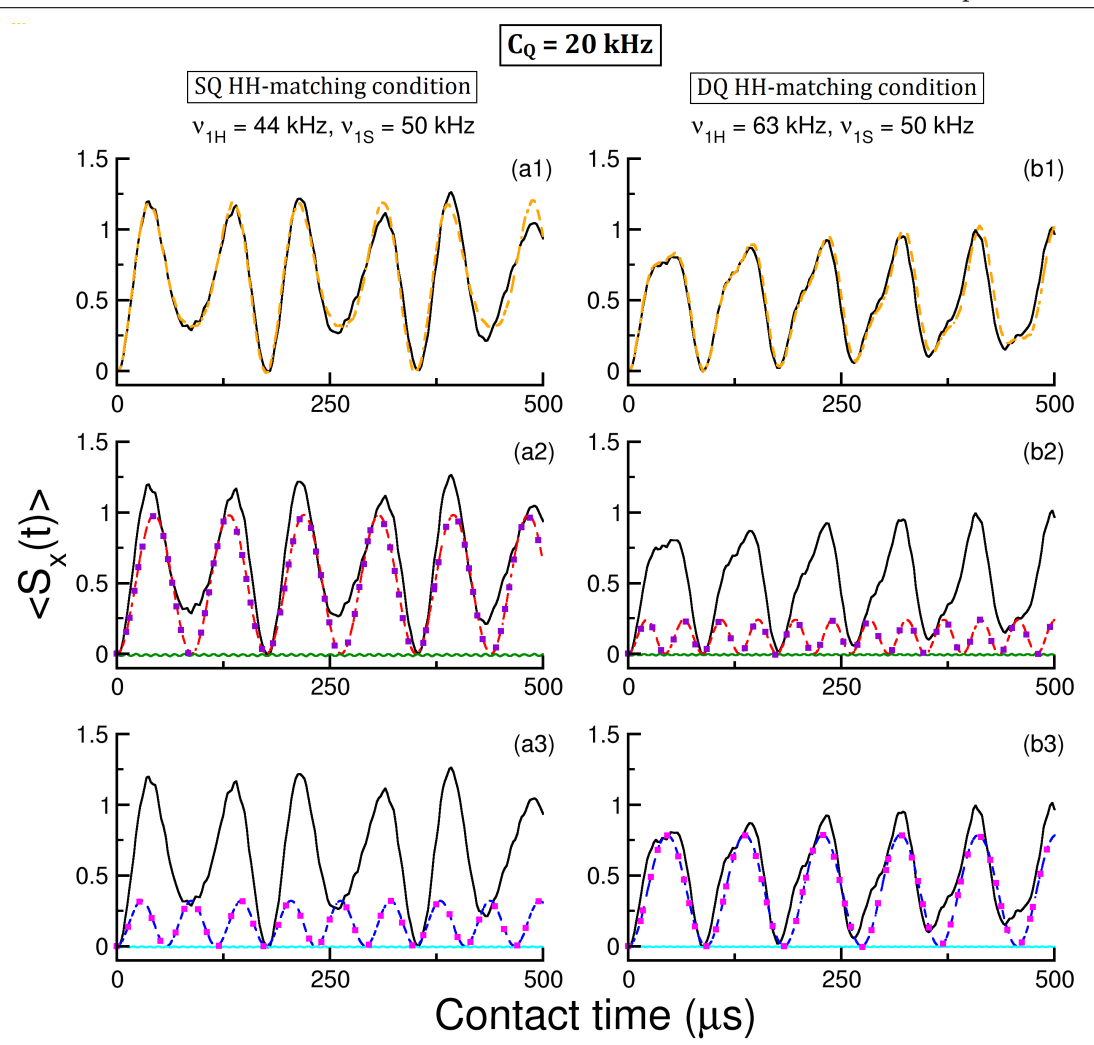


Figure 3.4: In the CP simulations depicted, the polarization build-up on the S-spin (due to transfer from the I-spin) is monitored in a single-crystal as a function of the CP mixing time under constant RF field strengths on both the spins. The RF amplitudes on the I-spin were chosen based on the two CP maxima observed in Figure 3.3, i.e. panels a1-a3 ($\nu_{1I}=44~\mathrm{kHz}$); panels b1-b3 ($\nu_{1I}=63~\mathrm{kHz}$). The numerical simulations (based on SIMPSON) are represented by solid black lines. The following parameters were employed in the simulations: Quadrupolar parameters ($C_Q=20~\mathrm{kHz},\,\eta_Q=0$, PAS angles α_Q and $\beta_Q=0^\circ$) and Dipolar parameters (internuclear distance $r_{IS}=1.05~\mathrm{Å}$ and dipolar PAS angle $\beta_d=0^\circ$). A constant RF amplitude of $\nu_{1S}=50~\mathrm{kHz}$ was employed on the quadrupole, S-spin. The remaining simulation parameters and descriptions are as given in the caption of Figure 3.3.

polarization transfer is monitored as a function of the CP mixing time. Hence, in the weak-coupling regime, contributions from both the SQ_{34} and DQ_{26} matching conditions are essential to describe the spin dynamics. This is in stark contrast to the model proposed by Pratum and Klein (discussed in section C.2 of Appendix C), wherein, only one of the matching conditions (SQ_{34} or DQ_{26}) was proposed to describe the CP dynamics. Hence, in the weak coupling regime, the contributions from the SQ_{34} and DQ_{26} matching conditions are essential to simulate the CP trajectories.

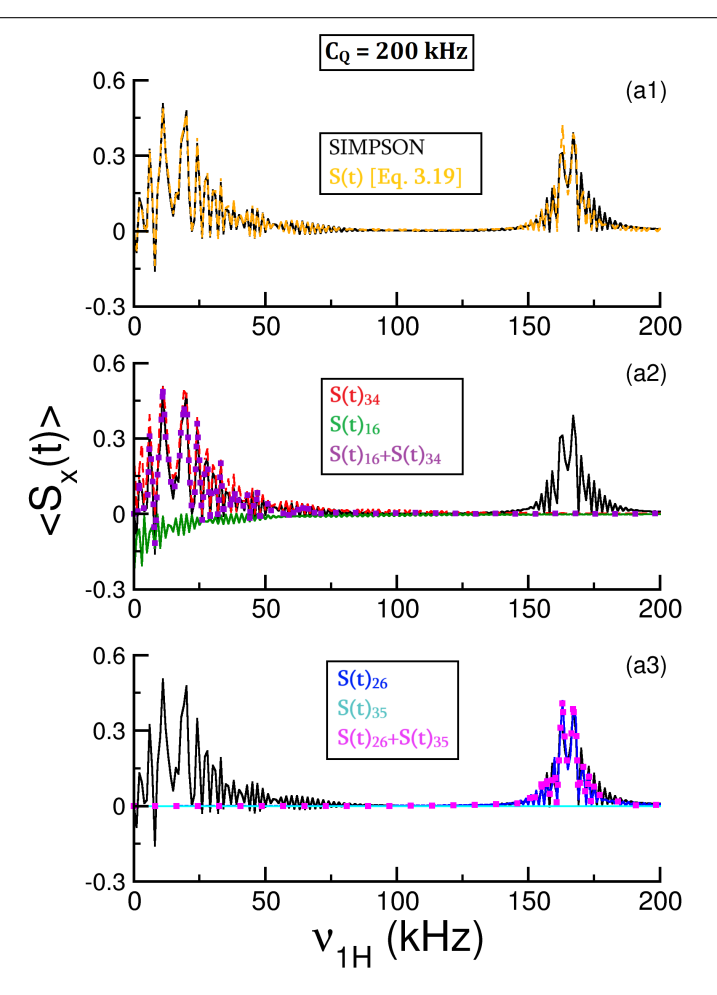


Figure 3.5: In the CP simulations depicted, the polarization build-up on the S-spin (due to transfer from the I-spin) is monitored in a single-crystal as a function of the RF field employed on the I-spin. The numerical simulations (based on SIMPSON) are represented by solid black lines. The following parameters were employed in the simulations: Quadrupolar parameters ($C_Q = 200 \text{ kHz}$, $\eta_Q = 0$, quadrupolar coupling PAS angles α_Q and $\beta_Q = 0^{\circ}$) and Dipolar parameters (internuclear distance $r_{IS} = 1.05$ Å and dipolar PAS angle $\beta_d = 0^{\circ}$). A constant RF amplitude of $\nu_{1S} = 50$ kHz was employed on the quadrupole, S-spin, and the mixing time during the CP experiment was held constant (say $t_{mix} = 0.5$ ms). In panel (a1) the analytic simulations comprise contributions from all the four CP matching conditions ($SQ_{34}+TQ_{16}+DQ_{26}+ZQ_{35}$) and is represented in orange color. In panel (a2) the analytic simulations based on the contributions from the SQ_{34} (red dashed curve), TQ₁₆ (green color), and SQ₃₄+TQ₁₆ (indigo color square) CP conditions are depicted. In panel (a3) the analytic simulations based on the contributions from the DQ_{26} (blue dashed curve), ZQ_{35} (cyan color), and $DQ_{26}+ZQ_{35}$ (magenta color square) CP conditions are depicted.

Regime-II ($C_Q = 200 \text{ kHz}$, Intermediate) 3.2.1.2

To explicate the role of the quadrupolar coupling constant in the individual contributions emerging from the four matching conditions, the CP transfer in the intermediate coupling regime, say $C_Q = 200$ kHz was employed in the simulations illustrated in Figure 3.5. Analogous to the description in the previous section, the polarization transfer is monitored as a function of the RF amplitude on the I-spin. In contrast to the CP profile in the

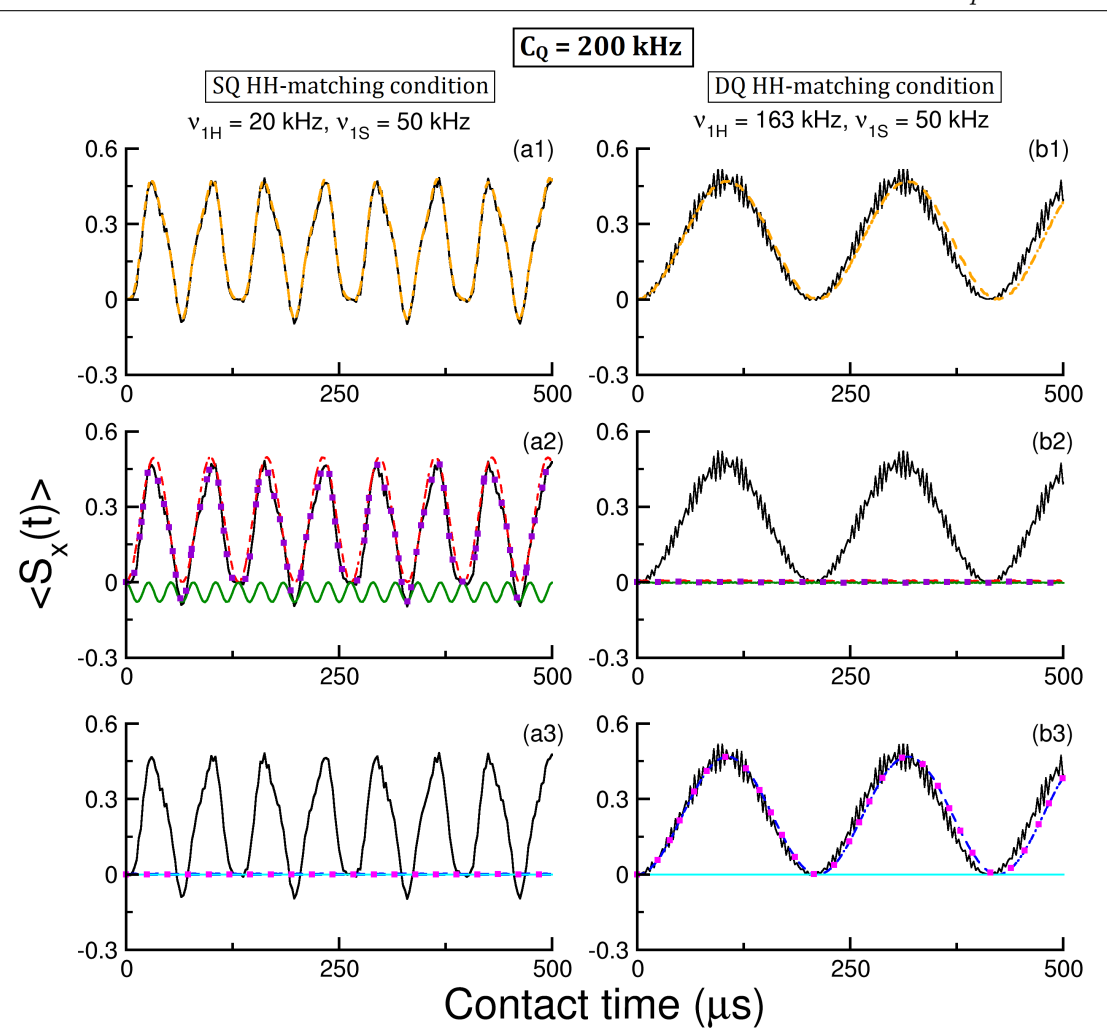


Figure 3.6: In the CP simulations depicted, the polarization build-up on the S-spin (due to transfer from the I-spin) is monitored in a single-crystal as a function of the CP mixing time under constant RF field strengths on both the spins. The RF amplitudes on the I-spin were chosen based on the two CP maxima observed in Figure 3.5 (in the main text) i.e., panels a1-a3 ($\nu_{1H}=20~\text{kHz}$); panels b1-b3 ($\nu_{1H}=167~\text{kHz}$). The following Quadrupolar parameters were employed in the simulations: ($C_Q=200~\text{kHz}$, $\eta_Q=0$, quadrupolar coupling PAS angles α_Q and $\beta_Q=0^\circ$). The remaining simulation parameters and descriptions are as given in the caption of Figure 3.5.

weak-coupling regime, the SQ_{34} and DQ_{26} matching conditions are well separated/resolved in the intermediate coupling regime. As illustrated in Figure 3.5 (panel a1), the analytic simulations based on Eq. (3.19) are in excellent agreement to those obtained from SIMPSON.

From a practical viewpoint, the simulation results illustrated in the second and third rows are relevant. As illustrated, at lower I-spin RF amplitudes, the CP profile has significant contributions from both the SQ_{34} and TQ_{16} matching conditions. At lower I-spin RF amplitudes, the magnitude of $\Sigma_{16} (= 4\omega_{1I} + \omega_e - \omega_Q^{(1)})$ term associated with otherwise high-frequency TQ_{16} matching condition is reduced and therefore the prefactor $\left(\frac{(\omega_d^{16,34})^2}{\Sigma_{16}^2 + (\omega_d^{16,34})^2}\right)$ becomes finite. In other words, the effective field during the mixing

3.2.1.3 Regime-III ($C_Q = 1.0 \text{ MHz}, \text{Strong}$)

To further substantiate the analytic framework, additional simulations depicting the polarization transfer in the strong-coupling regime were also examined (as depicted in Figure 3.7). In contrast to the CP profiles in the weak and intermediate coupling regimes, the separation between the two sets of matching conditions (TQ_{16}/SQ_{34} and DQ_{26}/ZQ_{35}) increases drastically. As illustrated, at lower I-spin RF amplitudes, both the SQ_{34} and TQ_{16} matching conditions have nearly similar contributions, while at higher I-spin RF amplitudes, the DQ₂₆ matching condition plays a decisive role in the CP experiments. The contributions from the ZQ₃₅ matching condition remain insignificant and is very similar to those observed in the weak and intermediate coupling regimes. These observations are also manifested in the mixing time plots depicted in Figure 3.8. As depicted in Figures 3.3, 3.5 and 3.7, the efficiency of polarization transfer decreases with increasing quadrupolar coupling strengths in accord with the factor $4\omega_{1S}/\omega_e$ in Eq. (3.19). The behavior of the spin-locking efficiency is expected to be analogous for the SQ₃₄ and TQ₁₆ matching conditions. An additional decrease in the CP efficiency observed at lower I-spin RF amplitude could be attributed to the competing nature of the SQ₃₄ and TQ₁₆ matching conditions *i.e.*, the prefactor $\left(\frac{(\omega_d^{16,34})^2}{\Sigma_{16}^2 + (\omega_d^{16,34})^2}\right)$ in the TQ₁₆ condition becomes similar to the prefactor in $\left(\frac{(\omega_d^{16,34})^2}{\Delta_{34}^2 + (\omega_d^{16,34})^2}\right)$ in the SQ₃₄ matching condition [refer to Eq. (3.19)]. The interplay between three CP matching conditions in the spin dynamics is significantly different from those observed in the weak and intermediate quadrupolar coupling regimes. The highly oscillatory behavior observed at lower I-spin RF amplitude results from the

interplay of various effective fields in spin dynamics. From an experimental perspective, the decrease in the CP efficiency observed in the strong quadrupolar coupling regime could

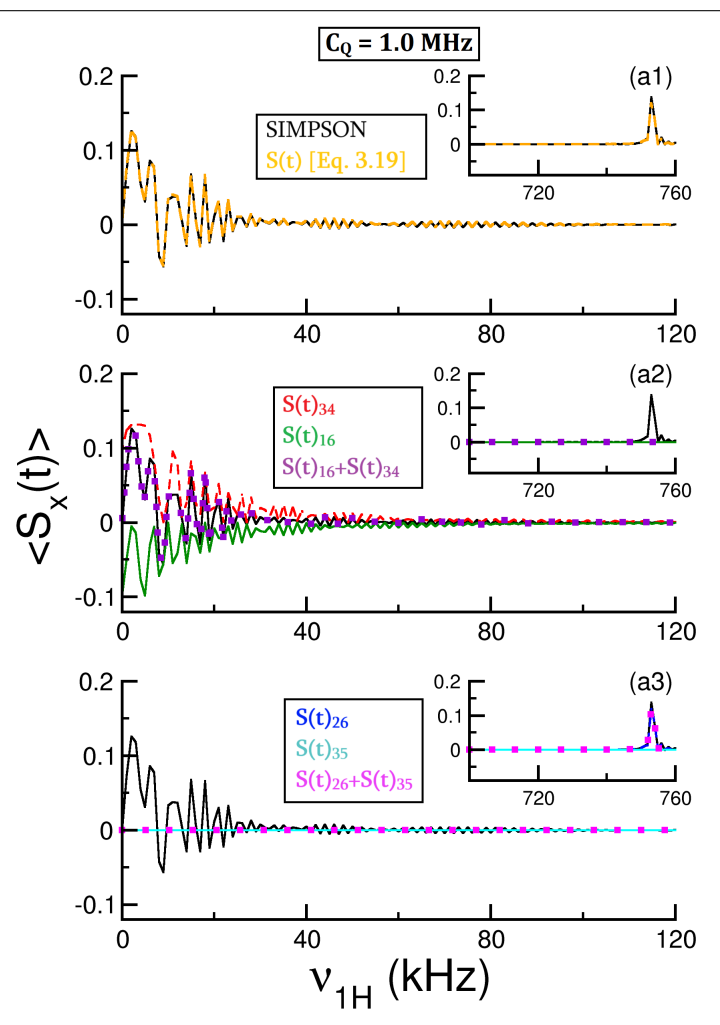


Figure 3.7: In the CP simulations depicted, the polarization build-up on the S-spin (due to transfer from the I-spin) is monitored in a single-crystal as a function of the RF field employed on the I-spin. The numerical simulations (based on SIMPSON) are represented by solid black lines. The following parameters were employed in the simulations: Quadrupolar parameters ($C_Q = 1.0 \text{ MHz}$, $\eta_Q = 0$, quadrupolar coupling PAS angles α_Q and $\beta_Q = 0^{\circ}$) and Dipolar parameters (internuclear distance $r_{IS} = 1.05$ Å and dipolar PAS angle $\beta_d = 0^{\circ}$). A constant RF amplitude of $\nu_{1S} = 50$ kHz was employed on the quadrupole, S-spin and the mixing time during the CP experiment was held constant (say $t_{mix} = 0.5$ ms). In panel (a1) the analytic simulations comprise contributions from all the four CP matching conditions $(SQ_{34}+TQ_{16}+DQ_{26}+ZQ_{35})$ and is represented in orange color. In panel (a2) the analytic simulations based on the contributions from the SQ₃₄ (red dashed curve), TQ₁₆ (green color), and SQ₃₄+TQ₁₆ (indigo color square) CP conditions are depicted. In panel (a3) the analytic simulations based on the contributions from the DQ₂₆ (blue dashed curve), ZQ₃₅ (cyan color), and DQ₂₆+ZQ₃₅ (magenta color square) CP conditions are depicted. The insets in panels a1-a3 depict the CP efficiency in the higher I-spin RF field range.

be improved by employing a higher RF field strength on the quadrupolar spin (S) and is in accord with the numerical factor $4\omega_{1S}/\omega_e$ in Eq. (3.19). This improvement in the CP efficiency could also be explained based on the decreased interference from the TQ₁₆ CP condition at lower I-spin RF amplitudes with increasing S-spin RF field strengths (refer to Figure C.1. in Appendix C).

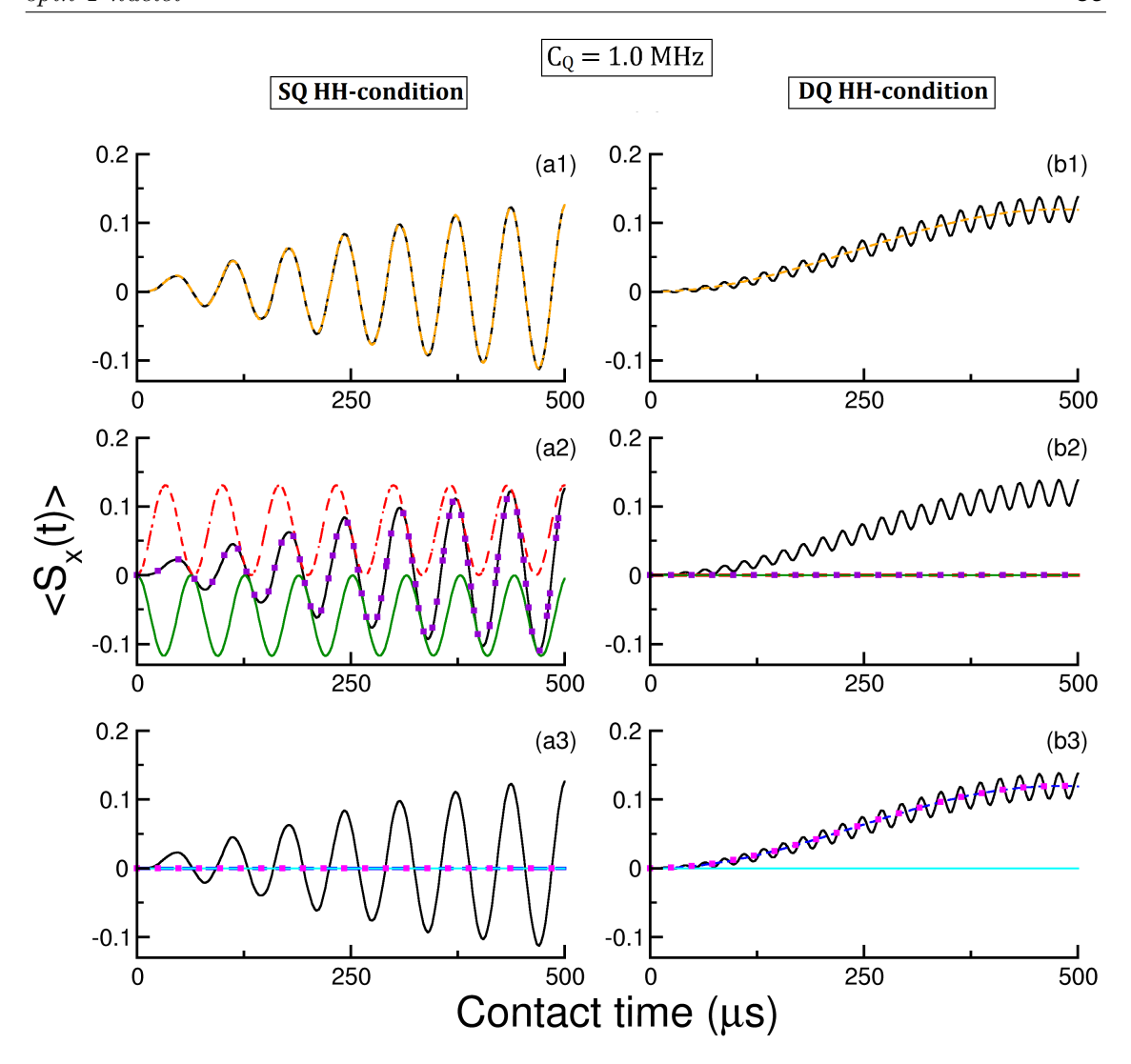


Figure 3.8: In the CP simulations depicted, the polarization build-up on the S-spin (due to transfer from the I-spin) is monitored in a single-crystal as a function of the CP mixing time under constant RF field strengths on both the spins. The RF amplitudes on the I-spin were chosen based on the two CP maxima observed in Figure 3.7 i.e., panels a1-a3 $(\nu_{1H}=2 \text{ kHz})$; panels b1-b3 $(\nu_{1H}=753 \text{ kHz})$. The following Quadrupolar parameters were employed in the simulations: $(C_Q = 1.0 \text{ MHz}, \eta_Q = 0, \text{ quadrupolar coupling PAS})$ angles α_Q and $\beta_Q = 0^{\circ}$). The remaining simulation parameters and descriptions are as given in the caption of Figure 3.4.

3.2.2Description of CP dynamics in a single-crystal (with general orientation α_Q and $\beta_Q \neq 0^{\circ}$)

To outline the orientation dependence of the quadrupolar interactions in CP experiments, additional simulations in single-crystal with general orientations were also carried out. As illustrated in Eq. (3.19), the quadrupolar interaction depends on the Euler angles (α_Q and β_Q). In the quadrupolar principal axis frame the angle β_Q denotes the angle between the static magnetic field and the z-axis of the quadrupolar PAS, while, α_Q represents its projection along the x-y plane. Considering the quadrupolar PAS coincides with the Molecular-axis systems (MolAS), the angles (α_Q, β_Q) will represent different crystallites

orientations. The graphical demonstration of this angular dependence is shown in the Figure C.2 (refer to Appendix C). The magnitude and sign of the first-order quadrupolar frequency are strongly influenced by the crystallite-orientations; therefore the overall CP behaviour anticipated to vary considerably and is presented below.

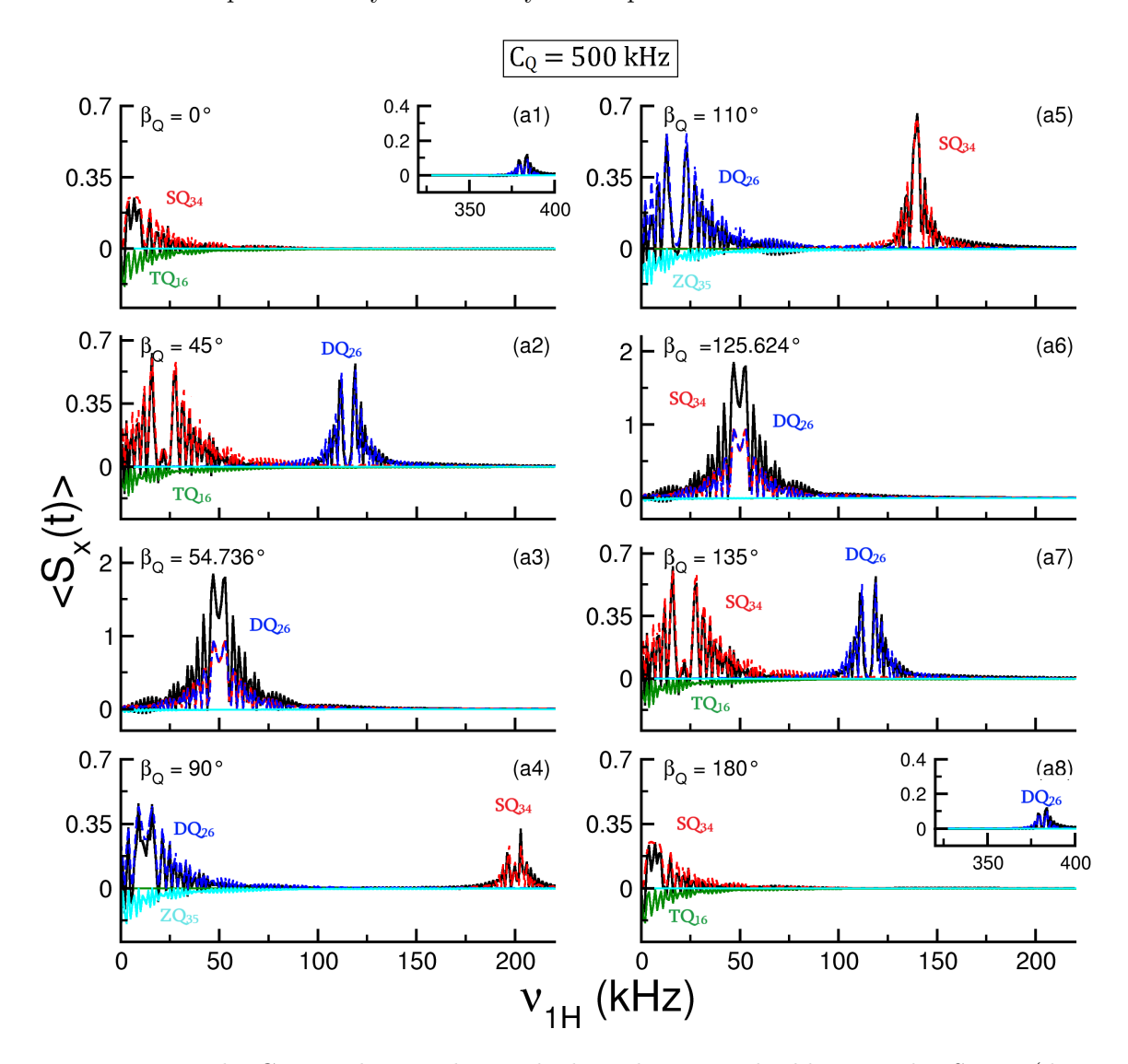


Figure 3.9: In the CP simulations depicted, the polarization build-up on the S-spin (due to transfer from the I-spin) is monitored in a single-crystal (with general orientation) as a function of the RF field employed on the I-spin. The numerical simulations (based on SIMPSON) are represented by solid black lines. In the simulations depicted, the effects of the variation of quadrupolar coupling PAS angle β_Q : 0° (a1), 45° (a2), 54.736° (a3) 90° (a4), 110° (a5), 125.624° (a6), 135° (a7) and 180°(a8) on the CP dynamics is illustrated. The following parameters were employed in all the simulations: $C_Q = 500$ kHz, $\eta_Q = 0$, quadrupolar coupling PAS angle $\alpha_Q = 0^\circ$, contact time (t_{mix}) = 0.5 ms, internuclear distance $r_{IS} = 1.05$ Å and dipolar PAS angle $\beta_d = 0^\circ$ and $\nu_{1S} = 50$ kHz. The analytic simulations based on signal expressions corresponding to various CP matching conditions are indicated: SQ₃₄ (red), TQ₁₆ (green), DQ₂₆ (blue) and ZQ₃₅ (cyan) [Eq. (3.19)]. The insets in panels a1 and a8 show CP maxima in the higher I-spin RF field range.

In the simulation depicted in Figure 3.9, the relative contributions from the four matching conditions are presented for a set of eight β_Q angles in the range $0^{\circ} \leq \beta_Q \leq 180^{\circ}$.

71

As depicted in Figure 3.9, when β_Q is less than 54.736 (0° $\leq \beta_Q <$ 54.736°), the CP profile approaches the weak coupling regime and the CP efficiency improves. At $\beta_Q = 54.736^{\circ}$, the quadrupolar interaction reduces to zero (for a symmetric tensor, $\eta_Q = 0$) and the trajectories emerging from the SQ₃₄ and DQ₂₆ matching conditions overlap. This observation could also be substantiated through the analytic expression given in Eq. (3.19). From an experimental perspective, the interesting observation emerges for cases where the angle β_Q in the range (54.736° $< \beta_Q < 125.624$ °). As illustrated in the simulations (refer to panels a4-a6), the CP profile approaches the intermediate coupling regimes along with

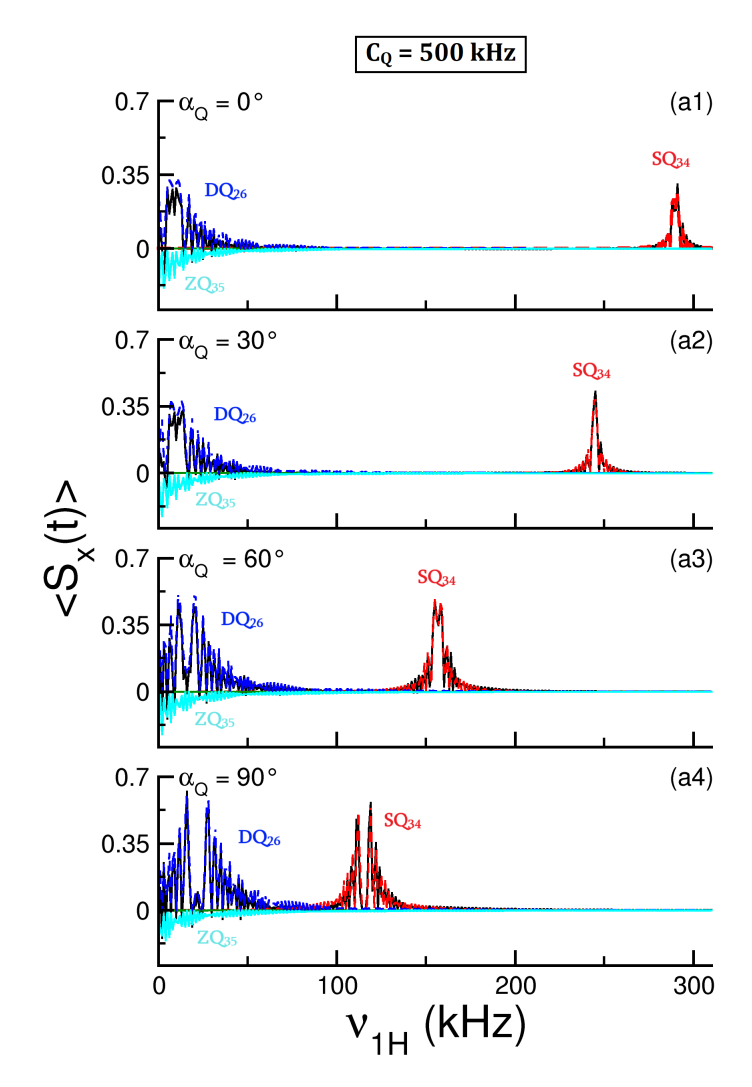


Figure 3.10: In the CP simulations depicted, the polarization build-up on the S-spin (due to transfer from the I-spin) is monitored in a single-crystal (with general orientation) as a function of the RF field employed on the I-spin. The numerical simulations (based on SIMPSON) are represented by solid black lines. In the simulations depicted, the effects of the variation of quadrupolar coupling PAS angle α_Q : 0° (a1), 30°(a2), 60° (a3) and 90° (a4) on the CP dynamics are illustrated. The following parameters were employed in all the simulations: $C_Q = 500$ kHz, $\eta_Q = 0.5$, quadrupolar coupling PAS angle $\beta_Q =$ 90°, contact time $(t_{mix}) = 0.5$ ms, internuclear distance $r_{IS} = 1.05$ Å and dipolar PAS angle $\beta_d = 0^{\circ}$ and $\nu_{1S} = 50$ kHz. The analytic simulations based on signal expressions corresponding to various CP matching conditions are indicated, SQ₃₄ (red), TQ₁₆ (green), DQ_{26} (blue) and ZQ_{35} (cyan) [Eq. (3.19)]

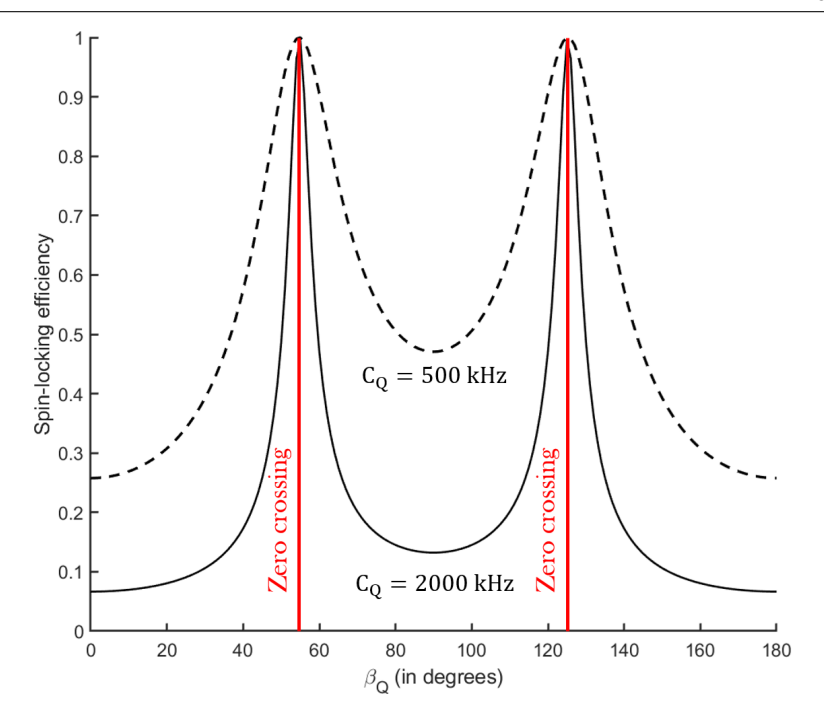


Figure 3.11: The effect of the variation of quadrupolar PAS angle β_Q on the spin-locking efficiency $(4\omega_{1S}/\omega_Q^{(1)})$ for single-crystal sample. Considering the quadrupolar PAS coincides with the MolAS, angles β_Q will represents different crystallites orientations. The following parameters were employed in all the simulations: $C_Q = 500$ kHz (dashed curve) and 2000 kHz (solid curve), $\eta_Q = 0$, quadrupolar coupling PAS angle $\alpha_Q = 0^\circ$ and $\nu_{1S} = 50$ kHz.

swapping in the position of the CP matching conditions due to the negative sign of $\omega_{\mathcal{O}}$ in the above range of β_Q . We observe a profound change in the relative contributions from the four CP matching conditions. As depicted, at lower I-spin RF amplitudes, the CP profile has a dominant contribution from the DQ_{26}/ZQ_{35} CP matching condition, while at higher I-spin RF amplitudes, the SQ_{34} matching condition contributes with negligible contribution from the TQ_{16} condition. This trend is completely opposite to those depicted in the weak (Figure 3.3), intermediate (Figure 3.5, and strong (Figure 3.7) coupling regimes in previous section. At $\beta_Q = 125.624^{\circ}$, the quadrupolar interaction reduces to zero for a symmetric tensor, and the CP profile is similar to the one observed at $\beta_Q = 54.736^{\circ}$. From $125.624^{\circ} \le \beta_Q \le 180^{\circ}$, the CP profile resembles to the one obtained for β_Q in the range 54.736° \geq β_Q \geq 0°. Interestingly, the relative contributions from the four matching conditions are reversed (in contrast to those observed in the range, $54.736^{\circ} < \beta_Q < 125.624^{\circ}$) and is in accord with those depicted in the earlier simulations (Figures 3.3, 3.5, and 3.7). Hence the value of β_Q plays an important role in quantifying the CP profile in terms of four matching conditions and highlights the non-uniformity of the CP transfer among different quadrupolar tensor orientations. The shift in positions of SQ_{34}/TQ_{16} and DQ_{26}/ZQ_{35} resonances with the variation of PAS β_Q angle depends strongly on the size of quadrupolar coupling strength C_Q . For instance, the variation of β_Q angle for $C_Q = 20$ kHz (refer to Figure C.3 in Appendix C) shows a similar pattern as discussed above, however, the change in positions of these resonances are not huge in comparison to those depicted in Figure 3.9. The quadrupolar PAS angle α_Q affects the magnitude of the quadrupolar frequency (not sign for $\beta_Q = 90^\circ$) in the case of asymmetric tensor and is shown in Figure 3.10. However, the behaviour of the first-order quadrupolar frequency with α_Q angle variation is strongly η_Q and β_Q dependent. From Eq. 3.19, it is evident that unlike spin-1/2 systems, the polarization transfer efficiency (intensity) is scaled by factor $4\omega_{1S}/\omega_Q^{(1)}$ at exact HH CP matching condition; hence this term will provide an idea on the extent of spin-locking and hence maximum polarization transfer efficiency. Figure 3.11 demonstrates the spin-locking efficiency $(4\omega_{1S}/\omega_Q^{(1)})$ as a function of crystallites orientations (β_Q) for a single-crystal sample. The crystallites which lie close to $\beta_Q = 54.736^\circ$ of the first-order quadrupolar frequency will have better spin-locking efficiency; hence better overall CP transfer efficiency. This behavior is consistently applicable across all C_Q values. Consequently, the CP excitation will not be uniform in the case of a sample with multiple crystallite orientations. The powder sample represents a more generalized system, characterized by statistically weighted random orientations of crystallites.

3.2.3 Description of the CP dynamics in a powder sample

In the simulations depicted in Figure 3.12, the CP dynamics in a powder sample is examined. The decrease in polarization transfer efficiency in comparison to single-crystal sample results from the interference effects between the different crystallites present in a powder sample and could also be explained in terms of the interference among the trigonometric terms in Eq. (3.19). Additionally, as depicted in the simulations, the CP profile broadens and splits into two maxima of unequal intensities with increasing quadrupolar strengths. This splitting pattern could be explained based on the contributions from the different CP matching conditions and the discussion presented in the previous subsections. As depicted in Figure 3.12, in the weak-coupling regime $(C_Q = 20 \text{ kHz})$, the CP efficiencies resulting from the SQ_{34} and DQ_{26} matching conditions overlap equally analogous to those obtained in the single-crystal studies (Figure 3.3) and have negligible contributions from the TQ_{16} and ZQ_{35} CP matching conditions. As illustrated, at lower I-spin RF amplitudes, the contribution from the DQ₂₆ matching condition dominates over those obtained from the SQ₃₄ matching condition (refer to second and third rows), while at higher I-spin RF amplitudes the contributions from the SQ_{34} matching condition are dominant.

This interesting observation however contradicts the discussion presented (in single-crystal) in section 3.1 (refer to Figures 3.3, 3.5 and 3.7) and could be explained based on the orientation (β_Q) dependence of quadrupolar coupling frequency (refer to Figure C.4 in Appendix C and Figure 3.9). Due to the high probability/weightage of the orientations in the plane perpendicular to the static Zeeman field, the contribution from the DQ₂₆ matching condition is higher at the lower *I*-spin RF amplitudes (due to the swapping of CP matching conditions). Similar behavior is also reflected at higher *I*-spin RF amplitudes, wherein the relative contributions from the DQ₂₆/ZQ₃₅ matching conditions decrease with increasing quadrupolar coupling strengths. At higher *I*-spin

RF amplitudes, the lower CP efficiency is due to strong quadrupolar coupling dependent polarization transfer $\left(\omega_{1I} = \frac{1}{4}(\omega_e + \omega_Q^{(1)})\right)$. In a powder sample, different crystallites undergo different HH-matching conditions at selected *I*-spin RF amplitude, therefore, the SQ_{34}/TQ_{16} and DQ_{26}/ZQ_{35} CP matching conditions become indistinguishable. Hence, the contributions from all the four CP matching conditions become essential to fit the

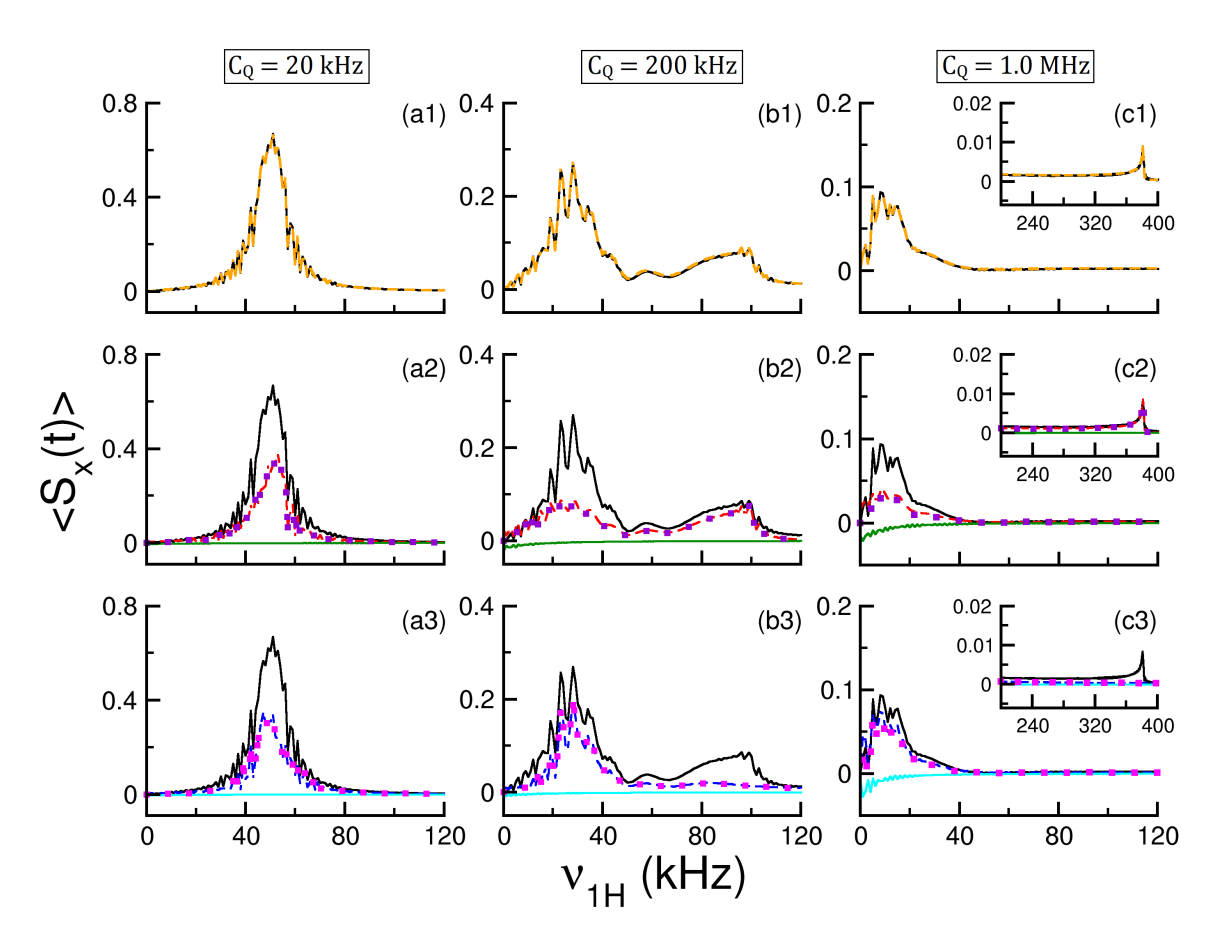


Figure 3.12: In the CP simulations depicted, the polarization build-up on the S-spin (due to transfer from the I-spin) is monitored in a powder sample as a function of the RF field employed on the I-spin. The numerical simulations (based on SIMPSON) are represented by solid black lines. The following parameters were employed in the simulations: panels a1-a3 ($C_Q=20$ kHz, $\eta_Q=0$); panels b1-b3 ($C_Q=200$ kHz, $\eta_Q=0$) and panels c1-c3 $(C_Q = 1.0 \text{ MHz}, \eta_Q = 0)$. All other parameters such as the quadrupolar coupling PAS angles α_Q and $\beta_Q = 0^{\circ}$), dipolar parameters (internuclear distance $r_{IS} = 1.05$ Å and dipolar PAS angle $\beta_d = 0^{\circ}$), RF amplitude of S-spin $\nu_{1S} = 50$ kHz and mixing time during the CP experiment (say $t_{mix} = 0.5$ ms) were identical in all the simulations. The analytic simulations in the panels have the following definitions: first row, the analytic simulations comprise contributions from all the four CP matching conditions $(SQ_{34}+TQ_{16}+DQ_{26}+ZQ_{35})$ and is represented in orange color. In the second row, the analytic simulations are based on the contributions from the SQ_{34} (red dashed curve), TQ_{16} (green color), and $SQ_{34}+TQ_{16}$ (indigo color square) CP conditions are depicted. In the third row, the analytic simulations based on the contributions from the DQ_{26} (blue dashed curve), ZQ_{35} (cyan color), and $DQ_{26}+ZQ_{35}$ (magenta color square) CP conditions are depicted. The powder simulations were performed using 4180 orientations (i.e., zcw4180) of α and β . The insets in panels c1-c3 depict the CP efficiency in the higher I-spin RF field range.

trajectories observed in CP experiments for powder samples. This could also be verified through the simulations depicted in Figure 3.12 (refer to the first row), wherein, all the four CP matching conditions have been employed to fit the trajectories. This aspect is further validated in the mixing time CP profiles illustrated in Figure 3.13. With increasing quadrupolar coupling strength, the time-domain oscillations become wiggled due to the interplay of various CP matching conditions therefore representing a complex CP transfer mechanism. Hence, the proposed analytic model presents a uniform framework for describing the CP dynamics in both single-crystal and powder samples across all regimes.

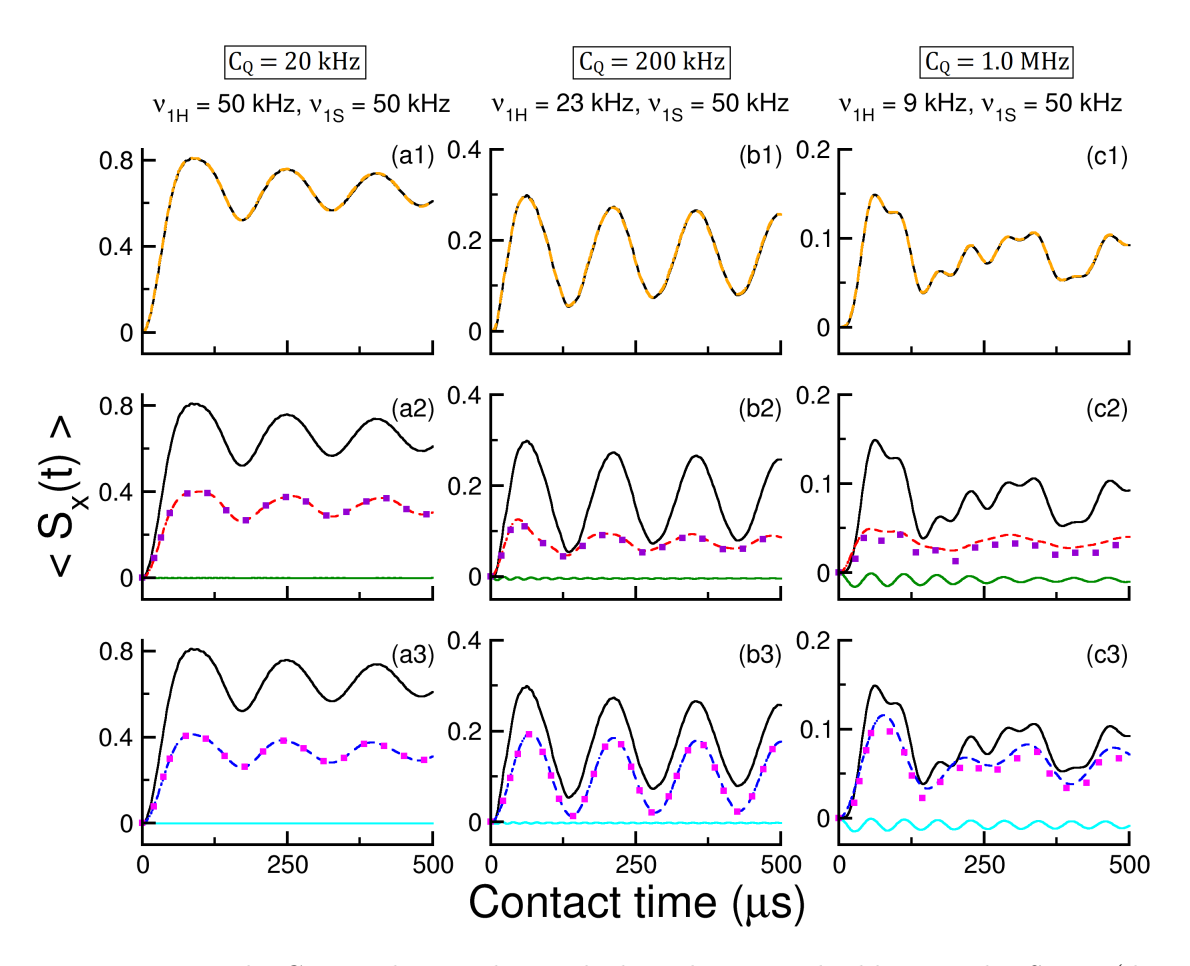


Figure 3.13: In the CP simulations depicted, the polarization build-up on the S-spin (due to transfer from the I-spin) is monitored in a powder sample as a function of the CP mixing time under constant RF amplitudes on the spins. The RF amplitudes on the I-spin were chosen based on the two CP maxima observed in Figure 3.12 i.e., panels a1-a3 ($\nu_{1H} = 50 \text{ kHz}$); panels b1-b3 ($\nu_{1H} = 23 \text{ kHz}$); panels c1-c3 ($\nu_{1H} = 9 \text{ kHz}$). The following parameters were employed in the simulations: panels a1-a3 ($C_Q = 20 \text{ kHz}$, $\eta_Q = 0$); panels b1-b3 ($C_Q = 200 \text{ kHz}$, $\eta_Q = 0$) and panels c1-c3 ($C_Q = 1.0 \text{ MHz}$, $\eta_Q = 0$). The remaining simulation parameters and descriptions are as given in the caption of Figure 3.12.

3.2.4 Extraction of the dipolar coupling parameters from the CP lineshapes

As discussed in the previous sections, the mechanism of polarization transfer in the CP experiment is complex both in the case of single-crystal and powder samples. Depending on the Euler angle β_Q and the quadrupolar coupling constant, the contributions from the four matching conditions vary. To further explore the utility of the proposed analytic theory, the extraction of dipolar parameters from the lineshape of the quadrupolar spin S (coupled to spin I=1/2) is investigated in the present section. To this end, we begin the present discussion with a single-crystal sample as an example. To extract the dipolar coupling parameters from the CP experiment, the CP efficiency is monitored as a function of the mixing time, and the resulting data is Fourier transformed (FT) to get the frequency-domain CP spectrum. This may be inferred through the equations given below: Depending on the matching conditions, the corresponding time-domain signal, $S(t)_{ij}$ is Fourier transformed to obtain the frequency-domain CP signal expression $[S(\omega)_{ij}]$,

$$S(\omega)_{ij} = C_{ij} \int_{-\infty}^{\infty} \sin^2\left(\frac{\omega_{e,ij}}{2}t\right) e^{-i\omega t} dt$$

$$= \frac{C_{ij}}{2} \int_{-\infty}^{\infty} \left(1 - \cos\omega_{e,ij}t\right) e^{-i\omega t} dt$$
(3.25)

where (ij) refers to 16 (TQ₁₆), 34 (SQ₃₄), 35 (ZQ₃₅), and 26 (DQ₂₆) matching conditions, and the constants C_{ij} are: $C_{16} = -\frac{4\omega_{1S}}{\omega_e} \left(\frac{\omega_d^{16,34}}{\omega_{eff}^{(16)}}\right)^2$, $C_{34} = \frac{4\omega_{1S}}{\omega_e} \left(\frac{\omega_d^{16,34}}{\omega_{eff}^{(34)}}\right)^2$,

$$C_{35} = -\frac{4\omega_{1S}}{\omega_e} \left(\frac{\omega_d^{26,35}}{\omega_{eff}^{(35)}}\right)^2$$
 and $C_{26} = \frac{4\omega_{1S}}{\omega_e} \left(\frac{\omega_d^{26,35}}{\omega_{eff}^{(26)}}\right)^2$. The Fourier-transformed CP signal expression is derived using the integral definition of the Dirac-delta function and is given

$$S(\omega)_{ij} = C_{ij}\pi \left[\delta(\omega) - \frac{1}{2} \left\{ \delta(\omega - \omega_{eff}^{(ij)}) + \delta(\omega + \omega_{eff}^{(ij)}) \right\} \right]. \tag{3.26}$$

Under the exact CP matching condition, the above equation reduces to the form given below:

• SQ₃₄/TQ₁₆ CP matching condition:

below:

$$S(\omega)_{ij} = C_{ij}\pi \left[\delta(\omega) - \frac{1}{2} \left\{ \underbrace{\delta(\omega - \omega_d^{16,34}) + \delta(\omega + \omega_d^{16,34})}_{\text{Purely dipolar splitting } (2\omega_d^{16,34})} \right\} \right]$$
(3.27)

• DQ_{26}/ZQ_{35} CP matching condition:

$$S(\omega)_{ij} = C_{ij}\pi \left[\delta(\omega) - \frac{1}{2} \left\{ \underbrace{\delta(\omega - \omega_d^{26,35}) + \delta(\omega + \omega_d^{26,35})}_{\text{Purely dipolar splitting } (2\omega_d^{26,35})} \right\} \right].$$
(3.28)

In the simulations depicted in Figure 3.14, the RF amplitudes employed on the two spins

77

(I and S) are adjusted carefully to satisfy one of the CP matching conditions. The FT CP spectra corresponding to the SQ_{34} matching conditions are depicted along the first column, while, those corresponding to the DQ_{26} matching condition are plotted along the second column under various quadrupolar coupling regimes. As illustrated in Figure 3.14(a1-a3), the FT spectra corresponding to the SQ_{34} CP matching conditions, comprise frequency contributions from the SQ_{34} (dominant), TQ_{16} or DQ_{26} (high-frequency) terms. Depending on the magnitude of the quadrupolar coupling constant, the relative

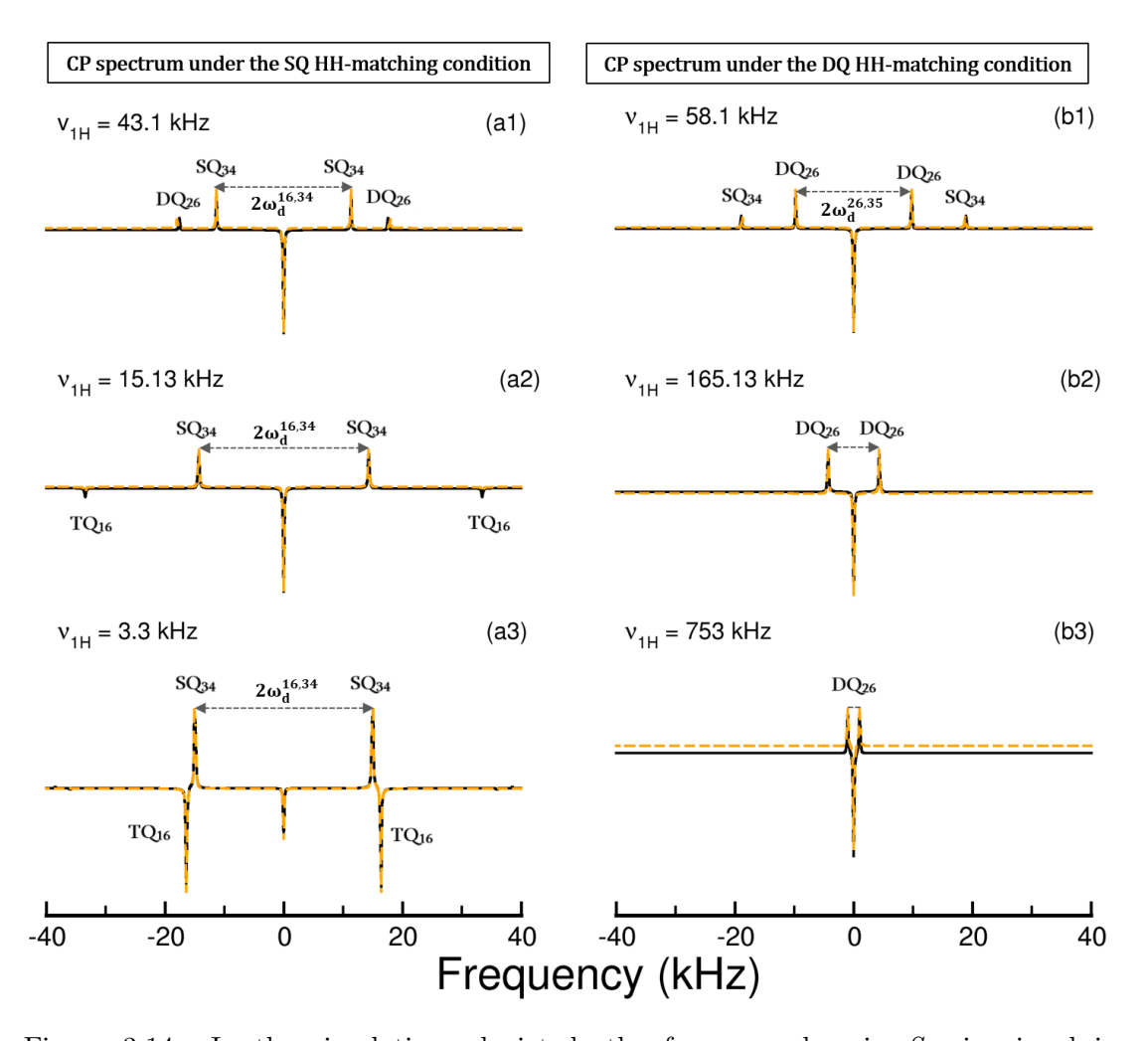


Figure 3.14: In the simulations depicted, the frequency-domain S-spin signal in a single-crystal emerging from Fourier transformation of the mixing time domain signal corresponding to the SQ₃₄ (first column) and DQ₂₆ CP matching conditions (second column) is shown for different quadrupolar coupling constants (depicted along the row): panels a1-b1 ($C_Q = 20 \text{ kHz}$), panels a2-b2 ($C_Q = 200 \text{ kHz}$) and panels a3-b3 ($C_Q = 1.0 \text{ MHz}$). All other parameters such as the quadrupolar coupling PAS angles α_Q and $\beta_Q = 0^{\circ}$, dipolar parameters (internuclear distance $r_{12} = 1.05 \text{ Å}$ and dipolar PAS angle $\beta_d = 0^{\circ}$) and RF amplitude of S-spin $\nu_{1S} = 50 \text{ kHz}$ were identical in all the simulations. Depending on the magnitude of the quadrupolar coupling constant, the RF amplitudes employed on the I-spin (indicated in the Figure) were carefully adjusted to match the SQ₃₄ (first column) and DQ₂₆ (second column) CP matching conditions. The solid black lines correspond to those obtained from SIMPSON, while the analytic simulations are indicated in orange color [based on Eq. (3.19)]. A line broadening of 50 Hz was used before the Fourier transform of the time-domain CP signal.

contributions emerging from the other two matching conditions (DQ_{26} and TQ_{16}) vary. As illustrated, in the weak-coupling regime, the FT spectrum comprises residual contributions from the DQ_{26} matching condition. With an increase in the quadrupolar coupling constant, the contributions from the TQ_{16} matching condition predominate (over the DQ_{26} matching) and become equivalent to the SQ_{34} matching condition in the strong coupling regime. As illustrated in Figure 3.14, the dominant peaks in the FT spectrum are derived from the frequency factor associated with the SQ₃₄ matching condition. The central peak at zero frequency ($\omega = 0$) corresponds to the non-oscillatory component of the time-domain signal, while the remaining two peaks (at $\omega = -\omega_{eff}^{(16)}$ and $\omega = \omega_{eff}^{(16)}$) symmetrically distributed about the central peak (at zero frequency) result from the effective-field corresponding to the SQ₃₄ matching condition. From a practical aspect, the dipolar parameter in the FT spectrum is extracted by measuring the frequency separation between the two symmetric peaks $(2\omega_d^{16,34})$ or $2\omega_d^{26,35}$. As the central peak is inverted or phase-shifted by 180°, it does not interfere with the extraction of the dipolar parameters. In a similar vein, the FT spectrum corresponding to the DQ₂₆ matching condition comprises contributions from the DQ_{26} term (dominant) and the SQ_{34} term. As illustrated, the frequency contribution from the residual SQ₃₄ CP matching condition decreases with an increase in the quadrupolar coupling constant. This trend is in accord with the earlier discussions on the CP dynamics presented in section 3.2.1. Analogous to the FT spectrum derived from the SQ₃₄ matching condition, the FT spectrum (second column in Figure 3.14) comprises symmetric peaks (at $\omega = -\omega_{eff}^{(34)}$ and $\omega = \omega_{eff}^{(34)}$, where $\omega_{eff}^{(34)}$ corresponds to the DQ₂₆ matching condition) distributed about the central peak (at $\omega = 0$). In contrast to the SQ₃₄ matching condition, the frequency separation between the two symmetric peaks is equal to the $4\omega_d \sin(\theta_1/2)$ and is in accord with the predictions emerging from the analytic theory [refer to Eq. (3.19)]. Therefore, the CP transfer in the spin-1 system introduces quadrupolar coupling dependent scaling factors as $2\cos\theta_1/2$ and $2\sin\theta_1/2$ under the SQ_{34}/TQ_{16} and DQ_{26}/ZQ_{35} HH matching conditions, respectively. Consequently, the magnitude and the orientation of the quadrupolar coupling tensor as well as the relative orientation of quadrupolar and dipolar coupling tensors will affect the intensity as well as the position of peaks/singularities in the CP spectrum. While the proposed analytic theory presents an accurate framework for describing the CP dynamics in both single-crystal and powder samples, the extraction of the dipolar parameters from the FT spectrum (derived from variable CP contact time experiment) remains less straightforward in a powder sample. The coupled orientation dependence of the quadrupolar and dipolar coupling frequencies results in an averaged CP behavior [150]. This is primarily because of the interference from various weighted powder orientations that lead to CP lineshape with well-defined singularities. The separation between the CP singularities will be a characteristic of the dipolar and quadrupolar coupling orientations $(4\omega_d \cos \theta_1/2 \text{ and } 4\omega_d \sin \theta_1/2).$

As illustrated in Figure 3.15, for $C_Q = 20$ kHz case, the overall CP powder lineshape generated by the overlapping of the SQ₃₄ and DQ₂₆ CP matching conditions resembles

79

a Pake-like doublet with a noticeable foot signal (refer to Figure C.5 in Appendix C for individual fitting of the CP lineshape.) With increasing magnitude of C_Q , the CP lineshapes get distorted due to appearance of additional singularities. Unlike $C_Q = 200$ kHz case in the stronger quadrupolar coupling regime, as the CP dynamics is a result of an interplay of all the four CP fields, and the CP spectrum suffers from additional distortions resulting from the high-frequency TQ_{16} and ZQ_{35} components. This is in accord with the results discussed in the previous sections (sections 3.2.1 and 3.2.2), wherein, the CP profiles

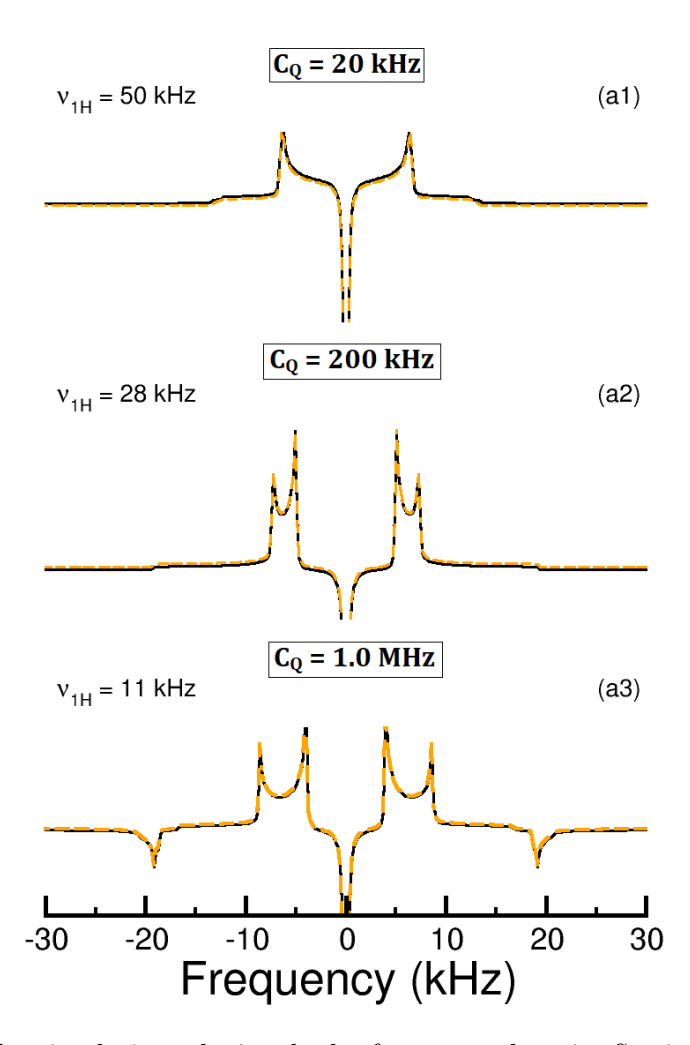


Figure 3.15: In the simulations depicted, the frequency-domain S-spin signal in powder sample emerging from Fourier transformation of the mixing time domain signal is shown for different quadrupolar coupling constants: panel a1 ($C_Q = 20 \text{ kHz}$); panel a2 ($C_Q = 200 \text{ kHz}$) kHz) and panel a3 ($C_Q = 1$ MHz). All other parameters such as the quadrupolar coupling PAS angles α_Q and $\beta_Q = 0^{\circ}$, dipolar parameters (internuclear distance $r_{12} = 1.05 \text{ Å}$ and dipolar PAS angle $\beta_d = 0^{\circ}$) and RF amplitude of S-spin $\nu_{1S} = 50$ kHz were identical in all the simulations. Depending on the magnitude of the quadrupolar coupling constant, the RF amplitudes employed on the I-spin (indicated in the Figure) were carefully selected by CP in maxima of the RF-domain simulation at the desired mixing time. The solid black lines correspond to those obtained from SIMPSON, while the analytic simulations are indicated in orange color [based on Eq. (3.19)]. The powder simulations were performed using 4180 orientations (i.e., zcw4180) of α and β . A line broadening of 50 Hz was used before the Fourier transform of the time-domain CP signal.

were simulated employing analytic expressions based on the four matching conditions. In such cases, the dipolar parameters are extracted through iterative fitting of the powder lineshapes employing Eq. (3.19). As illustrated in Figure 3.15, the analytic simulations based on Eq. (3.19) are in excellent agreement to those derived from numerical methods. Hence, the description of the CP dynamics based on the effective-field approach presents an attractive framework for describing the spin dynamics in non-rotating solids.

3.3 Conclusions

In summary, the proposed analytic theory presents an attractive framework for understanding the nuances of polarization transfer from spin I = 1/2 to spin S = 1 in static solids. As described, under on-resonance irradiation conditions (on both I and S spins), the CP dynamics during the spin-lock period is governed by contributions from the four Hartmann-Hahn CP matching conditions (namely, triple-quantum (TQ₁₆), single-quantum (SQ_{34}), zero-quantum (ZQ_{35}), and double-quantum (DQ_{26})). To present a comprehensive description of the CP dynamics, rotation operators derived from the concept of effective-fields were employed to derive effective CP Hamiltonians. contrast to the conventional operator-based perturbative methods, the effective-field approach facilitates the derivation of closed-form solutions requiring a minimal set of transformations. Employing the concept of effective-fields, the four possible matching conditions responsible for polarization transfer are identified and described within a single unified framework that is suitable for describing the exchange both in single-crystal and powder samples. In contrast to other existing theoretical frameworks, the present approach presents a unified description of the CP dynamics and facilitates in quantifying the polarization transfer in terms of the four matching conditions. Depending on the magnitude of the quadrupolar coupling constant and the orientation dependence of the quadrupolar interactions (say β_Q), the relative contributions emerging from the four matching conditions are quantified using simple analytic expressions. As illustrated, in the weak coupling regime, the SQ_{34} and DQ_{26} CP matching conditions overlap to result in a broad CP profile in the single-crystal sample. With increasing quadrupolar coupling strengths, these CP matching conditions separate resulting in lower transfer efficiency. Interestingly, in the case of a powder sample such a clear distinction between the contributions emerging from the four matching conditions is less plausible. In such cases, the proposed unified framework [Eq. (3.19)] is essential to quantify the CP Additionally, as demonstrated, the proposed analytic theory presents an attractive framework for extracting the dipolar parameters from the CP data in simple systems.

Chapter 4

Understanding the role of second-order quadrupolar coupling and off-resonance effects in CP dynamics

In the previous chapter of this thesis, the operator-based analytic theory of the CP dynamics between I = 1/2 and S = 1 is introduced through the application of the "effective-field method" considering the first-order quadrupolar coupling under the on-resonance RF irradiations [116]. As the quadrupolar coupling strength can be of the order of a few kHz to several MHz, it is essential to understand the role higher-order quadrupolar coupling [151] and the corresponding off-resonance effects [152, 153] in the CP dynamics. Although the higher-order quadrupolar coupling effects can be reduced with increasing static magnetic field strengths but only at the cost of increased size of the chemical shift anisotropy (CSA) and off-resonance effects. For half-integer quadrupolar nuclei, the presence of first-order quadrupolar coupling devoid single-quantum (SQ) central transition provides a relatively smaller spectral bandwidth for their efficient excitation with reduced off-resonance effects. Nonetheless, for integer nuclei wherein the central transition is absent, the off-resonance effects in the polarization transfer mechanism cannot be undermined even for spin systems with smaller quadrupolar coupling constants. To design an efficient CP pulse sequence for achieving a uniform excitation bandwidth, requires a careful manipulation of the pulse amplitude, phase, width and offset concerning all the possible transitions. In the case of broadband CP excitation, many variants of off-resonance irradiation schemes such as Lee-Goldberg CP (LGCP) [58] and broadband adiabatic inversion-CP (BRAIN-CP) [100, 154, 155] were introduced in the past for spin-1/2 as well as quadrupolar spins. However, a complete theoretical description of the CP transfer mechanism under S-spin off-resonance irradiation and higher-order quadrupolar coupling effects remain elusive [101,156]. During the polarization transfer, the hetero-nuclear dipolar coupling induces all the possible spin coherences in the S=1 spin system (i.e., two fundamental single-quantum (SQ) transitions $[(0 \leftrightarrow -1)]$ and $(1 \leftrightarrow 0)$] and one spin-forbidden double-quantum (DQ) transition $(1 \leftrightarrow -1)$). These transitions have different nutation behaviour under various pulse parameters and other internal spin-interactions [45, 90, 91, 111, 112], therefore, are expected to show

different CP transfer dynamics. Nevertheless, the excitation efficiency of a particular coherence depends on the strength of the effective dipolar coupling involved in a particular coherence transfer mode [116]. Previously, Vega et. al. [45] highlighted the effect of the S-spin off-resonant irradiation on the single-quantum CP while the double-quantum CP was described as an on-resonance phenomenon. In the case of a single-crystal sample involving quadrupolar spin, stronger off-resonant irradiation was shown to reduce the excitation efficiency of the DQ transitions, while an increase in the excitation efficiency was observed for the SQ transitions. Nevertheless, such a description may not be valid for the powder sample wherein different crystallite orientations have different excitation efficiencies due to variable quadrupolar frequency (magnitude and sign), and therefore, a complex polarization transfer mechanism is expected. To this end, it becomes essential to present a theoretical framework to understand the CP transfer mechanism valid both for single-crystal and powder samples across all the quadrupolar coupling regimes. In this chapter of the thesis, we attempt to derive an analytic signal expression to give a comprehensive description of the CP dynamics considering S-spin off-resonance irradiation and second-order quadrupolar coupling effects. In this study, we have evaluated individual contributions of various dipolar coupling-based polarization transfers in single-crystal and powder samples. We have correlated our operator-based analytic theory with the energy-level diagram and highlighted the role of population exchange at various Hartmann-Hahn matching conditions.

4.1 Theory

To gain insight into the mechanism of the CP dynamics under the S-spin off-resonance irradiation and the second-order quadrupolar coupling interactions, we begin with a simplified theoretical two-spin (say I=1/2 and S=1) model framework. In the doubly rotating frame, the CP Hamiltonian for such a system is described by the following equation:

$$\hat{H}_{CP} = \underbrace{\frac{\Omega_{S}\hat{S}_{z}}{\hat{H}_{S}^{off}} + \underbrace{\frac{\omega_{1S}\hat{S}_{x}}{\hat{H}_{S}^{RF}}}_{\hat{H}_{S}^{RF}} + \underbrace{\frac{\omega_{Q}^{(1)}(\alpha_{Q}, \beta_{Q})}{6}(3\hat{S}_{z}^{2} - \hat{S}^{2}) + \omega_{Q}^{(2)}(\alpha_{Q}, \beta_{Q})\hat{S}_{z}}_{\hat{H}_{S}^{Q} = \hat{H}_{Q}^{(1)} + \hat{H}_{Q}^{(2)}} + \underbrace{\frac{\omega_{1I}\hat{I}_{x}}{\hat{H}_{IS}^{RF}} + \underbrace{\frac{\omega_{d}\hat{I}_{z}\hat{S}_{z}}{\hat{H}_{IS}^{D}}}_{\hat{H}_{IS}}; \quad \hbar = 1.$$
(4.1)

In the above equation, Ω_S represents the strength of the off-resonance irradiation on S-spin, while on-resonance irradiation is considered on I-spin channel. $\omega_{1I}(\omega_{1S})$ represents the RF amplitude on I(S) spin. The term ω_d represents the dipolar coupling (I-S) frequency. H_S^Q represents quadrupolar Hamiltonian (including first and second-order quadrupolar effects) for the S-spin. The frequencies $\omega_Q^{(1)}(\alpha_Q,\beta_Q)$ and $\omega_Q^{(2)}(\alpha_Q,\beta_Q)$ denote the strength of first and second-order quadrupolar interactions, respectively. A detailed description of the first and second-order quadrupolar coupling Hamiltonians can be found in Chapter 1.

4.1.1 Derivation of the effective CP Hamiltonians via the effective-field method

The above Hamiltonian [Eq. (4.1)] is expressed in terms of single-transition operators (in coupled basis) as given below:

$$\hat{H}_{CP} = 2\Omega_S[\hat{S}_z^{13} + \hat{S}_z^{46}] + \sqrt{2}\omega_{1S}[\hat{S}_x^{12} + \hat{S}_x^{23} + \hat{S}_x^{45} + \hat{S}_x^{56}] + \frac{\omega_Q^{(1)}}{3}[\hat{S}_z^{12} - \hat{S}_z^{23} + \hat{S}_z^{45} - \hat{S}_z^{56}] + 2\omega_Q^{(2)}[\hat{S}_z^{13} + \hat{S}_z^{46}] + \omega_{1I}[\hat{S}_x^{14} + \hat{S}_x^{25} + \hat{S}_x^{36}] + 2\omega_d[\hat{S}_z^{13} - \hat{S}_z^{46}].$$

$$(4.2)$$

A detailed representation of the transition matrix connecting various Zeeman states and the energy-level representation can be found in Figure 3.1 of Chapter 3. The evaluation of Hartmann-Hahn (HH) cross-polarization matching conditions requires the diagonalization of both the S and I-spin Hamiltonians. To present a simplified description of the effective CP Hamiltonian derived using the "effective-field" approach, we split the above Hamiltonian [Eq. (4.2)] into three parts.

A: "Effective-field" for S = 1 spin system

Considering a similar spin-operator dependence of the S=1 off-resonance irradiation and second-order quadrupolar coupling Hamiltonians, we have combined these two interaction fields together in our subsequent calculations [115].

$$\hat{H}_S = 2(\Omega_S + \omega_Q^{(2)})[\hat{S}_z^{13} + \hat{S}_z^{46}] + \sqrt{2}\omega_{1S}[\hat{S}_x^{12} + \hat{S}_x^{23} + \hat{S}_x^{45} + \hat{S}_x^{56}] + \frac{\omega_Q^{(1)}}{3}[\hat{S}_z^{12} - \hat{S}_z^{23} + \hat{S}_z^{45} - \hat{S}_z^{56}]. \tag{4.3}$$
 Based on the magnitudes of various interactions, the unitary transformation $\hat{U}_1 = \exp\left\{-\frac{i\theta_1}{\sqrt{2}}\left[-\hat{S}_y^{12} + \hat{S}_y^{23} - \hat{S}_y^{45} + \hat{S}_y^{56}\right]\right\}$ [115,116] is used to calculate the effective field for RF and first-order quadrupolar interaction fields. Selecting angle θ_1 as $\left(\theta_1 = \tan^{-1}\frac{4\omega_{1S}}{\omega_Q^{(1)}}\right)$, the above Hamiltonian reduces to the following form.

$$\begin{split} \hat{H}_S &= \hat{U}_1 H_S \hat{U}_1^{\dagger} \\ &= 2(\Omega_S + \omega_Q^{(2)}) \cos \theta_1 / 2[\hat{S}_z^{13} + \hat{S}_z^{46}] - 2(\Omega_S + \omega_Q^{(2)}) \sin \theta_1 / 2[\hat{S}_x^{12} - \hat{S}_x^{23} + \hat{S}_x^{45} - \hat{S}_x^{56}] \\ &\quad + \Big(\frac{\omega_e^{(1)} - \omega_Q^{(1)}}{4}\Big) [\hat{S}_x^{13} + \hat{S}_x^{46}] + \Big(\frac{3\omega_e^{(1)} + \omega_Q^{(1)}}{12}\Big) [\hat{S}_z^{12} - \hat{S}_z^{23} + \hat{S}_z^{45} - \hat{S}_z^{56}] \\ \text{where, } \omega_e^{(1)} &= \sqrt{16\omega_{1S}^2 + (\omega_Q^{(1)})^2}. \end{split}$$

To further include the effect of off-resonance irradiation (second term), we employ the unitary transformations $\hat{U}_2 = \exp\left\{-i\theta_2\left[\hat{S}_y^{12} + \hat{S}_y^{23} + \hat{S}_y^{45} + \hat{S}_y^{56}\right]\right\}$ and choosing θ_2 as

$$\left(\sqrt{2}\theta_2 = \tan^{-1}\frac{8(\Omega_S + \omega_Q^{(2)})\sin\theta_1/2}{\omega_e^{(1)} + \omega_Q^{(1)}}\right), \text{ the Hamiltonian in Eq. (4.4) transformed as}$$

$$\hat{\hat{H}}_{S} = \hat{U}_{2}\hat{\hat{H}}_{S}\hat{U}_{2}^{\dagger}$$

$$= 2(\Omega_{S} + \omega_{Q}^{(2)})\cos\frac{\theta_{1}}{2}\cos\frac{\theta_{2}}{\sqrt{2}}[\hat{S}_{z}^{13} + \hat{S}_{z}^{46}] + \left(\frac{3\omega_{e}^{(1)} - \omega_{e}^{(2)} - \omega_{Q}^{(1)}}{8}\right)[\hat{S}_{x}^{13} + \hat{S}_{x}^{46}] + \left(\frac{3\omega_{e}^{(1)} + 3\omega_{e}^{(2)} - \omega_{Q}^{(1)}}{24}\right)[\hat{S}_{z}^{12} - \hat{S}_{z}^{23} + \hat{S}_{z}^{45} - \hat{S}_{z}^{56}]$$

$$+ \left(\frac{3\omega_{e}^{(1)} + 3\omega_{e}^{(2)} - \omega_{Q}^{(1)}}{24}\right)[\hat{S}_{z}^{12} - \hat{S}_{z}^{23} + \hat{S}_{z}^{45} - \hat{S}_{z}^{56}]$$

where, $\omega_e^{(2)} = \sqrt{\left\{8(\Omega_S + \omega_Q^{(2)})\sin\theta_1/2\right\}^2 + \left\{\omega_e^{(1)} + \omega_Q^{(1)}\right\}^2}$. Subsequently, the unitary transformation $\hat{U}_3\Big(=\exp\left\{-i\theta_3\big[\hat{S}_y^{13} + \hat{S}_y^{46}\big]\right\}\Big)$ is performed to achieve the S-spin effective Hamiltonian. The angle θ_3 is selected to keep the effective-field along the z-axis: $\tan\theta_3 = \frac{3\omega_e^{(1)} - \omega_e^{(2)} - \omega_Q^{(1)}}{16(\Omega_S + \omega_Q^{(2)})\cos\frac{\theta_1}{2}\cos\frac{\theta_2}{\sqrt{2}}}$. This transformation leads to the effective S-spin Hamiltonian, which is presented as follows:

$$\hat{H}_{S}^{eff} = \hat{U}_{3} \hat{\hat{H}}_{S} \hat{U}_{3}^{\dagger}$$

$$= \frac{\omega_{e}^{(3)}}{8} \left[\hat{S}_{z}^{13} + \hat{S}_{z}^{46} \right] + \left(\frac{3\omega_{e}^{(1)} + 3\omega_{e}^{(2)} - \omega_{Q}^{(1)}}{24} \right) \left[\hat{S}_{z}^{12} - \hat{S}_{z}^{23} + \hat{S}_{z}^{45} - \hat{S}_{z}^{56} \right]$$
where, $\omega_{e}^{(3)} = \sqrt{\left\{ 16(\Omega_{S} + \omega_{Q}^{(2)})\cos\frac{\theta_{1}}{2}\cos\frac{\theta_{2}}{\sqrt{2}} \right\}^{2} + \left\{ 3\omega_{e}^{(1)} - \omega_{e}^{(2)} - \omega_{Q}^{(1)} \right\}^{2}}.$
(4.6)

B: "Effective-field" for I = 1/2 spin system

As the *I*-spin Hamiltonian remains unaffected by the *S*-spin transformations $(\hat{U}_1\hat{U}_2\hat{U}_3)$ *i.e.* $\hat{\tilde{H}}_I^{RF} = \hat{H}_I^{RF}$. The unitary transformation $\hat{U}_4 = \exp\left\{i\frac{\pi}{2}\left[\hat{S}_y^{14} + \hat{S}_y^{25} + \hat{S}_y^{36}\right]\right\}$ is employed to diagonalized the *I*-spin Hamiltonian.

$$\tilde{\tilde{H}}_{I}^{RF} = \hat{U}_{4} \tilde{\tilde{H}}_{I}^{RF} \hat{U}_{4}^{\dagger}
= \omega_{1I} [\hat{S}_{z}^{14} + \hat{S}_{z}^{25} + \hat{S}_{z}^{36}].$$
(4.7)

C: Hetero-nuclear dipolar coupling Hamiltonian for IS-spin pair

Employing $\hat{U}_1\hat{U}_2\hat{U}_3\hat{U}_4$ unitary transformations, the heteronuclear dipolar coupling Hamiltonian in Eq. (4.2) has been transformed into the following form:

$$\overset{\tilde{\tilde{z}}}{\tilde{H}}_{IS}^{D} = \hat{U}_{4}\hat{U}_{3}\hat{U}_{2}\hat{U}_{1}\hat{H}_{IS}^{D}\hat{U}_{1}^{\dagger}\hat{U}_{2}^{\dagger}\hat{U}_{3}^{\dagger}\hat{U}_{4}^{\dagger} \\
= \underbrace{\omega_{d}^{A}\left[\hat{S}_{x}^{14} - \hat{S}_{x}^{36}\right] + \omega_{d}^{eff}\left[\hat{S}_{x}^{14} - 2\hat{S}_{x}^{25} + \hat{S}_{x}^{36}\right]}_{SQ_{I,d}} + \underbrace{2\omega_{d}^{B}\left[\hat{S}_{x}^{16} + \hat{S}_{x}^{34}\right]}_{TQ_{16}/SQ_{34}} - 2\underbrace{\left(\omega_{d}^{C} + \omega_{d}^{D}\right)\left[\hat{S}_{x}^{15} + \hat{S}_{x}^{24}\right]}_{DQ_{15}/ZQ_{24}} \\
+ \underbrace{\left(-\omega_{d}^{C} + \omega_{d}^{D}\right)\left[\hat{S}_{x}^{26} + \hat{S}_{x}^{35}\right]}_{DQ_{26}/ZQ_{35}} \tag{4.8}$$

where, $\omega_d^A = -\omega_d \left(\cos\frac{\theta_1}{2}\cos\frac{\theta_2}{\sqrt{2}}\cos\theta_3 + \frac{1}{2}\sin\frac{\theta_1}{2}\sin\sqrt{2}\theta_2\sin\theta_3\right),$ $\omega_d^B = \omega_d \left(\cos\frac{\theta_1}{2}\cos\frac{\theta_2}{\sqrt{2}}\sin\theta_3 - \frac{1}{2}\sin\frac{\theta_1}{2}\sin\sqrt{2}\theta_2\cos\theta_3\right),$ $\omega_d^C = \frac{\omega_d}{\sqrt{2}} \left(\cos\frac{\theta_1}{2}\sin\frac{\theta_2}{\sqrt{2}}\cos\frac{\theta_3}{2} - \sin\frac{\theta_1}{2}\cos\sqrt{2}\theta_2\sin\frac{\theta_3}{2}\right),$ $\omega_d^D = \frac{\omega_d}{\sqrt{2}} \left(\cos\frac{\theta_1}{2}\sin\frac{\theta_2}{\sqrt{2}}\sin\frac{\theta_3}{2} - \sin\frac{\theta_1}{2}\cos\sqrt{2}\theta_2\cos\frac{\theta_3}{2}\right),$ and $\omega_d^{eff} = -\frac{\omega_d}{2}\sin\frac{\theta_1}{2}\sin\sqrt{2}\theta_2.$

Unlike in on-resonance S-spin irradiation [116] (Chapter 3), the transformed dipolar coupling Hamiltonian [Eq. (4.8)] is comprised of four different sets of dipolar mediated transitions, therefore, CP transfer under the S-spin off-resonance irradiation is anticipated to display four modes/pathways of polarization transfer. The dipolar transitions are categorized according to the total change in the S and I-spin quantum numbers of the transitions involved i.e., $\{1,6\}/\{3,4\}$ labeled as TQ_{16}/SQ_{34} ; and both $\{1,5\}/\{2,4\}$ and $\{2,6\}/\{3,5\}$ are labeled as DQ_{ij}/ZQ_{ij} dipolar transitions. However, the dipolar transitions $\{1,4\}/\{2,5\}/\{3,6\}$ are purely induced by the *I*-spin flip, are referred to as single-quantum I-spin dipolar transition $(SQ_{I,d})$. The dipolar coupling terms involving the flipping of both S and I-spins are further quantified in terms of the S-spin involved dipolar transitions as follows: TQ_{16}/SQ_{34} involve double-quantum $(DQ_S): |1\rangle \leftrightarrow |-1\rangle$ S-spin transition; DQ_{15}/ZQ_{24} involve single-quantum $(SQ_S): |1\rangle \leftrightarrow |0\rangle$ S-spin transition; and DQ_{26}/ZQ_{35} involve SQ (SQ_S) : $|0\rangle \leftrightarrow |-1\rangle$ S-spin transition. All the dipolar coupling CP modes in Eq. (4.8) occur through single-quantum $(SQ_I): |1/2\rangle \leftrightarrow |-1/2\rangle$ I-spin flip. Having diagonalized the S and I-spin Hamiltonians and identifying the various dipolar transfer modes, we are well equipped to derive the spin dynamics for the cross-polarization process is presented in the section below. Combining the transformed Hamiltonians, \hat{H}_S , \hat{H}_I and \hat{H}_{IS}^{D} , the complete Hamiltonian describing the CP dynamics is represented by the following

equation:

$$\hat{\tilde{H}}_{CP} = \hat{U}_{4}\hat{U}_{3}\hat{U}_{2}\hat{U}_{1}\hat{H}\hat{U}_{1}^{\dagger}\hat{U}_{2}^{\dagger}\hat{U}_{3}^{\dagger}\hat{U}_{4}^{\dagger}$$

$$= \hat{\tilde{H}}_{S} + \hat{\tilde{H}}_{I} + \hat{\tilde{H}}_{IS}^{D}$$

$$= \frac{\omega_{e}^{(3)}}{8} [\hat{S}_{z}^{13} + \hat{S}_{z}^{46}] + (\frac{3\omega_{e}^{(1)} + 3\omega_{e}^{(2)} - \omega_{Q}^{(1)}}{24}) [\hat{S}_{z}^{12} - \hat{S}_{z}^{23} + \hat{S}_{z}^{45} - \hat{S}_{z}^{56}]$$

$$+ \omega_{1I} [\hat{S}_{z}^{14} + \hat{S}_{z}^{25} + \hat{S}_{z}^{36}] + \omega_{d}^{A} [\hat{S}_{x}^{14} - \hat{S}_{x}^{36}] + \omega_{d}^{eff} [\hat{S}_{x}^{14} - 2\hat{S}_{x}^{25} + \hat{S}_{x}^{36}]$$

$$+ 2\omega_{d}^{B} [\hat{S}_{x}^{16} + \hat{S}_{x}^{34}] - 2(\omega_{d}^{C} + \omega_{d}^{D}) [\hat{S}_{x}^{15} + \hat{S}_{x}^{24}] + (-\omega_{d}^{C} + \omega_{d}^{D}) [\hat{S}_{x}^{26} + \hat{S}_{x}^{35}].$$

$$+ 2\omega_{d}^{B} [\hat{S}_{x}^{16} + \hat{S}_{x}^{34}] - 2(\omega_{d}^{C} + \omega_{d}^{D}) [\hat{S}_{x}^{15} + \hat{S}_{x}^{24}] + (-\omega_{d}^{C} + \omega_{d}^{D}) [\hat{S}_{x}^{26} + \hat{S}_{x}^{35}].$$

$$+ 2\omega_{d}^{B} [\hat{S}_{x}^{16} + \hat{S}_{x}^{34}] - 2(\omega_{d}^{C} + \omega_{d}^{D}) [\hat{S}_{x}^{15} + \hat{S}_{x}^{24}] + (-\omega_{d}^{C} + \omega_{d}^{D}) [\hat{S}_{x}^{26} + \hat{S}_{x}^{35}].$$

$$+ 2\omega_{d}^{B} [\hat{S}_{x}^{16} + \hat{S}_{x}^{34}] - 2(\omega_{d}^{C} + \omega_{d}^{D}) [\hat{S}_{x}^{15} + \hat{S}_{x}^{24}] + (-\omega_{d}^{C} + \omega_{d}^{D}) [\hat{S}_{x}^{26} + \hat{S}_{x}^{35}].$$

Here, the first term in the dipolar coupling Hamiltonian i.e., $SQ_{I,d}$ involves solely I-spin dipolar transition, therefore, does not result in an independent CP transfer process like TQ_{ij}/SQ_{ij} and DQ_{ij}/ZQ_{ij} transitions but rather represents a pathway for the loss in magnetization of the I-spin. Therefore, it will prove beneficial to evaluate the effective-fields or nutation frequencies for individual I-spin transitions. This can be accomplished utilizing the unitary transformations $\hat{U}_5 = \hat{U}_5^{14}\hat{U}_5^{25}\hat{U}_5^{36} = \exp\left\{i\left(\frac{\pi}{2} - \theta_{14}^{(5)}\right)[\hat{S}_y^{14}]\right\} \exp\left\{i\left(\frac{\pi}{2} - \theta_{25}^{(5)}\right)[\hat{S}_y^{25}]\right\} \exp\left\{i\left(\frac{\pi}{2} - \theta_{36}^{(5)}\right)[\hat{S}_y^{36}]\right\}$. Subsequently, the aforementioned CP Hamiltonian undergoes a transformation:

$$\begin{split} \tilde{\hat{H}}_{CP} &= \hat{U}_5 \tilde{\hat{H}}_{CP} \hat{U}_5^{\dagger} \\ &= \frac{\omega_e^{(3)}}{8} \left[\hat{S}_z^{13} + \hat{S}_z^{46} \right] + \left(\frac{3\omega_e^{(1)} + 3\omega_e^{(2)} - \omega_Q^{(1)}}{24} \right) \left[\hat{S}_z^{12} - \hat{S}_z^{23} + \hat{S}_z^{45} - \hat{S}_z^{56} \right] + \omega_{1I}^{14} \left[\hat{S}_z^{14} \right] \\ &+ \omega_{1I}^{25} \left[\hat{S}_z^{25} \right] + \omega_{1I}^{36} \left[\hat{S}_z^{36} \right] + \underbrace{\omega_d^{16,34} \left[\hat{S}_x^{16} + \hat{S}_x^{34} \right]}_{TQ_{16}/SQ_{34}} + \underbrace{\omega_d^{15,24} \left[\hat{S}_x^{15} + \hat{S}_x^{24} \right]}_{DQ_{15}/ZQ_{24}} + \underbrace{\omega_d^{26,35} \left[\hat{S}_x^{26} + \hat{S}_x^{35} \right]}_{DQ_{26}/ZQ_{35}}. \end{split}$$

$$(4.10)$$
 where, $\omega_{1I}^{14} = \sqrt{(\omega_{1I})^2 + 4(\omega_d^A + \omega_d^E)^2}, \quad \omega_{1I}^{25} = \sqrt{(\omega_{1I})^2 + 16(\omega_d^E)^2} \text{ and } \omega_{1I}^{36} = \sqrt{(\omega_{1I})^2 + 4(\omega_d^A - \omega_d^E)^2}$ represent the effective I -spin nutation frequencies for $\{1,4\}/\{2,5\}/\{3,6\}$ transitions and $\omega_d^{16,34}, \omega_d^{15,24}$ and $\omega_d^{26,35}$ represent the effective dipolar coupling coefficients for various IS -dipolar transitions and their expressions are given in Table 4.1.

The single-spin terms in Hamiltonian in Eq. (4.10) are re-expressed in accordance with the operators associated with the dipolar coupling terms utilizing the relation $\hat{S}_z^{ij} + \hat{S}_z^{jk} = \hat{S}_z^{ik}$ between the single-transition operators.

$$\hat{\tilde{H}}_{CP} = \underbrace{\hat{H}_{16,34}}_{\hat{H}_{16} + \hat{H}_{34}} + \underbrace{\hat{H}_{15,24}}_{\hat{H}_{15} + \hat{H}_{24}} + \underbrace{\hat{H}_{26,35}}_{\hat{H}_{26} + \hat{H}_{35}}$$
(4.11)

Table 4.1: List of coefficients involved in the effective CP Hamiltonian [Eq. (4.10)] calculations

Longitudinal coefficients	Transverse (dipolar) coefficients	
$\Sigma_{16} = (4\omega_{1I}^{14} + 4\omega_{1I}^{36} + \omega_e^{(3)})/8$	$\omega_d^{16,34} = 2\omega_d^B \sin\left(\frac{\theta_{14} + \theta_{36}}{2}\right)$	
$\Delta_{34} = (4\omega_{1I}^{14} + 4\omega_{1I}^{36} - \omega_e^{(3)})/8$	$\omega_d = 2\omega_d \sin\left(\frac{1}{2}\right)$	
$\Sigma_{15} = (8\omega_{1I}^{14} + 8\omega_{1I}^{25} + \omega_e^{(3)} + 3\omega_e^{(1)} + 3\omega_e^{(2)} - \omega_Q^{(1)})/16$	$\omega_d^{15,24} = -2(\omega_d^C + \omega_d^D) \sin\left(\frac{\theta_{14} + \theta_{25}}{2}\right)$	
$\Delta_{24} = (8\omega_{1I}^{14} + 8\omega_{1I}^{25} - \omega_e^{(3)} - 3\omega_e^{(1)} - 3\omega_e^{(2)} + \omega_Q^{(1)})/16$	$\omega_d = -2(\omega_d^2 + \omega_d^2) \sin\left(\frac{1}{2}\right)$	
$\Sigma_{35} = (8\omega_{1I}^{25} + 8\omega_{1I}^{36} + \omega_e^{(3)} - 3\omega_e^{(1)} - 3\omega_e^{(2)} + \omega_Q^{(1)})/16$	$\omega_d^{26,35} = 2(-\omega_d^C + \omega_d^D) \sin\left(\frac{\theta_{26} + \theta_{35}}{2}\right)$	
$\Delta_{26} = (8\omega_{1I}^{14} + 8\omega_{1I}^{25} - \omega_e^{(3)} + 3\omega_e^{(1)} + 3\omega_e^{(2)} - \omega_Q^{(1)})/16$	$\omega_d = 2(-\omega_d + \omega_d)\sin(\frac{\omega_d}{2})$	

or

$$\underbrace{\hat{\tilde{H}}_{CP}}_{\hat{H}_{16}} = \underbrace{\Sigma_{16} \left[\hat{S}_{z}^{16} \right] + \omega_{d}^{16,34} \left[\hat{S}_{x}^{16} \right]}_{\hat{H}_{16}} + \underbrace{\Delta_{34} \left[\hat{S}_{z}^{34} \right] + \omega_{d}^{16,34} \left[\hat{S}_{x}^{34} \right]}_{\hat{H}_{34}} + \underbrace{\Sigma_{15} \left[\hat{S}_{z}^{15} \right] + \omega_{d}^{15,24} \left[\hat{S}_{x}^{15} \right]}_{\hat{H}_{15}} + \underbrace{\Delta_{24} \left[\hat{S}_{z}^{24} \right] + \omega_{d}^{15,24} \left[\hat{S}_{x}^{24} \right]}_{\hat{H}_{24}} + \underbrace{\Sigma_{35} \left[\hat{S}_{z}^{35} \right] + \omega_{d}^{26,35} \left[\hat{S}_{x}^{35} \right]}_{\hat{H}_{35}} + \underbrace{\Delta_{26} \left[\hat{S}_{z}^{26} \right] + \omega_{d}^{26,35} \left[\hat{S}_{x}^{26} \right]}_{\hat{H}_{26}} + \underbrace{\Delta_{26} \left[\hat{S}_{z}^{26} \right] + \omega_{d}^{26,35} \left[\hat{S}_{x}^{26} \right]}_{\hat{H}_{26}} + \underbrace{\Delta_{26} \left[\hat{S}_{z}^{26} \right] + \omega_{d}^{26,35} \left[\hat{S}_{x}^{26} \right]}_{\hat{H}_{26}} + \underbrace{\Delta_{26} \left[\hat{S}_{z}^{26} \right] + \omega_{d}^{26,35} \left[\hat{S}_{x}^{26} \right]}_{\hat{H}_{26}} + \underbrace{\Delta_{26} \left[\hat{S}_{z}^{26} \right] + \omega_{d}^{26,35} \left[\hat{S}_{x}^{26} \right]}_{\hat{H}_{26}} + \underbrace{\Delta_{26} \left[\hat{S}_{z}^{26} \right] + \omega_{d}^{26,35} \left[\hat{S}_{x}^{26} \right]}_{\hat{H}_{26}} + \underbrace{\Delta_{26} \left[\hat{S}_{z}^{26} \right] + \omega_{d}^{26,35} \left[\hat{S}_{x}^{26} \right]}_{\hat{H}_{26}} + \underbrace{\Delta_{26} \left[\hat{S}_{z}^{26} \right] + \omega_{d}^{26,35} \left[\hat{S}_{x}^{26} \right]}_{\hat{H}_{26}} + \underbrace{\Delta_{26} \left[\hat{S}_{z}^{26} \right] + \omega_{d}^{26,35} \left[\hat{S}_{x}^{26} \right]}_{\hat{H}_{26}} + \underbrace{\Delta_{26} \left[\hat{S}_{z}^{26} \right] + \omega_{d}^{26,35} \left[\hat{S}_{x}^{26} \right]}_{\hat{H}_{26}} + \underbrace{\Delta_{26} \left[\hat{S}_{z}^{26} \right] + \omega_{d}^{26,35} \left[\hat{S}_{x}^{26} \right]}_{\hat{H}_{26}} + \underbrace{\Delta_{26} \left[\hat{S}_{z}^{26} \right] + \omega_{d}^{26,35} \left[\hat{S}_{x}^{26} \right]}_{\hat{H}_{26}} + \underbrace{\Delta_{26} \left[\hat{S}_{z}^{26} \right] + \omega_{d}^{26,35} \left[\hat{S}_{x}^{26} \right]}_{\hat{H}_{26}} + \underbrace{\Delta_{26} \left[\hat{S}_{z}^{26} \right] + \omega_{d}^{26,35} \left[\hat{S}_{x}^{26} \right]}_{\hat{H}_{26}} + \underbrace{\Delta_{26} \left[\hat{S}_{z}^{26} \right] + \omega_{d}^{26,35} \left[\hat{S}_{x}^{26} \right]}_{\hat{H}_{26}} + \underbrace{\Delta_{26} \left[\hat{S}_{z}^{26} \right] + \omega_{d}^{26,35} \left[\hat{S}_{x}^{26} \right]}_{\hat{H}_{26}} + \underbrace{\Delta_{26} \left[\hat{S}_{z}^{26} \right] + \omega_{d}^{26,35} \left[\hat{S}_{x}^{26} \right]}_{\hat{H}_{26}} + \underbrace{\Delta_{26} \left[\hat{S}_{z}^{26} \right] + \omega_{d}^{26,35} \left[\hat{S}_{x}^{26} \right]}_{\hat{H}_{26}} + \underbrace{\Delta_{26} \left[\hat{S}_{z}^{26} \right] + \omega_{d}^{26,35} \left[\hat{S}_{x}^{26} \right]}_{\hat{H}_{26}} + \underbrace{\Delta_{26} \left[\hat{S}_{x}^{26} \right] + \omega_{d}^{26,35} \left[\hat{S}_{x}^{26} \right]}_{\hat{H}_{26}} + \underbrace{\Delta_{26} \left[\hat$$

In Eq. (4.12), the CP Hamiltonian is rearranged in accordance with the CP matching conditions requirement for these CP modes. The details of the coefficients can be found in Table 4.1. The last two terms are not responsible for any CP transfer and, therefore, can be ignored in the further calculation. As the different HH CP matching conditions have different energies requirements and act in different dipolar subspaces, therefore, the CP Hamiltonian [Eq. (4.12)] is considered independent in these subspaces which simplifies the diagonalization process. A pictorial representation of this division is shown in Figure 4.1. The above CP Hamiltonian [Eq. (4.12)] comprises longitudinal (\hat{S}_z^{ij}) and transverse (\hat{S}_x^{ij}) components in each subspace and, therefore, can be diagonalized through rotation operators $\hat{U}_6 = \hat{U}_6^{(16)} \hat{U}_6^{(34)} \hat{U}_6^{(15)} \hat{U}_6^{(24)} \hat{U}_6^{(35)} \hat{U}_6^{(26)}$ (refer to Table 4.2). The above-mentioned transformation results in the derivation of the effective CP Hamiltonian, which is presented as follows:

$$\begin{split} \hat{H}_{CP}^{eff} &= \hat{H}_{16}^{eff} + \hat{H}_{34}^{eff} + \hat{H}_{15}^{eff} + \hat{H}_{24}^{eff} + \hat{H}_{35}^{eff} + \hat{H}_{26}^{eff} \\ &= \omega_{eff}^{(16)} \big[\hat{S}_z^{16} \big] + \omega_{eff}^{(34)} \big[\hat{S}_z^{34} \big] + \omega_{eff}^{(15)} \big[\hat{S}_z^{15} \big] + \omega_{eff}^{(24)} \big[\hat{S}_z^{24} \big] + \omega_{eff}^{(35)} \big[\hat{S}_z^{35} \big] + \omega_{eff}^{(26)} \big[\hat{S}_z^{26} \big] \end{split}$$

$$(4.13)$$

where the effective-fields/frequencies ($\omega_{eff}^{(ij)}$) in each subspace can be found in Table 4.2. A pictorial representation of this diagonalization process is shown in Figure 4.2. In comparison with effective CP Hamiltonian [Eq. (3.12)] presented in previous chapter

Table 4.2: List of all the unitary operators involved in diagonalization of the CP Hamiltonian [Eq. (4.12)] and associated coefficients.

Unitary transformations and rotation angles	Effective frequencies
$\hat{U}_{6}^{16} = \exp\left\{i\left(\frac{\pi}{2} - \theta_{4}^{16}\right)\left[\hat{S}_{y}^{16}\right]\right\}; \tan\theta_{4}^{16} = \frac{\Sigma_{16}}{\omega_{d}^{16,34}}$	$\omega_{eff}^{(16)} = \sqrt{\Sigma_{16}^2 + (\omega_d^{16,34})^2}$
$\hat{U}_{6}^{34} = \exp\left\{i\left(\frac{\pi}{2} - \theta_{4}^{34}\right)\left[\hat{S}_{y}^{34}\right]\right\}; \tan\theta_{4}^{34} = \frac{\Delta_{34}}{\omega_{d}^{16,34}}$	$\omega_{eff}^{(34)} = \sqrt{\Delta_{34}^2 + (\omega_d^{16,34})^2}$
$\hat{U}_{6}^{15} = \exp\left\{i\left(\frac{\pi}{2} - \theta_{4}^{15}\right)\left[\hat{S}_{y}^{15}\right]\right\}; \tan\theta_{4}^{15} = \frac{\Sigma_{15}}{\omega_{d}^{15,24}}$	$\omega_{eff}^{(15)} = \sqrt{\Sigma_{15}^2 + (\omega_d^{15,24})^2}$
$\hat{U}_{6}^{24} = \exp\left\{i\left(\frac{\pi}{2} - \theta_{4}^{24}\right)\left[\hat{S}_{y}^{24}\right]\right\}; \tan\theta_{4}^{24} = \frac{\Delta_{24}}{\omega_{d}^{15,24}}$	$\omega_{eff}^{(24)} = \sqrt{\Delta_{24}^2 + (\omega_d^{15,24})^2}$
$\hat{U}_{6}^{35} = \exp\left\{i\left(\frac{\pi}{2} - \theta_{4}^{35}\right)\left[\hat{S}_{y}^{35}\right]\right\}; \tan\theta_{4}^{35} = \frac{\Sigma_{35}}{\omega_{d}^{26,35}}$	$\omega_{eff}^{(35)} = \sqrt{\Sigma_{35}^2 + (\omega_d^{26,35})^2}$
$\hat{U}_{6}^{26} = \exp\left\{i\left(\frac{\pi}{2} - \theta_{4}^{26}\right)\left[\hat{S}_{y}^{26}\right]\right\}; \tan\theta_{4}^{26} = \frac{\Delta_{26}}{\omega_{d}^{26,35}}$	$\omega_{eff}^{(26)} = \sqrt{\Delta_{26}^2 + (\omega_d^{26,35})^2}$

under on-resonance irradiation where CP transfer is described by a sum of four modes of

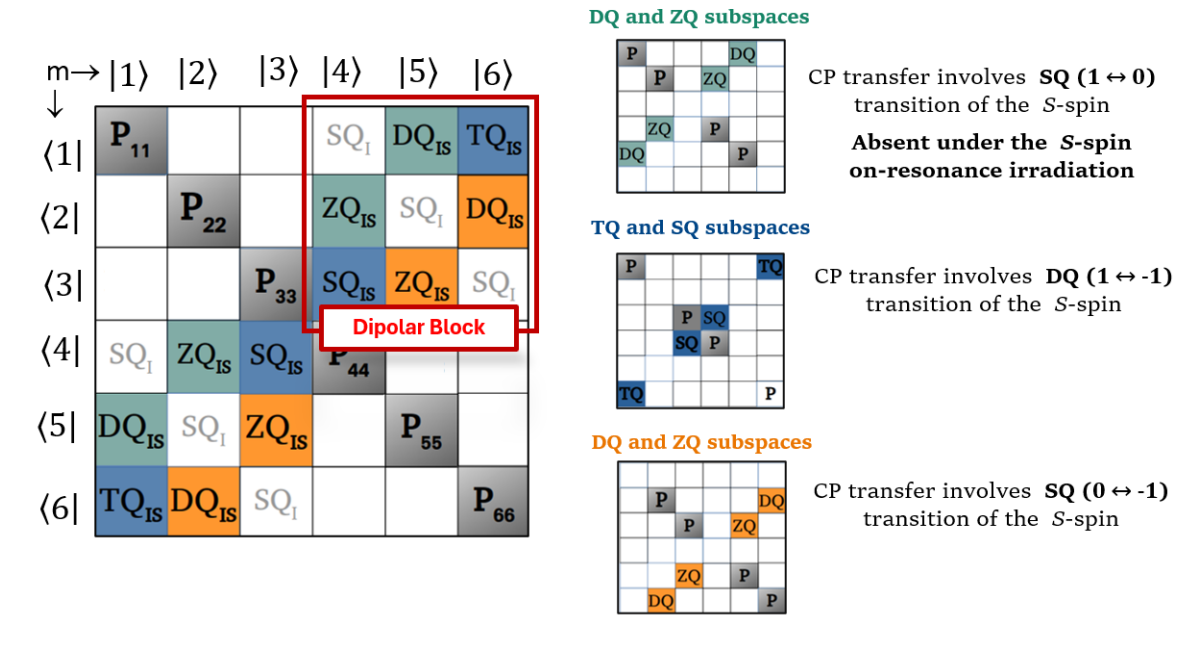


Figure 4.1: Pictorial representation of splitting of the CP Hamiltonian into six subspaces which are governed by the three S-spin transitions i.e. two subspaces shown in orange and green-colors (DQ_{IS}/ZQ_{IS}) corresponds to two S-spin single-quantum (SQ_S) transitions ((-1 \leftrightarrow 0) and (0 \leftrightarrow +1) respectively) while two subspaces shown in blue-color (TQ_{IS}/SQ_{IS}) correspond to S-spin double-quantum (DQ_S) transition (+1 \leftrightarrow -1). Although these subspaces are not independent, they can be considered as such because each HH-matching condition can effectively transfers polarization through a specific CP mode only.

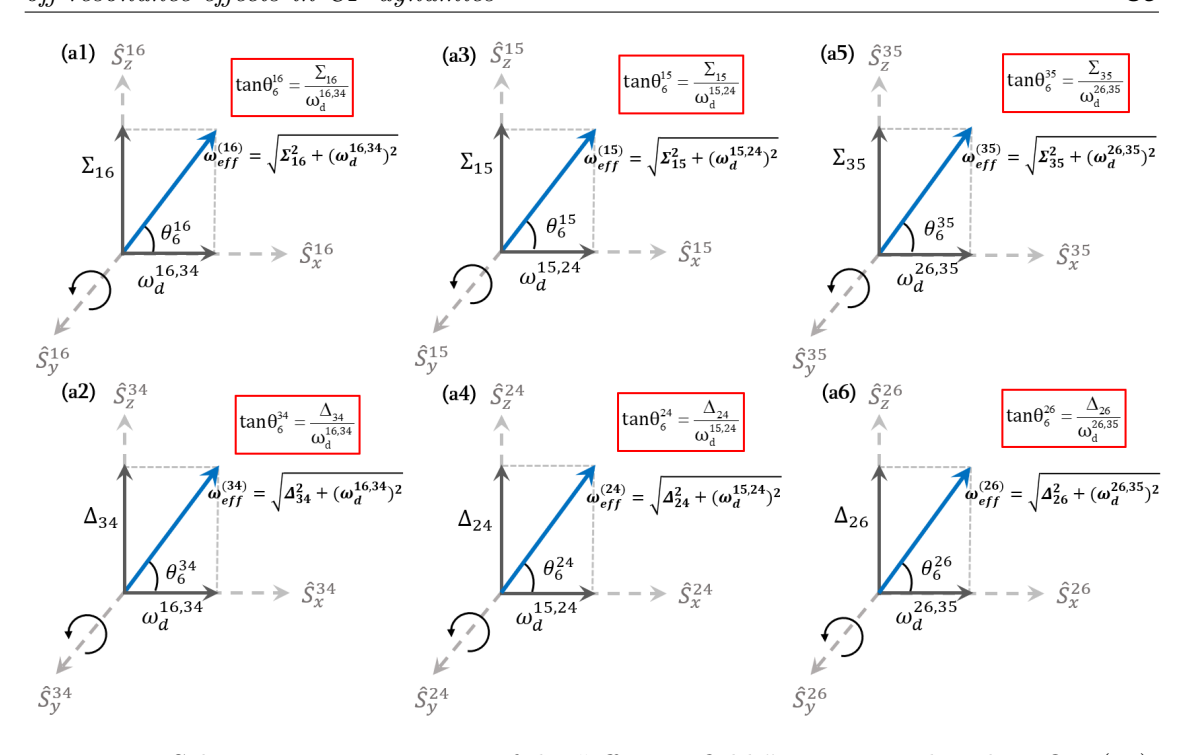


Figure 4.2: Schematic representation of the "effective-fields" experienced in the TQ_{16} (a1), SQ_{34} (a2), DQ_{15} (a3), ZQ_{24} (a4), ZQ_{35} (a5) and DQ_{26} (a6) sub-spaces.

the polarization transfer, the effective Hamiltonian in Eq. (4.13) contains all six modes of the polarization transfer. This is in stark contrast to the theoretical description presented by Vega *et. al.* [45] which lacks unified single framework for the effective CP Hamiltonian.

4.1.2 Time-evolution of the spin-system

As described in Chapter 1, the time-evolution of the spin system is evaluated by the following expression.

$$\hat{\rho}_{eff}(t) = \exp\left\{-\frac{i}{\hbar}\hat{H}_{CP}^{eff}t\right\}\hat{\rho}_{eff}(0)\exp\left\{\frac{i}{\hbar}\hat{H}_{CP}^{eff}t\right\}$$
(4.14)

where, $\hat{\rho}(0) = \hat{I}_x$ represents the initial density operator. Employing the unitary transformations involved in the calculation of the S and I-spin Hamiltonians $i.e.\ \hat{U}_1\hat{U}_2\hat{U}_3\hat{U}_4\hat{U}_5$, the initial density matrix is transformed as

$$\hat{\hat{\hat{\rho}}}(0) = \hat{U}_5 \hat{U}_4 \hat{U}_3 \hat{U}_2 \hat{U}_1 \hat{\rho}(0) \hat{U}_1^{\dagger} \hat{U}_2^{\dagger} \hat{U}_3^{\dagger} \hat{U}_4^{\dagger} \hat{U}_5^{\dagger}
= \left[\hat{S}_z^{14} \right] \sin \theta_{14} - \left[\hat{S}_x^{14} \right] \cos \theta_{14} + \left[\hat{S}_z^{25} \right] \sin \theta_{25} - \left[\hat{S}_x^{25} \right] \cos \theta_{25} + \left[\hat{S}_z^{36} \right] \sin \theta_{36} - \left[\hat{S}_x^{36} \right] \cos \theta_{36}.$$
(4.15)

In the following section, we describe the time-evolution of spin system in individual subspaces.

A: Time-evolution density matrix in $TQ_{16}+SQ_{34}$ subspace

Using Eq. (4.14), the time-evolution of spin-system under effective Hamiltonians \hat{H}_{16}^{eff} + \hat{H}_{34}^{eff} is given as

$$\begin{split} \hat{\rho}_{16,34}^{eff}(t) &= \exp\left\{-\frac{i}{\hbar}(\hat{H}_{16}^{eff} + \hat{H}_{34}^{eff})t\right\} \underbrace{\hat{U}_{6}^{16}\hat{U}_{6}^{34}}^{\tilde{z}} \underbrace{\hat{\tilde{\rho}}(0)\hat{U}_{6}^{34,\dagger}\hat{U}_{6}^{16,\dagger}}_{\text{cos}} \exp\left\{\frac{i}{\hbar}(\hat{H}_{16}^{eff} + \hat{H}_{34}^{eff})t\right\} \\ &= \frac{1}{2}(\sin\theta_{14} + \sin\theta_{36}) \left\{ \left[\hat{S}_{z}^{16}\right] \sin\theta_{16} - \cos\theta_{16} \left(\left[\hat{S}_{x}^{16}\right] \cos\omega_{eff}^{16}t + \left[\hat{S}_{y}^{16}\right] \sin\omega_{eff}^{16}t \right) \right\} \\ &+ \frac{1}{2}(\sin\theta_{14} + \sin\theta_{36}) \left\{ \left[\hat{S}_{z}^{34}\right] \sin\theta_{34} - \cos\theta_{34} \left(\left[\hat{S}_{x}^{34}\right] \cos\omega_{eff}^{34}t + \left[\hat{S}_{y}^{34}\right] \sin\omega_{eff}^{34}t \right) \right\} \\ &- \frac{1}{2}\rho_{14}^{16,34} \left\{ \left[\hat{S}_{x}^{14}\right] \cos\left(\frac{\omega_{eff}^{16} + \omega_{eff}^{34}}{2}t\right) + \left[\hat{S}_{y}^{14}\right] \sin\left(\frac{\omega_{eff}^{16} + \omega_{eff}^{34}}{2}t\right) \right\} \\ &- \frac{1}{2}\rho_{13}^{16,34} \left\{ \left[\hat{S}_{x}^{13}\right] \cos\left(\frac{\omega_{eff}^{16} - \omega_{eff}^{34}}{2}t\right) - \left[\hat{S}_{y}^{13}\right] \sin\left(\frac{\omega_{eff}^{16} - \omega_{eff}^{34}}{2}t\right) \right\} \\ &+ \frac{1}{2}\rho_{46}^{16,34} \left\{ \left[\hat{S}_{x}^{36}\right] \cos\left(\frac{\omega_{eff}^{16} - \omega_{eff}^{34}}{2}t\right) - \left[\hat{S}_{y}^{46}\right] \sin\left(\frac{\omega_{eff}^{16} - \omega_{eff}^{34}}{2}t\right) \right\} \\ &+ \frac{1}{2}\rho_{36}^{16,34} \left\{ \left[\hat{S}_{x}^{36}\right] \cos\left(\frac{\omega_{eff}^{16} + \omega_{eff}^{34}}{2}t\right) + \left[\hat{S}_{y}^{36}\right] \sin\left(\frac{\omega_{eff}^{16} + \omega_{eff}^{34}}{2}t\right) \right\} \\ &+ \left\{ \left[\hat{S}_{z}^{25}\right] \sin\theta_{25} - \cos\theta_{25} \left[\hat{S}_{x}^{25}\right] \right\} + \frac{1}{2}(\sin\theta_{14} - \sin\theta_{36}) \left[\hat{S}_{z}^{14} - \hat{S}_{z}^{36}\right]. \end{split}$$

The coefficients $\rho_{14}^{16,34}$, $\rho_{13}^{16,34}$, $\rho_{46}^{16,34}$ and $\rho_{36}^{16,34}$ of the density matrix $\hat{\rho}_{16,34}^{eff}(t)$ can be found in the Table D.1 in Appendix-D.

B: Time-evolution density matrix in $DQ_{15}+ZQ_{24}$ subspace

The time-evolution of spin-system under the effective Hamiltonians $\hat{H}_{15}^{eff} + \hat{H}_{24}^{eff}$ is given as

$$\begin{split} \hat{\rho}_{15,24}^{eff}(t) &= \exp\Big\{-\frac{i}{\hbar}(\hat{H}_{15}^{eff} + \hat{H}_{24}^{eff})t\Big\}\underbrace{\hat{\underline{U}}_{6}^{15}\hat{\underline{U}}_{6}^{24}\overset{\tilde{z}}{\hat{\rho}}(0)\hat{\underline{U}}_{6}^{24,\dagger}\hat{\underline{U}}_{6}^{15,\dagger}}_{\text{cos}} \exp\Big\{\frac{i}{\hbar}(\hat{H}_{15}^{eff} + \hat{H}_{24}^{eff})t\Big\} \\ &= \frac{1}{2}(\sin\theta_{14} + \sin\theta_{25})\Big\{\big[\hat{S}_{z}^{15}\big]\sin\theta_{15} - \cos\theta_{15}\Big(\big[\hat{S}_{x}^{15}\big]\cos\omega_{eff}^{15}t + \big[\hat{S}_{y}^{15}\big]\sin\omega_{eff}^{15}t\Big)\Big\} \\ &+ \frac{1}{2}(\sin\theta_{14} + \sin\theta_{25})\Big\{\big[\hat{S}_{z}^{24}\big]\sin\theta_{24} - \cos\theta_{24}\Big(\big[\hat{S}_{x}^{24}\big]\cos\omega_{eff}^{24}t + \big[\hat{S}_{y}^{24}\big]\sin\omega_{eff}^{24}t\Big)\Big\} \\ &+ \frac{1}{2}\rho_{14}^{15,24}\Big\{\big[\hat{S}_{x}^{14}\big]\cos\Big(\frac{\omega_{eff}^{15} + \omega_{eff}^{24}}{2}t\Big) + \big[\hat{S}_{y}^{14}\big]\sin\Big(\frac{\omega_{eff}^{15} + \omega_{eff}^{24}}{2}t\Big)\Big\} \\ &+ \frac{1}{2}\rho_{12}^{15,24}\Big\{\big[\hat{S}_{x}^{12}\big]\cos\Big(\frac{\omega_{eff}^{15} - \omega_{eff}^{24}}{2}t\Big) + \big[\hat{S}_{y}^{12}\big]\sin\Big(\frac{\omega_{eff}^{15} - \omega_{eff}^{24}}{2}t\Big)\Big\} \\ &+ \frac{1}{2}\rho_{45}^{15,24}\Big\{\big[\hat{S}_{x}^{45}\big]\cos\Big(\frac{\omega_{eff}^{15} - \omega_{eff}^{24}}{2}t\Big) + \big[\hat{S}_{y}^{45}\big]\sin\Big(\frac{\omega_{eff}^{15} - \omega_{eff}^{24}}{2}t\Big)\Big\} \\ &+ \frac{1}{2}\rho_{25}^{15,24}\Big\{\big[\hat{S}_{x}^{45}\big]\cos\Big(\frac{\omega_{eff}^{15} - \omega_{eff}^{24}}{2}t\Big) + \big[\hat{S}_{y}^{25}\big]\sin\Big(\frac{\omega_{eff}^{15} - \omega_{eff}^{24}}{2}t\Big)\Big\} \\ &+ \Big\{\big[\hat{S}_{z}^{36}\big]\sin\theta_{36} - \cos\theta_{36}\big[\hat{S}_{x}^{36}\big]\Big\} + \frac{1}{2}(\sin\theta_{14} - \sin\theta_{25})\big[\hat{S}_{z}^{14} - \hat{S}_{z}^{25}\big]. \end{split} \tag{4.17}$$

The coefficients $\rho_{14}^{15,24}$, $\rho_{12}^{15,24}$, $\rho_{45}^{15,24}$ and $\rho_{25}^{15,24}$ of the density matrix $\hat{\rho}_{15,24}^{eff}(t)$ can be found in the Table D.1 in Appendix-D.

C: Time-evolution density matrix in $DQ_{26}+ZQ_{35}$ subspace

The time-evolution of spin-system under effective Hamiltonians $\hat{H}_{26}^{eff} + \hat{H}_{35}^{eff}$ is given as

$$\begin{split} \hat{\rho}_{26,35}^{eff}(t) &= \exp\left\{-\frac{i}{\hbar}(\hat{H}_{26}^{eff} + \hat{H}_{35}^{eff})t\right\} \underbrace{\hat{U}_{26}^{26}\hat{U}_{6}^{35}}_{\hat{\rho}_{26,35}(0)}^{\tilde{z}_{6}^{26}} \underbrace{\exp\left\{\frac{i}{\hbar}(\hat{H}_{26}^{eff} + \hat{H}_{35}^{eff})t\right\}}_{\hat{\rho}_{26,35}(0)} \\ &= \frac{1}{2}(\sin\theta_{25} + \sin\theta_{36})\left\{\left[\hat{S}_{z}^{26}\right]\sin\theta_{26} - \cos\theta_{26}\left(\left[\hat{S}_{x}^{26}\right]\cos\omega_{eff}^{26}t + \left[\hat{S}_{y}^{26}\right]\sin\omega_{eff}^{26}t\right)\right\} \\ &+ \frac{1}{2}(\sin\theta_{25} + \sin\theta_{36})\left\{\left[\hat{S}_{z}^{35}\right]\sin\theta_{35} - \cos\theta_{36}\left(\left[\hat{S}_{x}^{35}\right]\cos\omega_{eff}^{35}t + \left[\hat{S}_{y}^{35}\right]\sin\omega_{eff}^{35}t\right)\right\} \\ &+ \frac{1}{2}\rho_{25}^{26,35}\left\{\left[\hat{S}_{x}^{25}\right]\cos\left(\frac{\omega_{eff}^{26} + \omega_{eff}^{35}}{2}t\right) + \left[\hat{S}_{y}^{25}\right]\sin\left(\frac{\omega_{eff}^{26} + \omega_{eff}^{35}}{2}t\right)\right\} \\ &+ \frac{1}{2}\rho_{23}^{26,35}\left\{\left[\hat{S}_{x}^{23}\right]\cos\left(\frac{\omega_{eff}^{35} - \omega_{eff}^{26}}{2}t\right) + \left[\hat{S}_{y}^{23}\right]\sin\left(\frac{\omega_{eff}^{35} - \omega_{eff}^{26}}{2}t\right)\right\} \\ &+ \frac{1}{2}\rho_{56}^{26,35}\left\{\left[\hat{S}_{x}^{36}\right]\cos\left(\frac{\omega_{eff}^{35} - \omega_{eff}^{26}}{2}t\right) + \left[\hat{S}_{y}^{36}\right]\sin\left(\frac{\omega_{eff}^{35} - \omega_{eff}^{26}}{2}t\right)\right\} \\ &+ \frac{1}{2}\rho_{36}^{26,35}\left\{\left[\hat{S}_{x}^{36}\right]\cos\left(\frac{\omega_{eff}^{26} + \omega_{eff}^{35}}{2}t\right) + \left[\hat{S}_{y}^{36}\right]\sin\left(\frac{\omega_{eff}^{25} - \omega_{eff}^{26}}{2}t\right)\right\} \\ &+ \left\{\left[\hat{S}_{z}^{14}\right]\sin\theta_{14} - \cos\theta_{14}\left[\hat{S}_{x}^{14}\right]\right\} + \frac{1}{2}(\sin\theta_{25} - \sin\theta_{36})\left[\hat{S}_{z}^{25} - \hat{S}_{z}^{36}\right]. \end{split}$$

$$(4.18)$$

The coefficients $\rho_{25}^{26,35}$, $\rho_{23}^{26,35}$, $\rho_{56}^{26,35}$ and $\rho_{36}^{26,35}$ of the density matrix $\hat{\rho}_{26,35}^{eff}(t)$ can be found in Table D.1 in Appendix-D.

4.1.3 Detection of the S-spin polarization: CP Signal calculation

Following the standard operational process, the expectation value of the observable $\langle \hat{S}_x(t) \rangle$ is derived employing Eqs. (4.16), (4.17) and (4.18) as follows

$$S(t) = \langle \hat{S}_x(t) \rangle = Trace\{\hat{S}_{eff,x}.\hat{\rho}_{eff}(t)\}$$

$$(4.19)$$

where, $\hat{S}_{eff,x}$ and $\hat{\rho}_{eff}(t)$ represent the detection operator and final density matrix in the same frame of reference as the effective CP Hamiltonians [Eq. (4.13)]. The final signal expressions in the TQ₁₆+SQ₃₄, DQ₁₅+ZQ₂₄ and DQ₂₆+ZQ₃₅ sub-spaces are as given below:

$$S(t) = S(t)_{16.34} + S(t)_{15.24} + S(t)_{26.35}$$

$$(4.20)$$

where,

$$S(t)_{16,34} = (\sin \theta_{14} + \sin \theta_{36}) \left[\left\{ -A_4 \underbrace{\cos^2 \theta_{16}}_{absorptive} + A_3 \sin \left(\frac{\theta_{36} - \theta_{14}}{2} \right) \underbrace{\cos \theta_{16} \sin \theta_{16}}_{dispersive} \right\} \sin^2 \frac{\omega_{eff}^{16}}{2} t$$

$$- \left\{ -A_4 \underbrace{\cos^2 \theta_{34}}_{absorptive} + A_3 \sin \left(\frac{\theta_{36} - \theta_{14}}{2} \right) \underbrace{\cos \theta_{34} \sin \theta_{34}}_{dispersive} \right\} \sin^2 \frac{\omega_{eff}^{34}}{2} t \right]$$

$$+ 2A_3 \cos \left(\frac{\theta_{36} - \theta_{14}}{2} \right) \left[(\rho_{13}^{16,34} + \rho_{46}^{16,34}) \underbrace{\cos \left(\frac{\theta_{34} - \theta_{16}}{2} \right)}_{interference} \cos \left(\frac{\omega_{eff}^{16} - \omega_{eff}^{34}}{2} t \right) \right]$$

$$+ (\rho_{14}^{16,34} - \rho_{36}^{16,34}) \underbrace{\sin \left(\frac{\theta_{34} - \theta_{16}}{2} \right)}_{interference} \cos \left(\frac{\omega_{eff}^{16} + \omega_{eff}^{34}}{2} t \right) \right], \tag{4.21}$$

$$S(t)_{15,24} = (\sin \theta_{14} + \sin \theta_{25}) \left[\left\{ -A_6 \cos^2 \theta_{15} + A_7 \cos \theta_{15} \sin \theta_{15} \right\} \sin^2 \frac{\omega_{eff}^{10}}{2} t \right.$$

$$\left. - \left\{ -A_6 \cos^2 \theta_{24} + A_7 \cos \theta_{24} \sin \theta_{24} \right\} \sin^2 \frac{\omega_{eff}^{24}}{2} t \right]$$

$$\left. + 2(A_1 + A_2) \cos \left(\frac{\theta_{25} - \theta_{14}}{2} \right) \left[(\rho_{12}^{15,24} + \rho_{45}^{15,24}) \cos \left(\frac{\theta_{24} - \theta_{15}}{2} \right) \cos \left(\frac{\omega_{eff}^{15} - \omega_{eff}^{24}}{2} t \right) \right.$$

$$\left. + (\rho_{14}^{15,24} - \rho_{25}^{15,24}) \sin \left(\frac{\theta_{24} - \theta_{15}}{2} \right) \cos \left(\frac{\omega_{eff}^{15} + \omega_{eff}^{24}}{2} t \right) \right],$$

$$(4.22)$$

and

given as

$$S(t)_{26,35} = (\sin \theta_{25} + \sin \theta_{36}) \left[\left\{ A_8 \cos^2 \theta_{26} - A_9 \cos \theta_{26} \sin \theta_{26} \right\} \sin^2 \frac{\omega_{eff}^{26}}{2} t - \left\{ A_8 \cos^2 \theta_{35} - A_9 \cos \theta_{35} \sin \theta_{35} \right\} \sin^2 \frac{\omega_{eff}^{35}}{2} t \right] - 2(A_1 - A_2) \cos \left(\frac{\theta_{25} - \theta_{14}}{2} \right) \left[(\rho_{25}^{26,35} - \rho_{36}^{26,35}) \sin \left(\frac{\theta_{35} + \theta_{26}}{2} \right) \cos \left(\frac{\omega_{eff}^{26} + \omega_{eff}^{35}}{2} t \right) - (\rho_{23}^{26,35} + \rho_{56}^{26,35}) \cos \left(\frac{\theta_{35} - \theta_{26}}{2} \right) \cos \left(\frac{\omega_{eff}^{35} - \omega_{eff}^{26}}{2} t \right) \right] - (\rho_{23}^{26,35} + \rho_{56}^{26,35}) \cos \left(\frac{\theta_{35} - \theta_{26}}{2} \right) \cos \left(\frac{\omega_{eff}^{35} - \omega_{eff}^{26}}{2} t \right) \right]$$

$$(4.23)$$
Here, $A_6 = \left(\frac{A_4 + 3A_5}{2} \right)$, $A_7 = (A_1 + A_2) \sin \left(\frac{\theta_{25} - \theta_{14}}{2} \right)$, $A_8 = \left(\frac{A_4 - 3A_5}{2} \right)$ and $A_9 = (A_1 - A_2) \sin \left(\frac{\theta_{25} - \theta_{36}}{2} \right)$.

The constants
$$A_1$$
, A_2 , A_3 , A_4 and A_5 are given as
$$A_1 = \frac{1}{\sqrt{2}} \left(\cos \theta_1 \cos \frac{\theta_2}{\sqrt{2}} \cos \frac{\theta_3}{2} + \frac{1}{2} \sin \theta_1 \sin \sqrt{2}\theta_2 \sin \frac{\theta_3}{2} \right),$$

$$A_2 = \frac{1}{\sqrt{2}} \left(\cos \theta_1 \cos \frac{\theta_2}{\sqrt{2}} \sin \frac{\theta_3}{2} - \frac{1}{2} \sin \theta_1 \sin \sqrt{2}\theta_2 \cos \frac{\theta_3}{2} \right),$$

$$A_3 = \left(-\cos \theta_1 \sin \frac{\theta_2}{\sqrt{2}} \sin \theta_3 + \frac{1}{4} \sin \theta_1 (3 - \cos \sqrt{2}\theta_2) \cos \theta_3 \right),$$

$$A_4 = \left(\cos \theta_1 \sin \frac{\theta_2}{\sqrt{2}} \cos \theta_3 + \frac{1}{4} \sin \theta_1 (3 - \cos \sqrt{2}\theta_2) \sin \theta_3 \right),$$
and
$$A_5 = \frac{1}{4} \sin \theta_1 (1 + \cos \sqrt{2}\theta_2).$$

As described above, the final signal expression has contribution of all the six possible CP transfer modes. Unlike the on-resonance S-spin irradiation [Eq. (3.19)], the CP signal expression in each subspace consists of sum of three different components: Absorptive $(\cos^2 \theta_{ij})$, dispersive $(\cos \theta_{ij} \sin \theta_{ij})$, and interference term $\left(\cos \frac{\theta_{ij} \pm \theta_{kl}}{2}\right)$.

4.1.4 Insights into the Hartmann-Hahn CP matching conditions

Using Eq. (4.20), the polarization transfer through a specific mode can be maximized by optimizing one to the six HH CP matching conditions as discussed below.

• Triple-quantum (TQ₁₆) CP matching condition: Setting $\Sigma_{16} = 0 \implies 4\omega_{1I}^{14} + 4\omega_{1I}^{36} = -\omega_e^{(3)}$. Under the exact TQ₁₆ CP matching condition, the resulting signal expression is

$$S(t) = (\sin \theta_{14} + \sin \theta_{36}) \left[-A_4 \cos^2 \theta_{16} + A_3 \sin \left(\frac{\theta_{36} - \theta_{14}}{2} \right) \cos \theta_{16} \sin \theta_{16} \right] \sin^2 \frac{\omega_d^{16,34} t}{2} + \underbrace{S(t)_{34} + S(t)_{15,24} + S(t)_{26,35}}_{\text{High-frequency components}}.$$

$$(4.24)$$

Exactly setting the TQ₁₆ HH CP condition will not only maximize the polarization

transfer through TQ_{16} CP mode (i.e. $S(t)_{16}$ component) but also increases the modulation frequencies of other signal components, therefore, further rendering them insignificant in the overall CP transfer. When the high-frequency terms are insignificant, the overall CP signal is reduce to a simplified form as given below:

$$S(t) \approx (\sin \theta_{14} + \sin \theta_{36}) \left[-A_4 \cos^2 \theta_{16} + A_3 \sin \left(\frac{\theta_{36} - \theta_{14}}{2} \right) \cos \theta_{16} \sin \theta_{16} \right] \sin^2 \frac{\omega_d^{16,34} t}{2}.$$

$$(4.25)$$

An important thing to note is that the effective nutation frequencies of the I-spin $(\omega_{1I}^{14},\,\omega_{1I}^{25})$ and (ω_{1I}^{36}) see Eq. 4.10) have an explicit dipolar dependence. Therefore, the position of the HH CP matching conditions will be associated with dipolar dependent shifts. A similar behaviour is observed under off-resonance irradiations in spin-1/2 CP in Chapter 2.

• Single-quantum (SQ₃₄) CP matching condition:

Setting $\Delta_{34} = 0 \implies 4\omega_{1J}^{14} + 4\omega_{1J}^{36} = \omega_e^{(3)}$.

The resulting signal expression is given as

$$S(t) = (\sin \theta_{14} + \sin \theta_{36}) \left[A_4 \cos^2 \theta_{34} - A_3 \sin \left(\frac{\theta_{36} - \theta_{14}}{2} \right) \cos \theta_{34} \sin \theta_{34} \right] \sin^2 \frac{\omega_d^{16,34} t}{2} + \underbrace{S(t)_{16} + S(t)_{15,24} + S(t)_{26,35}}_{\text{High-frequency components}}.$$

$$(4.26)$$

• Double-quantum (DQ₁₅) CP matching condition:

Setting $\Sigma_{15} = 0 \implies 8\omega_{1I}^{14} + 8\omega_{1I}^{25} = -(\omega_e^{(3)} + 3\omega_e^{(1)} + 3\omega_e^{(2)} - \omega_O^{(1)})$

The resulting CP signal expression is given as

$$S(t) = \underbrace{\left(\sin\theta_{14} + \sin\theta_{25}\right) \left[-A_5 + A_7 \sin\theta_{15} \right] \sin^2 \frac{\omega_d^{15,24} t}{2}}_{S(t)_{15}} + \underbrace{S(t)_{16,34} + S(t)_{24} + S(t)_{26,35}}_{\text{High-frequency components}}.$$

$$(4.27)$$

• Zero-quantum (ZQ₂₄) CP matching condition:

Setting $\Delta_{24} = 0 \implies 8\omega_{1I}^{14} + 8\omega_{1I}^{25} = (\omega_e^{(3)} + 3\omega_e^{(1)} + 3\omega_e^{(2)} - \omega_Q^{(1)}).$

The resulting CP signal expression is given as

$$S(t) = \underbrace{\left(\sin\theta_{14} + \sin\theta_{25}\right) \left[A_5 - A_7\sin\theta_{15}\right] \sin^2\frac{\omega_d^{15,24}t}{2}}_{S(t)_{24}} + \underbrace{S(t)_{16,34} + S(t)_{15} + S(t)_{26,35}}_{\text{High-frequency components}}.$$

$$(4.28)$$

• Double-quantum (DQ₂₆) CP matching condition:

Setting
$$\Delta_{26} = 0 \implies 8\omega_{1I}^{25} + 8\omega_{1I}^{36} = -(\omega_e^{(3)} - 3\omega_e^{(1)} - 3\omega_e^{(2)} + \omega_Q^{(1)}).$$

The resulting CP signal expression is given as

$$S(t) = \underbrace{(\sin \theta_{25} + \sin \theta_{36}) \left[A_8 - A_9 \sin \theta_{26} \right] \sin^2 \frac{\omega_d^{26,35} t}{2}}_{S(t)_{26}} + \underbrace{S(t)_{16,34} + S(t)_{15,24} + S(t)_{35}}_{\text{High-frequency components}}.$$

$$(4.29)$$

• Zero-quantum (ZQ₃₅) CP matching condition:

Setting $\Sigma_{35} = 0 \implies 8\omega_{1I}^{25} + 8\omega_{1I}^{36} = (\omega_e^{(3)} - 3\omega_e^{(1)} - 3\omega_e^{(2)} + \omega_Q^{(1)}).$

The resulting CP signal expression is given as

$$S(t) = \underbrace{(\sin \theta_{25} + \sin \theta_{36}) \left[-A_8 + A_9 \sin \theta_{35} \right] \sin^2 \frac{\omega_d^{26,35} t}{2}}_{S(t)_{35}} + \underbrace{S(t)_{16,34} + S(t)_{15,24} + S(t)_{26}}_{\text{High-frequency components}}.$$

$$(4.30)$$

The signal expression for the TQ_{16} (and ZQ_{35} and DQ_{15}) and SQ_{34} (and DQ_{26} and ZQ_{24}) CP conditions are governed by similar effective dipolar coupling strengths $\omega_d^{16,34}$ (and $\omega_d^{26,35}$ and $\omega_d^{15,24}$) and are just phase-shifted versions of each other. Therefore, these modes of the CP transfer are expected to display similar CP dynamics. Experimentally, $TQ_{16}/ZQ_{35}/DQ_{15}$ transfer can be achieved by shifting the phase of I-spin RF-field by 180°. In addition to these normal modes of CP transfer, the interference terms can also be maximized setting $\omega_{eff}^{ij} = \pm \omega_{eff}^{jk}$. This is only possible at $\omega_{1I} = 0$. However, it is important to note that this condition is not a typical resonance condition that involves two different nuclear spins (simultaneous I and S-spin energy matching). Nevertheless, it is a pathway for the loss in the I-spin polarization, but there is no gain in the S-spin polarization. Such losses can be studied by simultaneously observing the loss in the I-spin polarization via $\langle \hat{I}_x(t) \rangle$ and build-up in the S-spin polarization via $\langle \hat{S}_x(t) \rangle$. occurrence of this condition is solely attributed to off-resonance irradiation and second-order quadrupolar coupling effects. No such conditions were observed under on-resonance irradiations for spin-1/2 as well as quadrupolar CP. Due to finite I-spin RF-requirements for an efficient CP process, such zero-field condition are not expected to have influence on the overall CP transfer. However, situations with weaker S-spin RF-irradiations require additional caution.

4.2 Results and discussion

4.2.1 Description of CP spin-dynamics under the second-order quadrupolar coupling interaction

4.2.1.1 CP dynamics in Single-crystal

For systems with larger electronic asymmetry (eq) and quadrupole moments (Q), the higher-order quadrupolar effects can alter the spin dynamics of the cross-polarization

Table 4.3: The expressions and transitions associated with various HH CP matching conditions for the CP transfer between I = 1/2 and S = 1 spin systems.

CP matching conditions and associated transitions	Expression
Triple-quantum (TQ ₁₆) $ -1/2, -1\rangle \leftrightarrow 1/2, 1\rangle$	$4\omega_{1I}^{14} + 4\omega_{1I}^{36} = -\omega_e^{(3)}$
Single-quantum (SQ ₃₄) $ 1/2, -1\rangle \leftrightarrow -1/2, 1\rangle$	$4\omega_{1I}^{14} + 4\omega_{1I}^{36} = \omega_e^{(3)}$
Double-quantum (DQ ₁₅) $ 1/2, 1\rangle \leftrightarrow -1/2, 0\rangle$	$8\omega_{1I}^{14} + 8\omega_{1I}^{25} = -(\omega_e^{(3)} + 3\omega_e^{(1)} + 3\omega_e^{(2)} - \omega_Q^{(1)})$
Zero-quantum (ZQ ₂₄) $ -1/2,1\rangle \leftrightarrow 1/2,0\rangle$	$8\omega_{1I}^{14} + 8\omega_{1I}^{25} = (\omega_e^{(3)} + 3\omega_e^{(1)} + 3\omega_e^{(2)} - \omega_Q^{(1)})$
Double-quantum (DQ ₂₆) $ 1/2, -1\rangle \leftrightarrow -1/2, 0\rangle$	$8\omega_{1I}^{25} + 8\omega_{1I}^{36} = -(\omega_e^{(3)} - 3\omega_e^{(1)} - 3\omega_e^{(2)} + \omega_Q^{(1)})$
Zero-quantum (ZQ ₃₅) $ -1/2, -1\rangle \leftrightarrow 1/2, 0\rangle$	$8\omega_{1I}^{25} + 8\omega_{1I}^{36} = (\omega_e^{(3)} - 3\omega_e^{(1)} - 3\omega_e^{(2)} + \omega_Q^{(1)})$

experiment. To explicate the exact mechanism of the polarization transfer in the presence of second-order quadrupolar interaction, we evaluated the RF-domain CP efficiency profile for $C_Q = 1.5$ MHz at ¹H Larmor precession frequency 400 MHz (Figure 4.3) for a single-crystal sample with and without S-spin off-resonance irradiation. In the simulation depicted, the CP efficiency is plotted as a function of I-spin RF amplitude at constant mixing/contact time ($\tau_c = 500 \,\mu s$) and S-spin RF amplitude ($\nu_{1S} = 80 \,\text{kHz}$). All other simulation parameters used in the simulations are listed in the caption of Figure 4.3. The analytic simulations emerging from Eq. (4.20) (shown in indigo color in panels a1-a4) are in good agreement with the numerically generated SIMPSON simulations (black curve) which validates the exactness of the proposed analytic theory. To further explicate the exact mechanism of polarization transfer, the individual signal contributions corresponding to six dipolar coupling based transfer modes are evaluated in panels b1-b4. In the presence of the first-order quadrupolar coupling and under on-resonance S-spin irradiation CP dynamics (panels a1-b1) is described predominantly by the SQ_{34} ($|1/2, -1\rangle \leftrightarrow |-1/2, 1\rangle$) and DQ_{26} ($|1/2, -1\rangle \leftrightarrow |-1/2, 0\rangle$) HH matching conditions [116]. A detailed theoretical description of the CP dynamics can be found in previous Chapter. [116]. In the presence of econd-order quadrupolar coupling (panels a2-b2), the overall CP efficiency profile varies significantly with respect to the first-order quadrupolar coupling-driven CP dynamics under on-resonance S-spin irradiation. More specifically, we observe the following striking differences: (i) The appearance of an additional CP resonance at high I-spin RF amplitude, (ii) a shift in the relative positions of the CP resonances, (iii) variation in the CP efficiencies and resonance widths (iv) a minor dispersion in the CP resonance at lower I-spin RF amplitude. Under the influence of the second-order quadrupolar coupling induced shift (panels a2-b2) ($\Omega_{1S} = 0$), the SQ₃₄ and DQ₂₆ CP matching conditions shift at higher and lower I-spin RF amplitudes, respectively. Besides, the CP efficiency profile demonstrates

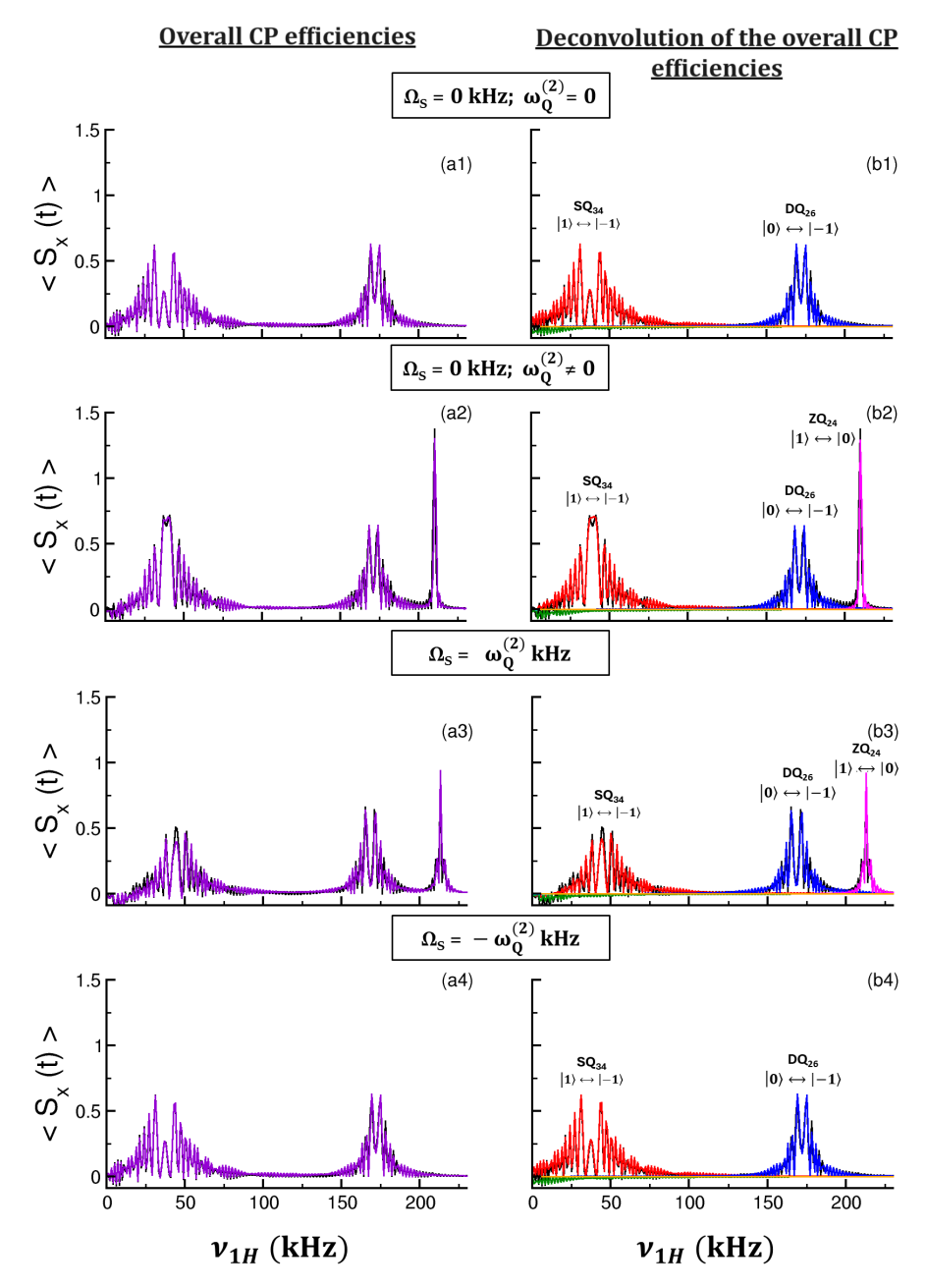


Figure 4.3: The second-order quadrupolar coupling driven cross-polarization transfer efficiency as a function of the $^1\mathrm{H}$ RF field for a single-crystal sample from the numerical simulation (SIMPSON) and the analytic theory. These simulations demonstrate the effect of S-spin off-resonance irradiations on the CP efficiency profile (a1-b1) $\Omega_{1S}=0$ kHz and $\omega_Q^{(2)}=0$ kHz, (a2-b2) $\Omega_{1S}=0$ kHz and $\omega_Q^{(2)}\neq0$ kHz, (a3-b3) $\Omega_{1S}=\omega_Q^{(2)}=-6.8921$ kHz and (a4-b4) $\Omega_{1S}=-\omega_Q^{(2)}=6.8921$ kHz . The parameters used for generating the CP efficiency profiles are: $C_Q=1.5$ MHz, $\eta_Q=0$, quadrupolar coupling PAS angles α_Q and $\beta_Q=50^\circ$, contact time = 0.5 ms, $^1\mathrm{H}$ Larmor precession frequency = 400 MHz, $\nu_{1S}=80$ kHz internuclear distance $r_{IS}=1.05$ Å and dipolar PAS angle $\beta_d=0^\circ$. SIMPSON simulations (black curve) are fitted with the total analytic signal expressions (indigo curve) [Eq. (4.20)] in panels a1-a4; SQ₃₄ (red curve) and TQ₁₆ (green curve); DQ₂₆ (blue curve) and ZQ₃₅ (cyan curve); ZQ₂₄ (magenta curve) and DQ₁₅ (orange curve) in panels b1-b4.

an additional sharp CP matching condition ZQ_{24} ($|1/2,1\rangle \leftrightarrow |-1/2,0\rangle$) at higher I-spin RF field in contrast to the first-order quadrupolar driven CP dynamics, wherein the transition operator corresponding to the ZQ₂₄ dipolar-based transfer was absent (panels a1-b1). This observation is consistent with the argument that the second-order quadrupolar coupling induces shift equivalent to the off-resonance irradiation [115]. The off-resonance irradiation reduces the energy difference associated with the single quantum (SQ_S) transitions while enhancing the energy difference for double quantum (DQ_S) transitions. Hence, the S-spin off-resonance irradiation strengthens the CP signal corresponding to the DQ₂₆ and ZQ₂₄ conditions which transfer polarization into the SQ_S transitions while the quite opposite behavior is observed for the SQ₃₄ condition. At lower ¹H RF amplitude, we observe a minor contribution from the otherwise high-frequency TQ₁₆ signal component. This could be attributed to the decrease in the magnitude of $\Sigma_{16} = (4\omega_{1I}^{14} + 4\omega_{1I}^{36} + \omega_e^{(3)})/8$ which make the prefactor in the TQ₁₆ $\left\{ (\omega_d^{16,34})^2/[\Sigma_{16}^2+(\omega_d^{16,34})^2] \right\}$ signal component finite; hence it's contribution becomes significant. It should be noted that the overall CP efficiency from the high-frequency term will vary according to the orientation of the quadrupolar coupling tensor. Interestingly, a noticeable dispersion at the SQ₃₄ matching condition at lower I-spin RF amplitudes is also observed. The observed dispersion at the SQ_{34} matching condition originates from the single-quantum I-spin dipolar transitions ($SQ_{d,I}$) (as shown through the dispersive components of the signal expression i.e., $\sin \theta_{ij} \cos \theta_{ij}$). Therefore, the SQ₃₄ CP condition demonstrates a much more complex interplay of various CP signals and exhibits a non-unidirectional polarization transfer behavior. Due to the high I-spin RF requirements, the contributions from the high-frequency ZQ_{35} and DQ_{15} components are absent in the DQ_{26} and ZQ_{24} CP matching conditions, respectively.

To achieve an efficient CP transfer, the width of the CP matching condition under consideration is an important aspect to explore. The relative widths of the CP matching conditions decrease with the decrease in the effective dipolar coupling strengths acting between the states (refer to Eq. 4.8). For instance, the ZQ₂₄ transition is associated with the smallest effective dipolar coupling strength than the SQ₃₄ and DQ₂₆ transitions ($\omega_d^{16,34} > \omega_d^{26,35} > \omega_d^{15,24}$), and the CP resonance widths are manifested accordingly (Figure 4.3). This observation is also substantiated through the rate of CP buildup in the mixing time profile under different CP matching conditions in Figure 4.4.

It is essential to highlight that the overall CP efficiency profile is unaffected by the change in the sign of the quadrupolar coupling constant (C_Q) ; however, the individual analytic fittings of the CP efficiency profile reveal that the SQ₃₄ and DQ₂₆ CP conditions are swapped with changing the sign of quadrupolar coupling constant $(C_Q = -1.5 \text{ MHz})$ while the ZQ₂₄ condition remains unaffected (Figure 4.5). This is because the CP dynamics associated with ZQ₂₄ transition is solely governed by the second-order quadrupolar coupling, which is independent of the sign of the C_Q . Whereas the SQ₃₄ and DQ₂₆ transitions are primarily governed by the first-order quadrupolar coupling frequency, which is sensitive to the sign of C_Q . In the current discussion, all the simulations have been plotted by assuming a constant Zeeman magnetic field strength. The second-order

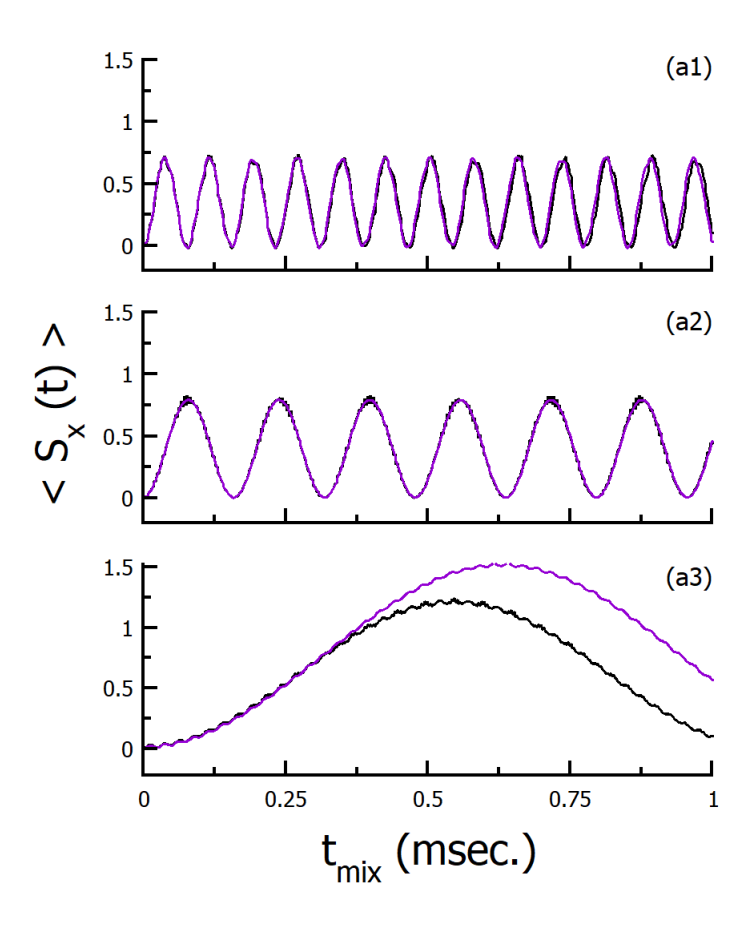


Figure 4.4: In the CP simulations depicted, the polarization build-up on the S-spin (due to transfer from the I-spin) is monitored in a single crystal as a function of the CP mixing time under constant RF field strengths on both the spins. The RF amplitudes on the I-spin were chosen based on exact HH CP conditions (SQ₃₄, DQ₂₆ and ZQ₂₄) expression and are given as $\nu_{1H} = 38.98$ kHz (a1); $\nu_{1H} = 171$ kHz (a2) and $\nu_{1H} = 210.22$ kHz (a3) under $\Omega_S = 0$ kHz. The remaining simulation parameters and descriptions are as given in the caption of Figure 4.3(a2-b2). SIMPSON simulations (black curve) are fitted with the total analytic signal expressions (indigo curve) [Eq. (4.20)] in panels a1-a2.

quadrupolar effects are scaled by the Zeeman field strength; therefore, working at the high magnetic field strengths, these effects can be minimized (refer to Figure 4.6 at $\omega_{01H}=800$ MHz and 200 MHz), respectively. With increasing strength of the second-order quadrupolar coupling constant (Figure 4.6 at $\beta_Q=45^{\circ}$), the efficiency of the SQ₃₄ CP condition decreases, while it increases for the DQ₂₆ and ZQ₂₄ CP conditions. This observation could be explained based on the nature of S-spin transitions and their respective offset dependence involved in each of the CP resonance. The double-quantum S-spin transition (SQ₃₄ CP condition) is devoid of the first-order quadrupolar coupling, therefore, it is much more exposed to the second-order quadrupolar effects, while the excitation efficiency of first-order quadrupolar dependent S-spin SQ transitions (DQ₂₆ and ZQ₂₄ conditions) improves. Additionally, it shifts the DQ₂₆ CP condition at lower I-spin RF field amplitude. The detrimental effects of the second-order quadrupolar

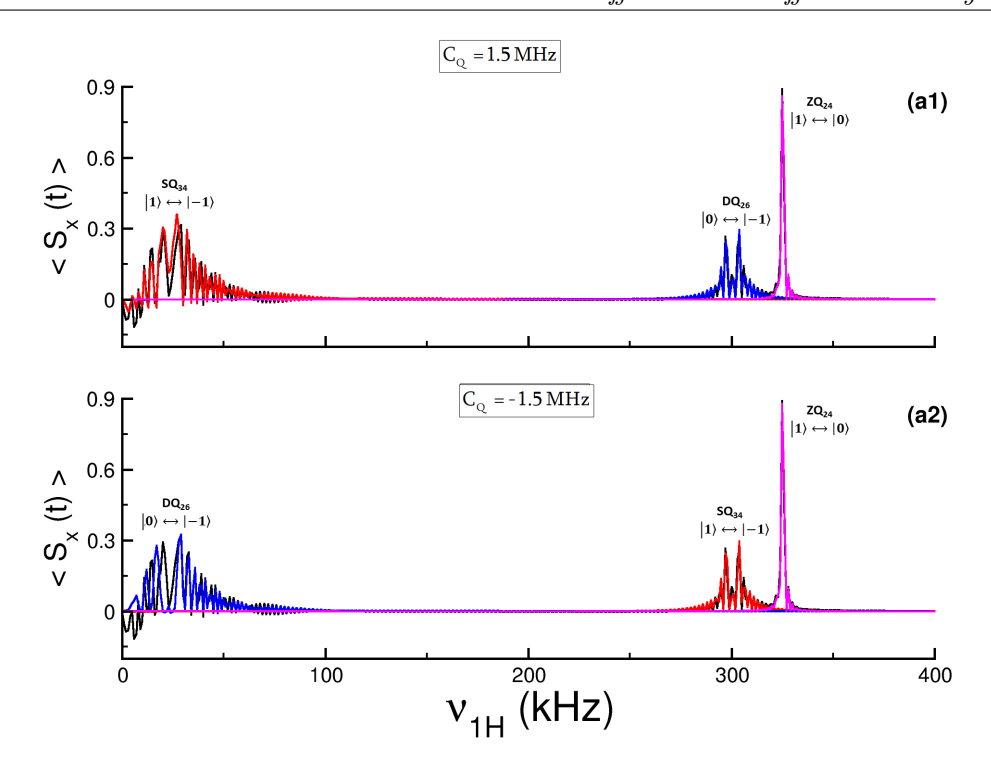


Figure 4.5: Effect of the sign of the quadrupolar coupling constant on the cross-polarization transfer efficiency as a function of the ^{1}H RF field for a single-crystal sample from the numerical simulation (SIMPSON) and the analytic theory. The following parameters were used in the simulations: $C_Q = 1.5$ MHz, $\eta_Q = 0$, quadrupolar coupling PAS angles (0°, 45°, 0°), $\omega_{01H} = 400$ kHz, $\nu_{1S} = 80$ kHz and S-spin off-resonance irradiation strength $\Omega_{1S} = 0$ kHz. SIMPSON simulations (black curve) are fitted with the analytic signal expressions $SQ_{34}+TQ_{16}$ (red curve); $DQ_{26}+ZQ_{35}$ (blue curve); $ZQ_{24}+DQ_{15}$ (magenta curve) in panels a1-a2 [Eq. (4.20)].

coupling on the SQ_{34} CP condition can be minimized by working at the higher magnetic field strengths. However, the obvious disadvantage of working at higher magnetic fields is that it increases the size of offsets, which deteriorates the CP efficiency at lower I-spin RF fields and induces undesired I-spin dipolar transitions ($SQ_{d,I}$). Therefore, it becomes necessary to look for alternative methods to compensate for these second-order quadrupolar effects. In the context of spin-1 nuclei, the second-order quadrupolar coupling and S-spin off-resonance irradiation share a similar operator dependency (\hat{S}_z) , therefore, are expected to have a similar effect on the CP spin-dynamics with an exception that the second-order quadrupolar coupling has a complex orientation dependence in the LAB frame. In this section, we are focusing on the single-crystal sample. Therefore, another way to compensate for these second-order quadrupolar effects is to set the strength of off-resonance irradiation exactly at the negative of the second-order quadrupolar frequency. Panels a3-b3 and a4-b4 in Figure 4.3 demonstrate the effect of off-resonance irradiation at $\Omega_S = \omega_Q^{(2)}$ and $\Omega_S = -\omega_Q^{(2)}$ in presence of second-order quadrupolar effects. From the above simulations, it is evident that the off-resonant irradiation exactly at the negative of the second-order quadrupolar frequency $(\Omega_S = -\omega_Q^{(2)})$ leads to compensation for its deteriorating effect on CP spin-locking efficiency. In this case, the sharp resonance due

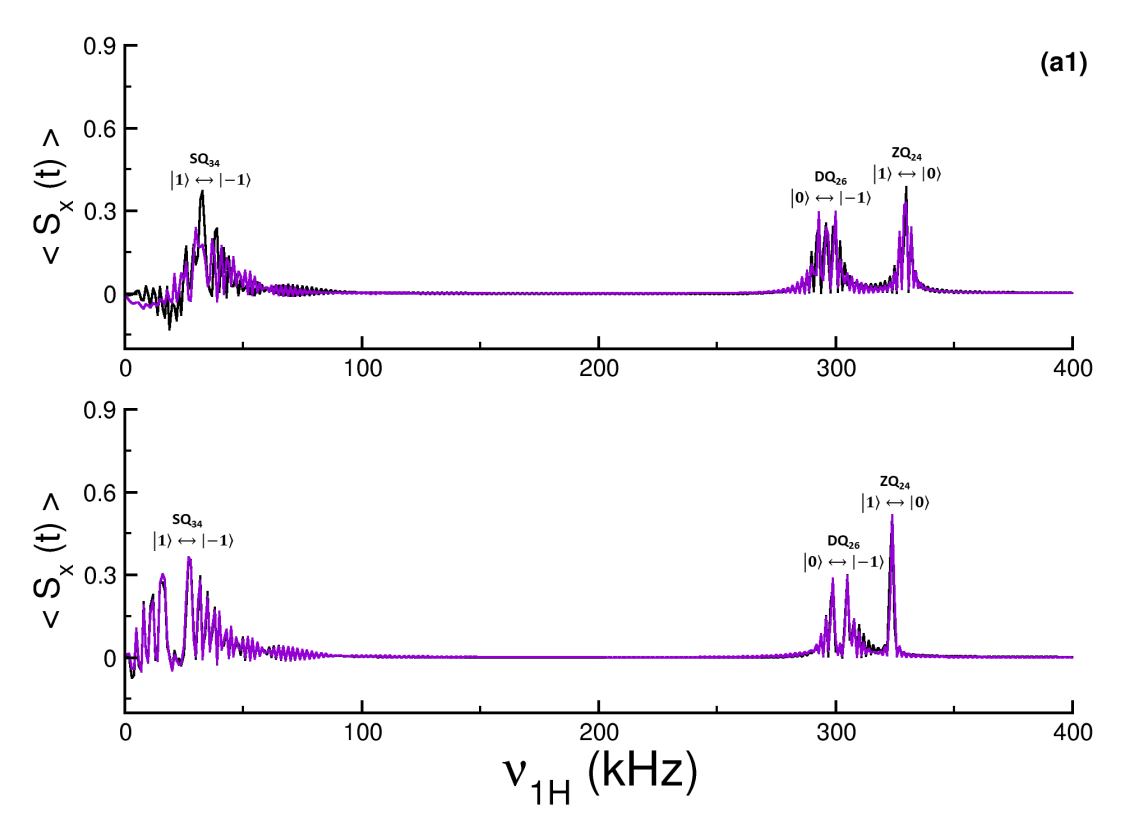


Figure 4.6: The second-order quadrupolar driven cross-polarization transfer efficiency as a function of the $^1\mathrm{H}$ RF field for a single-crystal sample from the numerical simulation (SIMPSON) and the analytic theory. These simulations demonstrate the effect of Zeeman field strengths (a1) $\omega_{01H} = 200$ kHz and (a2) $\omega_{01H} = 800$ kHz on the CP efficiency profile for a single-crystal sample. The parameters used for generating the CP efficiency profiles are: $C_Q = 1.5$ MHz, $\eta_Q = 0$, quadrupolar coupling PAS angles $\alpha_Q = 0^\circ$ and $\beta_Q = 45^\circ$, contact time = 0.5 ms, $\nu_{1S} = 80$ kHz internuclear distance $r_{IS} = 1.05$ Å and dipolar PAS angle $\beta_d = 0^\circ$. SIMPSON simulations (black curve) are fitted with the total analytic signal expressions (indigo curve) [Eq. (4.20)] in panels a1-a2.

to ZQ₂₄ CP transfer is absent, and the overall CP efficiency profile looks identical to the first-order quadrupolar driving CP profiles (panels a1-b1) under on-resonance S-spin irradiation. Therefore, the off-resonance irradiation for larger C_Q systems (discussed in Figure 4.3) could work in favor of improving the spin-locking efficiency for a larger C_Q sample by mitigating the second-order quadrupolar effects. On the other hand, the S-spin irradiation at $\Omega_S = \omega_Q^{(2)}$ doubles the overall effect resulting due to the second-order coupling effect.

From an experimental standpoint, it seems rationale to study the effect of the off-resonance irradiation strengths other than $\Omega_S = \pm \omega_Q^{(2)}$. Figure 4.7 shows the CP efficiency profiles at $\Omega_S = 0, -20$ and 20 kHz under first-order (panels a1-c1) and first+second-order (panels d1-f1) quadrupolar coupling effects for single-crystal sample. The position and efficiency of HH CP matching conditions does not show any dependence on the sign of the S-spin off-resonance irradiation (Figure 4.7 panels b1-c1), however, the effective dipolar coupling constants derived from the analytic theory for the DQ₂₆/ZQ₃₅ and

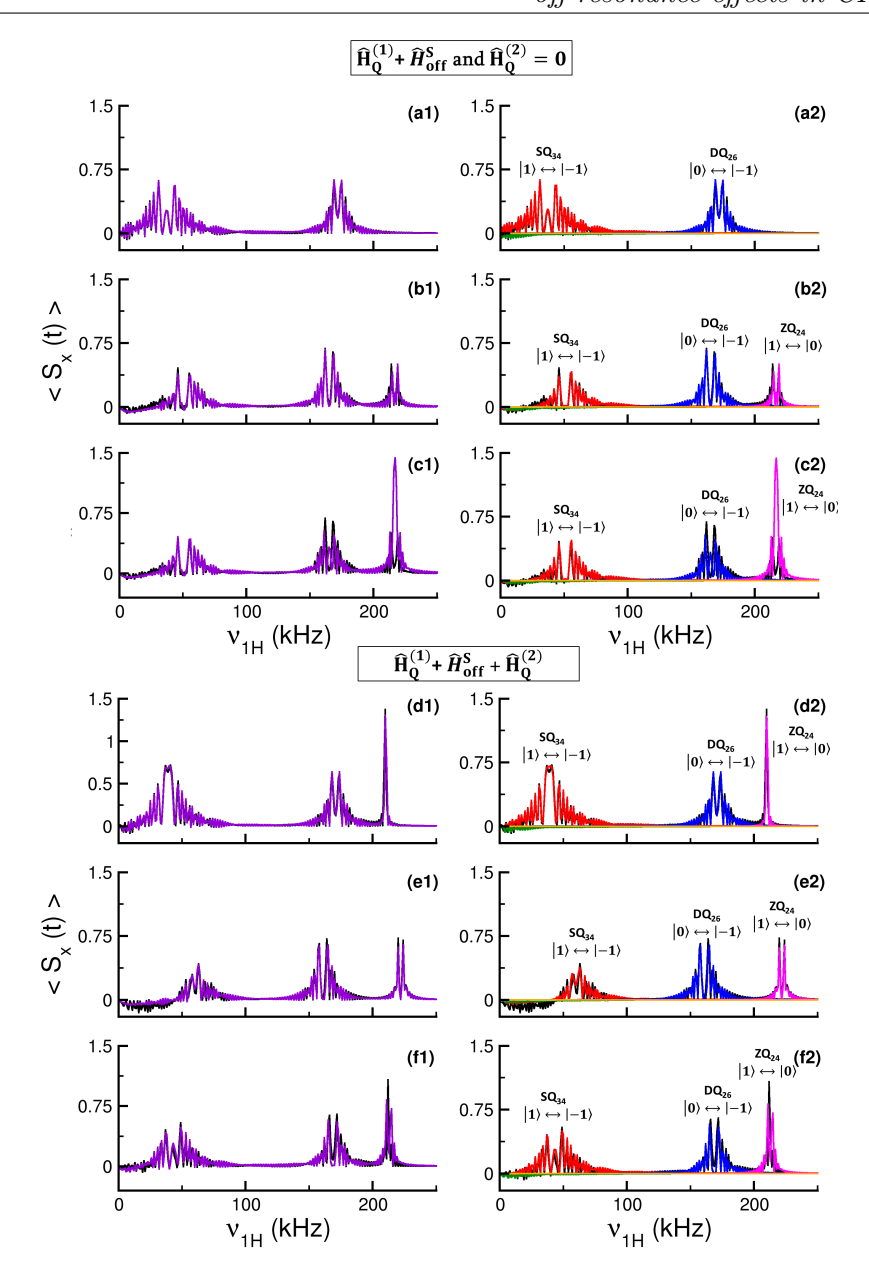


Figure 4.7: The cross-polarization transfer efficiency as a function of the ¹H RF field for a single-crystal sample from the numerical simulation (SIMPSON) and the analytic theory. These simulations demonstrate the effect of S-spin off-resonance irradiations on the CP efficiency profile $\Omega_{1S}=0$ kHz (a1-a2; d1-d2), $\Omega_{1S}=-20$ kHz (b1-b2; e1-e2) and $\Omega_{1S}=20$ kHz (c1-c2; f1-f2). The simulations are performed considering the quadrupolar coupling effects upto the first and second-orders in panels (a1-c1 and a2-c2) and (d1-f1 and d2-f2), respectively. The parameters used for generating the CP efficiency profiles are: $C_Q=1500$ kHz, $\eta_Q=0$, quadrupolar coupling PAS angles α_Q and $\beta_Q=50^\circ$, contact time = 0.5 ms, $\nu_{1S}=80$ kHz internuclear distance $r_{IS}=1.05$ Å and dipolar PAS angle $\beta_d=0^\circ$. SIMPSON simulations (black curve) are fitted with the total analytic signal expressions (indigo curve) [Eq. (4.20)] in panels a1-f1 and the individual contributions from the SQ₃₄ (red curve) and TQ₁₆ (green curve); DQ₂₆ (blue curve) and ZQ₃₅ (cyan curve); ZQ₂₄ (magenta curve) and DQ₁₅ (orange curve) CP conditions are depicted in panels a2-f2.

 ZQ_{24}/DQ_{15} CP conditions show such dependence (refer to Figure D.1 in Appendix D for $C_Q = 200$ kHz). However, at larger $\omega_Q^{(1)}$ values, no such dependence is observed. This

sign dependence could be omitted by redefining the unitary transformation \hat{U}_5 , which would add to the complexity in subsequent calculations. This sign dependence can be disregarded as the off-resonant effects are only significant for the higher $\omega_Q^{(1)}$ systems. From an experimental standpoint, Figures D.2-D.3 (refer to Appendix-D) demonstrates that while setting CP in the presence of multiple quadrupolar spins, it is advisable to employ on-resonance irradiation with the larger C_Q nuclei. This is due to the dramatic effect of the off-resonance for the SQ₃₄ CP conditions, which occur at RF amplitudes that are experimentally feasible for the I-spin. However, for smaller C_Q nuclei, the S-spin off-resonance irradiation $(\Omega_S = \omega_Q^{(1)})$ or $-\omega_Q^{(1)}$ is advisable while setting the DQ₂₆ or ZQ₂₄ CP matching conditions. The rationale behind this selective implementation originates from the fact that the SQ_{34} CP conditions necessitate the conversion of DQ_S coherence into observable SQ_S coherence, which generally leads to loss of coherence. In the presence of second-order quadrupolar interaction, the sign of off-resonant irradiation has either detrimental or favorable effects on spin-locking CP efficiency (panels e1-f1). This further strengthens the argument that off-resonance irradiation works well for the higher C_Q systems. Nevertheless, the quadrupolar systems with smaller C_Q values have nearly negligible second-order quadrupolar coupling effects and therefore, work well under on-resonance irradiation. Omitting the operator similarities between the second-order quadrupolar interaction and S-spin-off-resonance irradiation, the CP dynamics in the former case is altered by the second and forth-rank quadrupolar tensor. Therefore, the orientation behavior of the CP efficiency profile will vary for the powder sample.

4.2.1.2 CP dynamics for Single-Crystal: Varying orientation

In our previous chapter, we have explicitly highlighted the role of the quadrupolar PAS angles α_Q and β_Q in describing the CP dynamics for single-crystal samples when subjected to on-resonance S-spin irradiation. The presence of additional quadrupolar-dependent HH CP matching condition in the presence of second-order quadrupolar coupling interaction leads to an escalated complexity in the polarization transfer behavior.

Figures 4.8 and D.4 (refer to Appendix-D) outline the mechanistic changes observed in the CP efficiency with the variation of quadrupolar PAS angle β_Q within the range $0^{\circ} \leq \beta_Q \leq 180^{\circ}$ for an axially symmetric tensor. The simulations were carried out for a single-crystal sample with quadrupolar coupling constant $C_Q = 1.5$ MHz at ¹H larmor frequency 400 MHz. The orientation dependence of the $\omega_Q^{(1)}$ and $\omega_Q^{(2)}$ with β_Q variation is shown in Figure D.5 in Appendix-D. On varying the polar angle β_Q from $0^{\circ} \leq \beta_Q \leq 180^{\circ}$, the first-order quadrupolar frequency ($\omega_Q^{(1)}$) shows two zero-passages at angles $\beta_Q = 54.736^{\circ}$ and 125.624° where the sign changes from positive/negative to negative/positive. Therefore, we anticipate a change in the dynamics of various CP resonances while passing through these conditions. Unlike $\omega_Q^{(1)}$, the second-order quadrupolar coupling frequency $\omega_Q^{(2)}$ shows a different behavior and does not change the sign on varying β_Q angle in the range $0^{\circ} \leq \beta_Q \leq 180^{\circ}$. Consequently, CP behavior with quadrupolar PAS angles (β_Q and α_Q) variation will follow characteristics of $\omega_Q^{(1)}$, while $\omega_Q^{(2)}$ will simply induce a shift in

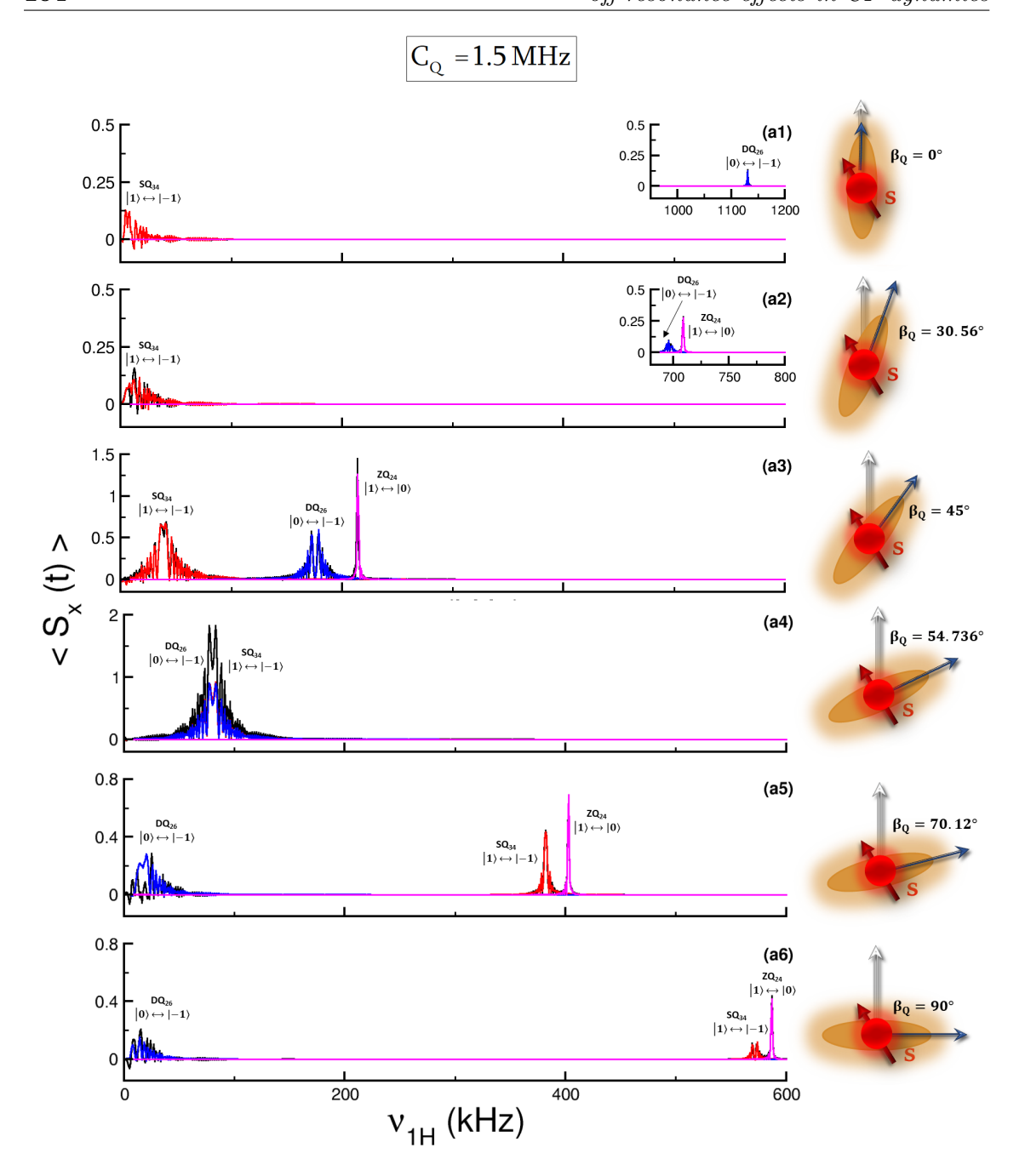


Figure 4.8: Effect of the variation of quadrupolar coupling PAS angle β_Q : 0° (a1), 30.56° (a2), 45° (a3), 54.736° (a4), 70.12° (a5) and 90° (a6) on the second-order quadrupolar interaction driven cross-polarization transfer efficiency for a single-crystal sample. The parameters used for generating the CP efficiency profiles are: $C_Q = 1500$ kHz, $\eta_Q = 0$, and quadrupolar coupling PAS angle $\alpha_Q = 0^{\circ}$, $\nu_{1S} = 80$ kHz, contact time = 0.5 ms, ¹H Larmor precession frequency = 400 MHz and $r_{IS} = 1.05$ Åunder on-resonance S-spin irradiation. SIMPSON simulations (black curve) are fitted with the SQ₃₄+TQ₁₆ (red curve), DQ₂₆+ZQ₃₅ (blue curve) and DQ₁₅+ZQ₂₄ (magenta curve) in all panels.

positions of HH-CP matching conditions and the degree of shift will directly depend on the orientation of quadrupolar PAS angles.

For $\beta_Q = 0^{\circ}$ [Figure 4.8(a1)], the CP efficiency profiles resemble the CP behavior observed in Figure 4.3(a1-b1); this is because in case of axially symmetric tensor the second-order

quadrupolar coupling strength is zero for this particular orientation. Therefore, CP transfer is predominantly governed by the SQ_{34} ($|1/2,-1\rangle \leftrightarrow |-1/2,1\rangle$) and DQ_{26} $(|1/2,-1\rangle \leftrightarrow |-1/2,0\rangle)$ CP matching conditions and the CP resonances are labeled accordingly. In the range $0^{\circ} < \beta_Q < 54.736^{\circ}$ (panels a2-a3), it is evident that the second-order quadrupolar coupling excites an additional ZQ₂₄ dipolar transition, which appears at quite high I-spin RF amplitude. Additionally, the magnitude of first-order quadrupolar coupling frequency decreases, resulting in the CP resonances becoming closer. At $\beta_Q = 54.736^{\circ}$, the magnitude of first-order quadrupolar coupling frequency reduces to zero, the SQ₃₄ and DQ₂₆ CP matching conditions become degenerate which overlap to produce a single CP maxima as observed for spin-1/2 behavior and dipolar coupling constant becomes zero for the ZQ₂₄ CP condition; hence we don't observe the ZQ₂₄ CP resonance. Unlike on-resonance irradiation, the SQ_{34} and DQ_{26} CP matching conditions do not provide an equivalent contribution to the overall CP efficiency. This is due to the favorable and detrimental effect of the second-order quadrupolar interaction on the DQ₂₆ and SQ₃₄ CP matching conditions, respectively. The interesting observations are made in the range $54.736^{\circ} < \beta_Q \leq 90^{\circ}$, where the sign of quadrupolar coupling frequency $(\omega_Q^{(1)})$ becomes negative. Therefore, the relative positions of CP matching conditions undergo swapping i.e., the SQ_{34} and DQ_{26} CP resonances swap their positions while the ZQ_{24} CP matching condition still appearing at the higher I-spin RF amplitudes. In panel (a6), the DQ_{26} CP condition displays a little dispersion due to additional single-quantum I-spin dipolar-transition ($SQ_{d,I}$). Moreover, a significant contribution is also observed from the high-frequency ZQ₃₅ CP matching condition. In the range $90^{\circ} < \beta_Q < 125.624^{\circ}$, the magnitude of quadrupolar coupling frequency again decreases which leads to a transition of the CP spin-dynamics from the regime of intermediate to weak quadrupolar coupling. At $\beta_Q = 125.624^{\circ}$, the quadrupolar coupling frequency again crosses zero and CP efficiency profiles demonstrate behavior equivalent to $\beta_Q = 54.736^{\circ}$. From $125.624^{\circ} < \beta_Q < 180^{\circ}$, the sign of the $\omega_Q^{(1)}$ becomes positive and magnitude increases. Consequently, the relative positions of the CP matching conditions are again reversed, resulting in a resemblance of the CP behavior to that observed in the range $54.736^{\circ} > \beta_{Q} > 0^{\circ}$ where it transitions from weak to stronger quadrupolar coupling regime. Based on the above observations, it is fair to conclude that the CP dynamic shows swapping in nature of CP matching conditions at each zero-crossing, and in between these zero-crossings, the CP dynamics show a transition from strong to weak or weak to strong CP behaviors. The above conclusions have been made $C_Q = 1.5$ MHz; however, they can be generalized to include all quadrupolar coupling strengths, where the scale of the behavioral shift may be relatively small, but CP dynamics displays a similar pattern of β_Q variation. Although, the second-order quadrupolar effects get reduced at smaller C_Q systems.

In the case of an axially symmetric quadrupolar tensor, azimuthal PAS angle α_Q does not affect the CP behavior. However, it's the contribution of CP dynamics cannot be ignored for highly asymmetric quadrupolar tensors, especially for β_Q values around 50° to 90°. The orientation dependence with varying α_Q is shown in Figure D.6 and D.7 in Appendix-D

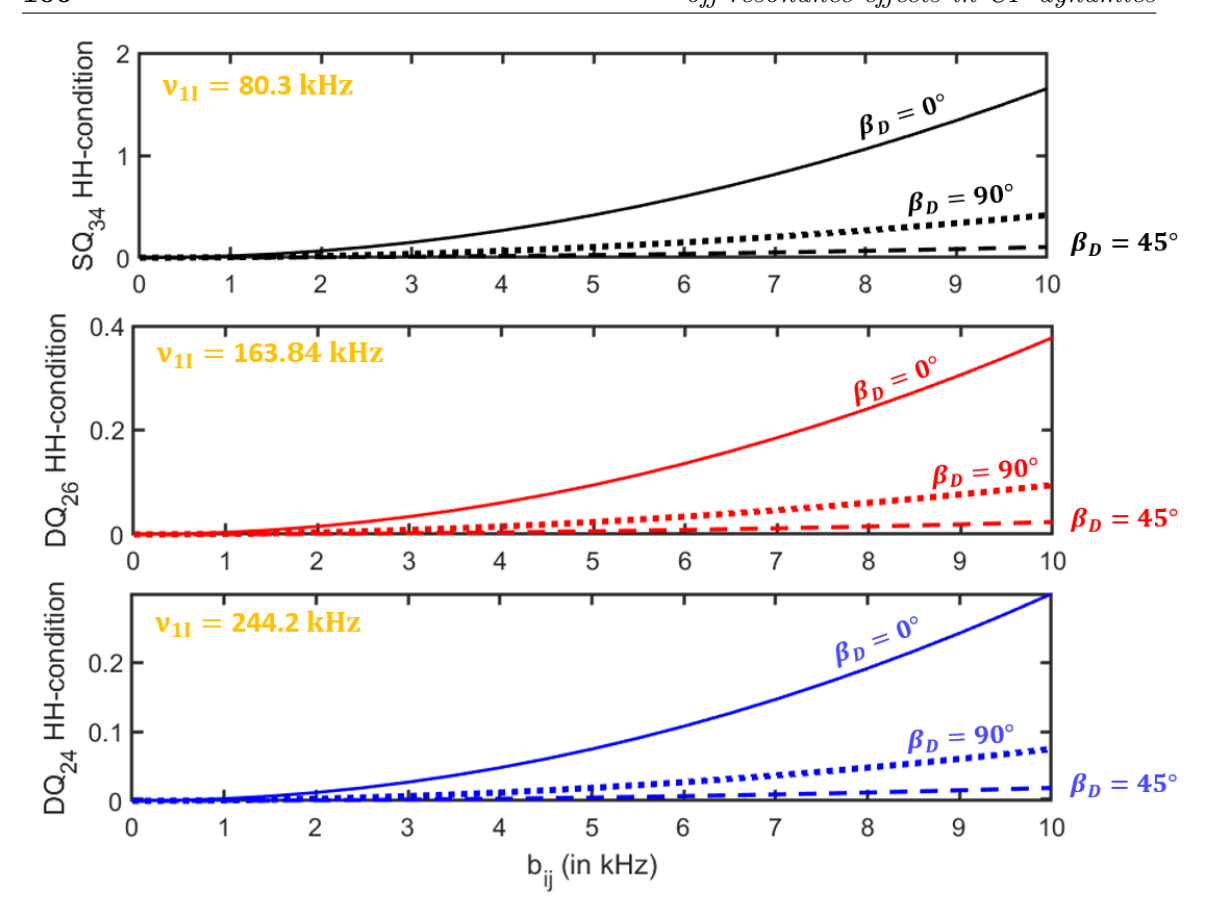


Figure 4.9: Effect of strength and orientation of heteronuclear dipolar coupling tensor on the positions of various HH CP matching conditions (i.e. terms Δ_{34} , Δ_{26} and Δ_{24} are plotted). The following parameters were used in the simulations: $C_Q = 200$ kHz, $\eta_Q = 0$, quadrupolar coupling PAS angles (0°, 0°, 0°), $\nu_{1S} = 80$ kHz and S-spin off-resonance irradiation $\Omega_{1S} = 40$ kHz, considering the effect of the first-order quadrupolar driven coupling only. The ¹H RF field amplitudes mentioned in the various panels of the figure correspond to exact HH matching under zero heteronuclear dipolar coupling strength.

at different β_Q values. For β_Q values $0^{\circ} < \beta_Q$ or $\pi - \beta_Q < 45^{\circ}$, α_Q dependence shows only magnitude variation while at other β_Q it changes magnitude as well as a sign of the first-order quadrupolar frequency. We also observe dipolar coupling dependent shift of the SQ_{34} , DQ_{26} and ZQ_{24} CP conditions as shown in the Figure 4.9. The magnitude of these shifts will depend on the internal (quadrupolar and dipolar couplings) and external (RF irradiation) parameters for distance measurement.

4.2.1.3 CP dynamics for powder sample: Ensemble of orientation

The theoretical framework proposed is shown to explain the CP dynamics associated with a single-crystal sample. In the single-crystal simulation, it is evident that different HH conditions are affected by different degrees under the influence of second-order quadrupolar coupling interaction. Furthermore, it is observed that different crystallite orientations exhibit non-uniform CP behavior with and without second-order quadrupolar coupling interaction. Based on results obtained from the single-crystal studies, we extended our theory to describe the CP dynamics in a more complex powder sample under

static conditions. Figure 4.10 illustrates the CP efficiency for powder samples in the presence of second-order quadrupolar coupling interaction with and without off-resonance The analytical simulations based on Eq. (4.20) converge well with the numerical simulations under the off-resonance S-spin irradiation conditions. To explicate the underlying dynamics of CP transfer, we evaluated the individual signal contributions emerging from various CP matching conditions. Under the influence of the second-order quadrupolar coupling interaction ($\Omega_S = 0$, panels a1-a2), the CP efficiency profile shows three well-defined CP maxima of unequal widths and intensities. It has been observed that the CP maxima at lower I-spin RF amplitude is primarily governed by the overlaid SQ_{34} and DQ_{26} matching conditions. Conversely, the CP maxima observed at high I-spin RF amplitude solely manifests the ZQ₂₄ matching condition. The relative and absolute positions and intensities of all the CP matching conditions in deciphering the CP spin dynamics for the powder sample can be explained based on the interplay of various crystallite orientations in the single-crystal sample (Figure 4.8). The powder sample comprises a statistical ensemble of various crystallite orientations, with the weighting factor $sin\beta_Q$ serving as a probability distribution function. [4, 131, 137] The orientations in the plane perpendicular to the static Zeeman field are most probable and probability continuously decreases moving away from this orientation. Therefore, the overall CP efficiency profile observed in the powder sample has a close resemblance to the CP efficiency observed for the single-crystal sample in the β_Q range from 54.736° to 90° (Figure 4.8). With a full cycle variation in β_Q (0° to 180°) angle, the absolute position of ZQ₂₄ matching condition changes, relatively appear at the higher I-spin RF amplitudes. Consequently, in the powder sample, the ZQ_{24} CP matching condition does not provide any contribution at lower I-spin CP efficiency. The lower intensity and width of the CP matching conditions can be attributed to the interference of various powder orientations. Moreover, at and around $\beta_Q = 90^{\circ}$ which is a case suitable for the DQ ₂₆ CP matching condition, resulting in its higher CP efficiency than the SQ_{34} condition in the lower I-spin RF amplitude region. Whereas in the higher I-spin RF amplitude region, the SQ_{34} CP is more efficient due to the change in the sign of $\omega_Q^{(1)}$.

In stark contrast to the first-order quadrupolar coupling CP efficiency profile for powder sample, in the presence of the second-order quadrupolar coupling interaction the overall CP efficiency profiles shows a negative CP efficiency at lower I-spin RF amplitudes and these observations are consistent with the single-crystal sample. The individual signal contributions reveal that the CP maximum at the higher I-spin RF field is solely governed by the ZQ $_{24}$ CP matching condition which is spread over a range of I-spin RF field where the intensity is the product of the absorptive terms in the signal expression $\left(\frac{(\omega_d^{15,24})^2}{(\omega_d^{15,24})^2 + \Delta_{24}^2}\right)$ and $sin\beta_Q$. The range of β_Q variation for SQ₃₄ and DQ₂₆ CP matching conditions overlap at the CP maxima at lower I-spin RF amplitudes while the middle CP maxima is solely governed by the SQ₃₄ CP matching condition. The negative CP efficiency at the beginning of the I-spin variations is due to CP transfer mediated by the SQ_{d,I} dipolar transitions, which results in CP transfer modes that independent I-spin RF

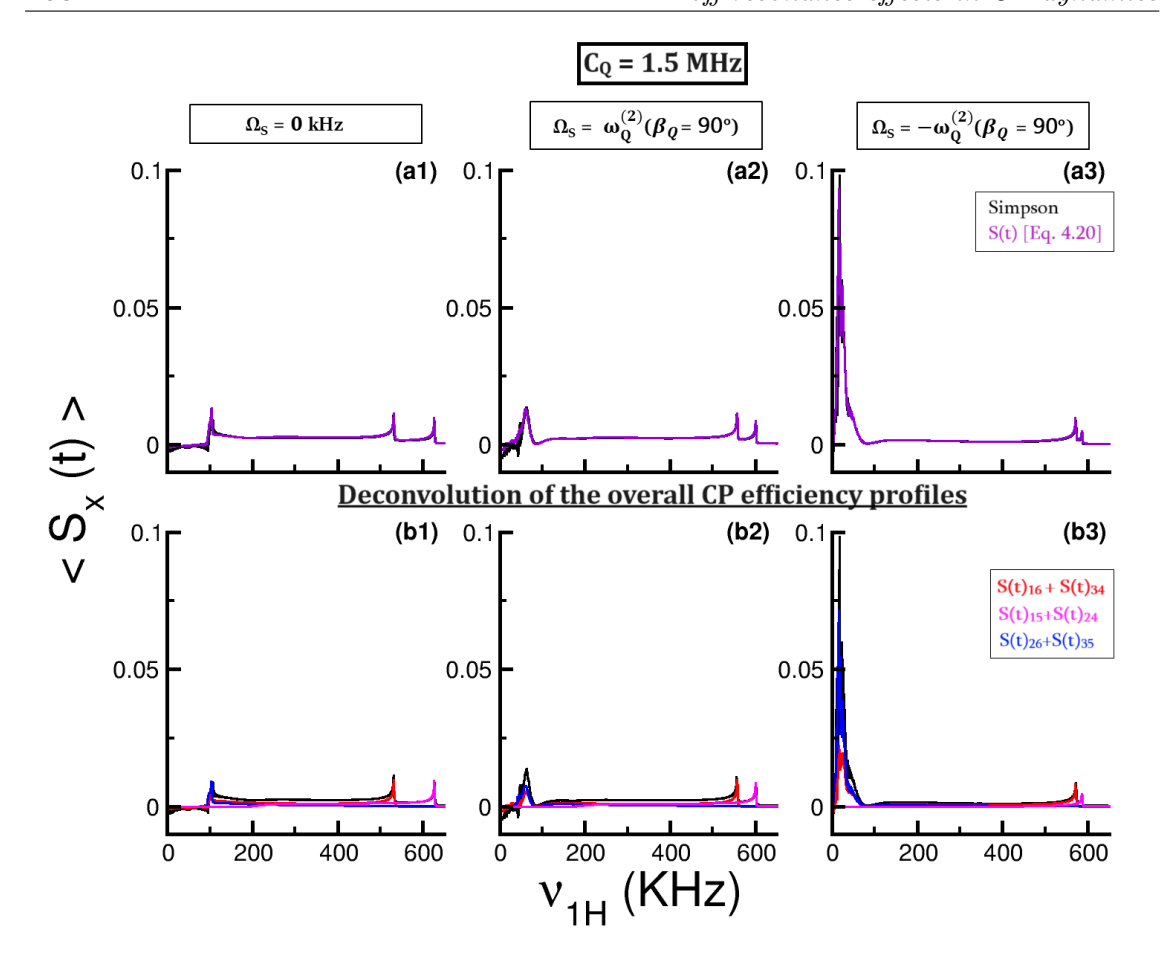


Figure 4.10: The second-order quadrupolar coupling driven cross-polarization transfer efficiency as a function of the $^1\mathrm{H}$ RF field for the powder sample from the numerical simulation (SIMPSON) and the analytic theory. These simulations demonstrate the combined effect of the second-order quadrupolar coupling and S-spin off-resonance irradiations (a1-b1) $\Omega_{1S}=-6.55$ kHz, (a2-b2) $\Omega_{1S}=0$ kHz and (a3-b3) $\Omega_{1S}=4.36$ kHz on the CP efficiency profiles. The parameters used for generating the CP efficiency profiles are: $C_Q=1.5$ MHz, $\eta_Q=0$, quadrupolar coupling PAS angles $\alpha_Q=0^\circ$ and $\beta_Q=0^\circ$, $^1\mathrm{H}$ Larmor precession frequency = 400 MHz, contact time = 0.5 ms, $\nu_{1S}=80$ kHz internuclear distance $r_{IS}=1.05$ Å and dipolar PAS angle $\beta_d=0^\circ$. SIMPSON simulations (black curve) are fitted with the total analytic signal expression (indigo dashed curve) [Eq. (4.20)], SQ₃₄+TQ₁₆ (red curve), DQ₂₆+ZQ₃₅ (blue curve) and DQ₁₅+ZQ₂₄ (magenta curve) in panels a1-a3. These simulations are generated with the zcw4180 crystal file.

amplitude, and in these signal expression these terms manifested by the dispersive terms $\left(\frac{\omega_d^{16,34}\Delta_{34}}{(\omega_d^{16,34})^2+\Delta_{34}^2},\frac{\omega_d^{16,34}\Sigma_{16}}{(\omega_d^{16,34})^2+\Sigma_{16}^2},\frac{\omega_d^{26,35}\Delta_{26}}{(\omega_d^{26,35})^2+\Delta_{26}^2}\right)$ and $\frac{\omega_d^{26,35}\Sigma_{35}}{(\omega_d^{26,35})^2+\Sigma_{35}^2}$. As discussed in the case of the single-crystal sample system, the second-order quadrupolar effects can be minimized by working at higher Zeeman field strength. However, when working at higher fields, spin dynamics become more prone to S-spin offsets and CSA effects. Therefore, such compensatory methods are seldom useful. Besides, exactly setting the S-spin off-resonance irradiation at $\Omega_S=-\omega_Q^{(2)}$ is not possible due to anisotropic quadrupolar orientation in powder, thus, complete compensation of second-order induced shifts is

not possible. In panel b1-c1, an off-resonance irradiation strength equal/negative to the second-order quadrupolar coupling frequency at $\beta_Q = 90^{\circ}$ is employed to compensate for the second-order effects in the powder sample. This off-resonance irradiation strength is best suited to compensate for the second-order quadrupolar effects for powder samples.

4.2.2 State-picture representation of the CP dynamics a single-crystal sample

In previous section, we have provided a detailed operator-based analytic treatment of the observed CP transfer trajectories for single-crystal and powder samples. Given that the CP process involves an exchange of the polarization (*i.e.*, population) between the different energy levels, we have provided an equivalent state picture representation to rationalize the polarization transfer process. Figure 4.11 demonstrates the energy eigen-level diagram obtained by numerical diagonalization of the CP Hamiltonian for a single-crystal sample using the parameters given in the caption of Figure 4.3 (panels a2-b2). In the presence of the second-order quadrupolar coupling (on-resonance S-spin irradiation), we observed a total of six regions of various avoided crossings or level anti-crossings (LAC) at ($\nu_{1H} \neq 0$) and are referred to as the HH CP matching conditions. These positions of LAC are in line with the HH matching conditions expression given in Table 4.3 and corroborate extremely well with the CP resonances observed in Figure 4.3 (panels a2-b2).

To understand the origin of these avoided crossings, it is important to access the CP Hamiltonian [Eq. (4.12)] presented in theory section. The transformed CP Hamiltonian [Eq. (4.12)] is comprised of six dipolar-based subspaces (pictorial representation of the splitting of CP Hamiltonian in Figure 4.1). The matrix representation of the above Hamiltonian in the coupled Zeeman basis is given as

$$\hat{H}_{CP} = \frac{1}{2} \begin{bmatrix} \Sigma_{16} + \Sigma_{15} & 0 & 0 & 0 & \omega_d^{15,24} & \omega_d^{16,34} \\ 0 & \Delta_{26} + \Delta_{24} & 0 & \omega_d^{15,24} & 0 & \omega_d^{26,35} \\ 0 & 0 & \Sigma_{35} + \Delta_{34} & \omega_d^{16,34} & \omega_d^{26,35} & 0 \\ 0 & \omega_d^{15,24} & \omega_d^{16,34} & -\Delta_{24} - \Delta_{34} & 0 & 0 \\ \omega_d^{15,24} & 0 & \omega_d^{26,35} & 0 & -\Sigma_{15} - \Sigma_{35} & 0 \\ \omega_d^{16,34} & \omega_d^{26,35} & 0 & 0 & 0 & -\Sigma_{16} - \Delta_{26} \end{bmatrix}.$$

$$(4.31)$$

For better visualization and the effectiveness of the various dipolar transitions involved in the CP process, the above Hamiltonian is separated in three coupled subspaces in accordance with Figure 4.1.

$$\hat{\tilde{\hat{E}}}_{CP} = \underbrace{\hat{H}_{16,34}}_{\hat{H}_{16} + \hat{H}_{34}} + \underbrace{\hat{H}_{15,24}}_{\hat{H}_{15} + \hat{H}_{24}} + \underbrace{\hat{H}_{26,35}}_{\hat{H}_{26} + \hat{H}_{35}}$$
(4.32)

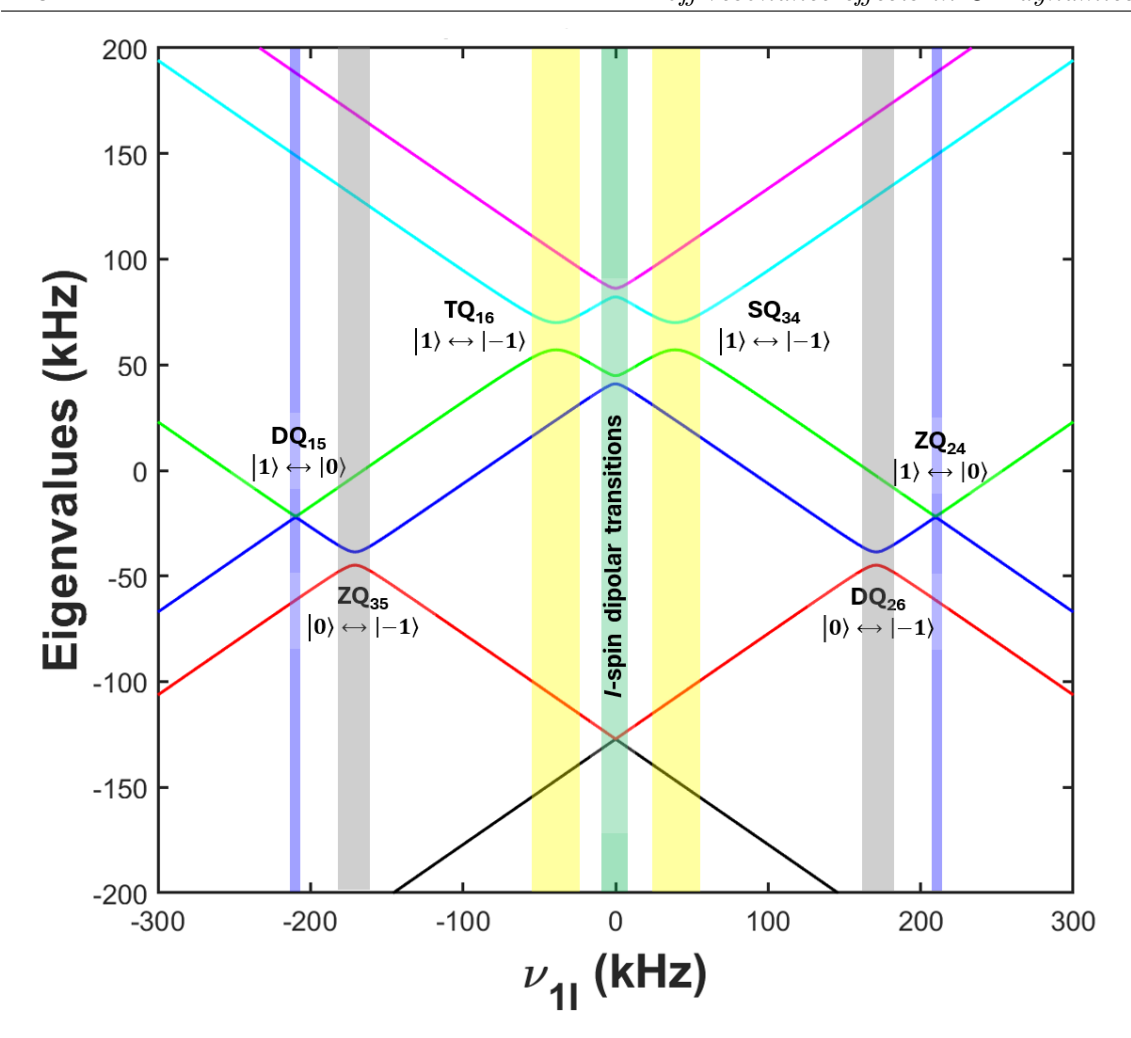


Figure 4.11: The eigen energy level plot as a function of $^1\mathrm{H}$ RF amplitude for a single-crystal sample. The following parameters are used for generating the plot: C_Q = 1.5 MHz, $\eta_Q = 0$, quadrupolar coupling PAS angles $\alpha_Q = 0^\circ$ and $\beta_Q = 50^\circ$, $^1\mathrm{H}$ Larmor precession frequency = 400 MHz, $\nu_{1S} = 80$ kHz internuclear distance $r_{IS} = 1.05$ Å and dipolar PAS angle $\beta_d = 0^\circ$. The regions of avoided crossings are referred to as HH CP matching conditions and are labeled in accordance with the CP efficiency profile in Figure 4.3 under on-resonance irradiation. The avoided crossing at zero $^1\mathrm{H}$ RF amplitude ($\nu_{1H} = 0$ kHz) are due to presence of I-spin dipolar transitions.

where

$$\hat{H}_{16,34} = \frac{1}{2} \begin{bmatrix} \Sigma_{16} & 0 & 0 & \omega_d^{16,34} \\ 0 & \Delta_{34} & \omega_d^{16,34} & 0 \\ 0 & \omega_d^{16,34} & -\Delta_{34} & 0 \\ \omega_d^{16,34} & 0 & 0 & -\Sigma_{16} \end{bmatrix}_{|1\rangle,|3\rangle,|4\rangle,|6\rangle}$$

$$\hat{H}_{(15,24)} = \frac{1}{2} \begin{bmatrix} \Sigma_{15} & 0 & 0 & \omega_d^{15,24} \\ 0 & \Delta_{24} & \omega_d^{15,24} & 0 \\ 0 & \omega_d^{15,24} & -\Delta_{24} & 0 \\ \omega_d^{15,24} & 0 & 0 & -\Sigma_{15} \end{bmatrix}_{|1\rangle,|2\rangle,|4\rangle,|5\rangle}$$
and
$$\hat{H}_{(26,35)} = \frac{1}{2} \begin{bmatrix} \Delta_{26} & 0 & 0 & \omega_d^{26,35} \\ 0 & \Sigma_{35} & \omega_d^{26,35} & 0 \\ 0 & \omega_d^{26,35} & -\Sigma_{35} & 0 \\ \omega_d^{26,35} & 0 & 0 & -\Sigma_{26} \end{bmatrix}_{|2\rangle,|3\rangle,|5\rangle,|6\rangle}$$

$$(4.33)$$

In accordance with Eq. (4.33), the CP Hamiltonian in each subspace (4×4, coupled) is equivalent to the matrix representation of a dipolar coupled two spin-1/2 systems [see Eq. (2.20) in Chapter 2]. Therefore, the polarization transfer in each subspace is expected to follow a similar mechanism. As shown in Eq. (4.12), each subspace of the CP Hamiltonian is associated with longitudinal (composed of the RF irradiation and quadrupolar coupling part) and transverse (effective dipolar coupling part) components, which correspond to the energy (position of avoided crossing/HH CP matching condition) and driving field/potential, respectively. From a mathematical perspective, the energy transfer in each subspace is analogous to a two-level system (TLS). Consequently, the polarization transfer mechanism in I = 1/2 and S = 1 spin systems will be a manifestation of six independent TLS. Therefore, various HH CP conditions are anticipated (also shown in previous section) to exhibit different spin-dynamics.

As shown in Figure 4.11, we observed a total of six LACs or resonance conditions at $\nu_{1H} \neq$ 0 kHz and these conditions are labeled in accordance with Figure 4.3. As shown previously, it is evident that the $TQ_{16}/DQ_{15}/ZQ_{35}$ HH CP conditions are just phase-shifted version of the $SQ_{34}/ZQ_{24}/DQ_{26}$ HH CP conditions. For single-crystal sample at $C_Q = 1.5$ MHz, we observed well-resolved LACs and the area beneath each LAC decrease continuously with increase in the ¹H RF field requirements for various LACs. The area under a LAC is direct manifestation of the strength of the perturbation (effective dipolar coupling) acting between the states involved in CP transfer. As the strength of the effective dipolar coupling decreases for the CP resonances occurring at a higher ¹H RF range, therefore, we observed different area under LACs. As seen in Figure 4.11, the ZQ_{24} transition has the weakest effective dipolar coupling constant indicating that the CP transfer occur through a non-adiabatic (sudden jump; $P_{i\to j}^{ad}$ decreases, for detail refer to Eq. 2.27 in Chapter 2), which falls rapidly away from the exact resonance condition. Consequently, this result in a sharp CP resonance as depicted in Figure 4.3 panels a2-b2. Whereas the SQ₃₄ CP resonance possess the strongest effective dipolar coupling constant $\omega_d^{16,34} > \omega_d^{26,35} > \omega_d^{15,24}$; this order is quadrupolar parameter dependent). At the specified quadrupolar coupling parameters and RF-field amplitudes, at the SQ₃₄ CP condition the adiabatic transitions have the maximum probability $(P_{i\to j}^{ad} \approx 1)$ for these transitions while the DQ₂₆ condition has finite probability for both adiabatic and sudden transitions. In addition to these normal modes of CP transfer, we also observe avoided crossings at $\nu_{1H} = 0$ kHz which are governed by the I-spin dipolar transitions ($SQ_{d,I}$). This zero-field avoided crossing is equivalent to the polarization pathway arising due to the interference terms $(\omega_{eff}^{(ij)} \pm \omega_{eff}^{(kl)})$ in the CP signal expression [Eq. (4.20)] (in operator-based analytic theory). It should also be noted that at this zero-field condition a significant loss in the I-spin polarization (refer to $\langle \hat{I}_x(t) \rangle$ detection in Figure D.8 in Appendix-D) is observed during the transfer process while the gain in the S-spin polarization (via $<\hat{S}_x(t)>$ detection) is minimal. This is primarily due to the involvement of $\hat{I}_x\hat{S}_z$ (SQ_{d,I}) transition operators in the polarization transfer process.

A quantitative measure of the degree of the polarization transfer in the state-picture



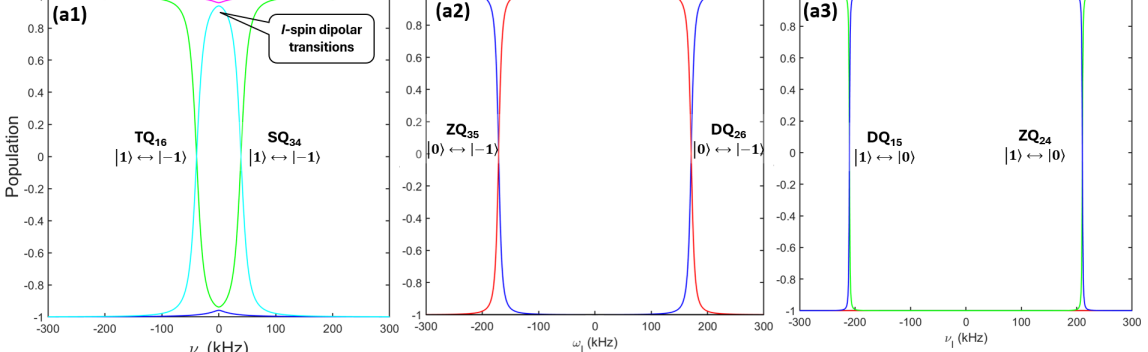


Figure 4.12: The population exchange dynamics for different HH CP Matching conditions as a function of $^1\mathrm{H}$ RF amplitude for a single-crystal sample. The population coefficients for different HH matching conditions are calculated based on the final density matrix calculation as given in Eqs. (4.16), (4.18), (4.17) and are given as (a1) SQ₃₄ (ρ_{33} , ρ_{44}): (sin² θ_{34} , -sin² θ_{34}) and TQ₁₆ (ρ_{11} , ρ_{66}): (sin² θ_{16} , -sin² θ_{16}); (a2) ZQ₃₅ (ρ_{33} , ρ_{55}): (sin² θ_{35} , -sin² θ_{35}) and DQ₂₆ (ρ_{22} , ρ_{66}): (sin² θ_{26} , -sin² θ_{26}); and (a3) ZQ₂₄ (ρ_{22} , ρ_{44}): (sin² θ_{24} , -sin² θ_{24}) and DQ₁₅ (ρ_{11} , ρ_{55}): (sin² θ_{15} , -sin² θ_{15}). The area between each avoided crossing can be correlated with the width of each CP resonance observed in Figure 4.3. Remaining simulation parameters are as given in the caption of Figure 4.11.

representation can be obtained by plotting the population exchange diagram at various LACs. Although, the state-picture representation necessitate the evaluation of populations of various Eigen-states by calculating degree of the overlaps between two Eigen-states $(\langle i' | \mathbb{I} | i' \rangle; \mathbb{I})$ is the identity operator and $|i'\rangle$ is the Eigen-states which is a superposition of the Zeeman-states governed by the unitary transformations involved in the calculation of the effective CP Hamiltonian). An analogous representation can be obtained by plotting the population coefficients from the density matrix calculation. The population exchange at various LACs are shown in Figure 4.12 where the population is plotted by selecting the coefficients of all Zeeman states in the final density matrix in Eqs. (4.16)-(4.18)(see Figure cation for more information). In the population diagram (panel a1), clearly $|1\rangle/|6\rangle$ and $|3\rangle/|4\rangle$ exchange their populations (i.e. population difference becomes zero $\hat{\rho}_{ii} - \hat{\rho}_{jj} = 0$) at exact HH CP matching condition which correlates well with the Figure 4.3 and point towards an adiabatic transfer. In this panel, we observe two additional avoided crossing at $\nu_{1H} = 0$ kHz, where there is no significant population exchange, again highlighting the presence of $SQ_{d,I}$ I-spin dipolar transitions. Nevertheless, the population exchange dynamics observed in the panels a2-a3 for the DQ_{26}/ZQ_{35} and ZQ_{24}/DQ_{15} CP matching conditions, respectively demonstrates a behavioural shift from adiabatic to sudden transitions. Besides, the area in between two population curves directly signifies the width of the overall CP transfer as observed in Figure 4.3. It is important to note that the aforementioned observations are based on the parameter used while generating the simulations and the nature of CP dynamics may change by selecting other parameters set while the analytic description will hold good. In summary, a detailed account of all the observations made by the analytic theory can be found in the energy level representation.

4.3 Conclusions

In summary, the operator-based analytic theory provides a single-unified framework for a detailed theoretical description of the CP dynamics between I=1/2 and S=1 spin systems under second-order quadrupolar coupling and S-spin off-resonance irradiation. The proposed analytic theory is rigorously compared with the numerical simulations under all experimentally relevant simulation parameters. The spin-dynamics is manifestation of six different HH CP matching conditions namely, SQ₃₄, TQ₁₆, ZQ₂₄, DQ₁₅, ZQ₃₅ and DQ₂₆, ZQ₂₄ and DQ₁₅. We have derived a CP signal expression quantifying the individual contribution from all possible CP conditions in the overall CP transfer. For single-crystal sample, due to a similar operator dependencies the second-order quadrupolar coupling and S-spin off-resonances display similar CP dynamics and it is demonstrated that off-resonant irradiation at $\Omega_{1S} = -\omega_Q^{(2)}$ can compensate the effect of the second-order quadrupolar coupling. It is shown that various CP resonances displays different CP dynamics under second-order quadrupolar coupling and S-spin off-resonance irradiations. For example, the intensity of the CP resonance observed at lower RF-field amplitude will decrease while the intensity of the CP resonance at higher RF-fields increases. We have explicitly shown the role of the orientation of the quadrupolar coupling tensor in alerting the polarization dynamics for the single-crystal sample, which simplified the understanding of more complex powder sample. In the powder sample, the second-order quadrupolar coupling and S-spin off-resonance irradiation does not displays similar dynamics due to complex orientation dependence later. Due to the interplay of various HH CP matching conditions, the overall CP transfer is an amalgamation of all six HH CP matching conditions, the individual CP condition will have no significance in such systems. The proposed theory is equally valid for single-crystal and powder samples across all regimes of the quadrupolar coupling. It is not possible to exactly compensate for the second-order quadrupolar coupling by off-resonance irradiations, however, by irradiating at $\Omega_{1S} = -\omega_Q^{(2)}(90^\circ)$ a compromise can be made. We have also provided a state-picture representation equivalent to the operator-based analytic theory.

Chapter 5

Analytic theory of cross-polarization (CP) dynamics between spin-1/2 and spin-3/2 nuclei

In this chapter of the thesis, a theoretical framework for understanding the CP spin-dynamics involving nuclei with I=1/2 and S=3/2 is presented. The half-integer quadrupolar nuclei account for approximately 70% of the total quadrupolar nuclei and are prevalent in many inorganic and bio-organic importance compounds [71, 157–160]. Consequently, these nuclei serve as an attractive tool for structural constraints. The presence of the first-order quadrupolar coupling devoid central transition (CT_s) ($|-1/2\rangle \leftrightarrow$ |1/2\) made half-integer nuclei a favourable choice for various structural investigations compared to nuclei with integer spins [161–164]. Nonetheless, the poor S/N ratio is often observed due to large quadrupolar coupling and their lower gyromagnetic ratio and/or natural abundance. As a result, the direct observation of the half-integer quadrupolar nuclei via the selective excitation of the CT_s has not gained significant popularity in quadrupolar NMR studies [53, 165]. Consequently, numerous experimental approaches have been developed to achieve an efficient excitation of quadrupolar NMR spectra. A widely accepted method for improving the sensitivity of spin-1/2 dilute spins involves the implementation of cross-polarization (CP) experiments. Nevertheless, CP involving quadrupolar spins is limited by the complicated mechanism of the polarization transfer due to the presence of multiple-energy levels and poor spin-locking efficiency [106,156,166–168]. Despite notable advancements [101, 106, 169–175], our complete understanding of the complex CP dynamics remained elusive. From a theoretical standpoint, Vega et. al. [47] and Amoureux et. al. [82] laid the foundation of quantitative analysis of numerous experimental studies based on CP. Using the fictitious spin-1/2 operator formalism, the analytic theory presented by Vega et. al. suggested the existence of various HH CP matching conditions; however, the major focus remained on the polarization transfer involving central and triple-quantum quadrupolar spin transitions, namely CT_S (SQ) and TQ_S CP transfer processes. Under on-resonance S-spin irradiation, they presented the analytical treatments in the extreme coupling regimes i.e. $\omega_{1S} > \omega_Q^{(1)}$ and $\omega_{1S} << \omega_Q^{(1)}$ for the static single-crystal sample. For the single-quantum (SQ) CP, the HH CP matching condition expressions were derived as $\omega_{1I} = \omega_{1S}$ and $\omega_{1I} = (S+1/2)\omega_{1S}$ in $\omega_{1S} > \omega_Q^{(1)}$ and $\omega_{1S} << \omega_Q^{(1)}$ coupling regimes, respectively, which mainly transfer the *I*-spin polarization

only to S-spin central transition. While for triple-quantum cross-polarization (TQCP), they presented the HH CP matching condition expressions as $\omega_{1I} = 3\omega_{1S}$ and $\omega_{1I} = \omega_{S,nut}$ [82] in $\omega_{1S} > \omega_Q^{(1)}$ and $\omega_{1S} << \omega_Q^{(1)}$ coupling regimes, respectively. Here, $\omega_{S,nut}$ is the nutation frequency for S=1 in the strong coupling regime ($\omega_{1S} << \omega_Q^{(1)}$). Nevertheless, in intermediate coupling regime $i.e., \omega_{1S} \approx \omega_Q^{(1)}$, due to complicated derivation no theoretical description was presented. The lack of unified description across all the quadrupolar coupling regimes, these description are of lesser utility in the single-crystal sample of arbitrary quadrupolar coupling strengths and crystallite-orientations. Importantly, the distribution of quadrupolar coupling frequencies limited the utility of these formulations in quantifying the CP profiles in powder samples. Later, Amoureux et. al. extended the analytical description provided by the Vega for spinning sample while the underlying shortcoming remained. To overcome these challenges, alternate description based on the quadrupolar interaction [109, 148, 149] were presented for describing the spin dynamics involving quadrupolar spins. The application of perturbative approach based on the Average Hamiltonian theory (AHT) and Floquet theory have led to the development of semi-analytical approaches designed to elucidate experimental findings associated with quadrupolar spins, relevant to both static and rotating solids. The theoretical limitation of these methods have been already pointed out in Chapter 1. Therefore, a detailed mathematical model framework based on the analytic theory described in the coupled spin operator basis that is valid for all the quadrupolar coupling regimes is not available. This forms the motivation behind this chapter. In this chapter of thesis, we have substantiated the theory behind the spin dynamics of the cross-polarization between an isolated spin pair I = 1/2 and S = 3/2 for static samples. We have used the effective field and density operator formalism to derive the effective Hamiltonian represented in the coupled spin operator basis.

5.1 Theory and Methodology

5.1.1 Derivation of the effective CP Hamiltonian

In order to describe the fundamental operational aspects of the CP experiment, we start with a model two-spin (say, I=1/2 and S=3/2) Hamiltonian. In the doubly rotating frame, the Hamiltonian of such a system under on-resonance irradiation (on the spins I and S) is represented by

$$\hat{H}_{CP} = \underbrace{\omega_{1S}\hat{S}_{x}}_{\hat{H}_{S}^{RF}} + \underbrace{\frac{\omega_{Q}^{(1)}(\alpha_{Q}, \beta_{Q})}{2}(3\hat{S}_{z}^{2} - \hat{S}^{2})}_{\hat{H}_{S}^{Q}} + \underbrace{\omega_{1I}\hat{I}_{x}}_{\hat{H}_{IS}} + \underbrace{2\omega_{d}\hat{I}_{z}\hat{S}_{z}}_{\hat{H}_{IS}^{D}}; \quad \hbar = 1.$$
(5.1)

In the above equation, ω_{1I} and ω_{1S} represent the RF amplitudes on I and S spins, respectively. \hat{H}_S^Q is the first-order quadrupolar Hamiltonian for the S-spin. A detailed description of the quadrupolar Hamiltonian can be found in Chapter 1. The matrix

representation of the various spin-operators [in Eq. (5.1)] for the both I and S-spins can be found in Appendix-E.

To simplify the description, the above Hamiltonian is re-expressed in terms of the single-transition operators [111,112] as given below:

$$\hat{H}_{CP} = \underbrace{\sqrt{3}\omega_{1S}(\hat{S}_{x}^{12} + \hat{S}_{x}^{34} + \hat{S}_{x}^{56} + \hat{S}_{x}^{78}) + 2\omega_{1S}(\hat{S}_{x}^{23} + \hat{S}_{x}^{67}) + \omega_{Q}^{(1)}(\hat{S}_{z}^{12} - \hat{S}_{z}^{34} + \hat{S}_{z}^{56} - \hat{S}_{z}^{78})}_{\hat{H}_{S}} + \underbrace{\omega_{1I}(\hat{S}_{x}^{15} + \hat{S}_{x}^{26} + \hat{S}_{x}^{37} + \hat{S}_{x}^{48})}_{\hat{H}_{IS}^{RF}} + \underbrace{\omega_{d}(3\hat{S}_{z}^{14} + \hat{S}_{z}^{23} - 3\hat{S}_{z}^{58} - \hat{S}_{z}^{67})}_{\hat{H}_{IS}^{D}}.$$
(5.2)

The superscript (i,j) in the operators \hat{S}_{α}^{ij} ($\alpha=x,y,z$) represents the spin-states in a coupled system and are defined according to the energy level diagram depicted in Figure 5.1(a). The definition of these single-transitions operators can be found in Chapter 1. A schematic description of the populations and coherences observed in a coupled spin-pair (I=1/2 and S=3/2) is given in Figure 5.1(b). While the matrix representation of the various spin-operators and their product Zeeman basis is given in Appendix-D. In order to gain insights into the CP spin dynamics and enable an analytical description, the Hamiltonian [Eq. (5.2)] is divided into three parts:

- 1. Hamiltonian for the S-spin system $(\hat{H}_S = \hat{H}_S^{RF} + \hat{H}_S^Q)$
- 2. Hamiltonian for the *I*-spin system (\hat{H}_I^{RF})
- 3. Hamiltonian for the *I-S* spin pair (\hat{H}_{IS}^D)

Subsequently, employing unitary transformations, the Hamiltonians are diagonalized using the procedure outlined below.

A: Derivation of effective Hamiltonian for the S-spin system

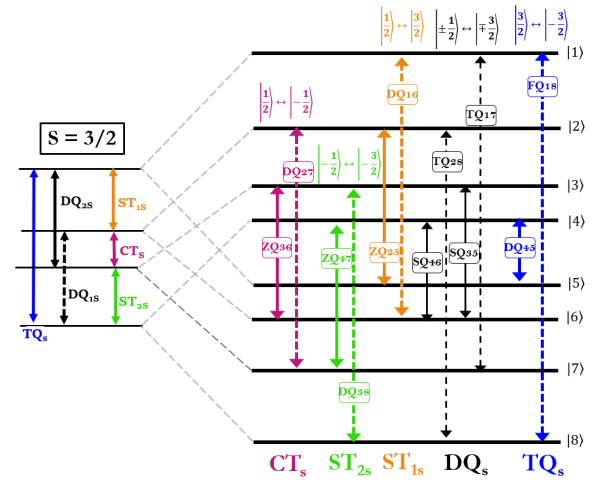
To diagonalize the S-spin Hamiltonian, we employ the following transformation that has been extensively discussed in literature [176].

$$\hat{U}_{1} = \exp\left\{\iota\frac{\pi}{2}(\hat{S}_{y}^{14} - \hat{S}_{y}^{23} + \hat{S}_{y}^{58} - \hat{S}_{y}^{67})\right\} \exp\left\{2\iota\theta_{2}(\hat{S}_{y}^{24} + \hat{S}_{y}^{68})\right\} \exp\left\{2\iota\theta_{1}(\hat{S}_{y}^{13} + \hat{S}_{y}^{57})\right\}. (5.3)$$

The unitary transformation function \hat{U}_1 is selected to ensure that the Hamiltonian is diagonal in the chosen coupled basis representation depicted in Figure 5.1(b). This is achieved by selecting the angles θ_1 and θ_2 as $\tan 2\theta_1 = \frac{\sqrt{3}\omega_{1S}}{\omega_O^{(1)} - \omega_{1S}}$ and $\tan 2\theta_2 = \frac{\sqrt{3}\omega_{1S}}{\omega_O^{(1)} - \omega_{1S}}$

$$\frac{\sqrt{3}\omega_{1S}}{\omega_{O}^{(1)}+\omega_{1S}}$$
. The S-spin Hamiltonian in Eq. (5.2) is transformed as

$$\tilde{\hat{H}}_S = \frac{\omega_{13,57}}{2} (\hat{S}_z^{13} + \hat{S}_z^{57}) - \frac{\omega_{24,68}}{2} (\hat{S}_z^{24} + \hat{S}_z^{68}) + \omega_{1S} (\hat{S}_z^{12} + \hat{S}_z^{34} + \hat{S}_z^{56} + \hat{S}_z^{78})$$
(5.4)



 $|1\rangle$ |3> |4> |5> |6> |7> |8) |2) SQ. DQ. TQ. SQ_{I} TQ_{IS} $\langle 1 |$ SQ_s P_{22} SQ_s DQ $SQ_{_{I}}$ TQ_{rs} (2) DQ_s SQ_s SQ_s SQ_{IS} (3| TQ_s $\mathrm{SQ}_{\mathrm{IS}}$ DQ_{s} SQ_{s} $SQ_{_{\rm I}}$ (4| ZQ_{rs} SQ_{is} $SQ_{_{\rm I}}$ SQ_s DQ_s TQ_{is} (5) DQ_{is} SQ_{I} SQ_s SQ_{IS} SQ_s DQ_s (6| $\mathrm{TQ}_{\mathrm{IS}}$ $SQ_{_{\rm I}}$ ZQ_{-} DQ_s SQ_{s} SQ_{s} (7) TQ_{IS} TQ_s DQ_s P_{88} (8)

Twelve different dipolar coupling mediated pathways

Figure 5.1: (a) Schematic depiction of the energy level diagram in a coupled two-spin (I = 1/2 and S = 1) system. The spin states $|1\rangle$, $|2\rangle$, $|3\rangle$, $|4\rangle$, $|5\rangle$, $|6\rangle$, $|7\rangle$ and $|8\rangle$ are representative of the product basis states $(|m_I, m_S\rangle)$ $|1/2, 3/2\rangle$, $|1/2, 1/2\rangle$, $|1/2, -1/2\rangle$, $|1/2, -3/2\rangle$ $|-1/2, 3/2\rangle$, $|-1/2, 1/2\rangle$, $|-1/2, -1/2\rangle$ and $|-1/2, -3/2\rangle$, respectively. (b) Matrix representation of the populations and coherences in the coupled two-spin (I andS) system. The diagonal elements depict the populations (of the states $|m_I, m_S\rangle$) and are represented through P_{ii} . The coherences wherein both spins change their states are represented as the four-quantum (FQ_{IS}), triple-quantum (TQ_{IS}), double-quantum (DQ_{IS}) , single-quantum (SQ_{IS}) , and zero-quantum (ZQ_{IS}) . The coherences where only the state of S-spin changes are represented by TQ_S , DQ_S and SQ_S , while, coherences where only the state of I-spin changes are represented by, SQ_I . The coherence/transitions involving the S-spin are further categorized as single-quantum central transition (CT_S: $|-1/2\rangle \leftrightarrow |1/2\rangle$), single-quantum satellite transitions ST_{1S} and ST_{2S} ($|3/2\rangle \leftrightarrow |1/2\rangle$ and $|-3/2\rangle \leftrightarrow |-1/2\rangle$, respectively) and double-quantum transitions DQ_{1S} and DQ_{2S} ($|3/2\rangle \leftrightarrow$ $|-1/2\rangle$ and $|-3/2\rangle \leftrightarrow |1/2\rangle$, respectively). The blue-colored (FQ_{IS}/DQ_{IS}) coherences involve triple-quantum transitions associated with the S-spin $(|+3/2\rangle \leftrightarrow |-3/2\rangle)$, while magenta, orange and green-colored (DQ_{IS}/ZQ_{IS}) coherences involve single-quantum transitions associated with S-spin, CT_S ($|1/2\rangle \leftrightarrow |1/2\rangle$), ST_{1S} ($|3/2\rangle \leftrightarrow |1/2\rangle$) and ST_{2S} ($|-3/2\rangle \leftrightarrow |-1/2\rangle$), respectively. The black-colored (TQ_{IS}/SQ_{IS}) coherences involve double-quantum transition associated with the S-spin transitions $(DQ_S | \pm 3/2) \leftrightarrow$ $|\pm 1/2\rangle$).

where, $\omega_{13,57} = \sqrt{3\omega_{1S}^2 + (\omega_Q^{(1)} - \omega_{1S})^2}$ and $\omega_{24,68} = \sqrt{3\omega_{1S}^2 + (\omega_Q^{(1)} + \omega_{1S})^2}$. Using the relation $\hat{S}_z^{ik} = \hat{S}_z^{ij} + \hat{S}_z^{jk}$, the above Hamiltonian can be re-arranged as follows:

$$\hat{\hat{H}}_{S} = \left\{ \frac{\omega_{13,57} - \omega_{24,68} + 2\omega_{1S}}{4} \right\} (\hat{S}_{z}^{14} + \hat{S}_{z}^{58}) + \left\{ \frac{\omega_{13,57} - \omega_{24,68} - 2\omega_{1S}}{4} \right\} (\hat{S}_{z}^{23} + \hat{S}_{z}^{67})
+ \left\{ \frac{\omega_{13,57} + \omega_{24,68} + 2\omega_{1S}}{4} \right\} (\hat{S}_{z}^{12} + \hat{S}_{z}^{56}) + \left\{ \frac{\omega_{13,57} + \omega_{24,68} - 2\omega_{1S}}{4} \right\} (-\hat{S}_{z}^{34} - \hat{S}_{z}^{78}).$$
(5.5)

The effectiveness of the Hamiltonian given in Eq. (5.5) has been evaluated in the existing literature [176] and is demonstrated to offer the convergent solutions to the spin-dynamics

across all quadrupolar coupling regimes.

B: Derivation of effective Hamiltonian for the *I*-spin system

Similarly, by utilising the unitary transformation $\hat{U}_2 = \exp\left\{i\frac{\pi}{2}(\hat{S}_y^{15} + \hat{S}_y^{26} + \hat{S}_y^{37} + \hat{S}_y^{48})\right\}$, the Hamiltonian for the *I*-spin is transformed such that it is diagonal in the chosen basis.

$$\hat{\hat{H}}_I = \omega_{1I}(\hat{S}_z^{15} + \hat{S}_z^{26} + \hat{S}_z^{37} + \hat{S}_z^{48}).$$
 (5.6)

C: Derivation of effective Hamiltonian for the IS-spin system

To have a consistent description, the dipolar coupling Hamiltonian (\hat{H}_{IS}) is also transformed by the same set of unitary transformations employed on the S and I-spin Hamiltonians.

$$\hat{\hat{H}}_{IS}^{D} = \hat{U}_{2}\hat{U}_{1}\hat{H}_{IS}^{D}\hat{U}_{1}^{\dagger}\hat{U}_{2}^{\dagger}
= \omega_{d}^{18,45}(\hat{S}_{x}^{18} + \hat{S}_{x}^{45}) + \omega_{d}^{27,36}(\hat{S}_{x}^{27} + \hat{S}_{x}^{36}) + \omega_{d}^{16,25}(\hat{S}_{x}^{16} + \hat{S}_{x}^{25}) + \omega_{d}^{38,47}(\hat{S}_{x}^{38} + \hat{S}_{x}^{47})
(5.7)$$

where, $\omega_d^{18,45}$, $\omega_d^{27,36}$, $\omega_d^{16,25}$ and $\omega_d^{38,47}$ are the effective dipolar coupling constants in various dipolar coupled subspaces as described below and are given in Table 5.1. As demonstrated previously, unlike single spin Hamiltonians [refer to Eqs. (5.5) and (5.6)], the transformed dipolar coupling Hamiltonian exhibits off-diagonalities in the chosen basis system. The transformed dipolar coupling Hamiltonian [Eq. (5.7)] consists of eight different sets of dipolar coupling mediated transitions, therefore, CP transfer under on-resonance irradiation is anticipated to display eight modes/pathways of polarization The dipolar transitions are classified based on the total change in the Stransfer. and I-spin quantum numbers of the transitions involved i.e. $\{1,8\}/\{2,5\}$ labeled as FQ_{18}/DQ_{25} ; and $\{1,6\}/\{2,5\}/$, $\{2,7\}/\{3,6\}/$ and $\{3,8\}/\{4,7\}$ are labeled as DQ_{ij}/ZQ_{ij} dipolar transitions. The dipolar coupling terms involving the flipping of both S and I-spins are further quantified in terms of the S-spin involved dipolar transitions as follows: FQ_{18}/DQ_{25} involves triple-quantum $(TQ_S): |3/2\rangle \leftrightarrow |-3/2\rangle$ S-spin transition; DQ_{27}/ZQ_{36} involves S-spin single-quantum central transition $(CT_S): |1/2\rangle \leftrightarrow |-1/2\rangle$; DQ_{16}/ZQ_{25} involves S-spin single-quantum satellite transition $(ST_{1S}): |3/2\rangle \leftrightarrow |1/2\rangle$; and DQ_{38}/ZQ_{47} involves S-spin single-quantum satellite transition $(ST_{21S}): |-3/2\rangle \leftrightarrow |-1/2\rangle$. The dipolar coupling transitions which involves double-quantum (DQ_S): $|-3/2\rangle \leftrightarrow$ $|1/2\rangle$ and $|3/2\rangle \leftrightarrow |-1/2\rangle$ S-spin transition were absent under on-resonance S-spin irradiations. All the dipolar coupling CP modes in Eq. (4.8) occur through single-quantum $(SQ_I): |1/2\rangle \leftrightarrow |-1/2\rangle$ *I*-spin flip.

Combining the transformed Hamiltonians $\hat{\tilde{H}}_S$, $\hat{\tilde{H}}_I^{RF}$ and $\hat{\tilde{H}}_{IS}^D$ [Eqs. (5.5), (5.6) and (5.7)], the complete Hamiltonian describing the CP dynamics is represented by the following

equation:

$$\begin{split} &\tilde{\hat{H}}_{CP} = \tilde{\hat{H}}_S + \tilde{\hat{H}}_I^{RF} + \tilde{\hat{H}}_{IS}^{D} \\ &= \Big\{ \frac{\omega_{13,57} - \omega_{24,68} + \omega_{1S}}{2} \Big\} (\hat{S}_z^{14} + \hat{S}_z^{58}) + \Big\{ \frac{\omega_{13,57} - \omega_{24,68} - \omega_{1S}}{2} \Big\} (\hat{S}_z^{23} + \hat{S}_z^{67}) \\ &+ \Big\{ \frac{\omega_{13,57} + \omega_{24,68} + \omega_{1S}}{2} \Big\} (\hat{S}_z^{12} + \hat{S}_z^{34} + \hat{S}_z^{56} + \hat{S}_z^{78}) + \omega_{1I} (\hat{S}_z^{15} + \hat{S}_z^{26} + \hat{S}_z^{37} + \hat{S}_z^{48}) \\ &+ \omega_d^{18,45} (\hat{S}_x^{18} + \hat{S}_x^{45}) + \omega_d^{27,36} (\hat{S}_x^{27} + \hat{S}_x^{36}) + \omega_d^{16,25} (\hat{S}_x^{16} + \hat{S}_x^{25}) + \omega_d^{38,47} (\hat{S}_x^{38} + \hat{S}_x^{47}). \end{split}$$

$$(5.8)$$

The transformed CP Hamiltonian in Eq. (5.8) is highly off-diagonal and hence, is of less utility in further descriptions of the spin dynamics. To overcome this issue, the transformed single spin Hamiltonians are re-expressed in terms of the operators employed in the description of the dipolar coupling Hamiltonian via the relation $\hat{S}_z^{ik} = \hat{S}_z^{ij} + \hat{S}_z^{jk}$ between the single-transition operators as given below:

$$\hat{\hat{H}}_{CP} = \Sigma_{18}\hat{S}_{z}^{18} + \Delta_{45}\hat{S}_{z}^{45} + \Sigma_{27}\hat{S}_{z}^{27} + \Delta_{36}\hat{S}_{z}^{36} + \Sigma_{16}\hat{S}_{z}^{16} + \Delta_{25}\hat{S}_{z}^{25} + \Sigma_{47}\hat{S}_{z}^{47} + \Delta_{38}\hat{S}_{z}^{38} + \omega_{d}^{18,45}(\hat{S}_{x}^{18} + \hat{S}_{x}^{45}) + \omega_{d}^{27,36}(\hat{S}_{x}^{27} + \hat{S}_{x}^{36}) + \omega_{d}^{16,25}(\hat{S}_{x}^{16} + \hat{S}_{x}^{25}) + \omega_{d}^{38,47}(\hat{S}_{x}^{38} + \hat{S}_{x}^{47}).$$
(5.9)

The coefficients in the above equation are mentioned in Table 5.1.

$$\begin{split} \tilde{\hat{H}}_{CP} &= \tilde{\hat{H}}_{18} + \tilde{\hat{H}}_{45} + \tilde{\hat{H}}_{27} + \tilde{\hat{H}}_{36} + \tilde{\hat{H}}_{16} + \tilde{\hat{H}}_{25} + \tilde{\hat{H}}_{47} + \tilde{\hat{H}}_{38} \\ &= \underbrace{\sum_{18} \hat{S}_z^{18} + \omega_d^{18,45} \hat{S}_x^{18}}_{\tilde{\hat{H}}_{18}} + \underbrace{\Delta_{45} \hat{S}_z^{45} + \omega_d^{18,45} \hat{S}_x^{45}}_{\tilde{\hat{H}}_{45}} + \underbrace{\sum_{27} \hat{S}_z^{27} + \omega_d^{27,36} \hat{S}_x^{27}}_{\tilde{\hat{H}}_{27}} + \underbrace{\Delta_{36} \hat{S}_z^{36} + \omega_d^{27,36} \hat{S}_x^{36}}_{\tilde{\hat{H}}_{36}} \\ &+ \underbrace{\sum_{16} \hat{S}_z^{16} + \omega_d^{16,25} \hat{S}_x^{16}}_{\tilde{\hat{H}}_{16}} + \underbrace{\Delta_{25} \hat{S}_z^{25} + \omega_d^{16,25} \hat{S}_x^{25}}_{\tilde{\hat{H}}_{25}} + \underbrace{\sum_{47} \hat{S}_z^{47} + \omega_d^{47} \hat{S}_x^{47}}_{\tilde{\hat{H}}_{47}} + \underbrace{\Delta_{38} \hat{S}_z^{83} + \omega_d^{38,47} \hat{S}_x^{38}}_{\tilde{\hat{H}}_{38}}. \end{split}$$

Thus, the new representation of the CP Hamiltonian include contributions emerging from the eight transitions (that involve flipping of both spins) present in the coupled basis [refer to Figure 5.1(a)]. The term $\tilde{\tilde{H}}_{18}$ is representative of the four-quantum (FQ₁₈) transition $\left(|1/2,3/2\rangle\leftrightarrow|-1/2,-3/2\rangle\right)$, while $\tilde{\tilde{H}}_{45}$ is representative of the double-quantum (DQ₄₅) transition $\left(|1/2,-3/2\rangle\leftrightarrow|-1/2,3/2\rangle\right)$. In a similar vein, the term $\tilde{\tilde{H}}_{27}$ is representative of the double-quantum (DQ₂₇) transition $\left(|-1/2,-1/2\rangle\leftrightarrow|1/2,1/2\rangle\right)$, while $\tilde{\tilde{H}}_{36}$ is representative of the zero-quantum (ZQ₃₆) transition $\left(|1/2,-1/2\rangle\leftrightarrow|-1/2,1/2\rangle\right)$ in a coupled spin basis. The term $\tilde{\tilde{H}}_{16}$ is representative of the double-quantum (DQ₁₆) transition $\left(|1/2,3/2\rangle\leftrightarrow|-1/2,1/2\rangle\right)$, while $\tilde{\tilde{H}}_{25}$ is representative of the zero-quantum (ZQ₂₅) transition $\left(|-1/2,3/2\rangle\leftrightarrow|1/2,1/2\rangle\right)$ in a coupled spin basis. Similarly, the term $\tilde{\tilde{H}}_{47}$ is representative of the zero-quantum (ZQ₄₇) transition $\left(|1/2,-3/2\rangle\leftrightarrow|-1/2,-1/2\rangle\right)$, while $\tilde{\tilde{H}}_{38}$ is representative of the double-quantum (DQ₃₈) transition

Table 5.1: List of coefficients involved in calculations of the CP Hamiltonian [Eq. (5.8)].

Longitudinal coefficients	Transverse (dipolar) coefficients
$\Sigma_{18} = \left\{ \frac{2\omega_{1I} + (\omega_{13,57} - \omega_{24,68} + 2\omega_{1S})}{4} \right\}$	$\omega_d^{18,45} = \omega_d(\sin\theta_1\sin\theta_2 + 3\cos\theta_1\cos\theta_2)$
$\Delta_{45} = \left\{ \frac{2\omega_{1I} - (\omega_{13,57} - \omega_{24,68} + 2\omega_{1S})}{4} \right\}$	<i>a</i>
$\Sigma_{27} = \left\{ \frac{2\omega_{1I} + (\omega_{13,57} - \omega_{24,68} - 2\omega_{1S})}{4} \right\}$	$\omega_d^{27,36} = \omega_d(-3\sin\theta_1\sin\theta_2 - \cos\theta_1\cos\theta_2)$
$\Delta_{36} = \left\{ \frac{2\omega_{1I} - (\omega_{13,57} - \omega_{24,68} - 2\omega_{1S})}{4} \right\}$	
$\Sigma_{16} = \left\{ \frac{2\omega_{1I} + (\omega_{13,57} + \omega_{24,68} + 2\omega_{1S})}{4} \right\}$	$\omega_d^{16,25} = \omega_d(-\sin\theta_1\sin\theta_2 + 3\cos\theta_1\cos\theta_2)$
$\Delta_{25} = \left\{ \frac{2\omega_{1I} - (\omega_{13,57} + \omega_{24,68} + 2\omega_{1S})}{4} \right\}$	
$\Sigma_{38} = \left\{ \frac{2\omega_{1I} - (\omega_{13,57} + \omega_{24,68} - 2\omega_{1S})}{4} \right\}$	$\omega_d^{38,47} = \omega_d(-3\sin\theta_1\sin\theta_2 + \cos\theta_1\cos\theta_2)$
$\Delta_{47} = \left\{ \frac{2\omega_{1I} + (\omega_{13,57} + \omega_{24,68} - 2\omega_{1S})}{4} \right\}$	

 $\left(|-1/2,-3/2\rangle\leftrightarrow|1/2,-1/2\rangle\right)$ in a coupled spin basis. It is important to note that the magnitude of the effective dipolar couplings (ω_d^{ij}) is different in DQ₄₅/FQ₁₈, ZQ₃₆/DQ₂₇, ZQ₂₅/DQ₁₆ and ZQ₄₇/DQ₃₈ sets of transitions.

In contrast to previous literature reports [47, 82], it is important to note that the Hamiltonian in Eq. (5.10) comprises all the modes of CP transfer in a single framework. This serves as the main focus of the current study and will be substantiated in the following sections. As shown in Eq. (5.10), the CP Hamiltonian within the effective-field framework reduces to the sum of transverse (\hat{S}_x^{ij}) and longitudinal (\hat{S}_z^{ij}) operators in eight subspaces (see Figure 5.2). Subsequently, employing the rotation operators, the Hamiltonians in the respective sub-spaces are diagonalized through rotation operators (analogous to the spin-1/2) $\hat{U}_3 = \hat{U}_3^{18} \hat{U}_3^{45} \hat{U}_3^{36} \hat{U}_3^{27} \hat{U}_3^{16} \hat{U}_3^{25} \hat{U}_3^{47} \hat{U}_3^{38}$ defined in Table 5.2. The angles θ_3^{18} , θ_3^{45} , θ_3^{36} , θ_3^{36} , θ_3^{36} , θ_3^{36} , θ_3^{36} , θ_3^{36} , are chosen such that the effective-fields in individual subspaces are quantized along the z-axis and are given in Table 5.2. Subsequently, the effective

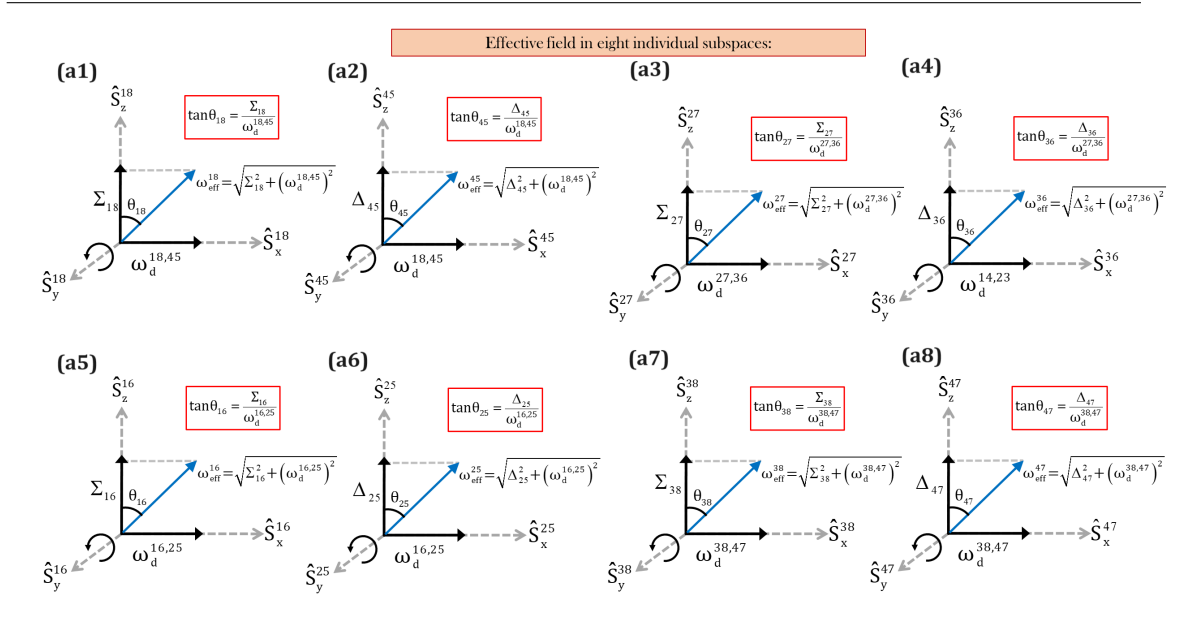


Figure 5.2: Schematic representation of the effective-fieldS in (a1) Four-quantum FQ_{18} , (a2) Double-quantum DQ_{45} , (a3) Double-quantum DQ_{27} , (a4) Zero-quantum ZQ_{36} , (a5) Double-quantum DQ_{16} , (a6) Zero-quantum ZQ_{25} , (a7) Double-quantum DQ_{38} and (a8) Zero-quantum ZQ_{47} subspaces.

Hamiltonian depicting the CP dynamics is represented by the following Eq.

$$\begin{split} \hat{H}_{eff} &= \hat{H}_{eff}^{18} + \hat{H}_{eff}^{45} + \hat{H}_{eff}^{27} + \hat{H}_{eff}^{36} + \hat{H}_{eff}^{16} + \hat{H}_{eff}^{25} + \hat{H}_{eff}^{38} + \hat{H}_{eff}^{47} \\ &= \hat{U}_{3}^{18} \hat{H}_{18} \hat{U}_{3}^{18\dagger} + \hat{U}_{3}^{45} \hat{H}_{45} \hat{U}_{3}^{45\dagger} + \hat{U}_{3}^{27} \hat{H}_{27} \hat{U}_{3}^{27\dagger} + \hat{U}_{3}^{36} \hat{H}_{36} \hat{U}_{3}^{36\dagger} \\ &+ \hat{U}_{3}^{16} \hat{H}_{16} \hat{U}_{3}^{16\dagger} + \hat{U}_{3}^{25} \hat{H}_{25} \hat{U}_{3}^{25\dagger} + \hat{U}_{3}^{38} \hat{H}_{38} \hat{U}_{3}^{38\dagger} + \hat{U}_{3}^{47} \hat{H}_{47} \hat{U}_{3}^{47\dagger} \\ &= \omega_{eff}^{18} \hat{S}_{z}^{18} + \omega_{eff}^{45} \hat{S}_{z}^{45} + \omega_{eff}^{27} \hat{S}_{z}^{27} + \omega_{eff}^{36} \hat{S}_{z}^{36} + \omega_{eff}^{16} \hat{S}_{z}^{16} + \omega_{eff}^{25} \hat{S}_{z}^{25} + \omega_{eff}^{38} \hat{S}_{z}^{38} + \omega_{eff}^{47} \hat{S}_{z}^{47}. \end{split} \tag{5.11}$$

where the effective frequencies (ω_{eff}^{ij}) in above Eq. are given in Table 5.2. The pictorial representation the effective fields in the effective CP Hamiltonian is presented in Figure 5.2.

5.1.2 Time-evolution of the spin-system during the CP mixing period

The time-evolution of spin-system is described using the standard operational process [Eq. (1.44)] [130,177]. For a consistent description, the initial density operator is transformed using the same set of unitary transformations on the S and I-spins.

$$\tilde{\hat{\rho}}(0) = \hat{U}_{3}\hat{U}_{2}\hat{U}_{1}\hat{\rho}(0)\hat{U}_{1}^{\dagger}\hat{U}_{2}^{\dagger}\hat{U}_{3}^{\dagger}
= \underbrace{\frac{1}{2}[\hat{S}_{z}^{18}]}_{\hat{\rho}_{18}(0)} + \underbrace{\frac{1}{2}[\hat{S}_{z}^{45}]}_{\hat{\rho}_{45}(0)} + \underbrace{\frac{1}{2}[\hat{S}_{z}^{27}]}_{\hat{\rho}_{27}(0)} + \underbrace{\frac{1}{2}[\hat{S}_{z}^{36}]}_{\hat{\rho}_{36}(0)} + \underbrace{\frac{1}{2}[\hat{S}_{z}^{16}]}_{\hat{\rho}_{16}(0)} + \underbrace{\frac{1}{2}[\hat{S}_{z}^{25}]}_{\hat{\rho}_{25}(0)} + \underbrace{\frac{1}{2}[\hat{S}_{z}^{38}]}_{\hat{\rho}_{38}(0)} + \underbrace{\frac{1}{2}[\hat{S}_{z}^{47}]}_{\hat{\rho}_{47}(0)}.$$
(5.12)

Table 5.2: List of all the unitary operators involved in diagonalization of the CP Hamiltonian [Eq. (5.10)] and associated coefficients.

Unitary transformations and rotation angles	Effective frequencies
$\hat{U}_{3}^{18} = \exp\left\{i\left(\frac{\pi}{2} - \theta_{3}^{18}\right)\hat{S}_{y}^{18}\right\}; \tan\theta_{3}^{18} = \frac{\Sigma_{18}}{\omega_{d}^{18,45}}$	$\omega_{eff}^{18} = \sqrt{\Sigma_{18}^2 + (\omega_d^{18,45})^2}$
$\hat{U}_{3}^{45} = \exp\left\{i\left(\frac{\pi}{2} - \theta_{3}^{45}\right)\hat{S}_{y}^{45}\right\}; \tan\theta_{3}^{45} = \frac{\Delta_{45}}{\omega_{d}^{18,45}}$	$\omega_{eff}^{45} = \sqrt{\Delta_{45}^2 + (\omega_d^{18,45})^2}$
$\hat{U}_{3}^{27} = \exp\left\{i\left(\frac{\pi}{2} - \theta_{3}^{27}\right)\hat{S}_{y}^{27}\right\}; \tan\theta_{3}^{27} = \frac{\Sigma_{27}}{\omega_{d}^{27,36}}$	$\omega_{eff}^{27} = \sqrt{\Sigma_{27}^2 + (\omega_d^{27,36})^2}$
$\hat{U}_{3}^{36} = \exp\left\{i\left(\frac{\pi}{2} - \theta_{3}^{36}\right)\hat{S}_{y}^{36}\right\}; \tan\theta_{3}^{36} = \frac{\Delta_{36}}{\omega_{d}^{27,36}}$	$\omega_{eff}^{36} = \sqrt{\Delta_{36}^2 + (\omega_d^{27,36})^2}$
$\hat{U}_{3}^{16} = \exp\left\{i\left(\frac{\pi}{2} - \theta_{3}^{16}\right)\hat{S}_{y}^{16}\right\}; \tan\theta_{3}^{16} = \frac{\Sigma_{16}}{\omega_{d}^{16,25}}$	$\omega_{eff}^{16} = \sqrt{\Sigma_{16}^2 + (\omega_d^{16,25})^2}$
$\hat{U}_{3}^{25} = \exp\left\{i\left(\frac{\pi}{2} - \theta_{3}^{25}\right)\hat{S}_{y}^{25}\right\}; \tan\theta_{3}^{25} = \frac{\Delta_{25}}{\omega_{d}^{16,25}}$	$\omega_{eff}^{25} = \sqrt{\Delta_{25}^2 + (\omega_d^{16,25})^2}$
$\hat{U}_{3}^{38} = \exp\left\{i\left(\frac{\pi}{2} - \theta_{3}^{38}\right)\hat{S}_{y}^{38}\right\}; \tan\theta_{3}^{38} = \frac{\Sigma_{38}}{\omega_{d}^{38,47}}$	$\omega_{eff}^{38} = \sqrt{\Sigma_{38}^2 + (\omega_d^{38,47})^2}$
$\hat{U}_{3}^{47} = \exp\left\{i\left(\frac{\pi}{2} - \theta_{3}^{47}\right)\hat{S}_{y}^{47}\right\}; \tan\theta_{3}^{47} = \frac{\Delta_{47}}{\omega_{d}^{38,47}}$	$\omega_{eff}^{47} = \sqrt{\Delta_{47}^2 + (\omega_d^{38,47})^2}$

The density operator at time 't' is calculated using the effective Hamiltonians [Eq. (5.11)] in respective sub-spaces as given below:

$$\hat{\rho}_{eff}(t) = \hat{\rho}_{eff}^{18}(t) + \hat{\rho}_{eff}^{45}(t) + \hat{\rho}_{eff}^{27}(t) + \hat{\rho}_{eff}^{36}(t) + \hat{\rho}_{eff}^{16}(t) + \hat{\rho}_{eff}^{25}(t) + \hat{\rho}_{eff}^{38}(t) + \hat{\rho}_{eff}^{47}(t)$$

$$(5.13)$$

where,

$$\begin{split} \hat{\rho}_{eff}^{18}(t) &= \exp\left\{-\frac{i}{\hbar}\hat{H}_{eff}^{18}t\right\} \hat{U}_{3}^{18}\hat{\rho}_{18}(0)\hat{U}_{3}^{18\dagger} \exp\left\{\frac{i}{\hbar}\hat{H}_{eff}^{18}t\right\} \\ &= \frac{1}{2}\hat{S}_{z}^{18}\sin 2\theta_{3}^{18} - \frac{1}{2}\left\{\hat{S}_{x}^{18}\cos \omega_{eff}^{18}t + \hat{S}_{y}^{18}\sin \omega_{eff}^{18}t\right\}\cos 2\theta_{3}^{18}, \end{split} \tag{5.14}$$

$$\begin{split} \hat{\rho}_{eff}^{45}(t) &= \exp\left\{-\frac{i}{\hbar}\hat{H}_{eff}^{45}t\right\} \hat{U}_{3}^{45}\hat{\rho}_{45}(0)\hat{U}_{3}^{45\dagger} \exp\left\{\frac{i}{\hbar}\hat{H}_{eff}^{45}t\right\} \\ &= -\frac{1}{2}\hat{S}_{z}^{45}\sin 2\theta_{3}^{45} - \frac{1}{2}\left\{\hat{S}_{x}^{45}\cos 2\omega_{eff}^{45}t + \hat{S}_{y}^{45}\sin 2\omega_{eff}^{45}t\right\}\cos 2\theta_{3}^{45}, \end{split} \tag{5.15}$$

$$\hat{\rho}_{eff}^{27}(t) = \exp\left\{-\frac{i}{\hbar}\hat{H}_{eff}^{27}t\right\}\hat{U}_{3}^{27}\hat{\rho}_{27}(0)\hat{U}_{3}^{27\dagger}\exp\left\{\frac{i}{\hbar}\hat{H}_{eff}^{27}t\right\}$$

$$= \frac{1}{2}\hat{S}_{z}^{27}\sin 2\theta_{3}^{27} - \frac{1}{2}\left\{\hat{S}_{x}^{27}\cos 2\omega_{eff}^{27}t + \hat{S}_{y}^{27}\sin 2\omega_{eff}^{27}t\right\}\cos 2\theta_{3}^{27},$$
(5.16)

$$\begin{split} \hat{\rho}_{eff}^{36}(t) &= \exp\left\{-\frac{i}{\hbar}\hat{H}_{eff}^{36}t\right\} \hat{U}_{3}^{36}\hat{\rho}_{36}(0)\hat{U}_{3}^{36\dagger} \exp\left\{\frac{i}{\hbar}\hat{H}_{eff}^{36}t\right\} \\ &= -\frac{1}{2}\hat{S}_{z}^{36}\sin 2\theta_{3}^{36} - \frac{1}{2}\left\{\hat{S}_{x}^{36}\cos 2\omega_{eff}^{36}t + \hat{S}_{y}^{36}\sin 2\omega_{eff}^{36}t\right\}\cos 2\theta_{3}^{36}, \end{split} \tag{5.17}$$

$$\hat{\rho}_{eff}^{16}(t) = \exp\left\{-\frac{i}{\hbar}\hat{H}_{eff}^{16}t\right\}\hat{U}_{3}^{16}\hat{\rho}_{16}(0)\hat{U}_{3}^{16\dagger}\exp\left\{\frac{i}{\hbar}\hat{H}_{eff}^{16}t\right\}$$

$$= \frac{1}{2}\left[\hat{S}_{z}^{16}\sin 2\theta_{3}^{16} - \frac{1}{2}\left\{\hat{S}_{x}^{16}\cos 2\omega_{eff}^{16}t + \hat{S}_{y}^{16}\sin 2\omega_{eff}^{16}t\right\}\cos 2\theta_{3}^{16},$$
(5.18)

$$\hat{\rho}_{eff}^{25}(t) = \exp\left\{-\frac{i}{\hbar}\hat{H}_{eff}^{25}t\right\}\hat{U}_{3}^{25}\hat{\rho}_{25}(0)\hat{U}_{3}^{25\dagger}\exp\left\{\frac{i}{\hbar}\hat{H}_{eff}^{25}t\right\}$$

$$= -\frac{1}{2}\hat{S}_{z}^{25}\sin 2\theta_{3}^{25} - \frac{1}{2}\left\{\hat{S}_{x}^{25}\cos 2\omega_{eff}^{25}t + \hat{S}_{y}^{25}\sin 2\omega_{eff}^{25}t\right\}\cos 2\theta_{3}^{25},$$
(5.19)

$$\hat{\rho}_{eff}^{38}(t) = \exp\left\{-\frac{i}{\hbar}\hat{H}_{eff}^{38}t\right\}\hat{U}_{3}^{38}\hat{\rho}_{38}(0)\hat{U}_{3}^{38\dagger}\exp\left\{\frac{i}{\hbar}\hat{H}_{eff}^{38}t\right\}
= -\frac{1}{2}\left[\hat{S}_{z}^{38}\sin 2\theta_{3}^{38} - \frac{1}{2}\left\{\hat{S}_{x}^{38}\cos 2\omega_{eff}^{38}t + \hat{S}_{y}^{38}\sin 2\omega_{eff}^{38}t\right\}\cos 2\theta_{3}^{38},$$
(5.20)

$$\hat{\rho}_{eff}^{47}(t) = \exp\left\{-\frac{i}{\hbar}\hat{H}_{eff}^{47}t\right\}\hat{U}_{3}^{47}\hat{\rho}_{47}(0)\hat{U}_{3}^{47\dagger}\exp\left\{\frac{i}{\hbar}\hat{H}_{eff}^{47}t\right\}$$

$$= \frac{1}{2}\hat{S}_{z}^{47}\sin 2\theta_{3}^{47} - \frac{1}{2}\left\{\hat{S}_{x}^{47}\cos 2\omega_{eff}^{47}t + \hat{S}_{y}^{47}\sin 2\omega_{eff}^{47}t\right\}\cos 2\theta_{3}^{47}.$$
(5.21)

5.1.3 Detection of the S-spin polarization

To ensure consistency in the description, the detection operator undergoes the same set of transformations. In the present context, polarization transfer from spin I to spin S is calculated. Accordingly, the expectation value of the observable $\langle \hat{S}_x(t) \rangle$ is derived employing Eq. (5.13).

$$S(t) = \langle \hat{S}_x(t) \rangle = Trace\{\hat{S}_{eff,x}.\hat{\rho}_{eff}(t)\}$$
(5.22)

where, $\hat{\rho}_{eff}(t) = \hat{\rho}_{eff}^{18}(t) + \hat{\rho}_{eff}^{45}(t) + \hat{\rho}_{eff}^{27}(t) + \hat{\rho}_{eff}^{36}(t) + \hat{\rho}_{eff}^{16}(t) + \hat{\rho}_{eff}^{25}(t) + \hat{\rho}_{eff}^{38}(t) + \hat{\rho}_{eff}^{47}(t)$. Accordingly, the final signal expression has separate contributions from the FQ₁₈, DQ₄₅, DQ₂₇, ZQ₃₆, DQ₁₆, ZQ₂₅, DQ₃₈ and ZQ₄₇ sub-spaces as given below:

$$S(t) = \langle \hat{S}_{x,18} \rangle + \langle \hat{S}_{x,45} \rangle + \langle \hat{S}_{x,27} \rangle + \langle \hat{S}_{x,36} \rangle + \langle \hat{S}_{x,16} \rangle + \langle \hat{S}_{x,25} \rangle + \langle \hat{S}_{x,38} \rangle + \langle \hat{S}_{x,47} \rangle$$

$$= \left\{ \frac{B+D}{4} \right\} \left[-\frac{(\omega_d^{18,45})^2}{\Sigma_{18}^2 + (\omega_d^{18,45})^2} \sin^2 2\omega_{eff}^{18}t + \frac{(\omega_d^{18,45})^2}{\Delta_{45}^2 + (\omega_d^{18,45})^2} \sin^2 2\omega_{eff}^{45}t \right]$$

$$+ \left\{ \frac{B+D+2}{4} \right\} \left[-\frac{(\omega_d^{27,36})^2}{\Sigma_{27}^2 + (\omega_d^{27,36})^2} \sin^2 2\omega_{eff}^{27}t + \frac{(\omega_d^{27,36})^2}{\Delta_{36}^2 + (\omega_d^{27,36})^2} \sin^2 2\omega_{eff}^{36}t \right]$$

$$+ \left\{ \frac{B-D+1}{4} \right\} \left[-\frac{(\omega_d^{16,25})^2}{\Sigma_{16}^2 + (\omega_d^{16,25})^2} \sin^2 2\omega_{eff}^{16}t + \frac{(\omega_d^{16,25})^2}{\Delta_{25}^2 + (\omega_d^{16,25})^2} \sin^2 2\omega_{eff}^{25}t \right]$$

$$+ \left\{ \frac{B-D-1}{4} \right\} \left[-\frac{(\omega_d^{38,47})^2}{\Sigma_{38}^2 + (\omega_d^{38,47})^2} \sin^2 2\omega_{eff}^{38}t + \frac{(\omega_d^{38,47})^2}{\Delta_{47}^2 + (\omega_d^{38,47})^2} \sin^2 2\omega_{eff}^{47}t \right]$$

$$(5.23)$$

where, $B = \frac{1}{2} \left(\sqrt{3} \sin 2\theta_1 + (\cos 2\theta_1 - 1) \right)$ and $D = \frac{1}{2} \left(-\sqrt{3} \sin 2\theta_2 - (\cos 2\theta_2 - 1) \right)$. As described above, the final signal expression has contributions from all the eight possible CP transfer modes and is significantly different from those derived based on existing reports in the literature [47, 82].

5.1.4 Insights into the Hartmann-Hahn CP matching conditions

According to the analytic expression [Eq. (5.23)], the CP signal can theoretically be maximised by optimising one of the eight matching conditions outlined below.

• FQ₁₈ CP matching condition:

Setting $\Sigma_{18} = 0 \implies 2\omega_{1I} = -(\omega_{13.57} - \omega_{24.68} + 2\omega_{1S}).$

Under the exact FQ_{18} CP matching condition, the resulting signal expression is given as

$$S(t) = -\left\{\frac{B+D}{4}\right\} \sin^2 2\omega_d^{18,45}t + \underbrace{S(t)_{45} + S(t)_{27} + S(t)_{36} + S(t)_{16} + S(t)_{25} + S(t)_{38} + S(t)_{47}}_{\text{High-frequency components}}.$$
(5.24)

Exactly setting the FQ₁₈ HH CP condition will not only maximize the polarization transfer through FQ₁₈ CP modes (*i.e.*, $S(t)_{18}$ component) but also increases the modulation frequencies of other signal components therefore further rendering them insignificant in the overall CP transfer. When the high-frequency terms are insignificant, the overall CP signal is reduce to a simplified form as given below:

$$S(t) = -\left\{\frac{B+D}{4}\right\} \sin^2 2\omega_d^{18,45} t. \tag{5.25}$$

This behavior could also be displayed at other HH CP conditions as well.

• DQ₄₅ CP matching condition:

Setting $\Delta_{45} = 0 \implies 2\omega_{1I} = (\omega_{13,57} - \omega_{24,68} + 2\omega_{1S}).$

The resulting signal expression is given as

$$S(t) = \left\{ \frac{B+D}{4} \right\} \sin^2 2\omega_d^{18,45} t + \underbrace{S(t)_{18} + S(t)_{27} + S(t)_{36} + S(t)_{16} + S(t)_{25} + S(t)_{38} + S(t)_{47}}_{\text{High-frequency components}}.$$
(5.26)

• DQ_{27} CP matching condition:

Setting $\Sigma_{27} = 0 \implies 2\omega_{1I} = -(\omega_{13.57} - \omega_{24.68} - 2\omega_{1S}).$

The resulting signal expression is given as

$$S(t) = -\left\{\frac{B+D+2}{4}\right\} \sin^2 2\omega_d^{27,36}t + \underbrace{S(t)_{18} + S(t)_{45} + S(t)_{36} + S(t)_{16} + S(t)_{25} + S(t)_{38} + S(t)_{47}}_{\text{High-frequency components}}.$$
(5.27)

• ZQ₃₆ CP matching condition:

Setting $\Delta_{36} = 0 \implies 2\omega_{1I} = (\omega_{13,57} - \omega_{24,68} - 2\omega_{1S}).$

The resulting signal expression is given as

$$S(t) = \left\{ \frac{B+D+2}{4} \right\} \sin^2 2\omega_d^{27,36} t + \underbrace{S(t)_{18} + S(t)_{45} + S(t)_{27} + S(t)_{16} + S(t)_{25} + S(t)_{38} + S(t)_{47}}_{\text{High-frequency components}}.$$
(5.28)

• DQ₁₆ CP matching condition:

Setting $\Sigma_{16} = 0 \implies 2\omega_{1I} = -(\omega_{13.57} + \omega_{24.68} + 2\omega_{1S}).$

The resulting signal expression is given as

$$S(t) = -\left\{\frac{B - D + 1}{4}\right\} \sin^2 2\omega_d^{16,25}t + \underbrace{S(t)_{18} + S(t)_{45} + S(t)_{27} + S(t)_{36} + S(t)_{25} + S(t)_{38} + S(t)_{47}}_{\text{High-frequency components}}.$$
(5.29)

• **ZQ**₂₅ **CP** matching condition:

Setting $\Delta_{25} = 0 \implies 2\omega_{1I} = (\omega_{13,57} + \omega_{24,68} + 2\omega_{1S}).$

The resulting signal expression is given as

$$S(t) = \left\{ \frac{B - D + 1}{4} \right\} \sin^2 2\omega_d^{16,25} t + \underbrace{S(t)_{18} + S(t)_{45} + S(t)_{27} + S(t)_{36} + S(t)_{16} + S(t)_{38} + S(t)_{47}}_{\text{High-frequency components}}.$$
(5.30)

• DQ₃₈ CP matching condition:

Setting $\Sigma_{38} = 0 \implies 2\omega_{1I} = -(\omega_{13.57} + \omega_{24.68} - 2\omega_{1S}).$

The resulting signal expression is given as

$$S(t) = -\left\{\frac{B - D - 1}{4}\right\} \sin^2 2\omega_d^{38,47}t + \underbrace{S(t)_{18} + S(t)_{45} + S(t)_{27} + S(t)_{36} + S(t)_{16} + S(t)_{25} + S(t)_{47}}_{\text{High-frequency components}}.$$
(5.31)

• ZQ₄₇ CP matching condition:

Setting $\Delta_{47} = 0 \implies 2\omega_{1I} = (\omega_{13.57} + \omega_{24.68} - 2\omega_{1S}).$

The resulting signal expression is given as

$$S(t) = \left\{ \frac{B - D - 1}{4} \right\} \sin^2 2\omega_d^{38,47} t + \underbrace{S(t)_{18} + S(t)_{45} + S(t)_{27} + S(t)_{36} + S(t)_{16} + S(t)_{25} + S(t)_{38}}_{\text{High-frequency components}}.$$
(5.32)

The signal expression for the FQ₁₈/ZQ₃₆/DQ₁₆/DQ₃₈ and DQ₄₅/DQ₂₇/ZQ₂₅/ZQ₄₇ CP conditions are governed by similar effective dipolar coupling strengths $\omega_d^{18,45}/\omega_d^{27,36}/\omega_d^{16,25}/\omega_d^{38,47}$ and are just phase-shifted versions of each other. Therefore,

these modes of the CP transfer are expected to display similar CP dynamics. The various HH CP matching conditions are given in the Table 5.3. Experimentally, $FQ_{18}/ZQ_{36}/DQ_{16}/DQ_{38}$ transfer can be achieved by shifting the phase of *I*-spin RF-field by 180° .

Table 5.3: The expression and transitions associated with various HH CP matching conditions for the CP transfer between I = 1/2 and S = 3/2 spin systems.

CP matching conditions and associated transitions	$\omega_Q^{(1)} \neq 0$	$\omega_Q^{(1)} = 0$
Four-quantum (FQ ₁₈) $ -1/2, -3/2\rangle \leftrightarrow 1/2, 3/2\rangle$	$2\omega_{1I} = -(\omega_{13,57} - \omega_{24,68} + 2\omega_{1S})$	$\omega_{1I} = -\omega_{1S}$
Double-quantum (DQ ₄₅) $ 1/2, -3/2\rangle \leftrightarrow -1/2, 3/2\rangle$	$2\omega_{1I} = (\omega_{13,57} - \omega_{24,68} + 2\omega_{1S})$	$\omega_{1I} = \omega_{1S}$
Double-quantum (DQ ₂₇) $ 1/2, 1/2\rangle \leftrightarrow -1/2, -1/2\rangle$	$2\omega_{1I} = -(\omega_{13,57} - \omega_{24,68} - 2\omega_{1S})$	$\omega_{1I} = \omega_{1S}$
Zero-quantum (ZQ ₃₆) $ 1/2, -1/2\rangle \leftrightarrow -1/2, 1/2\rangle$	$2\omega_{1I} = (\omega_{13,57} - \omega_{24,68} - 2\omega_{1S})$	$\omega_{1I} = -\omega_{1S}$
Double-quantum (DQ ₁₆) $ 1/2, 3/2\rangle \leftrightarrow -1/2, -1/2\rangle$	$2\omega_{1I} = -(\omega_{13,57} + \omega_{24,68} + 2\omega_{1S})$	$\omega_{1I} = -3\omega_{1S}$
Zero-quantum (ZQ ₂₅) $ -1/2, 3/2\rangle \leftrightarrow 1/2, -1/2\rangle$	$2\omega_{1I} = (\omega_{13,57} + \omega_{24,68} + 2\omega_{1S})$	$\omega_{1I} = 3\omega_{1S}$
Double-quantum (DQ ₃₈) $ 1/2, -3/2\rangle \leftrightarrow -1/2, -1/2\rangle$	$2\omega_{1I} = -(\omega_{13,57} + \omega_{24,68} - 2\omega_{1S})$	$\omega_{1I} = -\omega_{1S}$
Zero-quantum (ZQ ₄₇) $ -1/2, -3/2\rangle \leftrightarrow 1/2, -1/2\rangle$	$2\omega_{1I} = (\omega_{13,57} + \omega_{24,68} - 2\omega_{1S})$	$\omega_{1I} = \omega_{1S}$

5.2 Results and discussion

Following the procedure described in previous chapters, the results emerging from the analytic theory are rigorously compared with the SIMPSON simulations. For this purpose, the polarization transfer from spin I=1/2 (say, $^1{\rm H}$ and $\gamma_{^1H}=26.752\times 10^7$ rad s $^{-1}{\rm T}^{-1}$) to S=3/2 (say, $^{23}{\rm Na}$ and $\gamma_{^{23}Na}=7.081\times 10^7$ rad s $^{-1}{\rm T}^{-1}$) at proton Larmor frequency 600 MHz was examined over a wide range of experimentally relevant parameters. The discussion presented below is equally valid for any set of spin-1/2 and spin-3/2 systems. In order to conduct a systematic investigation of the role of quadrupolar coupling strength (C_Q) and orientation, the polarization transfer dynamics is separately examined for single-crystal with specific orientation (α_Q and $\beta_Q=0^\circ$) and single-crystal with varying crystallite orientations (α_Q and $\beta_Q\neq0^\circ$), followed by the powder sample. To explicate the interplay between the quadrupolar coupling constant and the amplitude of the RF field employed on the S-spin, the discussion is split into three regimes in the present study: Regime-I ($C_Q=200~{\rm kHz}$, Weak), Regime-II ($C_Q=500~{\rm kHz}$, Intermediate) and Regime-III ($C_Q=2.0~{\rm MHz}$, Strong). This division is based on the available quadrupolar coupling strength for commonly found $^{23}{\rm Na}$ compounds (e.g. 0.5 to 5 MHz [178]).

5.2.1 Description of CP dynamics in a single-crystal (with specific orientation α_Q and $\beta_Q = 0^{\circ}$)

5.2.1.1 Regime-I ($C_Q = 200 \text{ kHz}, \text{Weak}$)

The CP efficiency profiles resulting from the numerical simulations (black curve) for a single-crystal sample with $C_Q = 200$ kHz are plotted in Figure 5.3. On scanning the ¹H RF field ranging from 0 to 300 kHz, we observe the following: (a) Two well-separated CP resonances; (b) the CP resonance in the lower ¹H RF field exhibits a significantly broader profile compared to the higher ¹H RF field region, (c) a finite CP efficiency opposite to the positive/negative CP resonance is observed in the lower ¹H RF field region from the first CP resonance. The observed CP efficiency profiles exhibit a substantial deviation from those of the S=1 spin system (in Chapter 3). The overall intensity of the polarization transfer is notably high, and the resonance spread is significantly large. The presence of the first-order quadrupolar devoid central transition (CT_S) is anticipated to result in a more intense CP transfer due to perfect spin-locking like in spin-1/2 systems. To understand the above observations, we employed the signal expressions derived for the eight HH CP conditions using the concept of the effective Hamiltonian [Eq. (5.23)] and generated the corresponding CP profiles. As shown in Figure 5.3(a1), our analytic theory matches well barring some minor deviations with the numerical simulation profiles, and therefore is capable of explaining underlying CP dynamics. Interestingly, the appearance of the two CP maxima in the lower and higher ¹H RF field regions are the direct manifestation of the presence of multiple CP resonance conditions in multi-level systems. In order to understand the origin of multiple CP resonances, we evaluated the individual contributions from all eight CP matching conditions using the signal expression provided in Eq. (5.23). In the present case, the broad CP resonance at lower ¹H RF field is the amalgamation of various HH CP conditions where the DQ₂₇, DQ_{45} and ZQ_{47} CP conditions overlapped to produce a quite broad CP resonance. In the range of high ¹H RF field, this resonance is predominately described by the DQ₂₇ CP condition $(|1/2, -1/2\rangle \leftrightarrow |-1/2, 1/2\rangle)$ exactly centered at $\omega_{11} = 117$ kHz and significant contribution is provided by the ZQ₄₇ CP condition $(|1/2, -1/2\rangle \leftrightarrow |-1/2, 1/2\rangle)$ (centered at $\omega_{11} = 95.74 \text{ kHz}$). The unequal intensity is due to the different spin-locking efficiency of the involved S-spin transitions. For example, the DQ_{27} and ZQ_{47} CP conditions transfer the polarization to the CT_S ($|+1/2\rangle \leftrightarrow |-1/2\rangle$) and ST_{1S} ($|-3/2\rangle \leftrightarrow |-1/2\rangle$) of the quadrupolar spin, respectively. The later is inefficiently spin-locked due to the presence of much stronger quadrupolar coupling dependence, which deteriorates the spin-locking process due to $\omega_Q^{(1)} > \omega_{1S}$. Moreover, the ZQ₃₆ and DQ₃₈ CP conditions retained its high-frequency behaviour and does not provide any significant contribution to the overall CP efficiency at the selected high S-spin RF field strength. At lower ¹H RF field, the CP profile is dominated by the DQ₄₅ CP condition $(|1/2, -3/2\rangle \leftrightarrow |-1/2, 3/2\rangle)$ centered at $\omega_{11}=42.83$ kHz, which transfers the polarization into the triple-quantum (TQ_S) S-spin transition ($|+3/2\rangle \leftrightarrow |-3/2\rangle$). Unlike other CP resonances, the phase-shifted FQ₁₈ signal

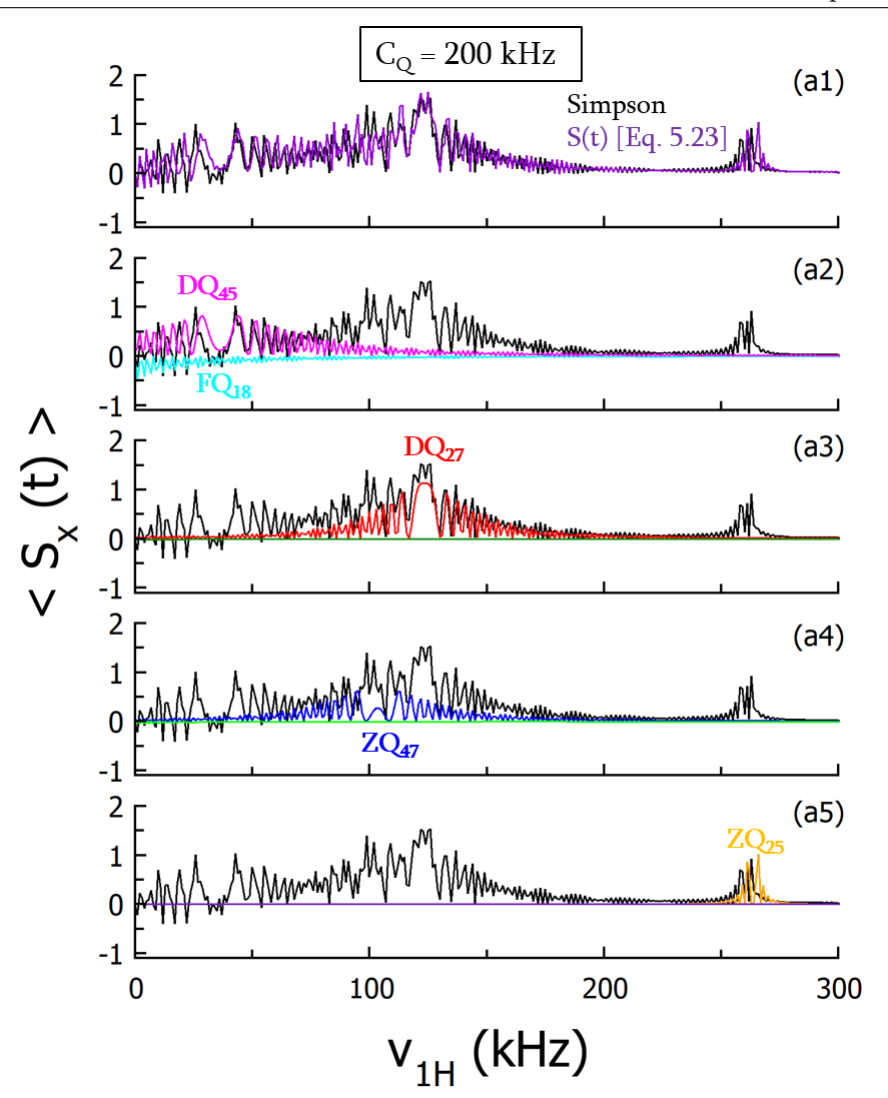


Figure 5.3: In the CP simulations depicted, the polarization build-up on the S-spin (due to transfer from the I-spin) is monitored in a single-crystal as a function of the RF field employed on the I-spin. The numerical simulations (based on SIMPSON) are represented The following parameters were employed in the simulations: by solid black lines. Quadrupolar parameters ($C_Q = 500$ kHz, $\eta_Q = 0$, quadrupolar coupling PAS angles α_Q and $\beta_Q=0^\circ)$ and dipolar coupling parameters (internuclear distance $r_{IS}=1.23$ Åand dipolar PAS angle $\beta_d = 0^{\circ}$). A constant RF amplitude of $\nu_{1S} = 80$ kHz was employed on the quadrupole, S-spin and the mixing time during the CP experiment was held constant (say $t_{mix} = 0.5$ ms). In panel (a1) the analytic simulations comprise contributions from all the eight CP matching conditions $(FQ_{18}+DQ_{45}+DQ_{27}+ZQ_{36}+DQ_{38}+ZQ_{47}+DQ_{16}+ZQ_{25})$ and is represented in violet color. In panel (a2) the analytic simulations based on the contributions from the FQ_{18} (cyan curve) and DQ_{45} (magenta color) CP conditions are depicted. In panel (a3) the analytic simulations based on the contributions from the DQ₂₇ (red curve) and ZQ₃₆ (green color) CP conditions are depicted. In panel (a4) the analytic simulations based on the contributions from the DQ_{38} (blue curve) and ZQ_{47} (light green color) CP conditions are depicted. In panel (a5) the analytic simulations based on the contributions from the DQ_{16} (indigo curve) and ZQ_{25} (orange color) CP condition are depicted.

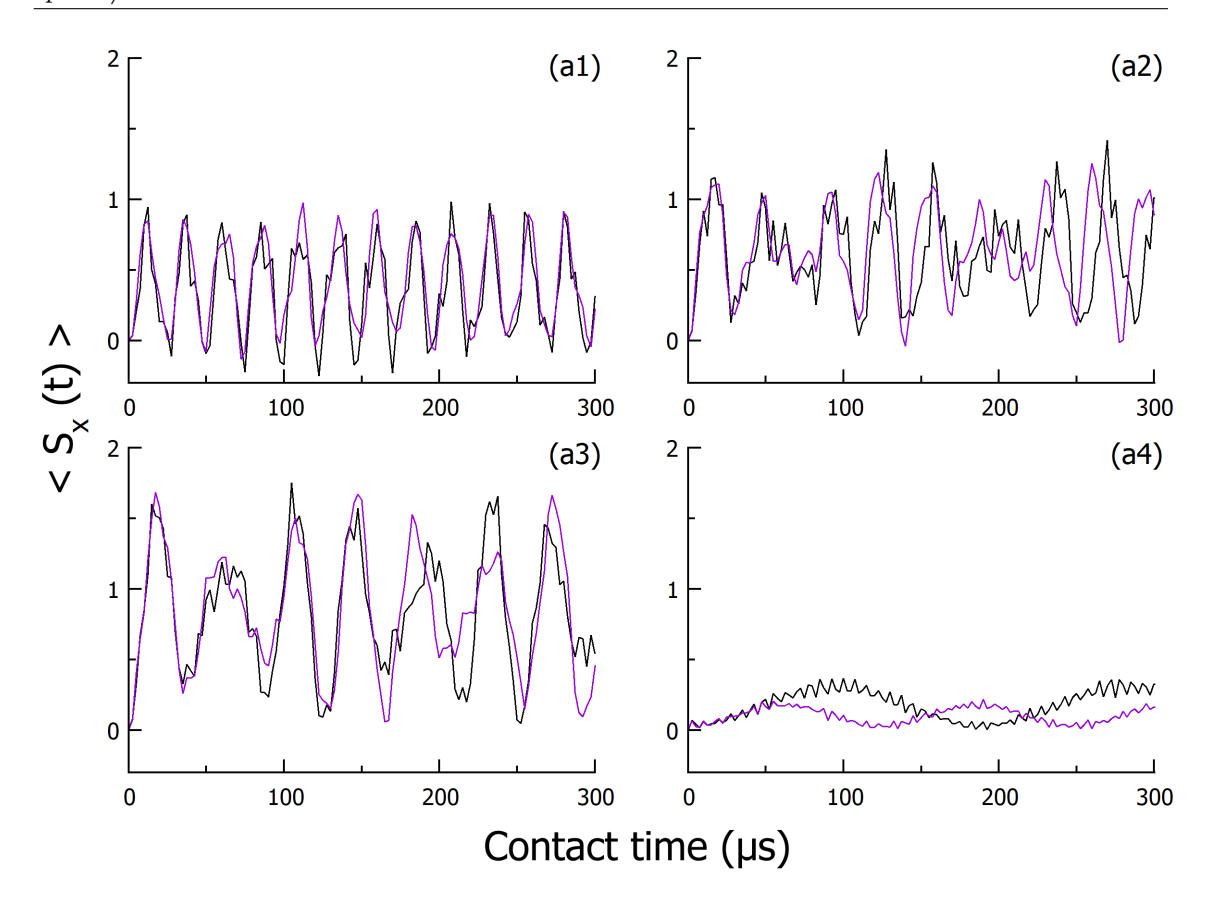


Figure 5.4: In the CP simulations depicted, the polarization build-up on the S-spin (due to transfer from the I-spin) is monitored in a single crystal as a function of the CP mixing time under constant RF field strengths on both the spins. The RF amplitudes on the I-spin were chosen based on the matching condition expression given in Table 5.3 i.e., (a1) $\nu_{1I} = 42.95$ kHz); (a2) $\nu_{1I} = 95.74$ kHz; (a3) $\nu_{1I} = 117.167$ kHz and (a1) $\nu_{1I} = 255.74$ kHz. The following parameters were employed in the simulations: Quadrupolar parameters ($C_Q = 200$ kHz, $\eta_Q = 0$, quadrupolar coupling PAS angles α_Q and $\beta_Q = 0^{\circ}$) and dipolar coupling parameters (internuclear distance $r_{IS} = 1.23$ Åand dipolar PAS angle $\beta_d = 0^{\circ}$). A constant RF amplitude of $\nu_{1S} = 80$ kHz was employed on the quadrupole, S-spin. The numerical simulations (based on SIMPSON) are represented by solid black lines and the analytic simulations comprise contributions from all the eight CP matching conditions (FQ₁₈+DQ₄₅+DQ₂₇+ZQ₃₆+DQ₃₈+ZQ₄₇+DQ₁₆+ZQ₂₅) and is represented in violet color.

component does not retain the high-frequency behaviour as explained in Eq. (5.26) and provides a significant contribution to the overall CP transfer. Therefore, the spin-locking at lower 1 H RF-field amplitudes is not uni-directional, a behaviour that is similar to the CP involving S=1. Nevertheless, the narrow CP resonance at high 1 H RF-field is solely described by the ZQ_{25} CP condition $(|1/2,3/2\rangle \leftrightarrow |-1/2,1/2\rangle)$. Whereas, due to the high RF-field requirements, the phase-shifted DQ_{16} signal component retains its high-frequency behaviour and does not contribute to the overall CP transfer. Interestingly, the CP efficiency of all the CP conditions is in the order as follows: $DQ_{27} \approx ZQ_{25} > DQ_{45} > ZQ_{47}$. The observed behaviour can be explained based on the spin-locking and excitation efficiencies of the involved S-spin transitions for various CP conditions.

As the quadrupolar coupling directly affects the spin-locking process, therefore, the CP conditions involving the CT_s and TQ_s transitions will have better CP efficiencies than the CP transitions involving the ST_s transition. However, the better CP efficiency of the ZQ_{25} can be explained based on its high excitation efficiency. This polarization transfer behaviour stands in stark contrast to S=1 spin systems, where the multi-quantum (DQ_S) transition dominates the polarization transfer at this crystallite orientation and coupling strength.

Another important parameter for consideration during polarization transfer is the widths of the various CP resonances. The widths is primarily decided by the magnitude of effective dipolar coupling strengths of the CP resonances that decreases in the order: $\omega_d^{18,45} > \omega_d^{27,36} > \omega_d^{38,47} > \omega_d^{16,25}$. These observations are manifested in the time-domain CP efficiency profiles, where the rate of polarization buildup is shown to be dependent on the strength of the effective dipolar coupling constant (Figure 5.4). The time-domain simulations at each HH CP matching condition are consistent with all the observation of the RF-domain CP efficiency profiles.

5.2.1.2 Regime-II ($C_Q = 500 \text{ kHz}$, Intermediate)

To further substantiate the above findings we studied the CP dynamics for a single-crystal sample associated with $C_Q = 500$ kHz (Figure 5.5). For a consistent description of the CP dynamics, we retained all other simulation parameters. In this coupling regime, the numerical simulation (black curves) shows three well-separated CP resonances of unequal intensities and widths. Interestingly, in contrast to contribution from the negative intensity a particular CP resonance, we observed a CP resonance with totally negative intensity which appears at quite high ¹H RF-field amplitudes. In order to comprehend the observed CP behaviour, we evaluated the analytic simulations [Eq. (5.23)], which converges well with the numerical simulations (panel a1). The individual analytic signal contributions reveal the origin of all the observed CP resonances (panel a2-a5). Due to strong quadrupolar coupling strength, the DQ_{45} and DQ_{27} CP resonances shift in the lower RF-field regions while the ZQ₂₅ CP resonance shift in the higher RF-fields region, therefore the overall CP efficiency profile widens. However, unlike the weaker quadrupolar coupling regime, the contribution from the DQ_{45} CP resonance is negligible as compared to much stronger DQ₂₇ polarization transfer. We observe almost zero CP efficiency from the ZQ_{47} CP resonances. Moreover, the phase-shifted signal components ZQ_{36} , DQ_{16} and DQ₃₈ retain their high-frequency behavior and does not contribute significantly to the all overall CP transfer. However the phase-shifted FQ₁₈ signal component is expected to provide a significant contribution as compared to the ZQ₃₆ signal component. However, due to the intense DQ₂₇ polarization transfer these smaller contribution becomes almost irrelevant in the overall polarization transfer. The overall width of various CP resonances increases with increasing the strength of the quadrupolar couplings, particularly for the ZQ₂₅ CP resonance. This is due to the quadrupolar coupling dependence of the effective dipolar coupling constant. This behaviour is reflected in the time-domain simulations in

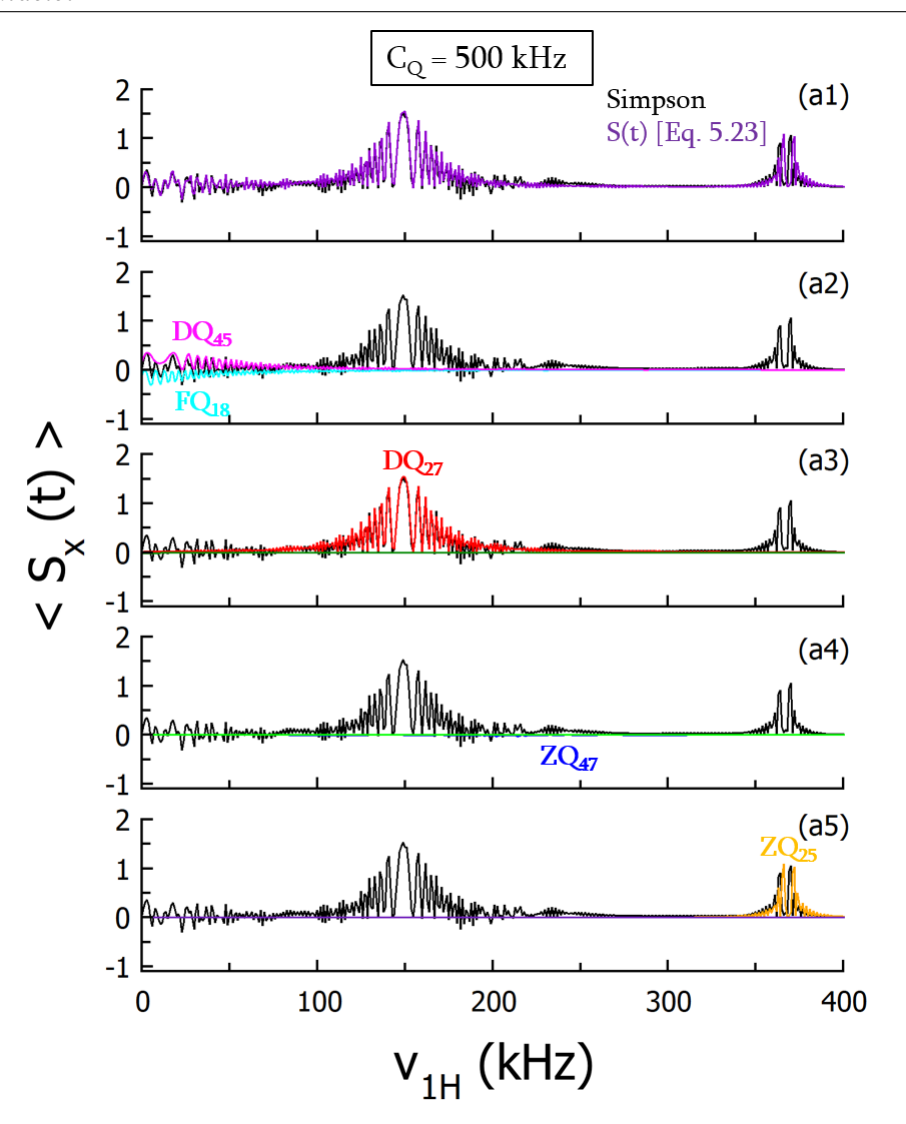


Figure 5.5: In the CP simulations depicted, the polarization build-up on the S-spin (due to transfer from the I-spin) is monitored in a single-crystal as a function of the RF field employed on the I-spin. The numerical simulations (based on SIMPSON) are represented The following parameters were employed in the simulations: by solid black lines. Quadrupolar parameters ($C_Q = 500 \text{ kHz}$, $\eta_Q = 0$, quadrupolar coupling PAS angles α_Q and $\beta_Q = 0^{\circ}$) and dipolar coupling parameters (internuclear distance $r_{IS} = 1.23$ Åand dipolar PAS angle $\beta_d = 0^{\circ}$). A constant RF amplitude of $\nu_{1S} = 80$ kHz was employed on the quadrupole, S-spin and the mixing time during the CP experiment was held constant (say $t_{mix} = 0.5$ ms). In panel (a1) the analytic simulations comprise contributions from all the eight CP matching conditions $(FQ_{18}+DQ_{45}+DQ_{27}+ZQ_{36}+DQ_{38}+ZQ_{47}+DQ_{16}+ZQ_{25})$ and is represented in violet color. In panel (a2) the analytic simulations based on the contributions from the FQ_{18} (cyan curve) and DQ_{45} (magenta color) CP conditions are depicted. In panel (a3) the analytic simulations based on the contributions from the DQ_{27} (red curve) and ZQ₃₆ (green color) CP conditions are depicted. In panel (a4) the analytic simulations based on the contributions from the DQ_{38} (blue curve) and ZQ_{47} (light green color) CP conditions are depicted. In panel (a5) the analytic simulations based on the contributions from the DQ_{16} (indigo curve) and ZQ_{25} (orange color) CP condition are depicted.

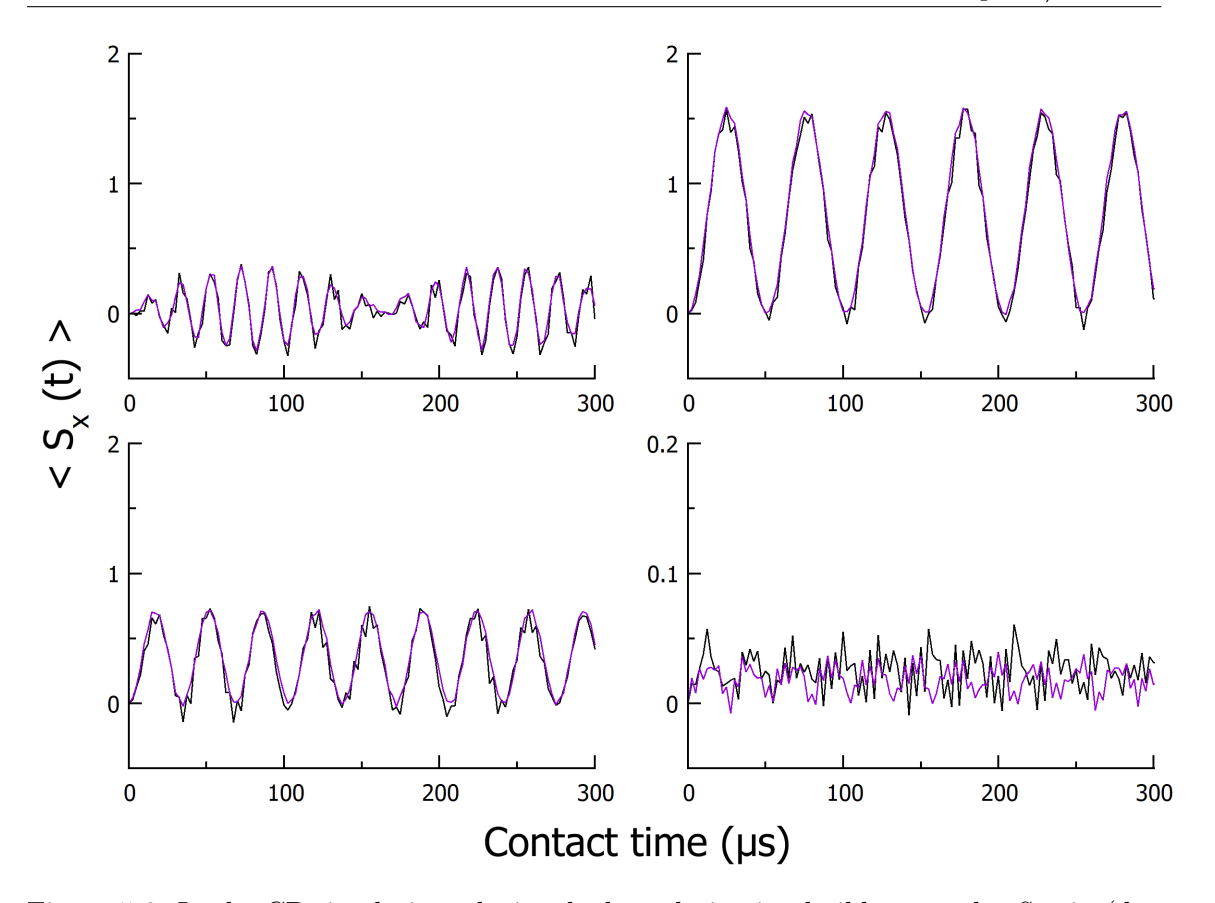


Figure 5.6: In the CP simulations depicted, the polarization build-up on the S-spin (due to transfer from the I-spin) is monitored in a single crystal as a function of the CP mixing time under constant RF field strengths on both the spins. The RF amplitudes on the I-spin were chosen based on the matching condition expression given in Table 5.3 i.e., (a1) $\nu_{1I}=14.95$ kHz); (a2) $\nu_{1I}=145.04$ kHz; (a3) $\nu_{1I}=171.07$ kHz and (a1) $\nu_{1I}=331.07$ kHz. The following parameters were employed in the simulations: Quadrupolar parameters ($C_Q=500$ kHz, $\eta_Q=0$, quadrupolar coupling PAS angles α_Q and $\beta_Q=0^\circ$) and dipolar coupling parameters (internuclear distance $r_{IS}=1.23$ Åand dipolar PAS angle $\beta_d=0^\circ$). A constant RF amplitude of $\nu_{1S}=80$ kHz was employed on the quadrupole, S-spin. The numerical simulations (based on SIMPSON) are represented by solid black lines and the analytic simulations comprise contributions from all the eight CP matching conditions (FQ₁₈+DQ₄₅+DQ₂₇+ZQ₃₆+DQ₃₈+ZQ₄₇+DQ₁₆+ZQ₂₅) and is represented in violet color.

Figure 5.6.

5.2.1.3 Regime-III ($C_Q = 2.0 \text{ MHz}, \text{Strong}$)

In the case of larger $C_Q = 2.0$ MHz (Figure 5.7), as expected the separation between the outermost DQ₄₅ and ZQ₂₅ CP conditions becomes wider in comparison to $C_Q = 500$ kHz case and the overall efficiency of the polarization transfer is diminished. Results emerging from our analytic theory rightly account for the appearance of CP resonances in the lower and higher ¹H RF regions corresponding to the DQ₄₅, DQ₂₇, ZQ₄₇ and ZQ₂₅ CP resonances barring a minor deviation in the high ¹H RF-field regions. In the region of lower ¹H RF-field, the DQ₄₅ transition become insignificant in leading any significant polarization

transfer and the overall CP transfer is dominated by the DQ_{27} CP condition. Interestingly, we observe a negative CP efficiency for the ZQ_{47} CP condition at this quadrupolar coupling strength. This quadrupolar coupling independence of this DQ_{27} CP condition has made the half-integer quadrupolar spin an interesting choice for most of the quadrupolar spins.

5.2.2 Description of CP dynamics in a single-crystal (with general orientation α_Q and $\beta_Q \neq 0^{\circ}$)

The CP efficiency of a single-crystal sample is expected to vary depending on the orientation of the quadrupolar coupling interaction tensor from the principal axis system (PAS), $(\beta_Q \text{ and } \alpha_Q)$ with respect to the lab axis frame. In order to manifest this aspect we carried out the numerical simulations and generated the CP efficiency profiles with a variation in the angle β_Q for $C_Q = 1.0$ MHz. As depicted in Figure 5.8 (0° $\leq \beta_Q \leq 180^\circ$, both the CP efficiency and position of CP resonances are highly orientation dependent. At $\beta_Q = 0^{\circ}$, the CP efficiency profile is described by the four (DQ₄₅, DQ₂₇, ZQ₄₇ and ZQ₂₅) CP resonances and there is almost negligible contribution from the DQ_{45} CP condition and the $\mathbb{Z}Q_{47}$ CP condition has negative intensity. From the analytic theory point of view, when varying orientation from $0^{\circ} < \beta_Q \le 45^{\circ}$, the CP dynamics is described by the DQ₄₅, DQ₂₇, ZQ₄₇ and ZQ₂₅ CP resonances and the overall spread of the CP efficiency profile decreases and the CP efficiency associated with the ZQ_{47} CP condition become positive. This is due to the decrease in the magnitude of the quadrupolar coupling frequency. At $\beta_Q = 45^{\circ}$, the ZQ₄₇ CP condition while the contribution from the phase-related signal components DQ_{45} and FQ_{18} becomes finite in the region of lower ¹H RF-field highlighting the non-unidirectional spin-locking behaviour. For $\beta_Q = 54.736^{\circ}$, the first-order quadrupolar coupling vanishes (Figure C.2 in Appendix-C) and the DQ₄₅, DQ₂₇, ZQ₄₇ CP conditions with equal CP efficiencies fully overlap to produce a single intense CP maxima centered at $\omega_{1I} = 80$ kHz. While the ZQ₂₅ CP resonances appear at $\omega_{1I} = 3\omega_{1S}$ (as mentioned in Table 5.3) and is relatively narrower. Although the analytic theory shows slightly deviation at this CP resonance. As shown previously, the signal contribution from the DQ₄₅, DQ₂₇, ZQ₄₇ CP conditions should be added to perfectly fit the numerical simulation profile at lower ¹H RF-field. At $\beta_Q = 54.736^{\circ}$, there is no contribution to the overall CP efficiency from the FQ₁₈ and ZQ₃₆, DQ₁₆ and DQ₃₈ CP conditions as the ¹H RF field at the matching condition is sufficiently high for any manifestation of these CP conditions. Furthermore, the first-order quadrupolar coupling frequency changes it's sign when $54.736^{\circ} \leq \beta_Q < 125.264^{\circ}$ [Eq. (4.1)]. As a consequence, the DQ₄₅ and ZQ₃₆ CP conditions are swapped and hence, the CP efficiency in the lower and higher ¹H RF field regions are now governed by the ZQ₃₆ and DQ₄₅ CP conditions, respectively, as shown in Figure 5.8 panels (a4-a6). Due to this swapping of CP conditions, the DQ_{45} CP condition will have the behaviour of transferring polarization into the central transitions CT_s and therefore will have higher intensity of the polarization transfer then rest of the CP conditions. Such behavior has not been presented in the

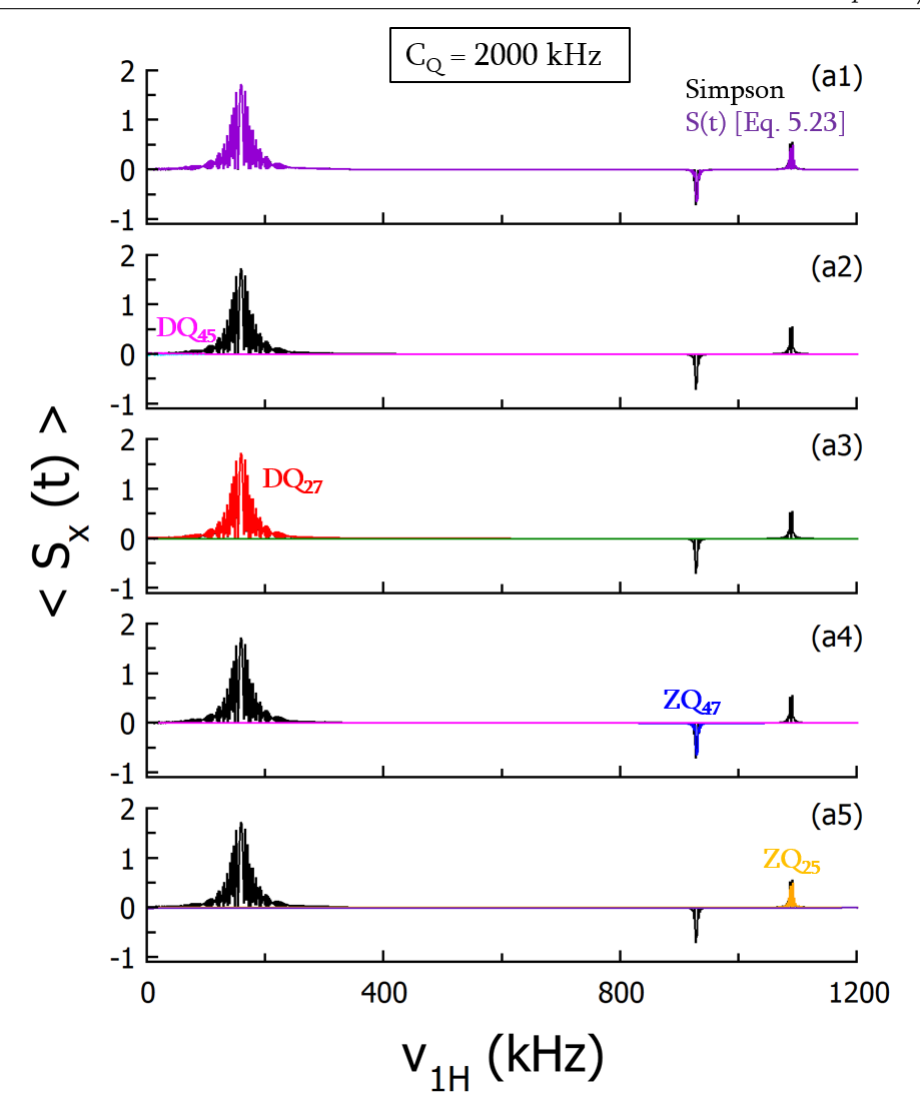


Figure 5.7: In the CP simulations depicted, the polarization build-up on the S-spin (due to transfer from the I-spin) is monitored in a single-crystal as a function of the RF field employed on the I-spin. The numerical simulations (based on SIMPSON) are represented by solid black lines. The following parameters were employed in the simulations: Quadrupolar parameters ($C_Q = 2.0$ MHz, $\eta_Q = 0$, quadrupolar coupling PAS angles α_Q and $\beta_Q=0^\circ)$ and dipolar coupling parameters (internuclear distance $r_{IS} = 1.23$ Åand dipolar PAS angle $\beta_d = 0^{\circ}$). A constant RF amplitude of $\nu_{1S} = 80$ kHz was employed on the quadrupole, S-spin and the mixing time during the CP experiment was held constant (say $t_{mix} = 0.5$ ms). (a1) the analytic simulations comprise contributions from all the eight CP matching conditions $(FQ_{18}+DQ_{45}+DQ_{27}+ZQ_{36}+DQ_{38}+ZQ_{47}+DQ_{16}+ZQ_{25})$ and is represented in violet color. In panel (a2) the analytic simulations based on the contributions from the FQ_{18} (cyan curve) and DQ_{45} (magenta color) CP conditions are depicted. In panel (a3) the analytic simulations based on the contributions from the DQ_{27} (red curve) and ZQ_{36} (green color) CP conditions are depicted. In panel (a4) the analytic simulations based on the contributions from the DQ_{38} (blue curve) and ZQ_{47} (light green color) CP conditions are depicted. In panel (a5) the analytic simulations based on the contributions from the DQ₁₆ (indigo curve) and ZQ₂₅ (orange color) CP condition are depicted.

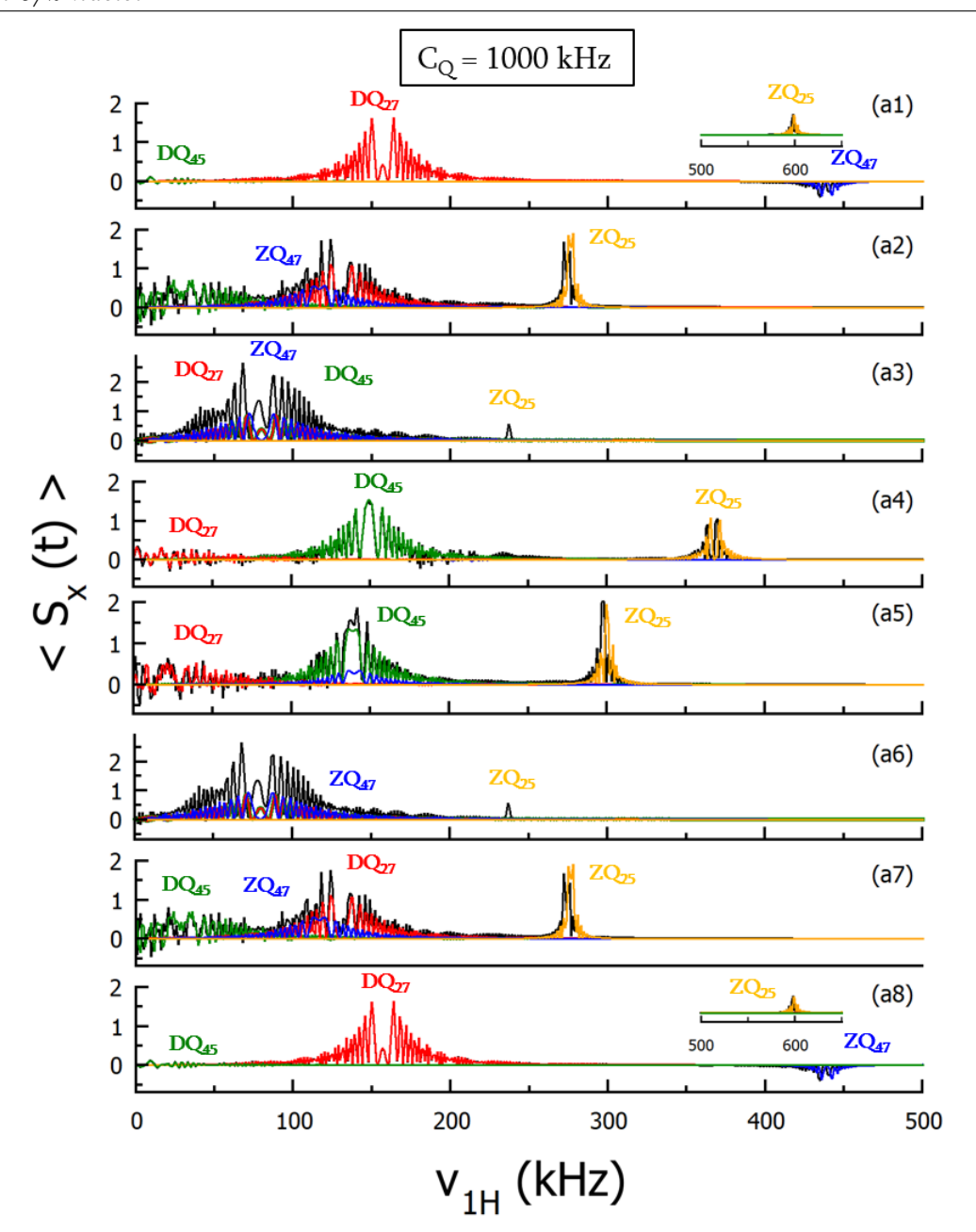


Figure 5.8: In the CP simulations depicted, the polarization build-up on the S-spin (due to transfer from the I-spin) is monitored in a single crystal (with general orientation) as a function of the RF field employed on the I-spin. In the simulations depicted, the effects of the variation of quadrupolar coupling PAS angle β_Q : 0° (a1), 45° (a2), 54.736° (a3) 90° (a4), 110° (a5), 125.624° (a6), 135° (a7) and 180°(a8) on the CP dynamics is illustrated. The following parameters were employed in all the simulations: $C_Q = 500$ kHz, $\eta_Q = 0$, quadrupolar coupling PAS angle $\alpha_Q = 0^{\circ}$, contact time $(t_{mix}) = 0.5$ ms, dipolar coupling parameters (internuclear distance $r_{IS} = 1.23$ Åand dipolar PAS angle $\beta_d = 0^{\circ}$) and $\nu_{1S} = 50$ kHz. SIMPSON simulations (black curve) are fitted with the total analytic signal expressions: FQ₁₈ + DQ₄₅ (green color), DQ₂₇+ ZQ₃₆ (red color), DQ₃₈ + ZQ₄₇ (blue color) and DQ₁₆ + ZQ₂₅ (orange color) in panels a1-a8. The insets in panels a1 and a8 show CP maxima in the higher I-spin RF field range.

theoretical description presented by the Vega at. al. [47]. Meanwhile, the ZQ_{47} and ZQ_{25} CP conditions retain their original behaviour and do not undergo any swapping. In the

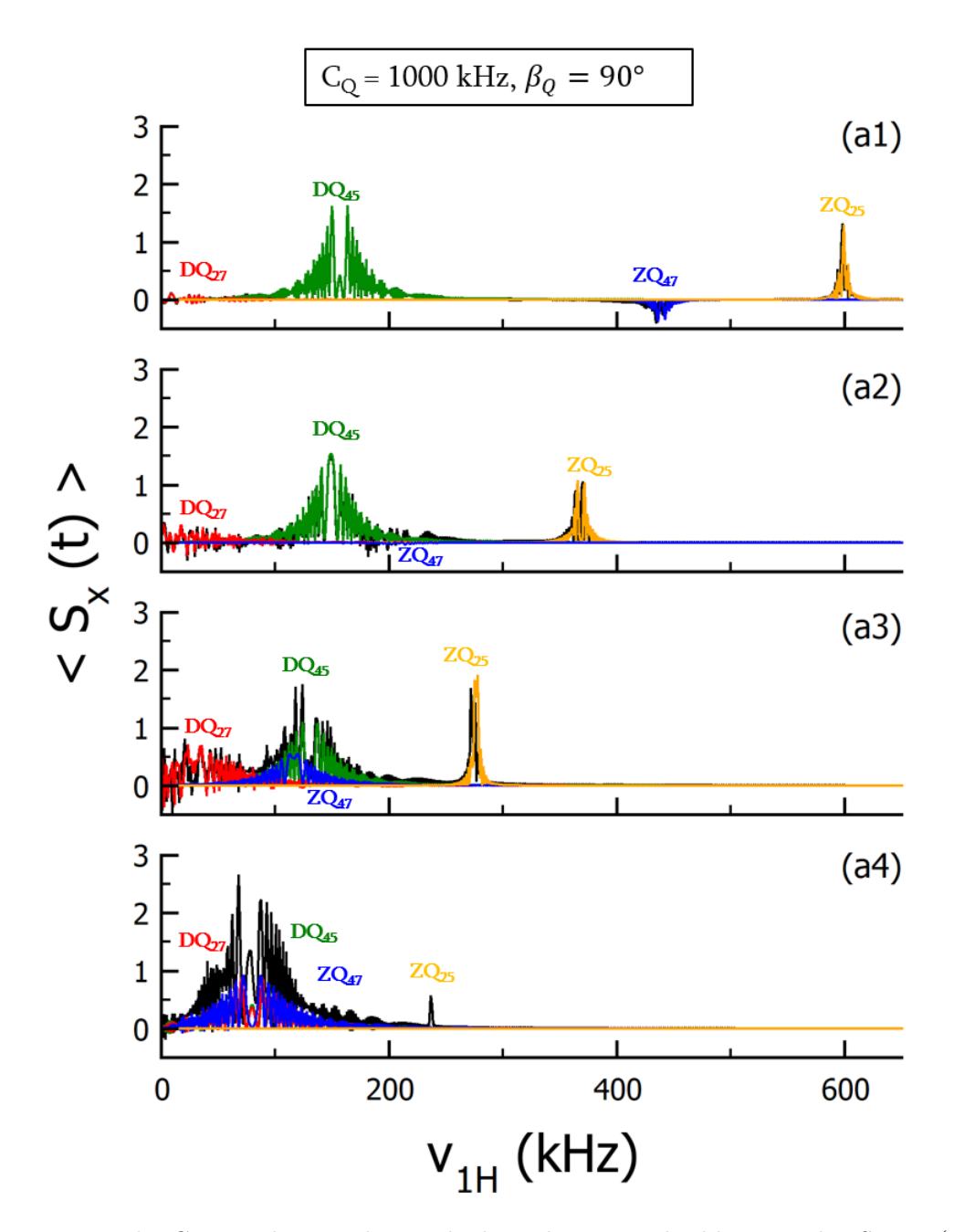


Figure 5.9: In the CP simulations depicted, the polarization build-up on the S-spin (due to transfer from the I-spin) is monitored in a single crystal (with general orientation) as a function of the RF field employed on the I-spin. In the simulations depicted, the effects of the variation of quadrupolar coupling PAS angle α_Q : 0° (a1), 30°(a2), 60° (a3) and 90° (a4) on the CP dynamics are illustrated. The following parameters were employed in all the simulations: $C_Q = 1.0$ MHz, $\eta_Q = 1.0$, quadrupolar coupling PAS angle $\beta_Q = 90^{\circ}$, contact time (t_{mix}) = 0.5 ms, dipolar coupling parameters (internuclear distance $r_{IS} = 1.23$ Åand dipolar PAS angle $\beta_d = 0^{\circ}$) and $\nu_{1S} = 80$ kHz. SIMPSON simulations (black curve) are fitted with the total analytic signal expressions: FQ₁₈ + DQ₄₅ (green color), DQ₂₇+ ZQ₃₆ (red color), DQ₃₈ + ZQ₄₇ (blue color) and DQ₁₆ + ZQ₂₅ (orange color) in panels a1-a4.

higher ¹H RF field region, the CP efficiency profile is dominated by the ZQ₄₇ and ZQ₂₅ CP conditions, where the ZQ_{47} CP condition will have negative CP efficiency. The ZQ_{47} and ZQ₂₅ resonances shift significantly in the range $0^{\circ} \leq \beta_Q \leq 180^{\circ}$ in contrast to the DQ_{45} and DQ_{27} CP resonances highlighting strong C_Q dependence of the ZQ_{47} and ZQ_{25} resonances due to the involvement of the satellite transitions. At $\beta_Q = 125.264^{\circ}$, the first-order quadrupolar coupling frequency again pass through zero and the behaviour is exactly similar to $\beta_Q = 54.736^{\circ}$. In the range $125.264^{\circ} < \beta_Q \le 180^{\circ}$, the CP efficiency profile exactly display a similar CP dynamics as in $54.736^{\circ} > \beta_Q \leq 0^{\circ}$. Interestingly, as the value of the quadrupolar coupling constant is scaled with the orientation of the quadrupolar coupling tensor with respect to the lab frame at a fixed C_Q , the CP efficiency profiles observed at variable orientations may correspond to the different quadrupolar coupling regimes as shown and discussed in the previous sections. For instance, $\beta_Q = 0^{\circ}$ and 90° refer to CP efficiency profile corresponding to the larger quadrupolar coupling case. Whereas $\beta_Q = 45^{\circ}$ and β_Q values in close proximity to 54.736° correspond to the CP efficiency profiles in the intermediate and weak quadrupolar coupling regimes, respectively. The quadrupolar PAS angle α_Q affects the magnitude and sign of quadrupolar frequency, therefore the position and efficiency of CP resonances vary with the variation of α_Q angles at a fixed β_Q angle. Such simulations are presented in Figure 5.9.

5.2.3 Description of the CP dynamics in a powder sample

The theoretical framework proposed is shown to explain the CP dynamics associated with a single-crystal sample. On the basis of results obtained from the single-crystal studies, we extended our theory to describe the CP dynamics in a more complex powder sample under static condition. Numerical simulations in Figures 5.10, 5.11 and 5.12 carried out on a powder sample led to the following observations: With increasing C_Q values (a) the CP efficiency profile broadens and splits into three maxima of unequal intensities, (b) the CP transfer efficiency decreases (c) one of the CP maxima shift towards the lower and others at the higher ¹H RF values with increasing C_Q . In order to get deeper insights into the above observations, we carried out analytic simulations using the signal expressions derived on the concept of effective Hamiltonian in the previous section [Eq. (5.23)]. The analytic simulations are in prefect convergence with the numerical simulation across all the quadrupolar coupling regimes. Therefore, the validates the proposed analytic theory in explaining the trajectory of the polarization in anistropic sample i.e., powder sample. Analogous to the single-crystal study, for a smaller C_Q (= 200 kHz) value (Figure 5.10), the resulting CP efficiencies from the DQ_{45} , DQ_{27} and ZQ_{47} CP conditions overlap and when co-added manifest exactly the CP profile observed from the numerical simulation in the lower ¹H RF-field region. While, in the higher ¹H RF-field region, the CP efficiency profile is dominated by the ZQ₂₅ CP condition. Under this condition the contributions from the phase-shifted FQ_{18} and ZQ_{36} , DQ_{16} and DQ_{38} CP conditions are negligible. The reason for the splitting of the pure DQ₄₅, DQ₂₇ and ZQ₂₅ CP resonances is due to the unequal distribution of the various crystallite orientations. Interestingly, with increasing

strength of the quadrupolar coupling constant, the broad CP resonance in the lower ¹H RF-field region splits into two maxima of unequal intensities. The individual analytic

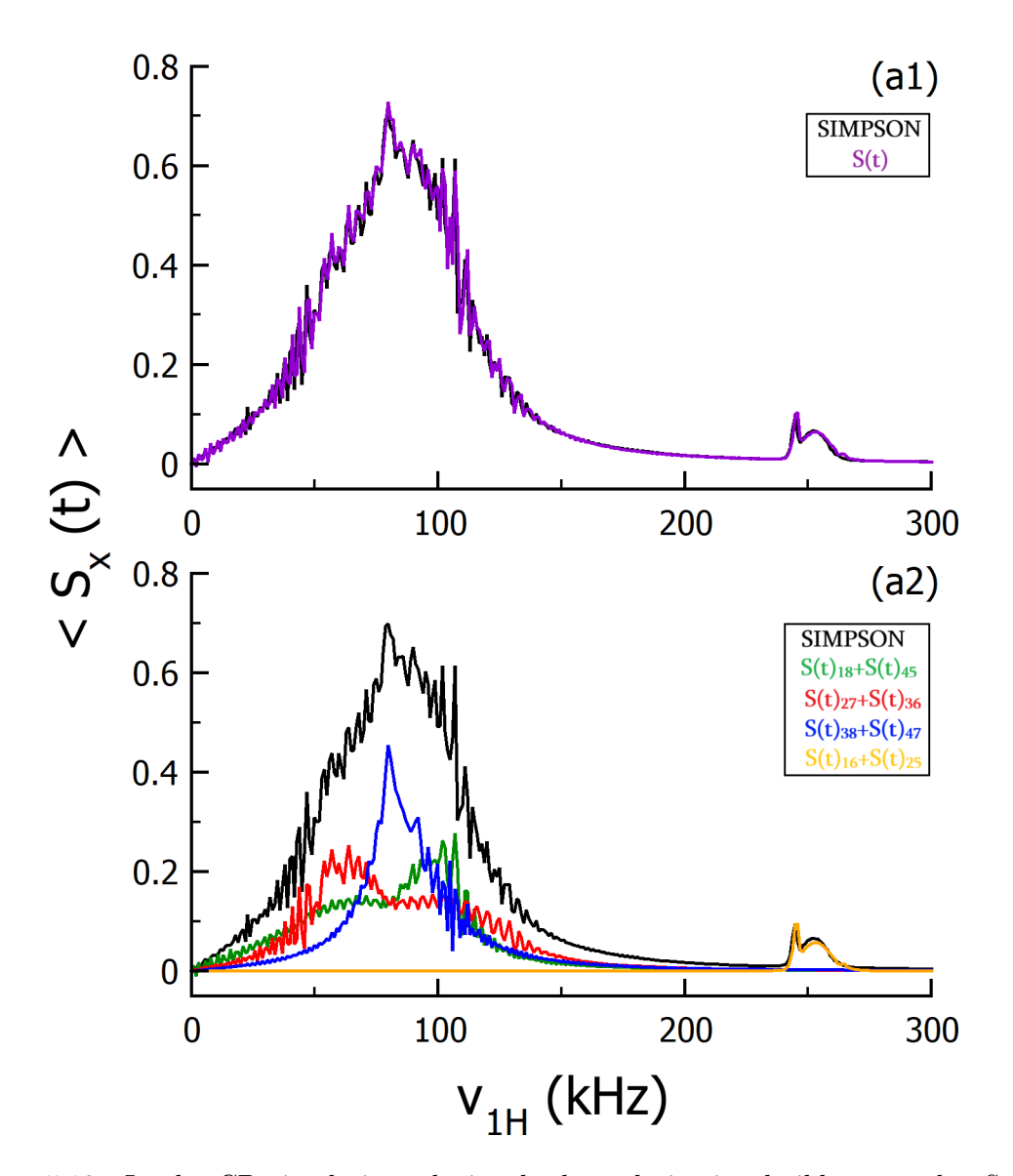


Figure 5.10: In the CP simulations depicted, the polarization build-up on the S-spin (due to transfer from the I-spin) is monitored in a powder sample as a function of the RF field employed on the I-spin. The numerical simulations (based on SIMPSON) are represented by solid black lines. The following parameters were employed in the simulations: $C_Q = 200$ kHz, $\eta_Q = 0$ and quadrupolar coupling PAS angles α_Q and $\beta_Q = 0^{\circ}$), dipolar coupling parameters (internuclear distance $r_{IS} = 1.23$ Åand dipolar PAS angle $\beta_d = 0^{\circ}$), RF amplitude of S-spin $\nu_{1S} = 80$ kHz and mixing time during the CP experiment (say $t_{mix} = 0.5$ ms) were identical in all the simulations. In the first row, the analytic simulations comprise contributions from all the eight CP matching conditions (FQ₁₈+DQ₄₅+DQ₂₇+ZQ₃₆+DQ₃₈+ZQ₄₇+DQ₁₆+ZQ₂₅) and is represented in violet color. In the second row, the analytic simulations based on the contributions: FQ₁₈ + DQ₄₅ (green color), DQ₂₇+ ZQ₃₆ (red color), DQ₃₈ + ZQ₄₇ (blue color) and DQ₁₆ + ZQ₂₅ (orange color). The powder simulations were performed using 4180 orientations (i.e., zcw4180) of α and β .

fittings reveal the contribution of the various CP conditions in leading to the overall CP transfer. Interestingly, the DQ_{45} condition is seen to be more efficient than the ZQ_{36} condition. The higher efficiency of the DQ_{45} condition can be explained on the basis of

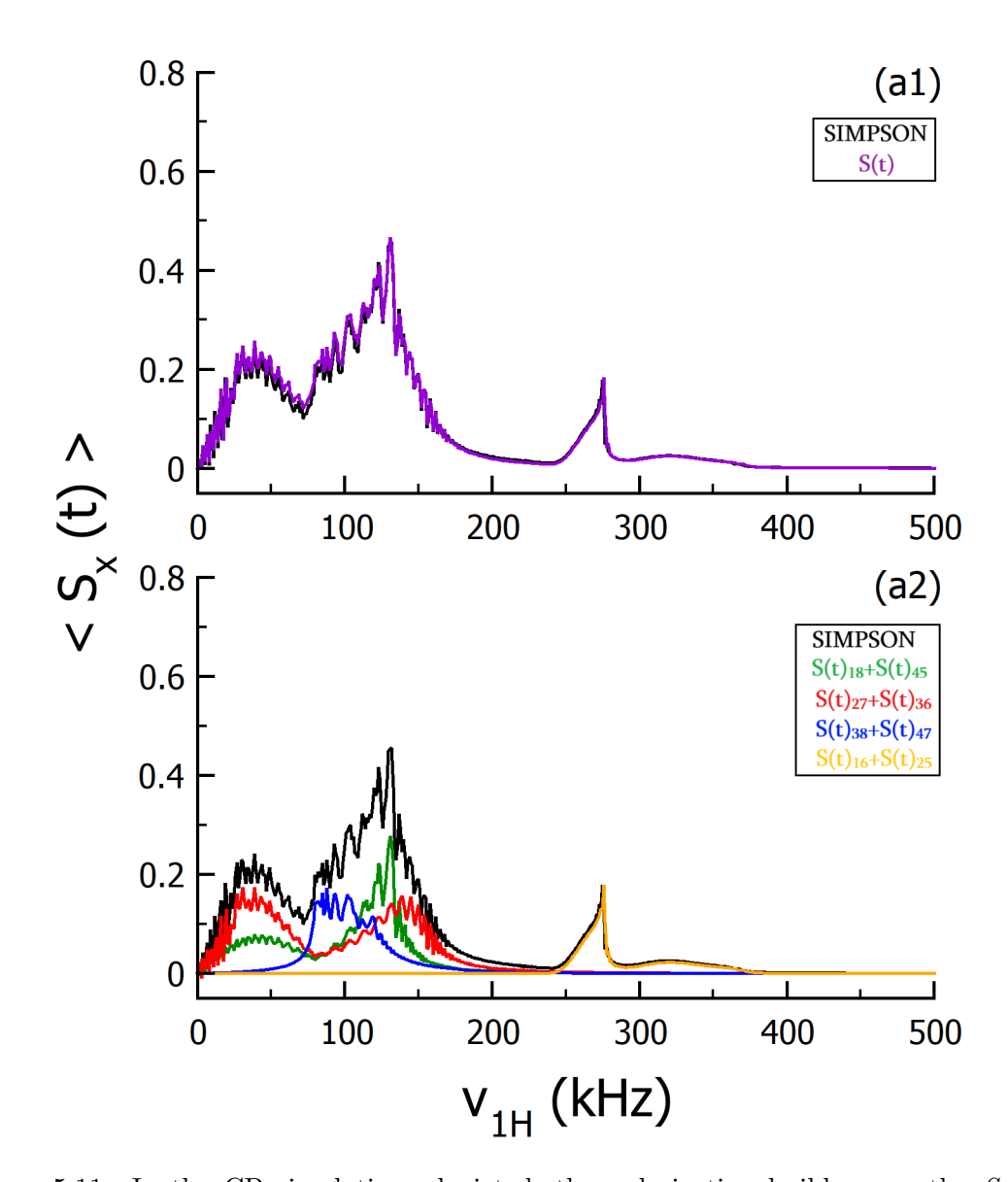


Figure 5.11: In the CP simulations depicted, the polarization build-up on the S-spin (due to transfer from the I-spin) is monitored in a powder sample as a function of the RF field employed on the I-spin. The numerical simulations (based on SIMPSON) are represented by solid black lines. The following parameters were employed in the simulations: $C_Q = 500$ kHz, $\eta_Q = 0$ and quadrupolar coupling PAS angles α_Q and $\beta_Q = 0^{\circ}$), dipolar coupling parameters (internuclear distance $r_{IS} = 1.23$ Åand dipolar PAS angle $\beta_d = 0^{\circ}$), RF amplitude of S-spin $\nu_{1S} = 80$ kHz and mixing time during the CP experiment (say $t_{mix} = 0.5$ ms) were identical in all the simulations. In first row, the analytic simulations comprise contributions from all the eight CP matching conditions (FQ₁₈+DQ₄₅+DQ₂₇+ZQ₃₆+DQ₃₈+ZQ₄₇+DQ₁₆+ZQ₂₅) and is represented in violet color. In the second row, the analytic simulations based on the contributions: FQ₁₈ + DQ₄₅ (green color), DQ₂₇+ ZQ₃₆ (red color), DQ₃₈ + ZQ₄₇ (blue color) and DQ₁₆ + ZQ₂₅ (orange color). The powder simulations were performed using 4180 orientations (i.e., zcw4180) of α and β .

the probability of the crystallite orientations in the plane perpendicular to the applied Zeeman magnetic field. The powder averaging expression described in Eq. (2.16). As shown in the single-crystal case above (Figure 5.8), the first-order quadrupolar coupling constant changes it's sign when $54.736^{\circ} \leq \beta_Q < 125.264^{\circ}$ [Eq. (4.1)] resulting in the

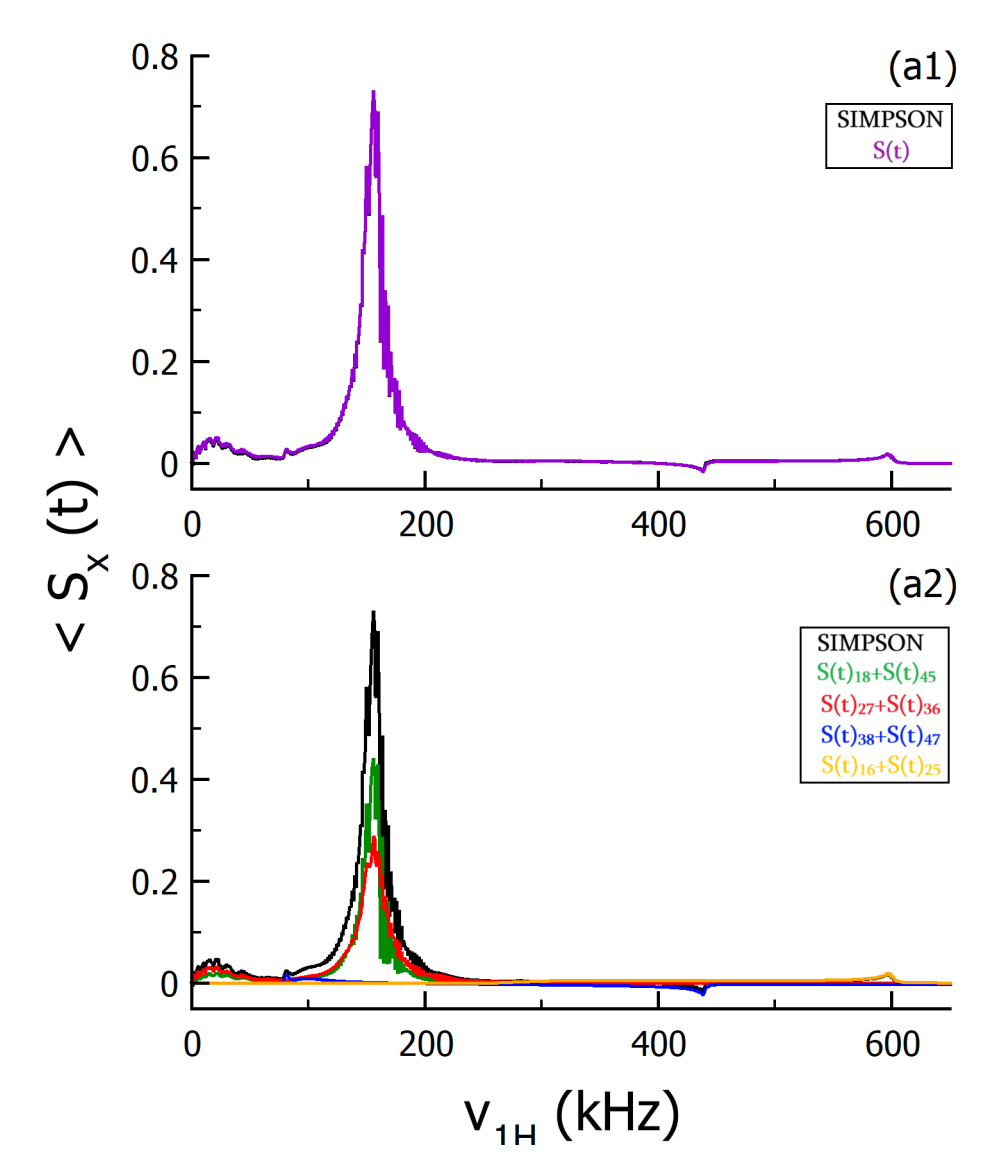


Figure 5.12: In the CP simulations depicted, the polarization build-up on the S-spin (due to transfer from the I-spin) is monitored in a powder sample as a function of the RF field employed on the I-spin. The numerical simulations (based on SIMPSON) are represented by solid black lines. The following parameters were employed in the simulations: $C_Q = 2.0$ MHz, $\eta_Q = 0$ and quadrupolar coupling PAS angles α_Q and $\beta_Q = 0^{\circ}$), dipolar coupling parameters (internuclear distance $r_{IS} = 1.23$ Åand dipolar PAS angle $\beta_d = 0^{\circ}$), RF amplitude of S-spin $\nu_{1S} = 80$ kHz and mixing time during the CP experiment (say $t_{mix} = 0.5$ ms) were identical in all the simulations. In first row, the analytic simulations comprise contributions from all the eight CP matching conditions (FQ₁₈+DQ₄₅+DQ₂₇+ZQ₃₆+DQ₃₈+ZQ₄₇+DQ₁₆+ZQ₂₅) and is represented in violet color. In the second row, the analytic simulations based on the contributions: FQ₁₈ + DQ₄₅ (green color), DQ₂₇+ ZQ₃₆ (red color), DQ₃₈ + ZQ₄₇ (blue color) and DQ₁₆ + ZQ₂₅ (orange color). The powder simulations were performed using 4180 orientations (i.e., zcw4180) of α and β .

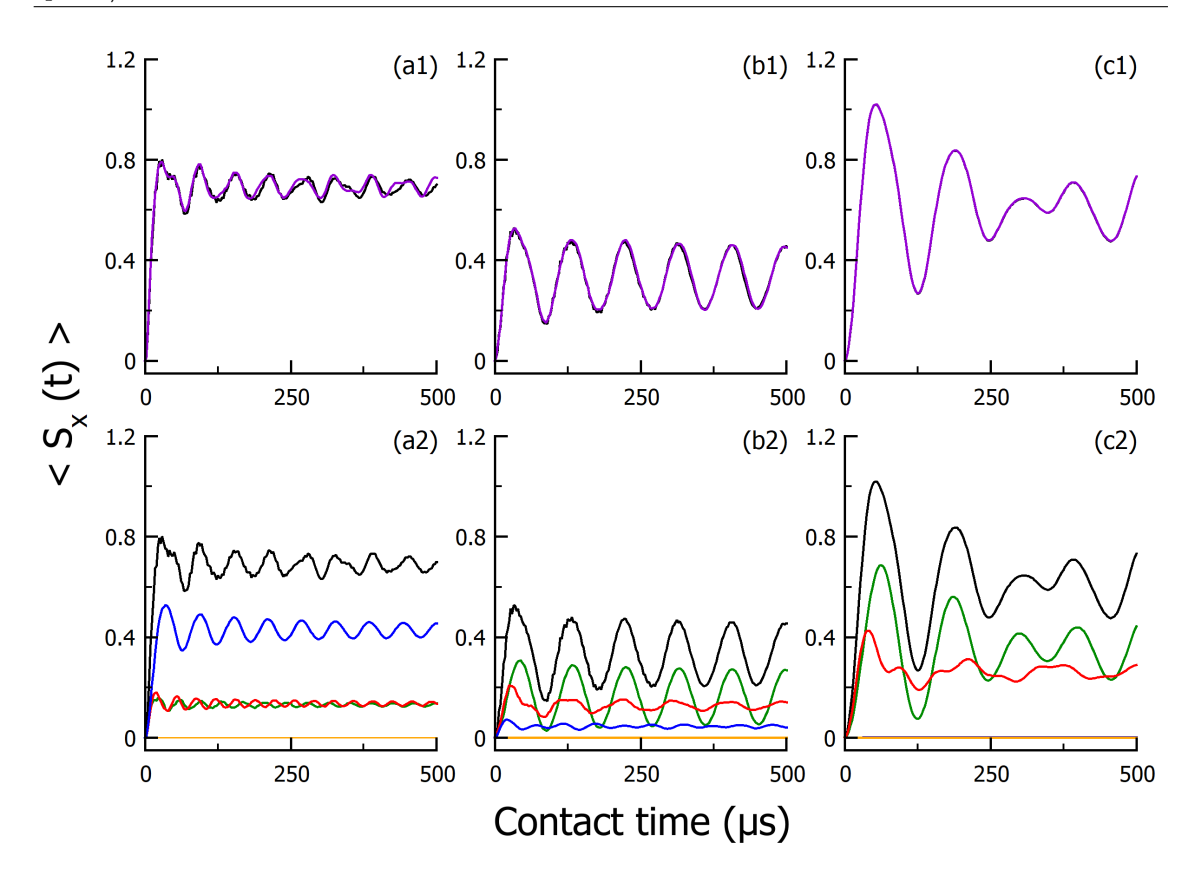


Figure 5.13: In the CP simulations depicted, the polarization build-up on the S-spin (due to transfer from the I-spin) is monitored in a powder sample as a function of the CP mixing time under constant RF amplitudes on the spins. The RF amplitudes on the I-spin were chosen based on the CP maxima observed in Figures 5.10, 5.11 and 5.12 i.e., panels a1-a2 ($\nu_{1H}=80~\mathrm{kHz}$); panels b1-b2 ($\nu_{1H}=132~\mathrm{kHz}$); panels c1-c2 ($\nu_{1H}=156~\mathrm{kHz}$). The following parameters were employed in the simulations: Panels a1-a3 ($C_Q=200~\mathrm{kHz}$, $\eta_Q=0$); panels b1-b3 ($C_Q=500~\mathrm{kHz}$, $\eta_Q=0$) and panels c1-c3 ($C_Q=2.0~\mathrm{MHz}$, $\eta_Q=0$). The remaining simulation parameters and descriptions are as given in the caption of Figure 5.10.

swapped DQ_{45} and DQ_{27} CP conditions. As the crystallite orientations for the powder sample are more probable in the plane perpendicular to the applied magnetic field which is a case suitable for the DQ_{45} CP condition [Figure 5.8(a4), $\beta_Q = 90^{\circ}$] resulting in the DQ_{45} CP efficiency being higher than the DQ_{27} CP efficiency for the most intense CP resonance. Whereas in the lower ¹H RF field region, the DQ_{27} CP is more efficient for the reason explained above. Notably, minor contributions from the phase-shifted ZQ_{36} CP condition to the overall CP conditions are also observed for the $C_Q = 2.0$ MHz case (Figure 5.12). However, for the simplified representation, we have not shown the individual contribution for all CP conditions in these figures. With increasing quadrupolar coupling strength the contributions to the CP efficiency from the phase-shifted components ZQ_{36} and FQ_{18} field increases further (Figure 5.12). With increasing C_Q , the position of the maximum CP transfer changes, while its intensity does not change significantly. This is due to the existence of the first-order quadrupolar coupling transition (CT_s), which under the influence of the powder averaging exchange the character with the TQ_s transition, but

retain its characteristic quadrupolar independent nature. While the CP efficiency of the CP condition involved in the satellite transitions (ST_{1s} and ST_{2s}) dramatically deceases with increasing C_Q . Apart from that the powder sample CP efficiency profile at $C_Q = 500$ kHz and 2 MHz, the overall CP transfer demonstrates the exchange behaviour (positive to negative CP efficiency) of the ZQ₄₇ CP condition which is solely governed by the magnitude of the quadrupolar coupling strength. Due to distribution of the quadrupolar coupling frequencies in case of powder sample, the ZQ_{47} condition is simultaneously satisfied for different crystallite orientation, thus, we observe both positive and negative contribution to the overall CP transfer. The time-domain simulations at $C_Q = 200$ kHz (weak), 500 kHz (intermediate), and 2.0 MHz (strong) are shown in Figure 5.13 respectively, supports the above findings. Unlike the single-crystal case wherein the time-domain profile from the respective CP matching conditions resulted in perfect sinusoidal oscillations, in the case of the powder sample the time-domain oscillations due to the interference of signal contributions from the different crystallite-orientations overlap to result in a non-sinusoidal behavior. Besides, with increasing quadrupolar coupling strength, the time-domain oscillations become more wiggled representing a non-uniform CP transfer due to the mixing of different CP fields. On the basis of the proposed analytic theory of the CP for a powder sample we can summarize the results as follows: (a) Depending on the strength of the quadrupolar coupling constant (C_Q) all the eight Hartmann-Hahn CP conditions are seen to contribute to the overall CP efficiencies when added together match perfectly well with the numerical simulation result. In other words, all the eight CP matching conditions become indistinguishable and mix together to result in the overall CP efficiency profiles, (b) the contribution due to the mixing of CP condition becomes more prominent with increasing C_Q , (c) unlike the S=1 system, the CP efficiency at the lower ¹H RF-field region (DQ₄₅ and ZQ₄₇) does not change much with increasing quadrupolar coupling constant, (d) the decrease in the CP transfer efficiency for the ZQ₄₇ and ZQ₂₅ CP conditions for the powder sample is a direct manifestation of the strength of the quadrupolar coupling and poor spin-lock efficiency. Hence, the presence of multiple crystallite orientations coupled with the strength of quadrupolar coupling in a multi-level system leads to a complex CP transfer mechanism. Unlike the spin-1/2 system, the concept of a unidirectional field to describe the CP dynamics is not valid in the case of CP involving the quadrupolar spins. The proposed analytic theory is capable of explaining the intricate CP dynamics by the interplay of the various CP condition.

5.2.4 Extraction of the dipolar coupling parameters from the CP lineshapes

The mathematical process of the dipolar coupling parameters estimation from the time-domain CP signal is already discussed in Chapters 2 and 3. The dipolar coupling parameters are extracted from the CP experiment by monitoring the CP efficiency as a function of the mixing time, and the resulting data is Fourier transformed (FT) to get the frequency-domain CP spectrum [165, 179]. The Fourier-transformed CP signal expression

[Eq. (5.23)] is given below:

$$S(\omega) = \sum_{ij} C_{ij} \pi \left[\delta(\omega) - \frac{1}{2} \left\{ \delta(\omega - \omega_{eff}^{ij}) + \delta(\omega + \omega_{eff}^{ij}) \right\} \right]$$
 (5.33)

where ij = 18, 45, 27, 36, 38, 47, 16, and 25. The coefficients C_{ij} can be found from Eq. (5.23). From Eq. (5.33), it is evident that the overall CP spectrum will feature conjugate symmetric peaks resulting from the effective frequencies of all possible HH CP matching conditions, in addition to their zero-frequency peaks. The zero-frequency peak will always be associated with opposite phase, thus does not hinder in the estimation of the dipolar coupling parameter. The above expressions can be simplified by setting the exact HH CP matching conditions as given below:

• DQ₄₅/FQ₁₈ CP matching condition:

$$S(\omega)_{ij} = C_{ij}\pi \left[\delta(\omega) - \frac{1}{2} \left\{ \underbrace{\delta(\omega - \omega_d^{18,45}) + \delta(\omega + \omega_d^{18,45})}_{\text{Purely dipolar splitting } (2\omega_d^{18,45})} \right\} \right]$$
(5.34)

• DQ_{27}/ZQ_{36} CP matching condition:

$$S(\omega)_{ij} = C_{ij}\pi \left[\delta(\omega) - \frac{1}{2} \left\{ \underbrace{\delta(\omega - \omega_d^{27,36}) + \delta(\omega + \omega_d^{27,36})}_{\text{Purely dipolar splitting } (2\omega_d^{27,36})} \right\} \right].$$
(5.35)

• DQ₃₈/ZQ₄₇ CP matching condition:

$$S(\omega)_{ij} = C_{ij}\pi \left[\delta(\omega) - \frac{1}{2} \left\{ \underbrace{\delta(\omega - \omega_d^{38,47}) + \delta(\omega + \omega_d^{38,47})}_{\text{Purely dipolar splitting } (2\omega_d^{38,47})} \right\} \right].$$
(5.36)

• DQ_{16}/ZQ_{25} CP matching condition:

$$S(\omega)_{ij} = C_{ij}\pi \left[\delta(\omega) - \frac{1}{2} \left\{ \underbrace{\delta(\omega - \omega_d^{16,25}) + \delta(\omega + \omega_d^{16,25})}_{\text{Purely dipolar splitting } (2\omega_d^{16,25})} \right\} \right].$$
(5.37)

where, C_{ij} are the coefficients shown in Eqs. (5.25) and (5.32) under various HH CP matching conditions. From a practical perspective, the dipolar parameter in the FT spectrum is determined by measuring the frequency separation between the two symmetric peaks ($2\omega_d^{18,45}$ or $2\omega_d^{27,36}$ or $2\omega_d^{38,47}$ or $2\omega_d^{16,25}$). However, on deviating from the exact HH CP condition, the frequency separation between the two symmetric peaks will be given by the effective-field for the particular CP condition (i.e. ω_{eff}^{ij}). Figure 5.14 illustrates the CP spectra for a single-crystal sample at $C_Q = 200$ kHz under the DQ₄₅, DQ₂₇ and ZQ₄₇ HH CP matching conditions in panels (a1-b1), (a2-b2) and (a3-b3), respectively. We have disregarded the ZQ₂₅ CP condition as it appear at RF-field amplitude beyond

experimental capabilities. The separation between the conjugate symmetric peaks in the resulting dipolar spectrum are inequivalent highlighting their unequal effective dipolar coupling constant at $C_Q \neq 0$ kHz. These effective dipolar coupling constant ($\omega_d^{18,45}$, $\omega_d^{27,36}$, $\omega_d^{38,47}$ and $\omega_d^{16,25}$) are strongly dependent on the quadrupolar coupling constant, therefore, the distance between the conjugate symmetric peak will vary with crystallite

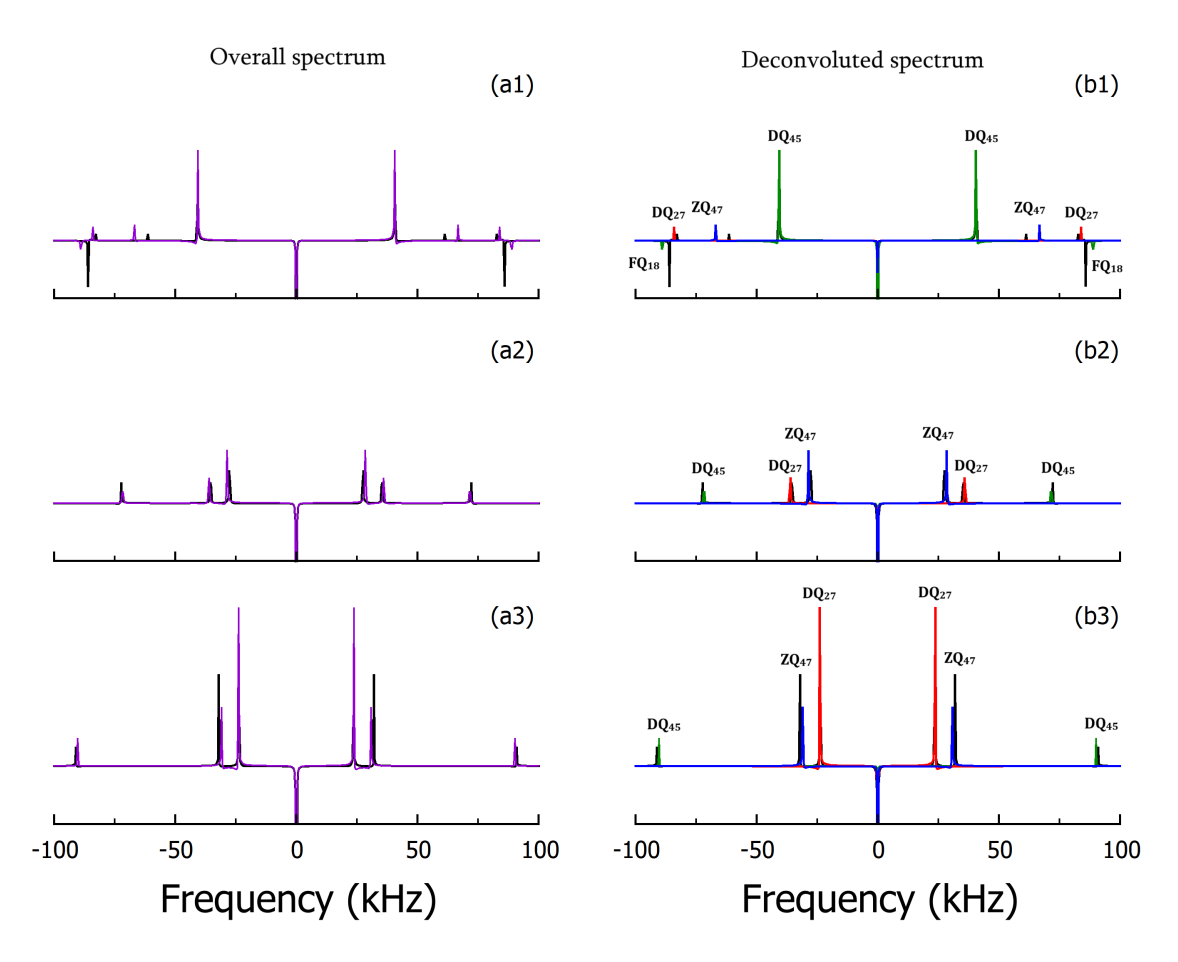


Figure 5.14: In the simulations depicted, the frequency-domain S-spin signal in a single-crystal emerging from Fourier transformation of the mixing time domain signal corresponding to the DQ_{45} (first column), ZQ_{47} (second column) and DQ_{27} (third column) CP matching conditions is shown at quadrupolar coupling constant C_Q =200 All other parameters such as the quadrupolar coupling PAS angles α_Q and $\beta_Q=0^\circ$, dipolar parameters (internuclear distance $r_{12}=1.23$ Å and dipolar PAS angle $\beta_d = 0^{\circ}$) and RF amplitude of S-spin $\nu_{1S} = 80$ kHz were identical in all the simulations. Depending on the magnitude of the quadrupolar coupling constant, the RF amplitudes employed on the I-spin were carefully adjusted to match the DQ₄₅ (first column), ZQ₄₇ (second column) and DQ₂₇ (third column) CP matching conditions. The analytic simulations in the panels have the following definitions: first row, the analytic simulations comprise contributions from all the eight CP matching conditions $(FQ_{18}+DQ_{45}+DQ_{27}+ZQ_{36}+DQ_{38}+ZQ_{47}+DQ_{16}+ZQ_{25})$ and is represented in violet color. In the second row, the analytic simulations based on the contributions: $FQ_{18} + DQ_{45}$ (green color), $DQ_{27}+ZQ_{36}$ (red color) and $DQ_{38}+ZQ_{47}$ (blue color). The analytic simulations based on DQ₁₆ and ZQ₂₅ CP signals are not shown due to their negligible contributions at the specified RF conditions. A line broadening of 50 Hz was used before the Fourier transform of the time-domain CP signal.

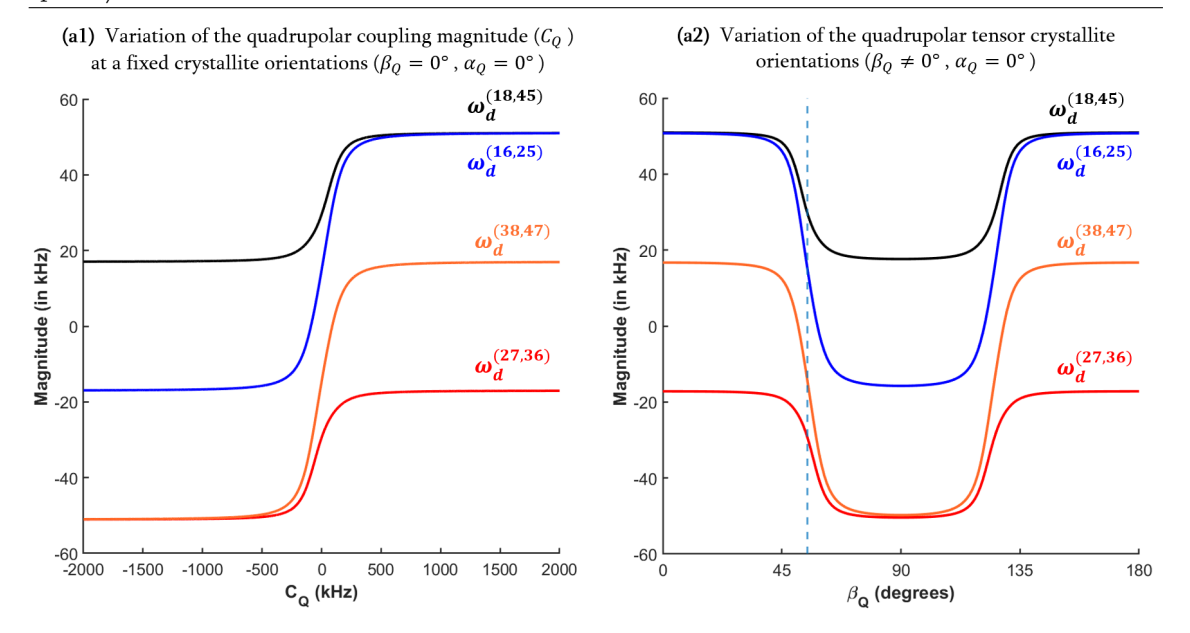


Figure 5.15: Effect of strength and orientation of quadrupolar tensor on the effective dipolar coupling constants. The following simulation parameters were employed: Quadrupolar parameters C_Q varied and PAS angles α_Q and $\beta_Q = 0^{\circ}$ (a1) and $C_Q = 200$ kHz and PAS angles α_Q and $\beta_Q = 0^{\circ}$ (a2); dipolar parameters (internuclear distance $r_{12} = 1.23$ Å and dipolar PAS angle $\beta_d = 0^{\circ}$) and RF amplitude of S-spin $\nu_{1S} = 80$ kHz were identical in all the simulations.

orientation orientations at a fixed internuclear distance and dipolar tensor orientation. The dependence of the effective dipolar coupling constant $(\omega_d^{18,45}, \omega_d^{27,36}, \omega_d^{38,47})$ and $(\omega_d^{16,25})$ with quadrupolar coupling magnitude and crystallite orientation is shown in Figure 5.15. At $C_Q = 200$ kHz, the resulting CP spectrum in the DQ₄₅ CP condition (panel b1) is predominately described by the DQ_{45} CP signal expression and the phase-shifted FQ_{18} components appear at higher-frequency (see the opposite phase). In addition, the CP spectrum will also be associated with a significant contributions from the DQ₂₇ and ZQ₄₇ CP conditions which appear in-phase with the DQ₄₅ CP signal. Although, we get minor deviations in the analytic theory in the weak coupling limit at lower ¹H RF-field amplitudes. Under the DQ₂₇ and ZQ₄₇ HH CP conditions, the resulting CP spectrum is dominated by the DQ_{27} and ZQ_{47} frequencies along with the contributions form the higher-frequency components (refer to figure caption for details). different magnitude of the effective dipolar coupling constants, the distance between the conjugate symmetric peaks are different for the DQ_{45} , DQ_{27} and ZQ_{47} CP spectra. Apart form the quadrupolar dependence, the magnitude of the effective dipolar coupling constants also dependent on the radio-frequency amplitude applied S-spin system (Figure Therefore, the separations between the conjugate symmetric peaks are highly system-specific and experimental parameter dependence at a fixed internuclear distance. Hence, the dipolar coupling measurement in quadrupolar systems are complicated and necessitates exact simulation of the experimental conditions. Figure 5.17 demonstrates the CP spectrum at $C_Q = 500$ kHz and 2.0 MHz under the DQ_{27} HH CP condition for

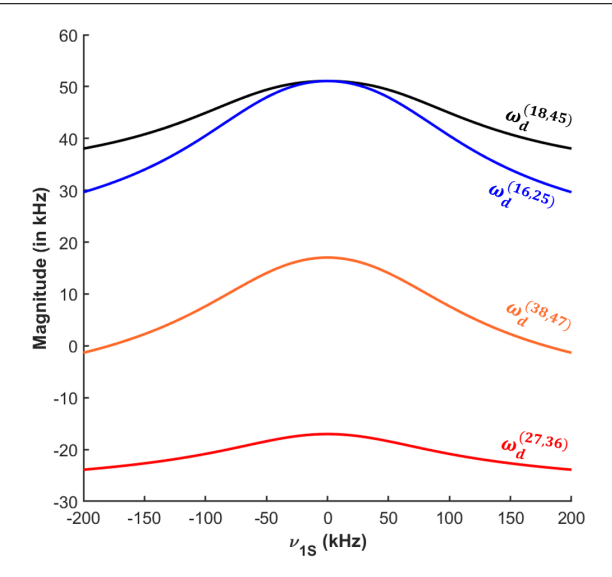


Figure 5.16: Effect of strength S-spin RF amplitude on the effective dipolar coupling constants. The following parameters were used in the simulations: $C_Q = 200 \text{ kHz}$, $\eta_Q = 0$, quadrupolar coupling PAS angles (0°, 0°, 0°), and $\nu_{1S} = 80 \text{ kHz}$.

a single-crystal sample. Unlike the weaker coupling regimes, the resulting CP spectrum consist of fewer high-frequency components and are dominantly described by the DQ_{27} conditions at the specified parameters.

The straightforward method presented for the single-crystal sample for estimation of the dipolar coupling through the separation between the symmetric peaks, will not hold for the powder sample. This is due to the coupled orientation dependence of the effective dipolar constants (dipolar and quadrupolar tensor orientations) which become complex in the powder sample. In addition, in powder sample various crystallite orientations will undergo different HH CP matching conditions at a specified RF conditions. Therefore, the resulting CP lineshape will not have pure pake like doublet observed in the spin-1/2 systems and will be highly distorted. Figure 5.18 illustrates the CP lineshape in various quadrupolar coupling regimes for the power sample. For comparison, we have shown the CP lineshape at $C_Q = 0$ kHz for powder sample at $\omega_{1I} = \omega_{1S}$ HH CP condition (panel a1). Likewise, the single-crystal sample, the CP lineshape in this coupling regime will have equivalent contributions from the DQ₄₅, DQ₂₇ and ZQ₄₇ CP conditions and the observed spectrum will have the characteristic shape of the heteronuclear dipolar pattern for idealized S=3/2 spin system coupled to a I=1/2 spin system except for the zero-frequency peak with negative intensity which is specific of the CP induced excitation spectra. The distance between the CP singularities will provide estimation of the dipolar coupling acting between the spin-system. At $C_Q = 200 \text{ kHz}$ (panel a2), the CP lineshape is distorted with multiple-singularities and no noticeable foot signal is observed. The overall CP lineshape is determined by the DQ₄₅, DQ₂₇ and ZQ₄₇ signal contributions and in this coupling regime, we don't observed any significant contributions from the high-frequency phase-shifted components. As the strength of the quadrupolar coupling constant increase, the overall CP lineshape become highly distorted and the degree of the contribution also

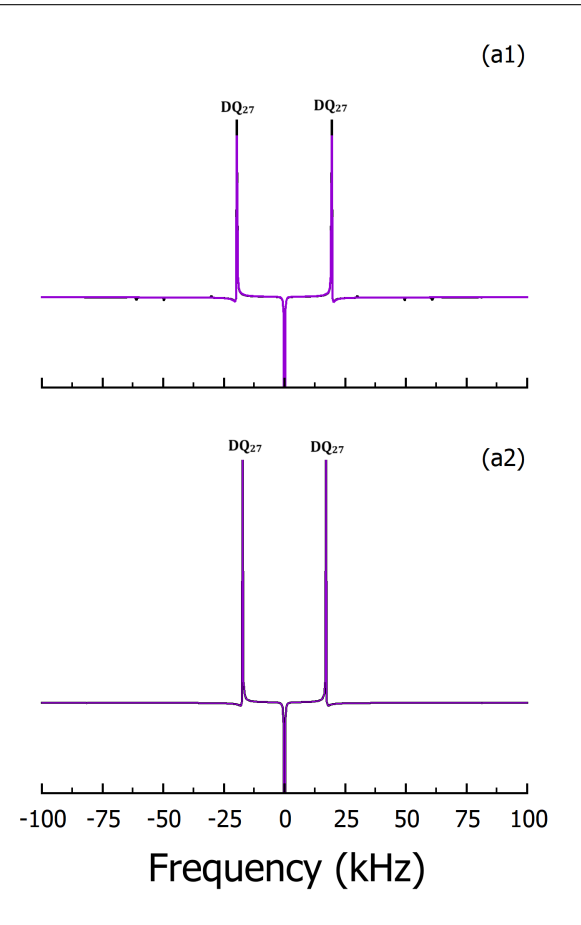


Figure 5.17: In the simulations depicted, the frequency-domain S-spin signal in a single-crystal emerging from Fourier transformation of the mixing time domain signal corresponding to the DQ₂₇ CP matching condition is shown at quadrupolar coupling constants $C_Q = 500$ kHz (a1) and 2000 kHz (a2). All other parameters such as the quadrupolar coupling PAS angles α_Q and $\beta_Q = 0^\circ$, dipolar parameters (internuclear distance $r_{12} = 1.23$ Å and dipolar PAS angle $\beta_d = 0^\circ$) and RF amplitude of S-spin $\nu_{1S} = 80$ kHz were identical in all the simulations. Depending on the magnitude of the quadrupolar coupling constant, the RF amplitudes employed on the I-spin were carefully adjusted to match the DQ₂₇ CP matching condition. The analytic simulations comprise contributions from all the eight CP matching conditions (FQ₁₈+DQ₄₅+DQ₂₇+ZQ₃₆+DQ₃₈+ZQ₄₇+DQ₁₆+ZQ₂₅) and is represented in violet color. A line broadening of 50 Hz was used before the Fourier transform of the time-domain CP signal.

varies. At $C_Q = 2.0$ MHz, the CP spectrum suffers from additional distortions resulting from the high-frequency phase-shifted components. Theses observation are in accord with the CP dynamics presented in the previous section which highlighted the interplay of all possible CP conditions in deciphering the polarization transfer in powder sample across all coupling regimes. The dipolar coupling estimation can be made by the iterative fittings of the CP lineshape using the Eq. (5.23). Apart from the dipolar coupling measurements, the frequency domain analysis will reveal the underlying spin-dynamics of the polarization transfer in the quadrupolar systems. The detailed analytical description presented herein provides account of the observation of the various distortion observed in single-crystal and powder samples.

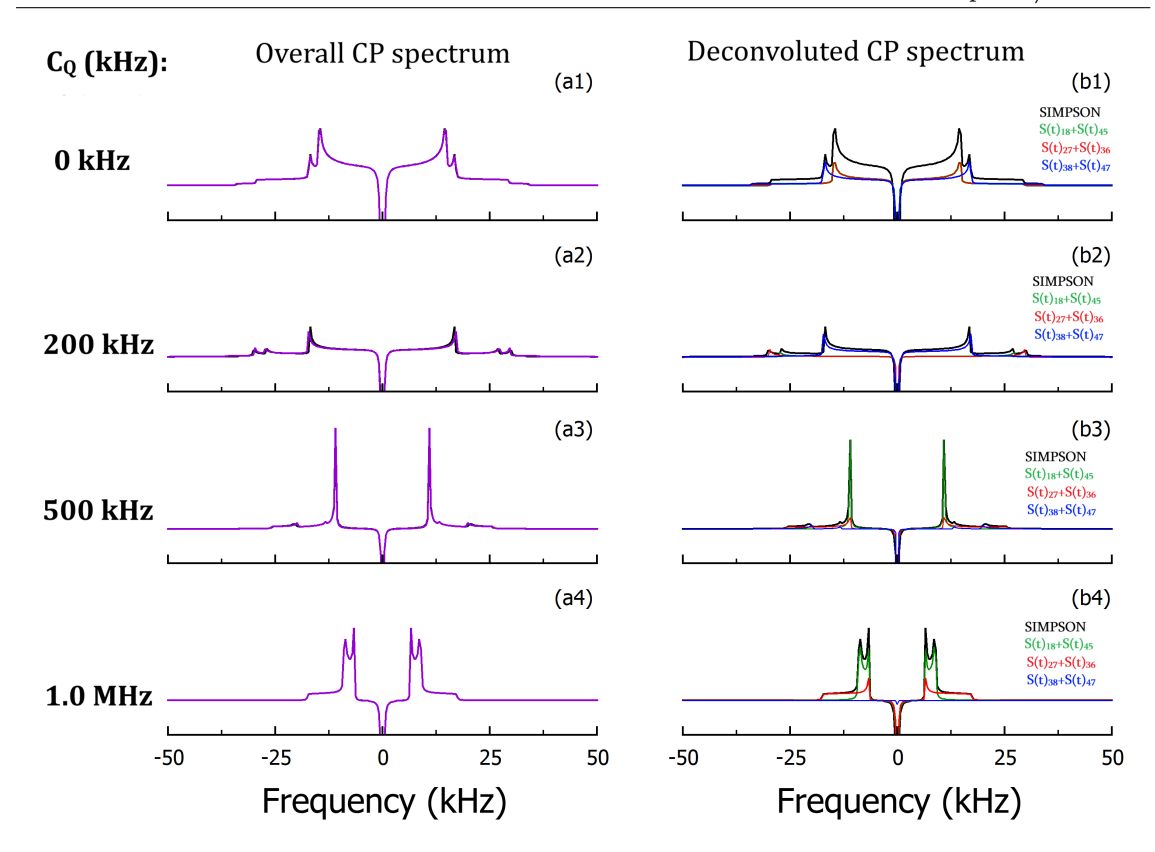


Figure 5.18: In the simulations depicted, the frequency-domain S-spin signal in powder sample emerging from Fourier transformation of the mixing time domain signal is shown for different quadrupolar coupling constants: panel a1-b1 ($C_Q = 0$ kHz); panel a2-b2 ($C_Q = 200$ kHz); panel a3-b3 ($C_Q = 500$ kHz) and panel a4-b4 ($C_Q = 2.0$ MHz). All other parameters such as the quadrupolar coupling PAS angles α_Q and $\beta_Q = 0^\circ$, dipolar parameters (internuclear distance $r_{12} = 1.23$ Å and dipolar PAS angle $\beta_d = 0^\circ$ kHz were identical in all the simulations. The RF amplitudes employed on the I-spin taken from the Figure 5.13. The analytic simulations in the panels have the following definitions: first column, the analytic simulations comprise contributions from all the eight CP matching conditions (FQ₁₈+DQ₄₅+DQ₂₇+ZQ₃₆+DQ₃₈+ZQ₄₇+DQ₁₆+ZQ₂₅) and is represented in violet color. In the second column, the analytic simulations based on the contributions: FQ₁₈ + DQ₄₅ (green color), DQ₂₇+ ZQ₃₆ (red color) and DQ₃₈ + ZQ₄₇ (blue color). The powder simulations were performed using 4180 orientations (i.e., zcw4180) of α and β . A line broadening of 50 Hz was used before the Fourier transform of the time-domain CP signal.

5.3 Conclusions

To summarize, we have presented a detailed analytic treatment for the CP experiment between I=1/2 and S=3/2 spin systems under on-resonance irradiation. Using the "effective-field" approach, the proposed theory provided a single unified analytic framework comprising all the eight possible HH CP matching conditions which is equally valid for single-crystal and powder samples. Unlike the existing analytic framework, the proposed theory provides a quantitative description of the individual contributions from all the possible CP matching conditions. The quantitative treatments reveal the role of quadrupolar coupling strength and crystallite orientation in deciphering the spin-dynamics

of the quadrupolar CP. This simplified description simplified the understanding of the CP dynamics in powder sample. From an experimental point of view, we have provided analytic description of the CP lineshapes for the dipolar coupling measurements.

Chapter 6

Summary and Conclusions

In summary, the thesis presents a unified description of cross-polarization (CP) dynamics in quadrupolar spins based on the concept of effective Hamiltonians derived using the "effective-field" approach. In the thesis, operator-based analytic theory of spin-dynamics is presented in a two-spin model framework described in a coupled spin operator basis for understanding the mechanism of polarization transfer between I=1/2 to S=1 and 3/2 spin systems in static/non-rotating solids. In contrast to the existing theoretical models based on the AHT and the Floquet theory, the proposed approach is shown to be an attractive option for describing the mechanism of the polarization transfer experiments in multi-level systems. The effective-field approach facilitates the derivation of effective CP Hamiltonians requiring a minimal set of unitary transformations, unlike existing operator-based perturbative methods that require perturbation corrections up to several orders of magnitude. Our theory is able to identify all the modes of polarization transfer and their individual contributions to the overall CP efficiency within a single mathematical framework suitable for both single crystal as well as powder samples. Below, we summarize the key findings of the thesis as discussed in the previous chapters.

A Theory and Methodology: An effective-field approach to understand the mechanism of cross-polarization dynamics between spin-1/2 systems

In order to test the validity of the effective-field based analytic theory in the description of CP dynamics, we have used an isolated spin-1/2 pair as a model system. In the coupled basis representation, the overall CP signal expression is shown to be the sum of contributions from the two HH CP matching conditions, namely the zero-quantum (ZQ_{23}) and the double-quantum (DQ_{14}) along with an additional term arising from the interference of the two HH CP conditions. Contrary to the existing literature reports, the proposed theory offers a closed form solution to the effective CP Hamiltonian capable of describing the CP dynamics across all coupling regimes under on/and off-resonance irradiations. Under on-resonance irradiation ($\Omega_S = 0$), the proposed analytic theory demonstrates an interplay of the double and zero-quantum CP conditions in deciphering the overall CP transfer efficiency in the strong coupling regime ($\omega_d \approx \omega_{1S}$). While in the weak coupling regime ($\omega_d << \omega_{1S}$), the CP dynamics is deciphered by either of the two CP conditions. We concluded that the effective spin-locking field is not uni-directional in the strong coupling regime. Nevertheless, under the S-spin off-resonance irradiation, the

involvement of the interference term further complicates the polarization transfer process. In the case of stronger off-resonant irradiation ($\Omega_S \approx \omega_{1S}$), we observed a dipolar coupling dependent shift in the position of the HH CP matching conditions along with dispersion of both the ZQ_{23} and DQ_{14} CP conditions. In strong coupling regimes ($\Omega_S \approx \omega_{1S}$ and $\omega_d \approx \omega_{1S}$), the spin-locking process is described by the contributions from the ZQ_{23} and DQ_{14} CP conditions and interference terms in the CP signal expression. The presence of the interference effect gives rise to an additional pathway for the loss in I-spin polarization near $\omega_{1I} = 0$ without S-spin gaining any polarization. The above findings encouraged the expansion of the proposed analytic framework to explore the CP dynamics in more complex quadrupolar nuclei.

B Analytic theory of cross-polarization (CP) dynamics between spin-1/2 and spin-1 nuclei

In this chapter of the thesis, an operator-based analytic theory employing the concept of the effective-field is presented to describe the mechanism of polarization transfer Under on-resonance irradiation (both I and between spin-1/2 and spin-1 nuclei. S-spins), the proposed theoretical framework that the CP dynamics is governed by the contributions from the four Hartmann-Hahn CP conditions, namely, triple-quantum (TQ_{16}) , single-quantum (SQ_{34}) , double-quantum (DQ_{26}) and zero-quantum (ZQ_{35}) transitions. In contrast to the existing theoretical framework, the effective Hamiltonian derived using the effective-field method requires a minimal set of unitary transformations. The effective CP Hamiltonian is shown to be valid across all the quadrupolar coupling This enabled a quantitative analysis of the CP efficiency profiles for the single-crystal and powder samples across all the quadrupolar coupling regimes. Utilizing the derived analytic CP signal expression, we were able to evaluate the individual contributions emerging from all the possible CP conditions in deciphering the CP efficiency profiles at variable quadrupolar coupling strengths (C_Q) , crystallite orientations $(\alpha_Q \text{ and } \beta_Q)$ and RF-field strengths (ω_{1S}) for single-crystal and powder samples. Nonetheless, for the powder sample, the interference of various crystallite orientations makes it less feasible to differentiate between the four matching conditions and the overall polarization trajectory is described by the full CP signal expression. From an experimental perspective, we have also presented a quantitative description of the CP lineshape for the extraction of the dipolar coupling parameter.

C Understanding the role of second-order quadrupolar coupling and off-resonance effects in CP dynamics

This chapter of the thesis extends the analytic framework presented in the previous chapter to include the effect of S-spin off-resonance irradiation and second-order quadrupolar coupling interactions. The effective Hamiltonian derived in the presence of second-order quadrupolar interaction results in additional modes of CP transfer in comparison to the on-resonance case. The derived CP signal expression contains a

sum of total six Hartmann-Hahn CP matching conditions, namely, triple-quantum TQ_{16} , single-quantum SQ_{34} , double-quantum DQ_{15} , zero-quantum ZQ_{24} , double-quantum DQ_{26} and zero-quantum ZQ_{35} . Besides, the single-quantum I-spin dipolar transitions ($SQ_{d,I}$) are shown to interfere with the CP trajectories. To the best of our knowledge, such predictions are unique to the current study. The results emerging from the analytic theory are well-corroborated through rigorous comparisons with the more exact numerical simulations in all the quadrupolar coupling regimes. Evaluation of the individual contribution provides a quantitative picture of the polarization transfer dynamics at variable quadrupolar coupling $(C_Q, \alpha_Q \text{ and } \beta_Q)$ and RF (ω_{1S}, Ω_S) parameters for both single-crystal and powder samples. Due to a similar operator dependency, the second-order quadrupolar coupling and off-resonance irradiation display exactly similar CP dynamics for single-crystal samples, and irradiating at $\Omega_S = -\omega_Q^{(2)}$ can compensate the effect from the second-order quadrupolar coupling. In the case of the powder sample, due to the complexity (second and fourth rank) of the second-order quadrupolar coupling, the exact compensation is not possible. However, it is possible to reach a compromise by irradiating in the range of the second-order quadrupolar coupling-driven broadening/shift. Likewise, in the on-resonance case presented in the previous chapter, the overall polarization transfer in powder sample display an interplay of various CP matching conditions. To provide an alternate description of the CP dynamics, we have also presented a state-picture description of the polarization transfer dynamics.

D Analytic theory of cross-polarization (CP) dynamics between spin-1/2 and spin-3/2 nuclei

In this chapter, we proposed an analytic theory of the CP dynamics in half-integer quadrupolar nuclei. We have provided a closed form solution to the CP signal efficiency that is valid across all the quadrupolar coupling regimes. Under on-resonance irradiation (for both I and S-spins), the polarization transfer is described by a total of eight HH CP matching conditions, namely, four-quantum FQ_{18} , double-quantum DQ_{45} , double-quantum DQ_{27} , zero-quantum ZQ_{36} , double-quantum DQ_{38} , zero-quantum ZQ_{47} , double-quantum DQ_{16} and zero-quantum ZQ_{24} . The results emerging from the analytic theory are well-corroborated through rigorous comparisons with the more exact numerical simulations in all the quadrupolar coupling regimes. Unlike spin-1 systems, we observed a good polarization transfer efficiency even in the stronger quadrupolar coupling regime for both single-crystal and powder samples. This is mainly attributed to the existence of the first-order quadrupolar devoid central transition (CT_S) , which exhibits good spin-locking efficiency. We have explicitly shown the role of the orientation of the quadrupolar coupling tensor in alerting the polarization dynamics for the single-crystal sample, which simplified the understanding of CP dynamics in a more complex powder sample. As discussed in the previous chapters, the polarization transfer trajectory in the powder sample will be an amalgamation of all the possible CP matching conditions. Moreover, we have also provided a quantitative description of the CP lineshapes for distance estimation.

The analytic framework presented in this thesis can be further extended to enhance our theoretical understanding of the CP dynamics in higher quantum numbers (S>3/2) nuclei. The integration of the proposed operator-based analytic theory with the reduced density matrix formalism, is anticipated to be a good choice for developing a theoretical framework for describing the multi-spin effects in the polarization transfer. We believe our theoretical framework will be a step forward in better understanding of the CP experiments under magic angle spinning (CPMAS) involving quadrupolar spins. We also hope that the present theory can be further extended to understand the mechanism of spin dynamics of polarization transfer using phase and/or amplitude modulated pulse sequences essential for optimal design and development of CP experiments involving quadrupolar spins.

- [1] F. Bloch. Nuclear induction. Physical review, 70(7-8):460, 1946.
- [2] E. M. Purcell, H. C. Torrey, and R. V. Pound. Resonance absorption by nuclear magnetic moments in a solid. *Physical review*, 69(1-2):37, 1946.
- [3] U. Haeberlen. High resolution NMR in solids. Academic Press, New York, 1976.
- [4] M. Mehring. *High resolution NMR spectroscopy in solids*, volume 11. Springer Science & Business Media, 1976.
- [5] E. R. Andrew, A. Bradbury, and R. G. Eades. Nuclear magnetic resonance spectra from a crystal rotated at high speed. *Nature*, 182(4650):1659–1659, 1958.
- [6] I. J. Lowe. Free induction decays of rotating solids. *Physical Review Letters*, 2(7):285, 1959.
- [7] R. R. Ernst and W. A. Anderson. Application of fourier transform spectroscopy to magnetic resonance. *Review of Scientific Instruments*, 37(1):93–102, 1966.
- [8] M. M. Maricq and J. S. Waugh. NMR in rotating solids. *Journal of Chemical Physics*, 70(7):3300–3316, 1979.
- [9] L. Mueller. Sensitivity enhanced detection of weak nuclei using heteronuclear multiple quantum coherence. *Journal of the American Chemical Society*, 101(16):4481–4484, 1979.
- [10] S. R. Hartmann and E. L. Hahn. Nuclear double resonance in the rotating frame. *Physical Review*, 128(5):2042, 1962.
- [11] G. A. Morris and R. Freeman. Enhancement of nuclear magnetic resonance signals by polarization transfer. *Journal of the American Chemical Society*, 101(3):760–762, 1979.
- [12] A. W. Overhauser. Polarization of nuclei in metals. *Physical Review*, 92(2):411, 1953.
- [13] K. D. Kramer, W. Müller-Warmuth, and J. Schindler. Molecular motion and relaxation in free-radical solutions of benzene, toluene, and some ethers as studied by dynamic nuclear polarization. *Journal of Chemical Physics*, 43(1):31–43, 1965.
- [14] J. Scheuer, I. Schwartz, S. Müller, Q. Chen, I. Dhand, M. B. Plenio, B. Naydenov, and F. Jelezko. Robust techniques for polarization and detection of nuclear spin ensembles. *Physical Review B*, 96(17):174436, 2017.

[15] E. O. Stejskal, J. Schaefer, and J. S. Waugh. Magic-angle spinning and polarization transfer in proton-enhanced NMR. *Journal of Magnetic Resonance* (1969), 28(1):105–112, 1977.

- [16] C. P. Slichter. *Principles of magnetic resonance*, volume 1. Springer Science & Business Media, 2013.
- [17] M. H. Levitt, D. Suter, and R. R. Ernst. Spin dynamics and thermodynamics in solid-state NMR cross polarization. *Journal of chemical physics*, 84(8):4243–4255, 1986.
- [18] I. Solomon. Étude de la relaxation en résonance magnétique par la méthode de précession forcée transitoire. CR Acad. Sci. Paris, 248:92–94, 1959.
- [19] Jacob Schaefer and E. O. Stejskal. Carbon-13 nuclear magnetic resonance of polymers spinning at the magic angle. *Journal of the American Chemical Society*, 98(4):1031–1032, 1976.
- [20] A. Pines, M. G. Gibby, and J. S. Waugh. Proton-enhanced nuclear induction spectroscopy. a method for high-resolution NMR of dilute spins in solids. Technical report, Massachusetts Inst. of Tech., Cambridge, 1972.
- [21] D. Marks and S. Vega. A theory for cross-polarization NMR of nonspinning and spinning samples. *Journal of Magnetic Resonance, Series A*, 118(2):157–172, 1996.
- [22] S. Hediger, B. H. Meier, and R. R. Ernst. Rotor-synchronized amplitude-modulated nuclear magnetic resonance spin-lock sequences for improved cross polarization under fast magic angle sample spinning. *Journal of chemical physics*, 102(10):4000–4011, 1995.
- [23] A. Verhoeven, R. Verel, and B. H. Meier. J cross polarization in magic-angle-spinning NMR. *Chemical physics letters*, 266(5-6):465–472, 1997.
- [24] B. H. Meier. Polarization transfer and spin diffusion in solid-state NMR. Advances in Magnetic and Optical Resonance, 18:1–116, 1994.
- [25] E. Nehra, N. Sehrawat, T. Kobayashi, Y. Nishiyama, and M. K. Pandey. Proton-detected ¹⁵N-¹H dipolar coupling/¹H chemical shift correlation experiment for the measurement of NH distances in biological solids under fast mas solid-state NMR. Journal of Magnetic Resonance Open, 10:100028, 2022.
- [26] N. Sehrawat, E. Nehra, K. K. Rohilla, T. Kobayashi, Y. Nishiyama, and M. K. Pandey. Determination of the relative orientation between ¹⁵N-¹H dipolar coupling and ¹H chemical shift anisotropy tensors under fast mas solid-state NMR. *Journal of Magnetic Resonance*, 350:107428, 2023.

[27] M. Baldus, A. T. Petkova, J. Herzfeld, and R. G. Griffin. Cross polarization in the tilted frame: assignment and spectral simplification in heteronuclear spin systems. *Molecular Physics*, 95(6):1197–1207, 1998.

- [28] W. Kolodziejski and J. Klinowski. Kinetics of cross-polarization in solid-state NMR: a guide for chemists. *Chemical Reviews*, 102(3):613–628, 2002.
- [29] V. Ladizhansky and S. Vega. Polarization transfer dynamics in lee-goldburg cross polarization nuclear magnetic resonance experiments on rotating solids. *Journal of Chemical Physics*, 112(16):7158–7168, 2000.
- [30] B. J. Van Rossum, C. P. De Groot, V. Ladizhansky, S. Vega, and H. J. M. De Groot. A method for measuring heteronuclear (¹H- ¹³C) distances in high speed mas NMR. *Journal of the American Chemical Society*, 122(14):3465–3472, 2000.
- [31] O. W. Sørensen. Polarization transfer experiments in high-resolution NMR spectroscopy. *Progress in nuclear magnetic resonance spectroscopy*, 21(6):503–569, 1989.
- [32] B. Q. Sun, P. R. Costa, and R. G. Griffin. Heteronuclear polarization transfer by radiofrequency-driven dipolar recoupling under magic-angle spinning. *Journal of Magnetic Resonance*, Series A, 112(2):191–198, 1995.
- [33] M. Bjerring and N. C. Nielsen. Solid-state NMR heteronuclear coherence transfer using phase and amplitude modulated rf irradiation at the hartmann–hahn sideband conditions. *Chemical physics letters*, 382(5-6):671–678, 2003.
- [34] S. Laage, A. Marchetti, J. Sein, R. Pierattelli, S. Sass, H. J.and Grzesiek, A. Lesage, G. Pintacuda, and L. Emsley. Band-selective ¹H- ¹³C cross-polarization in fast magic angle spinning solid-state NMR spectroscopy. *Journal of the American Chemical Society*, 130(51):17216-17217, 2008.
- [35] G. D. Paëpe, J. R. Lewandowski, A. Loquet, M. Eddy, S. Megy, A. Böckmann, and R. G. Griffin. Heteronuclear proton assisted recoupling. *Journal of chemical physics*, 134(9), 2011.
- [36] P. Paluch, J. Trébosc, Y. Nishiyama, M. J. Potrzebowski, M. Malon, and J-P Amoureux. Theoretical study of CPVC: a simple, robust and accurate mas NMR method for analysis of dipolar C-H interactions under rotation speeds faster than ca. 60 khz. *Journal of Magnetic Resonance*, 252:67–77, 2015.
- [37] P. Paluch, J. Trébosc, J-P Amoureux, and M. J. Potrzebowski. ¹H-³¹P CPVC NMR method under very fast magic angle spinning for analysis of dipolar interactions and dynamics processes in the crystalline phosphonium tetrafluoroborate salts. *Solid State Nuclear Magnetic Resonance*, 87:96–103, 2017.

[38] P. Hodgkinson and A. Pines. Cross-polarization efficiency in i_N s systems using adiabatic rf sweeps. *Journal of chemical physics*, 107(21):8742–8751, 1997.

- [39] K. J. Harris, A. Lupulescu, B. E. G. Lucier, L. Frydman, and R. W. Schurko. Broadband adiabatic inversion pulses for cross polarization in wideline solid-state NMR spectroscopy. *Journal of Magnetic Resonance*, 224:38–47, 2012.
- [40] R. Fu, J. Hu, and T. A Cross. Towards quantitative measurements in solid-state cpmas NMR: A lee-goldburg frequency modulated cross-polarization scheme. *Journal of Magnetic Resonance*, 168(1):8–17, 2004.
- [41] D. Rovnyak. Tutorial on analytic theory for cross-polarization in solid state NMR. Concepts in Magnetic Resonance Part A: An Educational Journal, 32(4):254–276, 2008.
- [42] P. Li, Q. Chen, and S. Zhang. Analytical solution of cross polarization dynamics. Journal of Magnetic Resonance, 250:76–79, 2015.
- [43] L. Müller, A. Kumar, T. Baumann, and R. R. Ernst. Transient oscillations in NMR cross-polarization experiments in solids. *Physical Review Letters*, 32(25):1402, 1974.
- [44] A. Abragam. The Principles of Nuclear Magnetism, volume 32. Oxford University Press, 1961.
- [45] S. Vega, T. W. Shattuck, and A. Pines. Double-quantum cross-polarization NMR in solids. *Physical Review A*, 22(2):638, 1980.
- [46] L. Müller. Proton—deuterium polarization transfer in magic angle spinning polycrystalline solids in the rotating frame. *Chemical Physics*, 61(1-2):235–248, 1981.
- [47] S. Vega. Multiple-quantum cross-polarization NMR on spin systems with I= 1/2 and S = 3/2 in solids. *Physical Review A*, 23(6):3152, 1981.
- [48] A. J. Vega. Mas NMR spin locking of half-integer quadrupolar nuclei. *Journal of Magnetic Resonance* (1969), 96(1):50–68, 1992.
- [49] A. J. Vega. Cpmas of quadrupolar S = 3/2 nuclei. Solid state nuclear magnetic resonance, 1(1):17–32, 1992.
- [50] R. S. Cantor and J. S. Waugh. Pulsed spin locking in pure nuclear quadrupole resonance. *Journal of Chemical Physics*, 73(3):1054–1063, 1980.
- [51] C. P. Grey, W. S. Veeman, and A. J. Vega. J. Chem. Phys., 98:7711-7724, 1993.
- [52] A. P. M. Kentgens. A practical guide to solid-state NMR of half-integer quadrupolar nuclei with some applications to disordered systems. *Geoderma*, 80(3-4):271–306, 1997.

[53] H. Schäfer, D. Iuga, R. Verhagen, and A. P. M. Kentgens. Population and coherence transfer in half-integer quadrupolar spin systems induced by simultaneous rapid passages of the satellite transitions: A static and spinning single crystal nuclear magnetic resonance study. *Journal of Chemical Physics*, 114(7):3073–3091, 2001.

- [54] S. E. Ashbrook and S. Wimperis. Single-and multiple-quantum cross-polarization in NMR of quadrupolar nuclei in static samples. *Molecular Physics*, 98(1):1–26, 2000.
- [55] S. E. Ashbrook and S. Wimperis. Multiple-quantum cross-polarization and two-dimensional MQMAS NMR of quadrupolar nuclei. *Journal of Magnetic Resonance*, 147(2):238–249, 2000.
- [56] D. Rovnyak, M. Baldus, and R. G. Griffin. Multiple-quantum cross polarization in quadrupolar spin systems during magic-angle spinning. *Journal of Magnetic Resonance*, 142(1):145–152, 2000.
- [57] B. Hu, J. P. Amoureux, J. Trébosc, and S. Hafner. Through-space mp-cpmas experiments between spin-1/2 and half-integer quadrupolar nuclei in solid-state NMR. *Journal of Magnetic Resonance*, 192(1):8–16, 2008.
- [58] T. Mizuno, K. Takegoshi, and T. Terao. ¹H to ²H uniform cross-polarization nuclear magnetic resonance using ²H lee-goldburg irradiation in static powders. *Journal of chemical physics*, 122(8), 2005.
- [59] I. Hung, P. Gor'kov, and Z. Gan. Efficient and sideband-free ¹H-detected ¹⁴N magic-angle spinning NMR. Journal of Chemical Physics, 151(15), 2019.
- [60] T. H. Walter, G. L. Turner, and E. Oldfield. Oxygen-17 cross-polarization NMR spectroscopy of inorganic solids. *Journal of Magnetic Resonance* (1969), 76(1):106–120, 1988.
- [61] K. Takegoshi, M. Ito, and T. Terao. Deuteron 2d exchange sample-turning NMR: determination of interbond angles. Chemical physics letters, 260(1-2):159–165, 1996.
- [62] D. Carnevale, X. Ji, and G. Bodenhausen. Double cross polarization for the indirect detection of nitrogen-14 nuclei in magic angle spinning NMR spectroscopy. *Journal* of Chemical Physics, 147(18), 2017.
- [63] S. E. Ashbrook. Recent advances in solid-state NMR spectroscopy of quadrupolar nuclei. Physical Chemistry Chemical Physics, 11(32):6892–6905, 2009.
- [64] D. Grekov, T. Vancompernolle, M. Taoufik, L. Delevoye, and R. M. Gauvin. Solid-state NMR of quadrupolar nuclei for investigations into supported organometallic catalysts: scope and frontiers. *Chemical Society Reviews*, 47(8):2572–2590, 2018.

[65] S. E. Ashbrook, J. M. Griffin, and K. E. Johnston. Recent advances in solid-state nuclear magnetic resonance spectroscopy. *Annual Review of Analytical Chemistry*, 11(1):485–508, 2018.

- [66] P. Sarv, C. Fernandez, J-P Amoureux, and K. Keskinen. Distribution of tetrahedral aluminium sites in ZSM-5 type zeolites: An ²⁷Al (multiquantum) magic angle spinning NMR study. *Journal of Physical Chemistry*, 100(50):19223–19226, 1996.
- [67] S. J. Hwang, C. Fernandez, J. P. Amoureux, J. Cho, S. W. Martin, and M. Pruski. Quantitative study of the short range order in B₂O₃ and B₂S₃ by mas and two-dimensional triple-quantum mas ¹¹B NMR. Solid State Nuclear Magnetic Resonance, 8(2):109–121, 1997.
- [68] E. Dib, T. Mineva, and B. Alonso. Recent advances in ¹⁴N solid-state NMR. Annual Reports on NMR Spectroscopy, 87:175–235, 2016.
- [69] R. V. SubbaRao, D. Srivastava, and R. Ramachandran. Concept of effective hamiltonians for transitions in multi-level systems. *Physical Chemistry Chemical Physics*, 15(6):2081–2104, 2013.
- [70] G. Vinay and R. Ramachandran. Analytic theory of multiple-quantum NMR of quadrupolar nuclei. Annual Reports on NMR Spectroscopy, 89:123–184, 2016.
- [71] D. Freude and J. Haase. Quadrupole effects in solid-state nuclear magnetic resonance. In *Special Applications*, Vol 29, pages 1–90. Springer, 1993.
- [72] J. Haase and M. S. Conradi. Sensitivity enhancement for NMR of the central transition of quadrupolar nuclei. *Chemical physics letters*, 209(3):287–291, 1993.
- [73] S. E. Ashbrook, J. McManus, K. J. D. MacKenzie, and S. Wimperis. Multiple-quantum and cross-polarized ²⁷Al mas NMR of mechanically treated mixtures of kaolinite and gibbsite. *Journal of Physical Chemistry B*, 104(27):6408–6416, 2000.
- [74] S. Ding and C. A. McDowell. Spin-locking spectral lineshapes of the central transition of half-integer quadrupole systems under magic-angle spinning. *Journal of molecular structure*, 355(1):135–142, 1995.
- [75] H.T. Kwak, S. Prasad, T. Clark, and P. J. Grandinetti. Enhancing sensitivity of quadrupolar nuclei in solid-state NMR with multiple rotor assisted population transfers. Solid state nuclear magnetic resonance, 24(2-3):71-77, 2003.
- [76] S. H. Alarcón, A. C. Olivieri, and R. K. Harris. Quadrupole effects of spin-32 nuclei on the solid-state magic-angle spinning nuclear magnetic resonance spectra of spin-12 nuclei deviations from first-order theory and implications concerning the sign of the indirect coupling constant. Solid State Nuclear Magnetic Resonance, 2(6):325–334, 1993.

[77] D. Freude, J Haase, J. Klinowski, T. A. Carpenter, and G. Ronikier. NMR line shifts caused by the second-order quadrupolar interaction. *Chemical physics letters*, 119(4):365–367, 1985.

- [78] M. K. Pandey and Y. Nishiyama. High-resolution heteronuclear correlations between spin-1/2 and half-integer quadrupolar nuclei under fast mas solid-state NMR. Biophysical Chemistry, 310:107254, 2024.
- [79] S. E. Ashbrook and S. Sneddon. New methods and applications in solid-state NMR spectroscopy of quadrupolar nuclei. *Journal of the American Chemical Society*, 136(44):15440–15456, 2014.
- [80] M. Bansal and R. Ramachandran. Theory of radio-frequency pulses on periodically driven three-level systems: challenges and perspectives. *Physical Chemistry Chemical Physics*, 24(47):29092–29111, 2022.
- [81] J. Haase, M. S. Conradi, C. P. Grey, and A. J. Vega. Population transfers for NMR of quadrupolar spins in solids. *Journal of Magnetic Resonance*, Series A, 109(1):90–97, 1994.
- [82] J-P Amoureux and M. Pruski. Theoretical and experimental assessment of single-and multiple-quantum cross-polarization in solid state NMR. Molecular Physics, 100(10):1595–1613, 2002.
- [83] D. Srivastava and R. Ramachandran. Nuances of multi-quantum excitation in solid state NMR of quadrupolar nuclei. *RSC Advances*, 3(47):25231–25236, 2013.
- [84] A. E. Aliev, K. D. M. Harris, and D. C. Apperley. Natural abundance high-resolution solid state ²H NMR spectroscopy. *Chemical physics letters*, 226(1-2):193–198, 1994.
- [85] T. N. Rudakov. Some aspects of spin-locking effect in nitrogen-14 quadrupolar spin-system. *Chemical physics letters*, 443(4-6):269–273, 2007.
- [86] X. Lu, O. Lafon, J. Trébosc, G. T., L. Delevoye, F. Méar, L. Montagne, and J-P Amoureux. Observation of proximities between spin-1/2 and quadrupolar nuclei: Which heteronuclear dipolar recoupling method is preferable? *Journal of chemical physics*, 137(14), 2012.
- [87] L. van Wüllen, L. Züchner, W. Müller-Warmuth, and H. Eckert. ¹¹B {²⁷Al} and al {¹¹B} double resonance experiments on a glassy sodium aluminoborate. *Solid State Nuclear Magnetic Resonance*, 6(3):203–212, 1996.
- [88] S. M. De Paul. Solid-state nuclear magnetic resonance studies of cross-polarization from quadrupolar nuclei. University of California, Berkeley, 1997.
- [89] S. H. Wang, S. M. De Paul, and L. M. Bull. High-resolution heteronuclear correlation between quadrupolar and spin-{1}/{2} nuclei using multiple-quantum magic-angle spinning. *Journal of Magnetic Resonance*, 125(2):364–368, 1997.

[90] P. Brunner, M. Reinhold, and R. R. Ernst. Double quantum cross polarization. heteronuclear excitation and detection of NMR double quantum transitions in solids. *Journal of Chemical Physics*, 73(3):1086–1094, 1980.

- [91] T. K. Pratum and M. P. Klein. Heteronuclear cross polarization of solid-state ¹⁴N NMR powder patterns. *Journal of Magnetic Resonance* (1969), 55(3):421–437, 1983.
- [92] P. Hodgkinson, Céline Auger, and L. Emsley. Deuterium to carbon cross-polarization in liquid crystals. *Journal of chemical physics*, 109(5):1873–1884, 1998.
- [93] D. Marks, N. Zumbulyadis, and S. Vega. Deuterium cross-polarization magic-angle spinning. *Journal of Magnetic Resonance*, Series A, 122(1):16–36, 1996.
- [94] K. Gopalakrishnan and G. Bodenhausen. Cross polarization from spins I= 1/2 to spin S= 1 in nuclear magnetic resonance with magic angle sample spinning. *Journal of chemical physics*, 124(19), 2006.
- [95] S. M. De Paul, M. Ernst, J. S. Shore, J. F. Stebbins, and A. Pines. Cross-polarization from quadrupolar nuclei to silicon using low-radio-frequency amplitudes during magic-angle spinning. *Journal of Physical Chemistry B*, 101(16):3240–3249, 1997.
- [96] C. A. Fyfe, H. Grondey, K. T. Mueller, K. C. Wong-Moon, and T. Markus. Coherence transfer involving quadrupolar nuclei in solids: aluminum-27. tautm. phosphorus-31 cross-polarization NMR in the molecular sieve vpi-5. *Journal of the American Chemical Society*, 114(14):5876–5878, 1992.
- [97] C. A. Fyfe, K. T. Mueller, H. Grondey, and K. C. Wong-Moon. Solid-state double-resonance NMR experiments involving quadrupolar and spin 1/2 nuclei. *Journal of Physical Chemistry*, 97(51):13484–13495, 1993.
- [98] R. K. Harris and G. J. Nesbitt. Cross polarization for quadrupolar nuclei—proton to sodium-23. *Journal of Magnetic Resonance* (1969), 78(2):245–256, 1988.
- [99] S. Wi, R. Schurko, and L. Frydman. ¹H–²H cross-polarization NMR in fast spinning solids by adiabatic sweeps. *Journal of chemical physics*, 146(10), 2017.
- [100] A. R. Altenhof, S. Wi, and R. W. Schurko. Broadband adiabatic inversion cross-polarization to integer-spin nuclei with application to deuterium NMR. *Magnetic Resonance in Chemistry*, 59(9-10):1009–1023, 2021.
- [101] S. V. Sajith, S.n Jayanthi, and A. Lupulescu. Effective hamiltonian and ¹H-¹⁴N cross polarization/double cross polarization at fast mas. *Journal of Magnetic Resonance*, 320:106832, 2020.
- [102] D. Srivastava, R. V. SubbaRao, and R. Ramachandran. Understanding multi-quantum NMR through secular approximation. *Physical Chemistry Chemical Physics*, 15(18):6699–6713, 2013.

[103] U. Haeberlen and J. S. Waugh. Coherent averaging effects in magnetic resonance. *Physical Review*, 175(2):453, 1968.

- [104] J. H. Shirley. Solution of the schrödinger equation with a hamiltonian periodic in time. *Physical Review*, 138(4B):B979, 1965.
- [105] A. Schmidt and S. Vega. The floquet theory of nuclear magnetic resonance spectroscopy of single spins and dipolar coupled spin pairs in rotating solids. *Journal of chemical physics*, 96(4):2655–2680, 1992.
- [106] G. Jeschke. Spin locking of I= 3/2 nuclei in static and spinning samples: A description by abstract spins and floquet formalism. *Journal of chemical physics*, 108(3):907–917, 1998.
- [107] R. Ramesh and M. S. Krishnan. Effective hamiltonians in floquet theory of magic angle spinning using van vleck transformation. *Journal of Chemical Physics*, 114(14):5967–5973, 2001.
- [108] M. K. Pandey and M. S. Krishnan. Effective floquet hamiltonians for dipolar and quadrupolar coupled n-spin systems in solid state nuclear magnetic resonance under magic angle spinning. *Journal of chemical physics*, 133(17), 2010.
- [109] V. Ganapathy and R. Ramachandran. Effective floquet hamiltonian theory of multiple-quantum NMR in anisotropic solids involving quadrupolar spins: Challenges and perspectives. *Journal of Chemical Physics*, 147(14), 2017.
- [110] S. Vega and A. Pines. Operator formalism for double quantum NMR. *Journal of Chemical Physics*, 66(12):5624–5644, 1977.
- [111] S. Vega. Fictitious spin 1/2 operator formalism for multiple quantum NMR. *Journal of Chemical Physics*, 68(12):5518–5527, 1978.
- [112] A. Wokaun and R. R. Ernst. Selective excitation and detection in multilevel spin systems: Application of single transition operators. *Journal of Chemical Physics*, 67(4):1752–1758, 1977.
- [113] N. Chandrakumar and N. Chandrakumar. NMR of spin-1 systems in the solid state. Spin-1 NMR, pages 59–109, 1996.
- [114] M. Bansal and R. Ramachandran. Theory of finite pulse effects beyond perturbation limit: Challenges and perspectives. *Journal of Magnetic Resonance Open*, 10:100042, 2022.
- [115] N. Bamola, M. Bansal, and R. Ramachandran. Quantifying quadrupole effects in the NMR spectra of spin-1/2 nuclei in rotating solids. *Physical Chemistry Chemical Physics*, 25(27):17877–17900, 2023.

[116] E. Nehra and M. K. Pandey. Unravelling the mechanism of polarization transfer from spin-1/2 to spin-1 system in solids. *Physical Chemistry Chemical Physics*, 26(4):2995–3007, 2024.

- [117] E. Nehra and M. K. Pandey. Analytic theory of cross-polarization dynamics between spin-1/2 to spin-1 under off-resonance irradiation and second-order quadrupolar effects. *To be submmitted*, 2025.
- [118] J. Keeler. Understanding NMR Spectroscopy. Wiley, 2011.
- [119] M. H. Levitt. Spin Dynamics: Basics of Nuclear Magnetic Resonance. Wiley, 2013.
- [120] I. I. Rabi. Space quantization in a gyrating magnetic field. *Physical Review*, 51(8):652, 1937.
- [121] S. A. Smith, W. E. Palke, and J. T. Gerig. The hamiltonians of NMR. part I. Concepts in magnetic resonance, 4(2):107–144, 1992.
- [122] M. H. Cohen and F. Reif. Quadrupole effects in nuclear magnetic resonance studies of solids. In *Solid state physics*, volume 5, pages 321–438. Elsevier, 1957.
- [123] P. P. Man. Quadrupole couplings in nuclear magnetic resonance, general. Encyclopedia of analytical chemistry, 10:9780470027318, 2000.
- [124] E. P. Wigner. On the matrices which reduce the kronecker products of representations of sr groups. In *Collected Works of Eugene Paul Wigner: Part A: The Scientific Papers*, pages 608–654. Springer, 1993.
- [125] M. E. Rose. Elementary theory of angular momentum. Courier Corporation, 1995.
- [126] H. B. G. Casimir. On the interaction between atomic nuclei and electrons. In *On the Interaction between Atomic Nuclei and Electrons*, pages 201–283. Springer, 1936.
- [127] A. R. Edmonds. Angular momentum in quantum mechanics, volume 4. Princeton university press, 1996.
- [128] M. M. Maricq. Application of average hamiltonian theory to the NMR of solids. *Physical Review B*, 25(11):6622, 1982.
- [129] U. Fano. Description of states in quantum mechanics by density matrix and operator techniques. *Reviews of modern physics*, 29(1):74, 1957.
- [130] K. Blum. Density matrix theory and applications, volume 64. Springer Science & Business Media, 2012.
- [131] M. Bak, J. T. Rasmussen, and N. C. Nielsen. Simpson: a general simulation program for solid-state nmr spectroscopy. *Journal of magnetic resonance*, 213(2):366–400, 2011.

[132] M. Bak, J. T. Rasmussen, and N. C. Nielsen. Simpson: A general simulation program for solid-state NMR spectroscopy. *Journal of magnetic resonance*, 213(2):366–400, 2011.

- [133] J. E. Campbell. On a law of combination of operators (second paper). *Proceedings* of the London Mathematical Society, 1(1):14–32, 1897.
- [134] R. Achilles and A Bonfiglioli. The early proofs of the theorem of campbell, baker, hausdorff, and dynkin. *Arch. Hist. Exact Sci.*, 66(2):295–358, 2012.
- [135] E. Nehra and M. K. Pandey. Analytic theory of CP transfer from I = 1/2 to S = 3/2 spin systems in solids. To be submmitted, 2025.
- [136] S. V. Dvinskikh, H. Zimmermann, A. Maliniak, and D. Sandström. Heteronuclear dipolar recoupling in solid-state nuclear magnetic resonance by amplitude, phase, and frequency-modulated lee-goldburg cross-polarization. *Journal of chemical* physics, 122(4), 2005.
- [137] M. Edén. Computer simulations in solid-state NMR. iii. powder averaging. Concepts in Magnetic Resonance Part A: An Educational Journal, 18(1):24–55, 2003.
- [138] S. M. Zhang, B. H. Meier, and R. R. Ernst. Mismatch-compensated cross polarization. W-MOIST, an improved pulse scheme. *Journal of Magnetic Resonance*, *Series A*, 108(1):30–37, 1994.
- [139] K. Chen. A practical review of NMR lineshapes for spin-1/2 and quadrupolar nuclei in disordered materials. *International journal of molecular sciences*, 21(16):5666, 2020.
- [140] Z. Qadri. Understanding Cross-Polarization NMR Experiments Using Multi-Mode Floquet Theory. PhD thesis, 2015.
- [141] L. Landau. Zur theorie der energieubertragung. ii. *Physikalische Zeitschrift der Sowjetunion*, 2:46, 1932.
- [142] C. Zener. Non-adiabatic crossing of energy levels. Proceedings of the Royal Society of London. Series A, Containing Papers of a Mathematical and Physical Character, 137(833):696–702, 1932.
- [143] C. P. Grey and W. S. Veeman. The detection of weak heteronuclear coupling between spin-1 and spin-12 nuclei in mas NMR; ¹⁴N/¹³C/¹H triple resonance experiments. *Chemical physics letters*, 192(4):379–385, 1992.
- [144] J. A. Jarvis, M. Concistre, I. M. Haies, R. W. Bounds, I. Kuprov, M. Carravetta, and Philip T. F. Williamson. Quantitative analysis of ¹⁴N quadrupolar coupling using ¹H detected ¹⁴N solid-state NMR. *Physical Chemistry Chemical Physics*, 21(11):5941–5949, 2019.

References 165

[145] F. Ferrage, T. R. Eykyn, and G. Bodenhausen. Coherence transfer by single-transition cross-polarization: Quantitation of cross-correlation effects in nuclear magnetic resonance. *Journal of Chemical Physics*, 113(3):1081–1087, 2000.

- [146] L. Müller, R. Eckman, and A. Pine. Chem. Phy. Lett., 76:149–154, 1980.
- [147] D. Carnevale, B. Grosjean, and G. Bodenhausen. Dipolar couplings in solid polypeptides probed by ¹⁴N NMR spectroscopy. Communications Chemistry, 1(1):73, 2018.
- [148] P. Caravatti, G. Bodenhausen, and R. R. Ernst. Selective pulse experiments in high-resolution solid state NMR. *Journal of Magnetic Resonance* (1969), 55(1):88–103, 1983.
- [149] A. J. Pell, K. J. Sanders, S. Wegner, G. Pintacuda, and C. P. Grey. Low-power broadband solid-state mas NMR of ¹⁴N. *Journal of Chemical Physics*, 146(19), 2017.
- [150] L. Chen, Q. Wang, B. Hu, O. Lafon, J. Trébosc, F. Deng, and J-P Amoureux. Measurement of hetero-nuclear distances using a symmetry-based pulse sequence in solid-state NMR. Physical Chemistry Chemical Physics, 12(32):9395–9405, 2010.
- [151] W. Sun, J. T. Stephen, L. D. Potter, and Y. Wu. Rotation-induced resonance and second-order quadrupolar effects on spin locking of half-integer quadrupolar nuclei. *Journal of Magnetic Resonance*, Series A, 116(2):181–188, 1995.
- [152] S. Odedra and S. Wimperis. Spin-locking of half-integer quadrupolar nuclei in NMR of solids: The far off-resonance case. Solid State Nuclear Magnetic Resonance, 84:4–13, 2017.
- [153] Ad Bax, B. L. Hawkins, and G. E. Maciel. Off resonance cross-polarization: A technique to reduce rf power requirements for magnetization transfer experiments in solids. *Journal of Magnetic Resonance* (1969), 59(3):530–535, 1984.
- [154] S. Wi, R. W. Schurko, and L. Frydman. Broadband adiabatic inversion cross-polarization phenomena in the NMR of rotating solids. Solid State Nuclear Magnetic Resonance, 94:31–53, 2018.
- [155] J. J. Kimball, A. R. Altenhof, M. J. Jaroszewicz, and R. W. Schurko. Broadband cross-polarization to half-integer quadrupolar nuclei: Wideline static NMR spectroscopy. *Journal of Physical Chemistry A*, 127(45):9621–9634, 2023.
- [156] S. E. Ashbrook and S. Wimperis. Spin-locking of half-integer quadrupolar nuclei in nuclear magnetic resonance of solids: second-order quadrupolar and resonance offset effects. *Journal of chemical physics*, 131(19), 2009.

166 References

[157] G. Wu, D. Rovnyak, and R. G. Griffin. Quantitative multiple-quantum magic-angle-spinning NMR spectroscopy of quadrupolar nuclei in solids. *Journal* of the American Chemical Society, 118(39):9326–9332, 1996.

- [158] D. Iuga, C. Morais, Z. Gan, D. R. Neuville, L. Cormier, and D. Massiot. NMR heteronuclear correlation between quadrupolar nuclei in solids. *Journal of the American Chemical Society*, 127(33):11540–11541, 2005.
- [159] G. Wu. Quadrupolar nuclei in biological systems. Encyclopedia of Analytical Chemistry: Applications, Theory and Instrumentation, 2006.
- [160] T. Polenova, A. S. Lipton, and P. D. Ellis. Quadrupolar NMR of metal nuclides in biological materials. NMR of Quadrupolar Nuclei in Solid Materials, 3:439, 2012.
- [161] A. P. M. Kentgens. Quantitative excitation of half-integer quadrupolar nuclei by a frequency-stepped adiabatic half-passage. 1991.
- [162] T. Wolf, M. J. Jaroszewicz, and L. Frydman. Quadrupolar isotope-correlation spectroscopy in solid-state NMR. Journal of Physical Chemistry C, 126(22):9386–9395, 2022.
- [163] Z. Yao, H. T. Kwak, D. Sakellariou, L. Emsley, and P. J. Grandinetti. Sensitivity enhancement of the central transition NMR signal of quadrupolar nuclei under magic-angle spinning. *Chemical Physics Letters*, 327(1-2):85–90, 2000.
- [164] A. Samoson and E. Lippmaa. Excitation phenomena and line intensities in high-resolution NMR powder spectra of half-integer quadrupolar nuclei. *Physical Review B*, 28(11):6567, 1983.
- [165] S. Hayashi. Magic-angle spinning nuclear magnetic resonance of half-integer quadrupole nuclei: effect of spin-locking efficiency on powder lineshapes. Solid State Nuclear Magnetic Resonance, 3(2):93–101, 1994.
- [166] Y. Zhang, F. Deng, J. Qiu, and C. Ye. Spin-locking mechanism of spin I = 3/2 quadrupolar nuclei undergo magic angle spinning. *Solid State Nuclear Magnetic Resonance*, 15(4):209–216, 2000.
- [167] S. E. Ashbrook and S. Wimperis. Spin-locking of half-integer quadrupolar nuclei in nuclear magnetic resonance of solids: creation and evolution of coherences. *Journal* of chemical physics, 120(6):2719–2731, 2004.
- [168] M. Edén. Quadrupolar coupling selective cross-polarization in solid state NMR. Physical Chemistry Chemical Physics, 8(17):1994–1999, 2006.
- [169] C. Fernandez, L. Delevoye, J-P Amoureux, D. P. Lang, and M. Pruski. ²⁷Al {¹H} cross polarization triple-quantum magic angle spinning NMR. *Journal of the American Chemical Society*, 119(29):6858–6862, 1997.

References 167

[170] K. H. Lim and C. P. Grey. ¹⁹F/²³Na multiple quantum cross polarization NMR in solids. *Journal of Chemical Physics*, 112(17):7490–7504, 2000.

- [171] M. Pruski, D. P. Lang, C. Fernandez, and J. P. Amoureux. Multiple-quantum magic-angle spinning NMR with cross-polarization: Spectral editing of high-resolution spectra of quadrupolar nuclei. Solid State Nuclear Magnetic Resonance, 7(4):327–331, 1997.
- [172] S. E. Ashbrook, S. P. Brown, and S. Wimperis. Multiple-quantum cross-polarization in mas NMR of quadrupolar nuclei. *Chemical physics letters*, 288(2-4):509–517, 1998.
- [173] J. C. C. Chan, M. Bertmer, and H. Eckert. Double-quantum cross-polarization between half-integer quadrupolar spin systems: $^{11}\text{B} \leftrightarrow ^{23}\text{Na}$ and $^{11}\text{B} \leftrightarrow ^{27}\text{Al}$. Chemical physics letters, 292(1-2):154–160, 1998.
- [174] J. C. C. Chan, M. Bertmer, and H. Eckert. Site connectivities in amorphous materials studied by double-resonance NMR of quadrupolar nuclei: High-resolution $^{11}B \leftrightarrow ^{27}Al$ spectroscopy of aluminoborate glasses. *Journal of the American Chemical Society*, 121(22):5238–5248, 1999.
- [175] J. C. C. Chan. High-resolution heteronuclear correlation between quadrupolar nuclei, 1999.
- [176] S. Vega and Y. Naor. Triple quantum NMR on spin systems with I= 3/2 in solids. Journal of Chemical Physics, 75(1):75–86, 1981.
- [177] H. P. Breuer and F. Petruccione. *The theory of open quantum systems*. Oxford University Press on Demand, 2002.
- [178] A. J. Vega. Quadrupolar nuclei in solids. Solid State NMR Studies of Biopolymers, 2007.
- [179] S. W. Ding and C. A. Mcdowell. Theoretical calculations of the cpmas spectral lineshapes of half-integer quadrupole systems. *Journal of Magnetic Resonance*, *Series A*, 114(1):80–87, 1995.

Appendix A

A.1 Matrix representation of the basis states and spin-operators for the S=1 spin-system

Table A.1: Matrix representation of the Zeeman basis for the S=1 spin system.

$$|1\rangle = |1\rangle_S = \begin{bmatrix} 1 \\ 0 \\ 0 \end{bmatrix}; \, |2\rangle = |0\rangle_S = \begin{bmatrix} 0 \\ 1 \\ 0 \end{bmatrix}; \, |3\rangle = |-1\rangle_S = \begin{bmatrix} 0 \\ 0 \\ 1 \end{bmatrix}$$

Table A.2: Matrix representation of the single-transition operators for the S=1 spin system.

$$\hat{S}_x = \frac{1}{\sqrt{2}} \begin{bmatrix} 0 & 1 & 0 \\ 1 & 0 & 1 \\ 0 & 1 & 0 \end{bmatrix}; \hat{S}_y = \frac{i}{\sqrt{2}} \begin{bmatrix} 0 & -1 & 0 \\ 1 & 0 & -1 \\ 0 & 1 & 0 \end{bmatrix}; \hat{S}_z = \begin{bmatrix} 1 & 0 & 0 \\ 0 & 0 & 0 \\ 0 & 0 & -1 \end{bmatrix}$$

Table A.3: Matrix representation of the Cartesian spin-operators for the single S=1 spin system.

$$\begin{split} \hat{S}_{x}^{12} &= \frac{1}{2} \begin{bmatrix} 0 & 1 & 0 \\ 1 & 0 & 0 \\ 0 & 0 & 0 \end{bmatrix}; \, \hat{S}_{x}^{23} = \frac{1}{2} \begin{bmatrix} 0 & 0 & 0 \\ 0 & 0 & 1 \\ 0 & 1 & 0 \end{bmatrix}; \, \hat{S}_{x}^{13} = \frac{1}{2} \begin{bmatrix} 0 & 0 & 1 \\ 0 & 0 & 0 \\ 1 & 0 & 0 \end{bmatrix} \\ \hat{S}_{y}^{12} &= \frac{i}{2} \begin{bmatrix} 0 & -1 & 0 \\ 1 & 0 & 0 \\ 0 & 0 & 0 \end{bmatrix}; \, \hat{S}_{y}^{23} = \frac{i}{2} \begin{bmatrix} 0 & 0 & 0 \\ 0 & 0 & -1 \\ 0 & 1 & 0 \end{bmatrix}; \, \hat{S}_{y}^{13} = \frac{i}{2} \begin{bmatrix} 0 & 0 & -1 \\ 0 & 0 & 0 \\ 1 & 0 & 0 \end{bmatrix} \\ \hat{S}_{z}^{12} &= \frac{1}{2} \begin{bmatrix} 1 & 0 & 0 \\ 0 & -1 & 0 \\ 0 & 0 & 0 \end{bmatrix}; \, \hat{S}_{z}^{23} = \frac{1}{2} \begin{bmatrix} 0 & 0 & 0 \\ 0 & 1 & 0 \\ 0 & 0 & -1 \end{bmatrix}; \, \hat{S}_{z}^{13} = \frac{1}{2} \begin{bmatrix} 1 & 0 & 0 \\ 0 & 0 & 0 \\ 0 & 0 & -1 \end{bmatrix} \end{split}$$

Table A.4: Single-transition operator representation of the spin-operators for the S=1 spin system.

$$\hat{S}_x = \sqrt{2}[\hat{S}_x^{12} + \hat{S}_x^{23}]; \ \hat{S}_y = \sqrt{2}[\hat{S}_y^{12} + \hat{S}_y^{23}]; \ \hat{S}_z = 2[\hat{S}_z^{12} + \hat{S}_z^{23}]$$

Table A.5: Matrix representation of the projection operators for the S=1 spin system.

$$\hat{P}_{11} = \begin{bmatrix} 1 & 0 & 0 \\ 0 & 0 & 0 \\ 0 & 0 & 0 \end{bmatrix}; \, \hat{P}_{12} = \begin{bmatrix} 0 & 1 & 0 \\ 0 & 0 & 0 \\ 0 & 0 & 0 \end{bmatrix}; \, \hat{P}_{13} = \begin{bmatrix} 0 & 0 & 1 \\ 0 & 0 & 0 \\ 0 & 0 & 0 \end{bmatrix}; \, \hat{P}_{21} = \begin{bmatrix} 0 & 0 & 0 \\ 1 & 0 & 0 \\ 0 & 0 & 0 \end{bmatrix}; \, \hat{P}_{22} = \begin{bmatrix} 0 & 0 & 0 \\ 0 & 1 & 0 \\ 0 & 0 & 0 \end{bmatrix}; \, \hat{P}_{23} = \begin{bmatrix} 0 & 0 & 0 \\ 0 & 0 & 1 \\ 0 & 0 & 0 \end{bmatrix}; \, \hat{P}_{31} = \begin{bmatrix} 0 & 0 & 0 \\ 0 & 0 & 0 \\ 1 & 0 & 0 \end{bmatrix}; \, \hat{P}_{32} = \begin{bmatrix} 0 & 0 & 0 \\ 0 & 0 & 0 \\ 0 & 1 & 0 \end{bmatrix}; \, \hat{P}_{33} = \begin{bmatrix} 0 & 0 & 0 \\ 0 & 0 & 0 \\ 0 & 0 & 1 \end{bmatrix}$$

Table A.6: Projection operators representation of the spin-operators for the S=1 spin system.

$$\hat{S}_x = \frac{1}{\sqrt{2}} [\hat{P}_{12} + \hat{P}_{21} + \hat{P}_{23} + \hat{P}_{32}]$$

$$\hat{S}_y = \frac{-i}{\sqrt{2}} [-\hat{P}_{12} + \hat{P}_{21} - \hat{P}_{23} + \hat{P}_{32}]$$

$$\hat{S}_z = [\hat{P}_{11} - \hat{P}_{33}]$$

Appendix B

B.1 Matrix representation of the product basis states and spin-operators for the I=1/2 and S=1/2 coupled spin-system

Table B.1: Matrix representation of the product basis for the I=1/2 and S=1/2 spin system.

$$|1\rangle = |1/2\rangle_I \bigotimes |1/2\rangle_S \equiv |1/2, 1/2\rangle = \begin{bmatrix} 1 \\ 0 \\ 0 \\ 0 \end{bmatrix}$$

$$|2\rangle = |1/2\rangle_I \bigotimes |-1/2\rangle_S \equiv |1/2, -1/2\rangle = \begin{bmatrix} 0 \\ 1 \\ 0 \\ 0 \end{bmatrix}$$

$$|3\rangle = |-1/2\rangle_I \bigotimes |1/2\rangle_S \equiv |-1/2,1/2\rangle = \begin{bmatrix} 0 \\ 0 \\ 1 \\ 0 \end{bmatrix}$$

$$|4\rangle = |-1/2\rangle_I \bigotimes |-1/2\rangle_S \equiv |-1/2, -1/2\rangle = \begin{bmatrix} 0 \\ 0 \\ 0 \\ 1 \end{bmatrix}$$

Table B.2: Matrix representation of six Cartesian operators for the I=1/2 and S=1/2 in product basis.

$$\hat{I}_{x} = \frac{1}{2} \begin{bmatrix} 0 & 0 & 1 & 0 \\ 0 & 0 & 0 & 1 \\ 0 & 1 & 0 & 0 \\ 0 & 1 & 0 & 0 \end{bmatrix} \qquad \hat{I}_{y} = \frac{i}{2} \begin{bmatrix} 0 & 0 & -1 & 0 \\ 0 & 0 & 0 & -1 \\ 0 & 1 & 0 & 0 \\ 0 & 1 & 0 & 0 \end{bmatrix} \qquad \hat{I}_{z} = \frac{1}{2} \begin{bmatrix} 1 & 0 & 0 & 0 \\ 0 & 1 & 0 & 0 \\ 0 & 0 & -1 & 0 \\ 0 & 0 & 0 & -1 \end{bmatrix}$$

$$\hat{S}_{x} = \frac{1}{2} \begin{bmatrix} 0 & 1 & 0 & 0 \\ 1 & 0 & 0 & 0 \\ 0 & 0 & 0 & 1 \\ 0 & 0 & 1 & 0 \end{bmatrix} \qquad \hat{S}_{y} = \frac{i}{2} \begin{bmatrix} 0 & -1 & 0 & 0 \\ 1 & 0 & 0 & 0 \\ 0 & 0 & 0 & -1 \\ 0 & 0 & 1 & 0 \end{bmatrix} \qquad \hat{S}_{z} = \frac{1}{2} \begin{bmatrix} 1 & 0 & 0 & 0 \\ 0 & -1 & 0 & 0 \\ 0 & 0 & -1 & 0 \\ 0 & 0 & 0 & 1 \end{bmatrix}$$

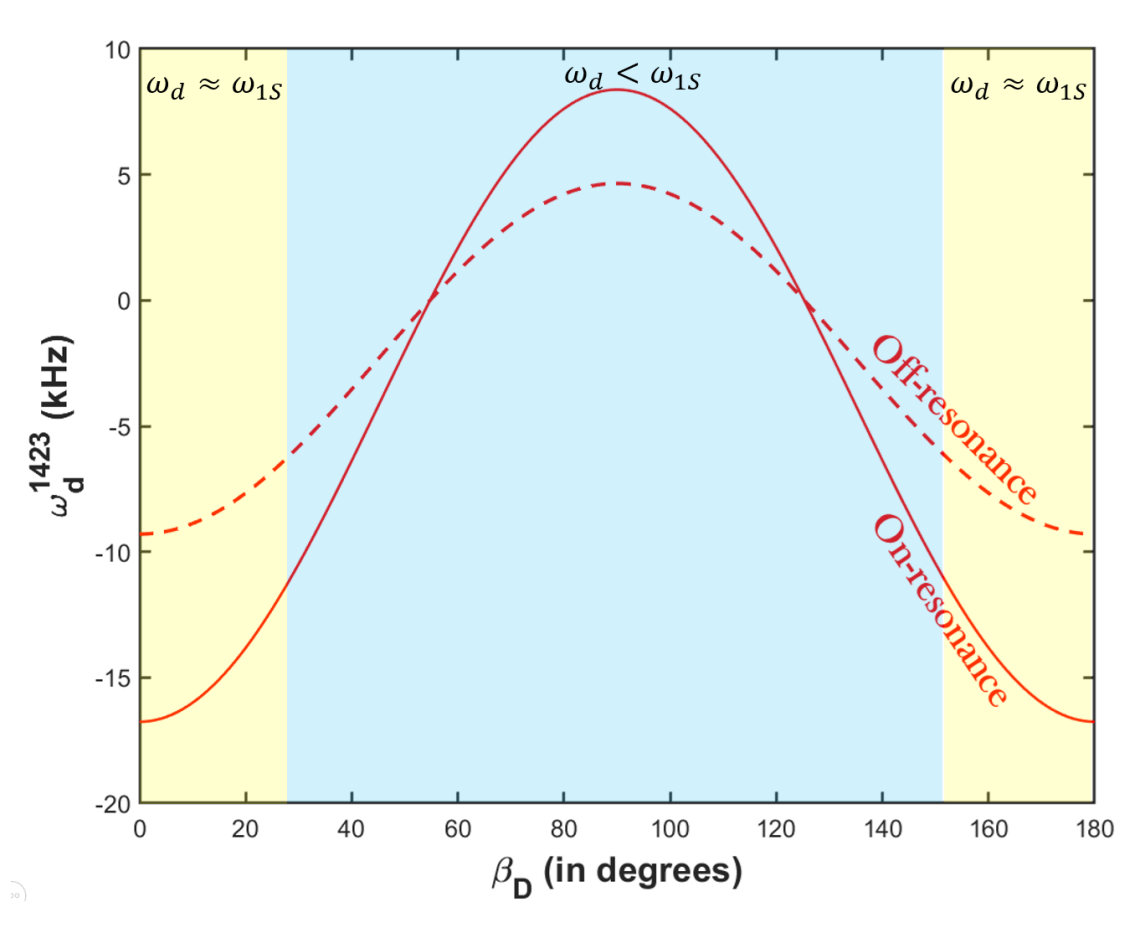


Figure B.1: The effect of dipolar coupling PAS angle β_d on the effective dipolar coupling frequency for both on and off-resonance irradiations. The following parameters were used in the simulations: Dipolar parameters (internuclear distance $r_{IS}=1.05$ Å), RF parameters: $\nu_{1H}=20$ kHz and $\nu_{1S}=20$ kHz and under off-resonance irradiation strength $\Omega_S=20$ kHz. This diagram shows the various coupling regimes based on the dipolar coupling magnitude and S-spin rf field strengths.

Appendix C

C.1 Matrix representation of the product basis states and spin-operators for the I=1/2 and S=1 coupled spin-system.

Table C.1: Matrix representation of the product basis for the I=1/2 and S=1 spins in product basis.

$$|1\rangle = |1/2\rangle_I \otimes |1\rangle_S \equiv |1/2, 1\rangle = \begin{bmatrix} 1\\0\\0\\0\\0\\0 \end{bmatrix}$$

$$|2\rangle = |1/2\rangle_I \otimes |0\rangle_S \equiv |1/2, 0\rangle = \begin{bmatrix} 0\\1\\0\\0\\0\\0 \end{bmatrix}$$

$$|3\rangle = |1/2\rangle_I \otimes |-1\rangle_S \equiv |1/2, -1\rangle = \begin{bmatrix} 0\\0\\1\\0\\0\\0 \end{bmatrix}$$

$$|4\rangle = |-1/2\rangle_I \otimes |1\rangle_S \equiv |-1/2, 1\rangle = \begin{bmatrix} 0\\0\\0\\1\\0\\0 \end{bmatrix}$$

$$[0]$$

$$|5\rangle = |-1/2\rangle_I \bigotimes |0\rangle_S \equiv |-1/2,0\rangle = \begin{bmatrix} 0\\0\\0\\0\\1\\0 \end{bmatrix} \qquad |6\rangle = |-1/2\rangle_I \bigotimes |-1\rangle_S \equiv |-1/2,-1\rangle = \begin{bmatrix} 0\\0\\0\\0\\1\\1 \end{bmatrix}$$

C.2 Description of CP spin dynamics based on existing reports

From equation (3.10) (in the main text), the CP Hamiltonian during the mixing (spin-locking/contact) period under the on-resonance S-spin irradiation is given as

$$\begin{split} & \tilde{\hat{H}} = \Big(\frac{\omega_e - \omega_Q^{(1)}}{4}\Big) \big[\hat{S}_z^{13} + \hat{S}_z^{46}\big] + \Big(\frac{3\omega_e + \omega_Q^{(1)}}{12}\Big) \big[\hat{S}_z^{12} - \hat{S}_z^{23} + \hat{S}_z^{45} - \hat{S}_z^{56}\big] + \omega_{1I} \big[\hat{S}_z^{14} + \hat{S}_z^{25} + \hat{S}_z^{36}\big] \\ & + 2\omega_d \cos\theta_1/2 \big[\hat{S}_x^{16} + \hat{S}_x^{34}\big] - 2\omega_d \sin\theta_1/2 \big[\hat{S}_x^{26} + \hat{S}_x^{35}\big]. \end{split} \tag{A1}$$

Table C.2: Matrix representation of six Cartesian operators for the I=1/2 and S=1 in product basis.

To explain the experimental results obtained from CP experiments, Pratum and Klein proposed an approach, wherein, the above Hamiltonian was re-expressed in two forms. In the first approach, the Hamiltonian was expressed in the TQ_{16} - SQ_{34} subspace ignoring the dipolar contributions resulting from the ZQ_{35} - DQ_{26} operators. Employing such an approach, the CP dynamics corresponding to the SQ_{34} matching condition was described qualitatively without any analytic expression. In the second approach, the same Hamiltonian was re-expressed in the ZQ_{35} - DQ_{26} subspace ignoring the dipolar contributions emerging from the TQ_{16} - SQ_{34} operators. While such an approach, presents a qualitative description of the CP dynamics observed in experiments, the method is of limited utility in quantifying the experimental data. Below, we present a brief description of the signal expressions derived from the effective Hamiltonians using their approach.

Method I: Description of the CP dynamics in the triple and single-quantum $(TQ_{16}+SQ_{34})$ sub-spaces

To describe the spin dynamics corresponding to the SQ_{34} and TQ_{16} matching conditions, the Hamiltonian in Eq. (A1) is re-expressed in terms of the TQ_{16}/SQ_{34} operators.

$$\tilde{\hat{H}}_{16,34} \approx \Sigma_{16} [\hat{S}_{z}^{16}] + \omega_{d}^{16,34} [\hat{S}_{x}^{16}] + \Delta_{34} [\hat{S}_{z}^{34}] + \omega_{d}^{16,34} [\hat{S}_{x}^{34}] + \omega_{1I} [\hat{S}_{z}^{25}] + \left(\frac{3\omega_{e} + \omega_{Q}^{(1)}}{12}\right) [\hat{S}_{z}^{12} - \hat{S}_{z}^{23} + \hat{S}_{z}^{45} - \hat{S}_{z}^{56}]$$
(A2)

where,
$$\Sigma_{16} = \left\{ \frac{4\omega_{1I} + (\omega_e - \omega_Q^{(1)})}{4} \right\}$$
, $\Delta_{34} = \left\{ \frac{4\omega_{1I} - (\omega_e - \omega_Q^{(1)})}{4} \right\}$, and $\omega_d^{16,34} = 2\omega_d \cos \theta_1/2$.

Employing the effective-field approach described in the main section, the above Hamiltonian is diagonalized sequentially and the final form of the signal observed in CP experiments is derived and summarized below:

$$\hat{H}_{eff,16,34} = \omega_{eff}^{16} \left[\hat{S}_z^{16} \right] + \omega_{eff}^{34} \left[\hat{S}_z^{34} \right] + \omega_{1I} \left[\hat{S}_z^{25} \right] + \left(\frac{3\omega_e + \omega_Q^{(1)}}{12} \right) \left[\hat{S}_z^{12} - \hat{S}_z^{23} + \hat{S}_z^{45} - \hat{S}_z^{56} \right]$$
where, $\omega_{eff}^{16} = \sqrt{\Sigma_{16}^2 + (\omega_d^{16,34})^2}$ and $\omega_{eff}^{34} = \sqrt{\Delta_{34}^2 + (\omega_d^{16,34})^2}$. (A3)

Using the density operator formalism, the signal expression in the $TQ_{16}+SQ_{34}$ space is given as

$$S(t)_{16,34} = \langle \hat{S}_{e,x}(t) \rangle$$

$$= \frac{4\omega_{1S}}{\omega_e} \left[\underbrace{-\frac{(\omega_d^{16,34})^2}{\sum_{16}^2 + (\omega_d^{16,34})^2} \sin^2 \frac{\sqrt{\sum_{16}^2 + (\omega_d^{16,34})^2}}{2}}_{TQ_{16}} t + \underbrace{\frac{(\omega_d^{16,34})^2}{\sum_{34}^2 + (\omega_d^{16,34})^2} \sin^2 \frac{\sqrt{\Delta_{34}^2 + (\omega_d^{16,34})^2}}{2}}_{SQ_{34}} t \right].$$

$$(A4)$$

Method II: Description of the CP dynamics in the zero and double-quantum $(\mathbf{ZQ}_{35}+\mathbf{DQ}_{26})$ sub-spaces

In a similar vein, to describe the CP dynamics in the ZQ_{35} - DQ_{26} subspace, Eq. (A1) is re-expressed in terms of the ZQ_{35}/DQ_{26} operators.

$$\hat{\tilde{H}}_{35,26} \approx \Sigma_{35} [\hat{S}_z^{35}] + \omega_d^{26,35} [\hat{S}_x^{35}] + \Delta_{26} [\hat{S}_z^{26}] + \omega_d^{26,35} [\hat{S}_x^{26}] + \omega_{1I} [\hat{S}_z^{14}] + \left(\frac{3\omega_e - \omega_Q^{(1)}}{12}\right) [\hat{S}_z^{12} + \hat{S}_z^{13} + \hat{S}_z^{45} + \hat{S}_z^{46}]$$
(A5)

where,
$$\Sigma_{35} = \left\{ \frac{4\omega_{1I} + (\omega_e + \omega_Q^{(1)})}{4} \right\}$$
, $\Delta_{26} = \left\{ \frac{4\omega_{1I} - (\omega_e + \omega_Q^{(1)})}{4} \right\}$ and $\omega_d^{26,35} = -2\omega_d \sin \theta_1/2$.

Employing the effective-field approach, the above Hamiltonian is diagonalized and the final form of the signal expression observed in CP experiments is derived and summarized below:

$$\hat{H}_{eff,35,26} = \omega_{eff}^{35} \left[\hat{S}_z^{35} \right] + \omega_{eff}^{26} \left[\hat{S}_z^{26} \right] + \omega_{1I} \left[\hat{S}_z^{14} \right] + \left(\frac{3\omega_e - \omega_Q^{(1)}}{12} \right) \left[\hat{S}_z^{12} + \hat{S}_z^{13} + \hat{S}_z^{45} + \hat{S}_z^{46} \right]$$
where $\omega_{eff}^{35} = \sqrt{\Sigma_{35}^2 + (\omega_d^{26,35})^2}$ and $\omega_{eff}^{26} = \sqrt{\Delta_{35}^2 + (\omega_d^{26,35})^2}$.

Utilizing the density operator formalism, the signal expression in the ZQ₃₅+DQ₂₆ space

is given as

$$S(t)_{35,26} = \frac{4\omega_{1S}}{\omega_e} \left[\underbrace{-\frac{(\omega_d^{26,35})^2}{\Sigma_{35}^2 + (\omega_d^{26,35})^2} \sin^2 \frac{\sqrt{\Sigma_{35}^2 + (\omega_d^{26,35})^2}}{2}}_{ZQ_{35}} t + \underbrace{\frac{(\omega_d^{26,35})^2}{\Delta_{26}^2 + (\omega_d^{26,35})^2} \sin^2 \frac{\sqrt{\Delta_{26}^2 + (\omega_d^{26,35})^2}}{2}}_{DQ_{26}} t \right]$$

$$(A7)$$

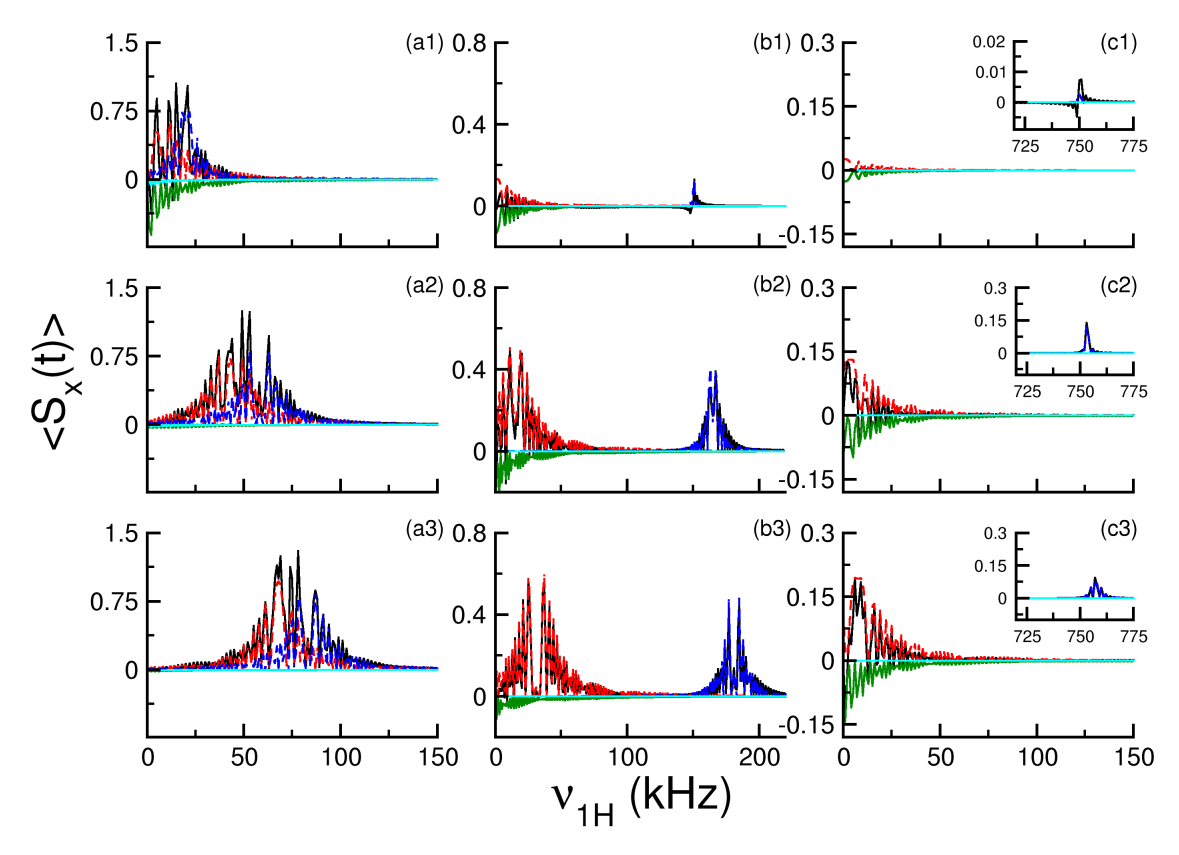


Figure C.1: In the CP simulations depicted, the polarization build-up on the S-spin (due to transfer from the I-spin) is monitored in a single crystal as a function of the rf field employed on the I-spin under different S-spin rf field strength ν_{1S} : 10 kHz (a1,b1,c1), 50 kHz (a2,b2,c2) and 75 kHz (a3,b3,c3). The numerical simulations (based on SIMPSON) are represented by solid black lines. The following parameters were employed in the simulations: Quadrupolar parameters ($C_Q = 20$ kHz (a1-a3), 200 kHz (b1-b3), and 1.0 MHz (c1-c3), $\eta_Q = 0$, quadrupolar coupling PAS angle α_Q and $\beta_Q = 0^{\circ}$), Dipolar parameters (internuclear distance $r_{IS} = 1.05$ Å) and the mixing time during the CP experiment was held constant (say $t_{mix} = 0.5$ ms). The analytic simulations based on signal expressions corresponding to various CP matching conditions are indicated: SQ₃₄ (red), TQ₁₆ (green), DQ₂₆ (blue) and ZQ₃₅ (cyan) [refer to Eq. (3.19) in the main text]. The insets in panels c1-c3 show CP maxima in the higher I-spin rf field range.

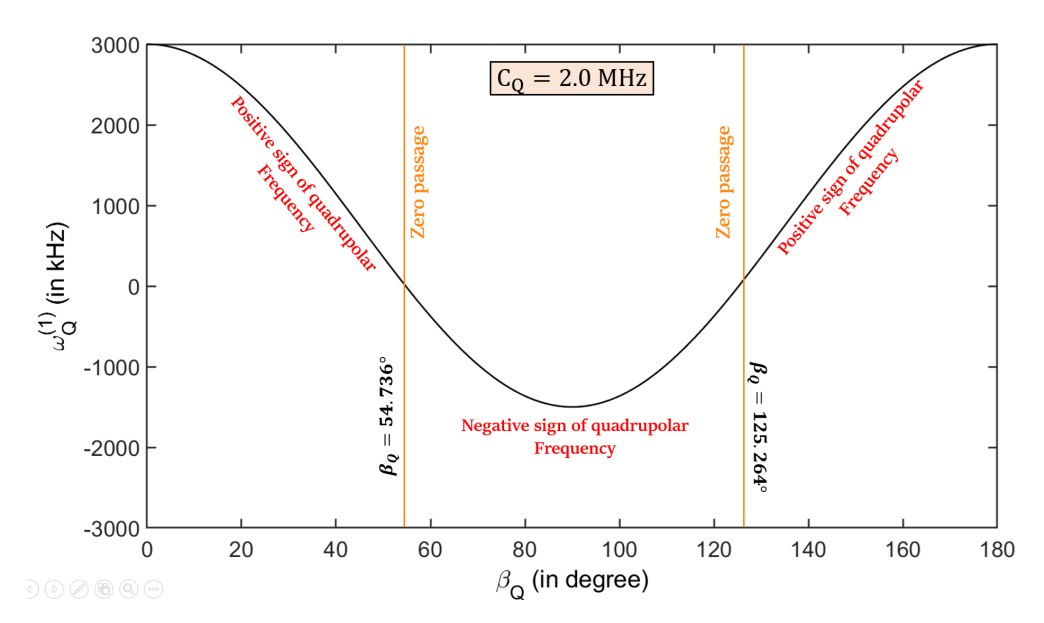


Figure C.2: Effect of the variation of quadrupolar coupling PAS angle β_Q on the first-order quadrupolar coupling frequency. Considering the quadrupolar PAS coincides with the Molecular-axis systems (MolAS), the angles β_Q will represent different crystallites orientations. The following simulation parameters were used: $C_Q = 2.0$ MHz, $\eta_Q = 0.0$, quadrupolar coupling PAS angle $\alpha_Q = 0^{\circ}$. The orange lines at $\beta_Q = 54.736^{\circ}$ and 125.264° show zero passage or zero-crossing of the quadrupolar frequency where the sign of quadrupolar coupling frequency changes from positive to negative.

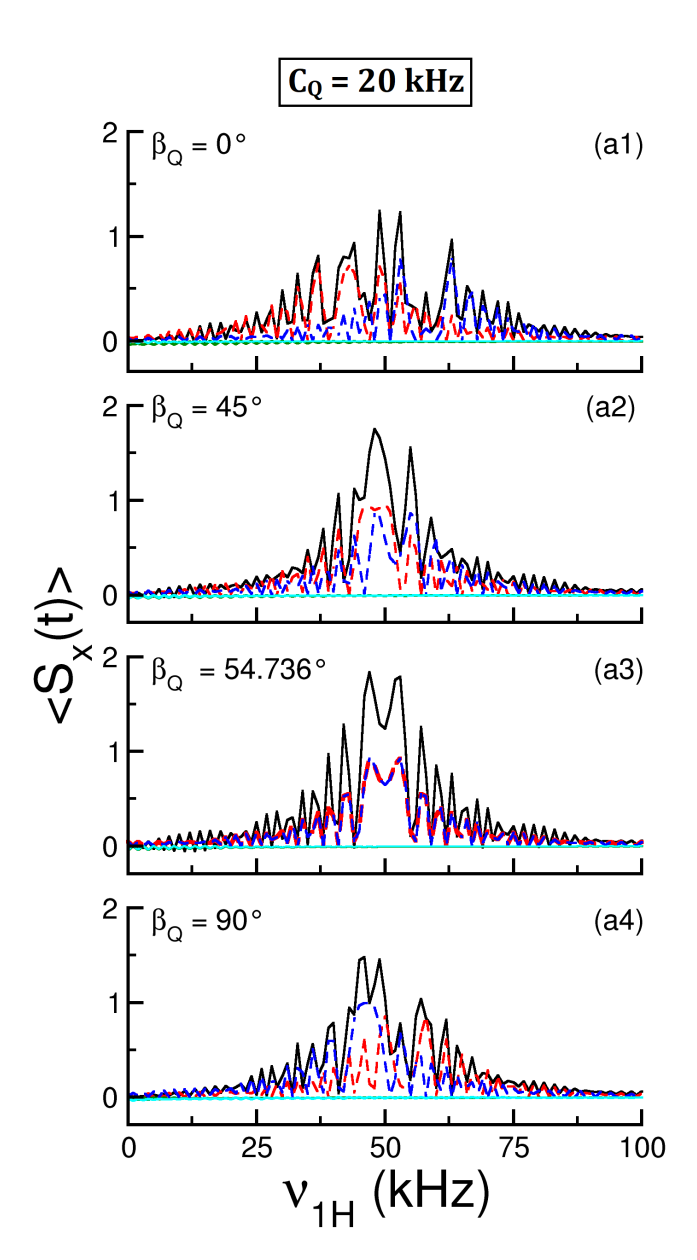


Figure C.3: In the CP simulations depicted, the polarization build-up on the S-spin (due to transfer from the I-spin) is monitored in a single crystal as a function of the rf field employed on the I-spin. The numerical simulations (based on SIMPSON) are represented by solid black lines. In the simulations depicted, the effects of the variation of quadrupolar coupling PAS angle β_Q : 0° (a1), 45° (a2), 54.736° (a3) and 90° (a4) on the CP dynamics are illustrated. The following parameters were employed in all the simulations: $C_Q = 20$ kHz, $\eta_Q = 0$, quadrupolar coupling PAS angle $\alpha_Q = 0$ °, contact time $(t_{mix}) = 0.5$ ms, internuclear distance $r_{IS} = 1.05$ Å and $\nu_{1S} = 50$ kHz. The analytic simulations based on signal expressions corresponding to various CP matching conditions are indicated, SQ₃₄ (red), TQ₁₆ (green), DQ₂₆ (blue) and ZQ₃₅ (cyan) [Eq. (3.19)].

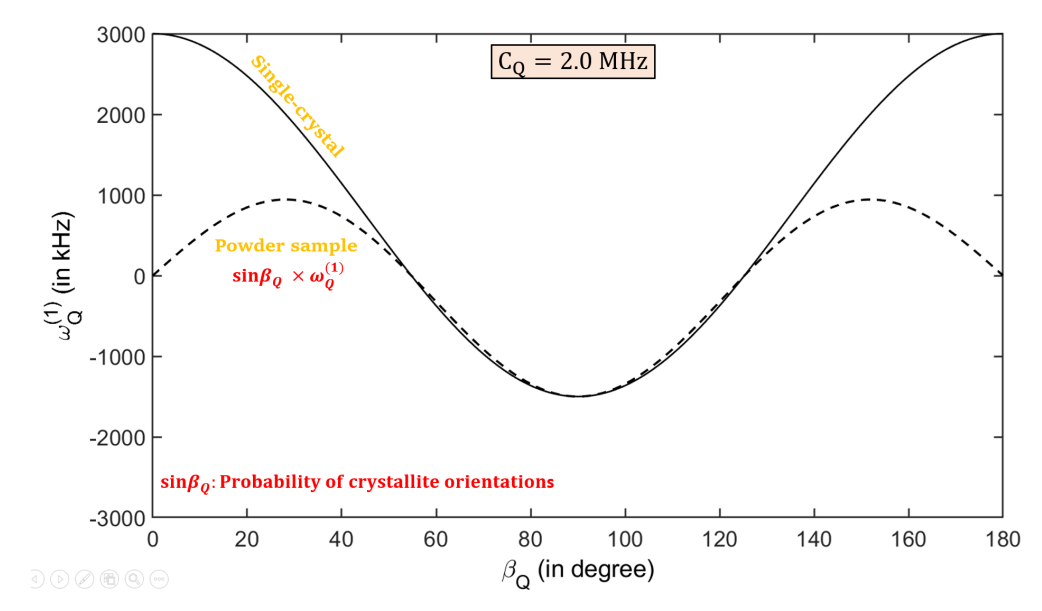


Figure C.4: Effect of the variation of quadrupolar coupling PAS angle β_Q on the weighted first-order quadrupolar coupling frequency. Considering the quadrupolar PAS coincides with the Molecular-axis systems (MolAS), the angles β_Q will represent different crystallites orientations. The following simulation parameters were used: $C_Q=2.0$ MHz, $\eta_Q=0$, quadrupolar coupling PAS angle $\alpha_Q=0^\circ$. The solid and dashed lines represent $\omega_Q^{(1)}$ and $\omega_Q^{(1)}\times\sin\beta_Q$, respectively. The weighted crystallite plots provide an account of the probability of the particular crystallite in powder sample.

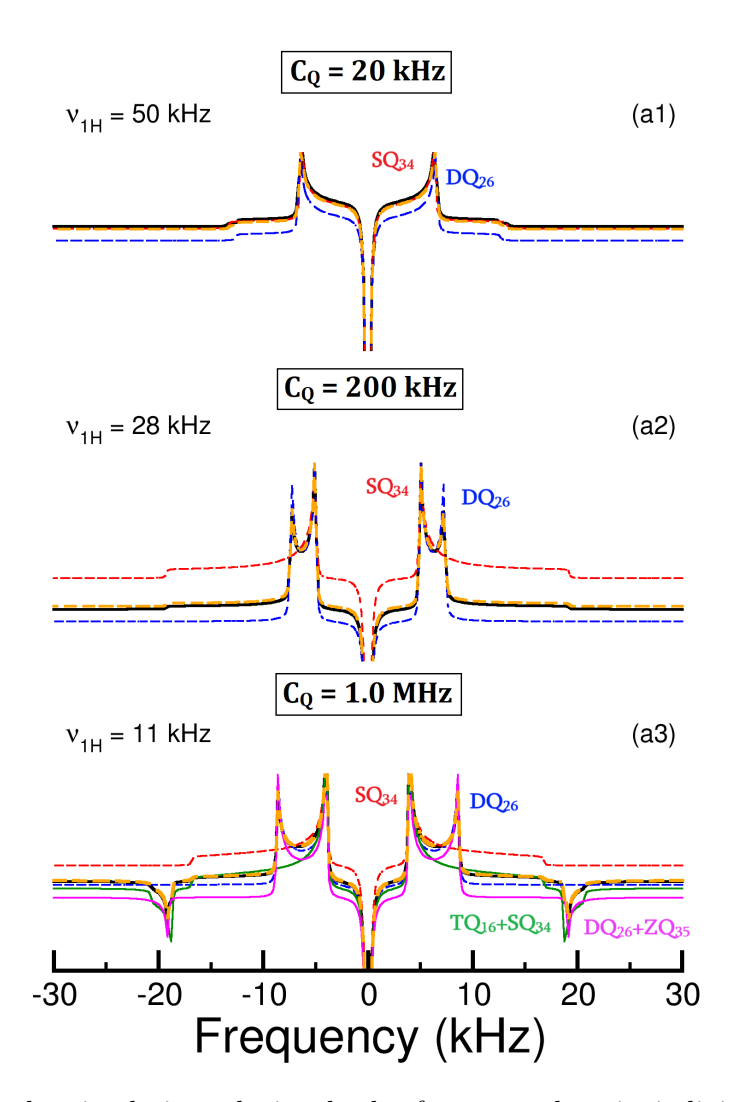


Figure C.5: In the simulations depicted, the frequency-domain individual S-spin CP signals in a powder sample emerging from the Fourier transformation of the mixing time domain signal is depicted for different quadrupolar coupling constants: panel a1 ($C_Q = 20$ kHz); panel a2 ($C_Q = 200 \text{ kHz}$) and panel a3 ($C_Q = 1.0 \text{ MHz}$). All other parameters such as the quadrupolar coupling PAS angles α_Q and $\beta_Q = 0^{\circ}$, dipolar parameters (internuclear distance $r_{12}=1.05$ Åand dipolar PAS angle $\beta_d=0^\circ$) and rf amplitude of S-spin $\nu_{1S}=50$ kHz were identical in all the simulations. Depending on the magnitude of the quadrupolar coupling constant, the rf amplitudes employed on the I-spin were carefully selected by CP in maxima of the rf-domain simulation at the desired contact time. The numerical simulations (based on SIMPSON) are represented by solid black lines. The analytic simulations in the panels have the following definitions: the analytic simulations comprise contributions from all the four CP matching conditions ($SQ_{34}+TQ_{16}+DQ_{26}+ZQ_{35}$) and is represented in orange color and the analytic simulations based on the contributions SQ_{34} (red), $SQ_{34}+TQ_{16}$ (green), DQ_{26} (blue) and $DQ_{26}+ZQ_{35}$ (magenta) are depicted [based on Eq. (3.19) in the main text. The powders simulations were performed using 4180 orientations (i.e., zcw4180) of α and β . A line broadening of 50 Hz was used before the Fourier transform of the time-domain CP signal.

Appendix D

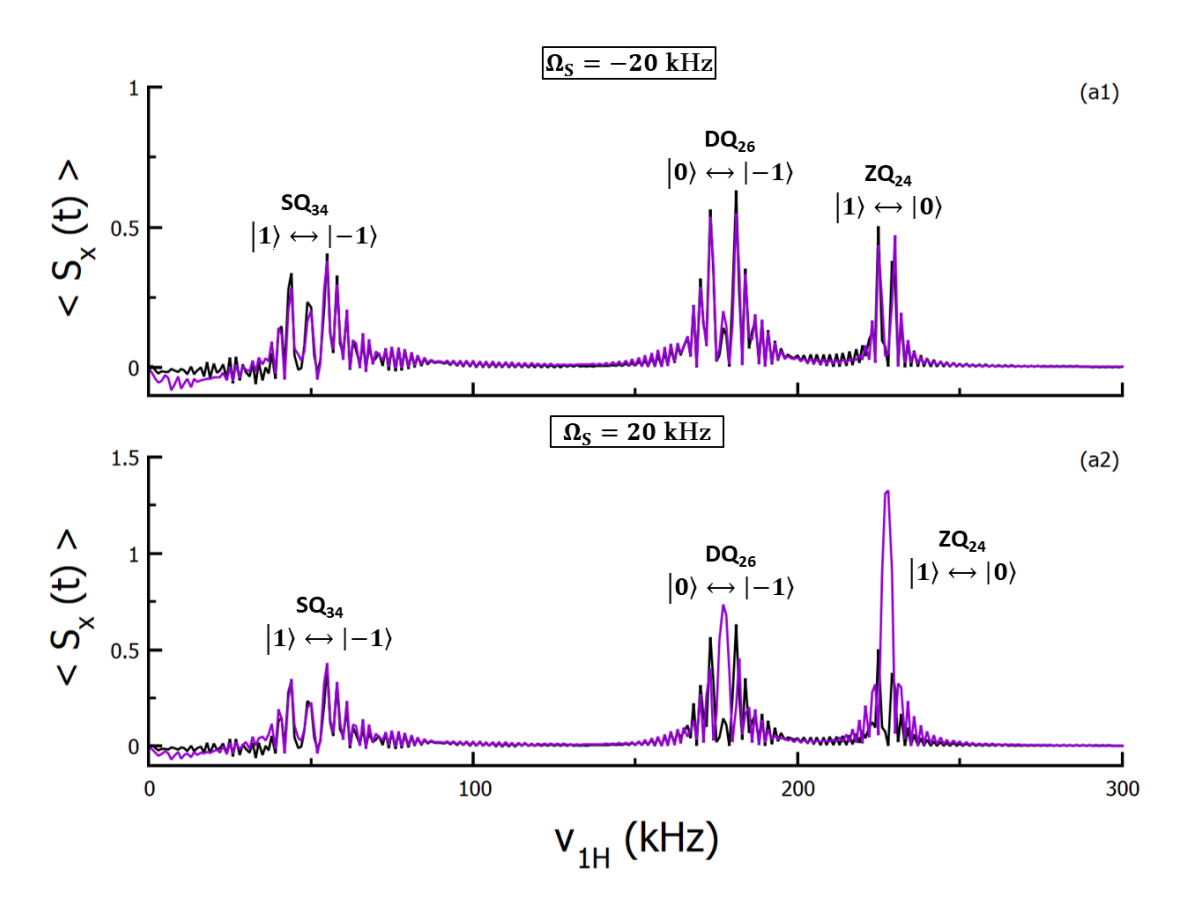


Figure D.1: The first-order quadrupolar driven cross-polarization transfer efficiency as a function of the $^1\mathrm{H}$ rf field for a single-crystal sample from the numerical simulation (SIMPSON) and the analytic theory. These simulations demonstrate the effect of S-spin off-resonance irradiations on the CP efficiency profile $\Omega_S=-20~\mathrm{kHz}$ (a1) and $\Omega_S=20~\mathrm{kHz}$ (a2). The parameters used for generating the CP efficiency profiles are: $C_Q=200~\mathrm{kHz}$, $\eta_Q=0$, quadrupolar coupling PAS angles α_Q and $\beta_Q=0^\circ$, contact time = 0.5 ms, $\nu_{1S}=80~\mathrm{kHz}$ and internuclear distance $r_{IS}=1.05~\mathrm{Å}$. SIMPSON simulations (black curve) are fitted with the total analytic signal expressions (indigo curve) [Eq. (4.20)] in panels a1-a3.

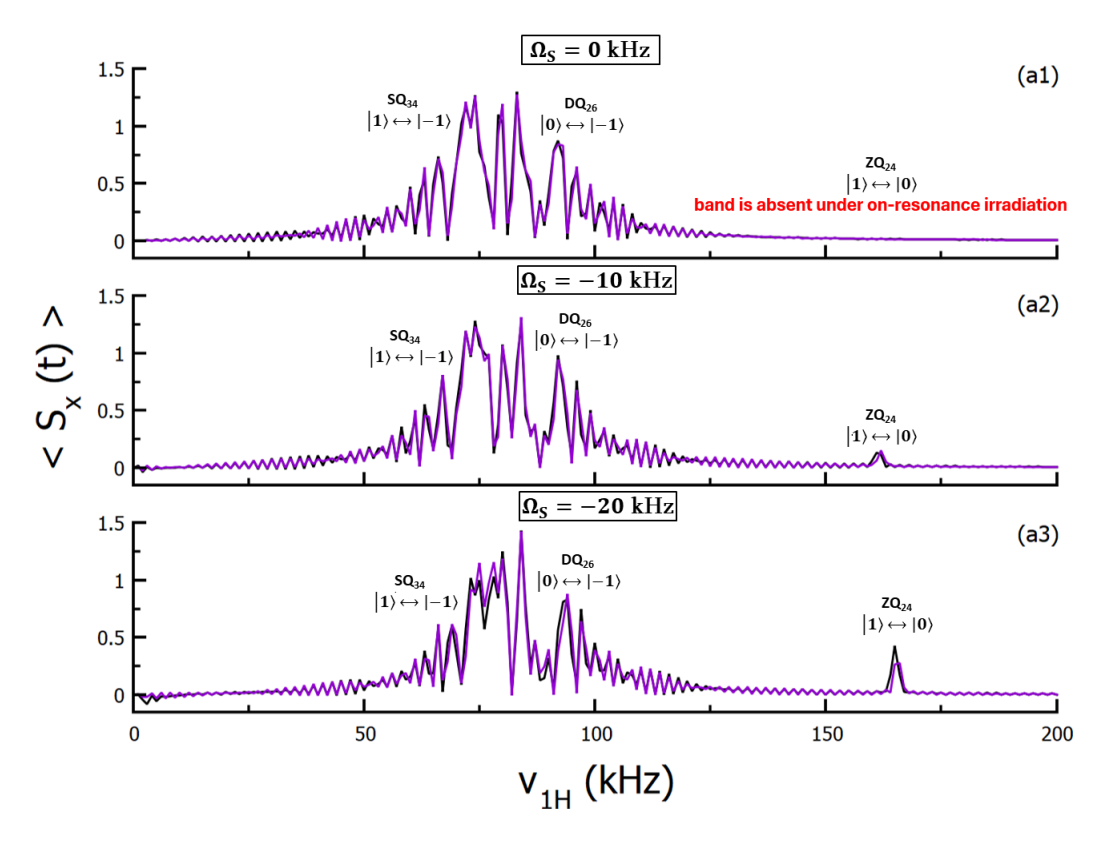


Figure D.2: The first-order quadrupolar driven cross-polarization transfer efficiency as a function of the $^1\mathrm{H}$ rf field for a single-crystal sample from the numerical simulation (SIMPSON) and the analytic theory. These simulations demonstrate the effect of S-spin off-resonance irradiations on the CP efficiency profile $\Omega_S=0$ kHz (a1), $\Omega_S=-10$ kHz (a2) and $\Omega_S=-20$ kHz (a3). The parameters used for generating the CP efficiency profiles are: $C_Q=20$ kHz, $\eta_Q=0$, quadrupolar coupling PAS angles α_Q and $\beta_Q=0^\circ$, contact time = 0.5 ms, $\nu_{1S}=80$ kHz and internuclear distance $r_{IS}=1.05$ Å. SIMPSON simulations (black curve) are fitted with the total analytic signal expressions (indigo curve) [Eq. (4.20)] in panels a1-a3.

D.1 Coefficients in the calculation of the density matrix in TQ_{16} , SQ_{34} , DQ_{15} , ZQ_{24} , DQ_{26} and ZQ_{35} subspaces

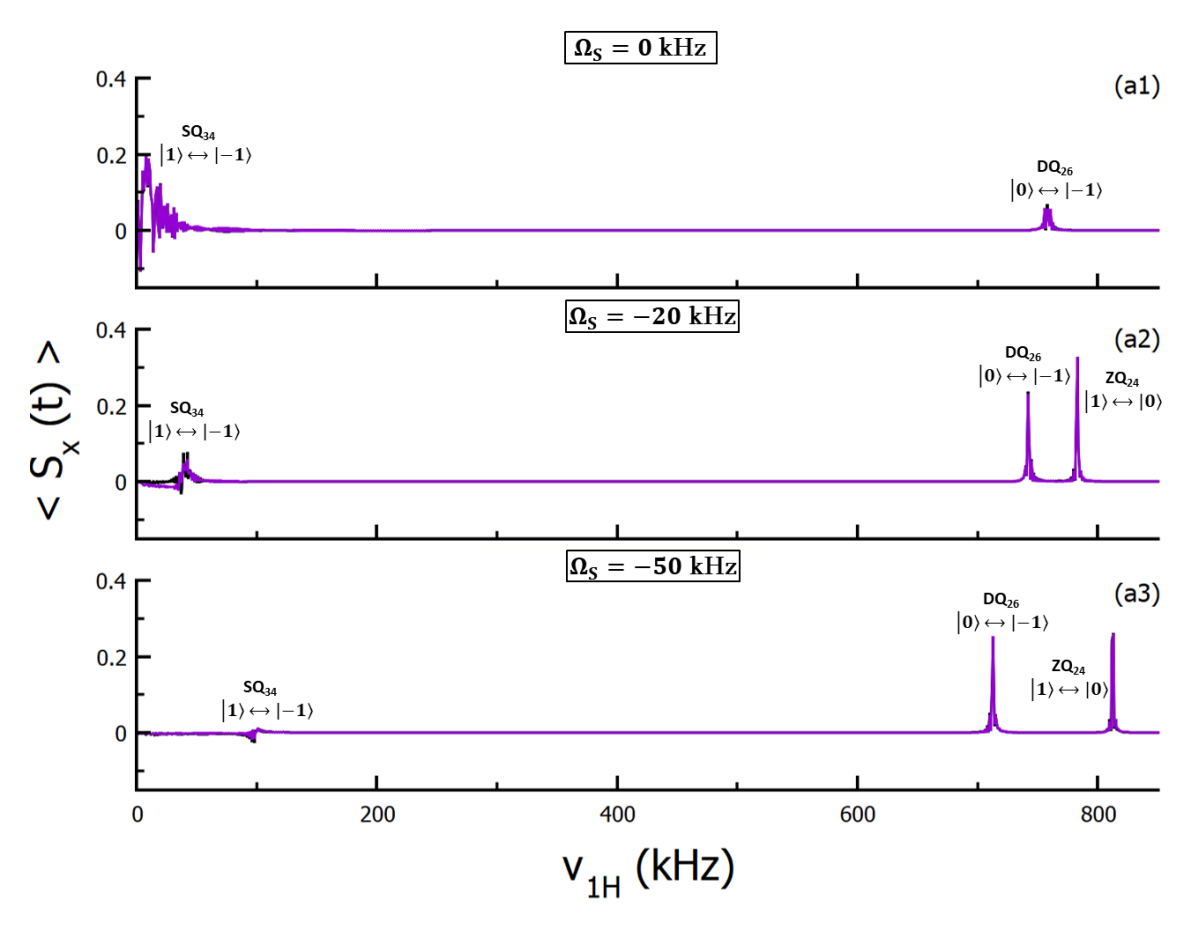


Figure D.3: The first-order quadrupolar driven cross-polarization transfer efficiency as a function of the $^1\mathrm{H}$ rf field for a single-crystal sample from the numerical simulation (SIMPSON) and the analytic theory. These simulations demonstrate the effect of S-spin off-resonance irradiations on the CP efficiency profile $\Omega_S=0$ kHz (a1), $\Omega_S=-20$ kHz (a2) and $\Omega_S=-50$ kHz (a3). The parameters used for generating the CP efficiency profiles are: $C_Q=1000$ kHz, $\eta_Q=0$, quadrupolar coupling PAS angles α_Q and $\beta_Q=0^\circ$, contact time = 0.5 ms, $\nu_{1S}=80$ kHz and internuclear distance $r_{IS}=1.05$ Å. SIMPSON simulations (black curve) are fitted with the total analytic signal expressions (indigo curve) [Eq. (4.20)] in panels a1-a3.

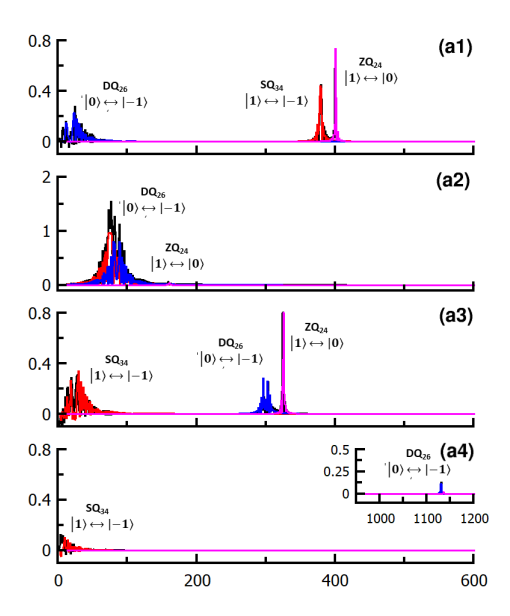


Figure D.4: Effect of the variation of the quadrupolar coupling PAS angle β : 110° (a1), 125.624° (a2), 135° (a3) and 180° (a4) on the second-order quadrupolar interaction driven cross-polarization transfer efficiency for a single-crystal sample. The parameters used for generating the CP efficiency profiles are: $C_Q = 1500$ kHz, $\eta = 0$, and quadrupolar coupling PAS angle $\alpha = 0^{\circ}$, $\nu_{1S} = 80$ kHz, contact time = 0.5 ms, ¹H Larmor precession frequency = 400 MHz and $r_{1S} = 1.05$ Åunder on-resonance S-spin irradiation. SIMPSON simulations (black curve) are fitted with the SQ₃₄+TQ₁₆ (red curve), DQ₂₆+ZQ₃₅ (blue curve) and DQ₁₅+ZQ₂₄ (magenta curve) in all panels.

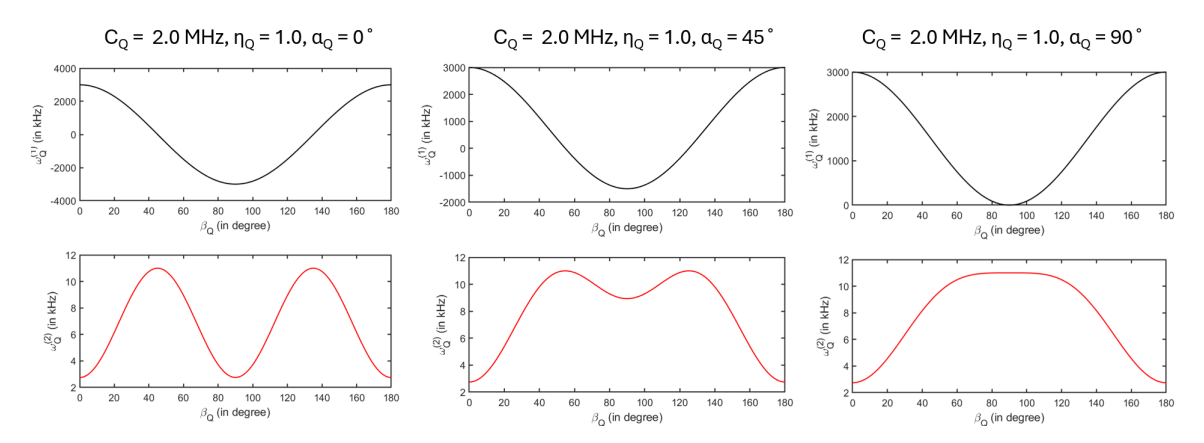


Figure D.5: Effect of the variation of the quadrupolar coupling PAS angle β_Q on first and second-order quadrupolar coupling frequencies. The following simulation parameters were used: $C_Q = 2.0$ MHz, $\eta_Q = 1.0$, quadrupolar coupling PAS angle α_Q : (a1) 0°, (a2) 45° and (a3) 90°. The exact expression for these frequencies can be found in Eqs. (1.32) and (1.36).

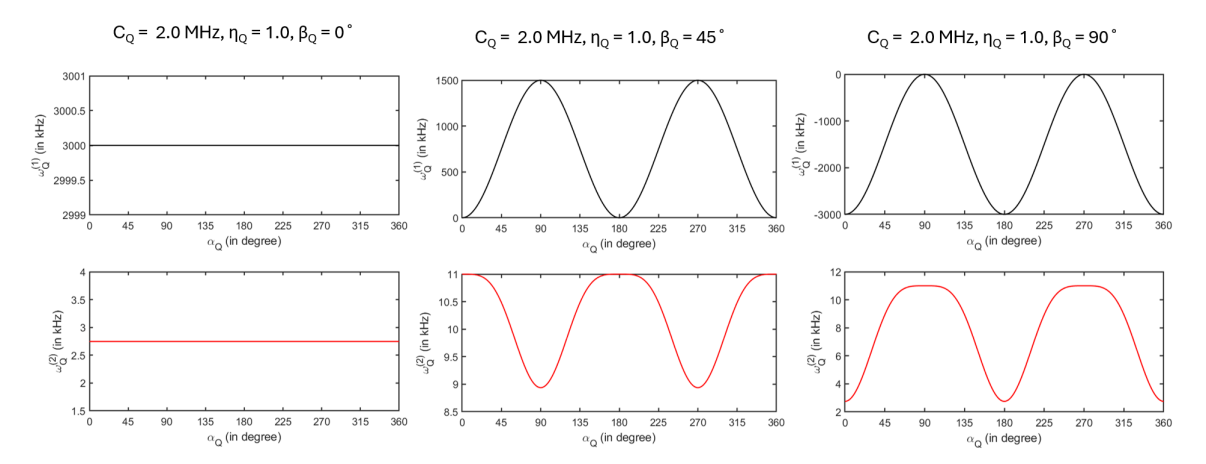


Figure D.6: Effect of the variation of the quadrupolar coupling PAS angle α_Q on the first and second-order quadrupolar coupling frequencies. The following simulation parameters were used: $C_Q=2.0$ MHz, $\eta_Q=1.0$, quadrupolar coupling PAS angle β_Q : (a1) 0°, (a2) 45° and (a3) 90°. The exact expression for these frequencies can be found in Eqs. (1.32) and (1.36).

Zero-passage in the first-order quadrupolar frequency

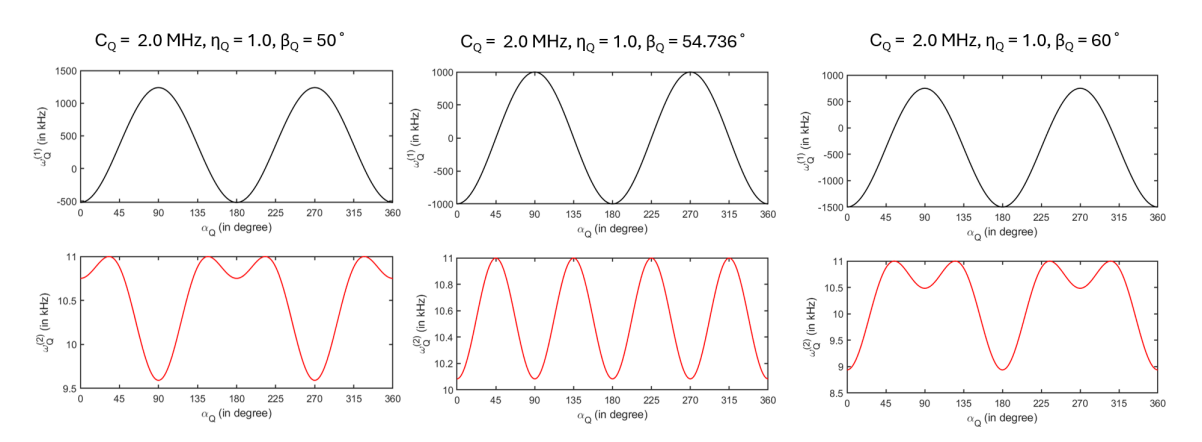


Figure D.7: Effect of the variation of the quadrupolar coupling PAS angle α_Q on the first and second-order quadrupolar coupling frequencies. The following simulation parameters were used: $C_Q = 2.0$ MHz, $\eta_Q = 1.0$, quadrupolar coupling PAS angle β_Q : (a1) 50°, (a2) 54.736° and (a3) 60°. The exact expression for these frequencies can be found in Eqs. (1.32) and (1.36).

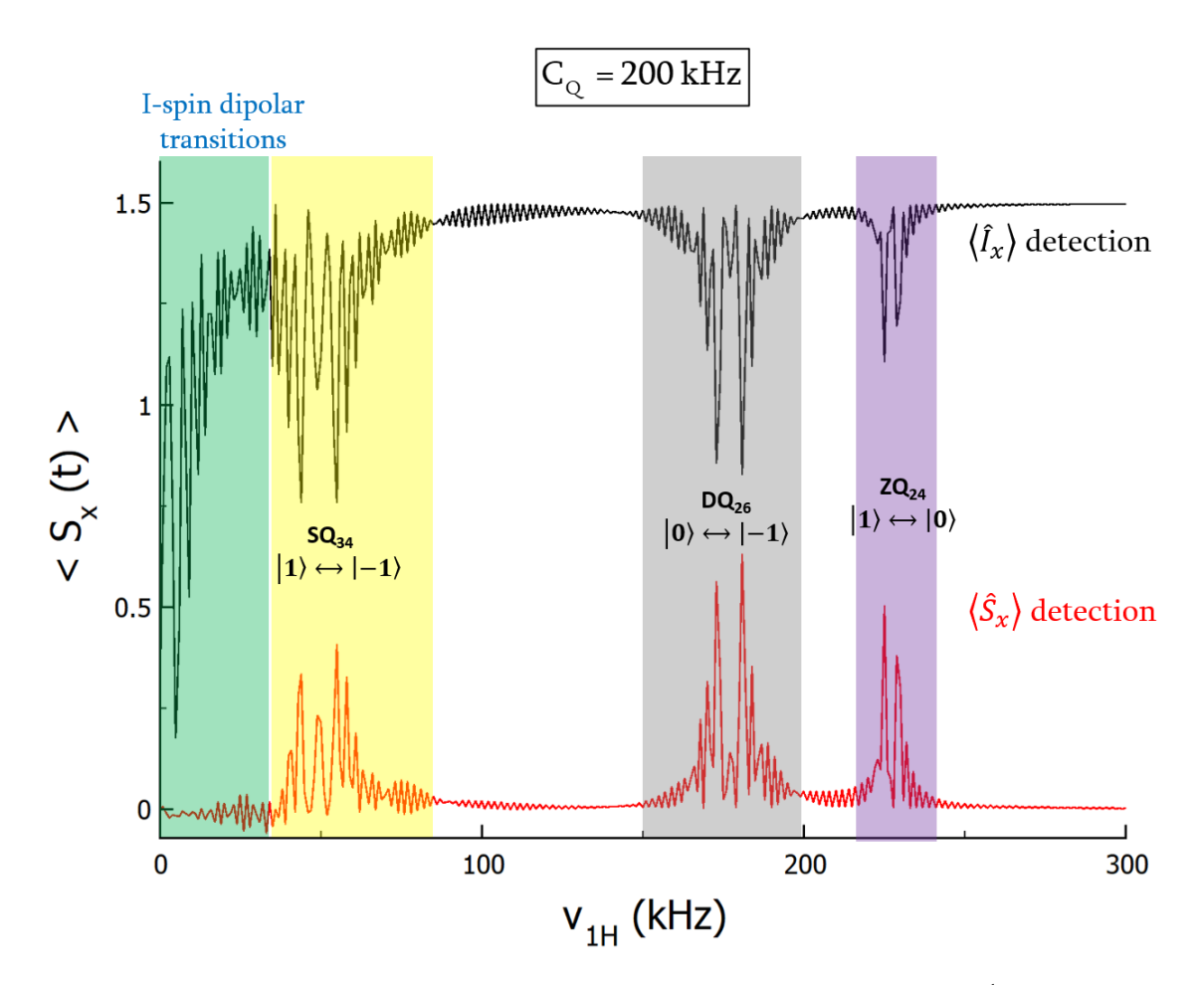


Figure D.8: The cross-polarization trajectories as a function of the ¹H RF field for a single-crystal sample from the numerical simulation (SIMPSON). The following parameters were used in the simulations: $C_Q = 200$ kHz, $\eta_Q = 0$, quadrupolar coupling PAS angles (0°, 0°, 0°), $\nu_{1S} = 80$ kHz and S-spin off-resonance irradiation strength $\Omega_{1S} = 40$ kHz. Here the black and red curves correspond to the $\langle I_x(t) \rangle$ and $\langle S_x(t) \rangle$ detection, respectively.

Table D.1: The coefficients associated with the density matrix calculations in all subspaces.

The coefficients associated with the density matrix calculations	\mathbf{DQ}_{26} and \mathbf{ZQ}_{35} subspace	$\rho_{25,35}^{26,35} = -\frac{1}{2}(\cos\theta_{25} - \cos\theta_{36})\cos\left(\frac{\theta_{35} - \theta_{26}}{2}\right) -\frac{1}{2}(\cos\theta_{25} + \cos\theta_{36})\sin\left(\frac{\theta_{35} + \theta_{26}}{2}\right)$	$\rho_{23}^{26,35} = -\frac{1}{2}(\cos\theta_{25} + \cos\theta_{36})\cos\left(\frac{\theta_{35} + \theta_{26}}{2}\right) + \frac{1}{2}(\cos\theta_{25} - \cos\theta_{36})\sin\left(\frac{\theta_{35} - \theta_{26}}{2}\right)$	$\rho_{56}^{26,35} = \frac{1}{2} (\cos \theta_{25} + \cos \theta_{36}) \cos \left(\frac{\theta_{35} + \theta_{26}}{2} \right) + \frac{1}{2} (\cos \theta_{25} - \cos \theta_{36}) \sin \left(\frac{\theta_{35} - \theta_{26}}{2} \right)$	$\rho_{36}^{26,35} = \frac{1}{2} (\cos \theta_{25} - \cos \theta_{36}) \cos \left(\frac{\theta_{35} - \theta_{26}}{2} \right) - \frac{1}{2} (\cos \theta_{25} + \cos \theta_{36}) \sin \left(\frac{\theta_{35} + \theta_{26}}{2} \right)$
	$ m DQ_{15}$ and $ m ZQ_{24}$ subspace	$\rho_{14}^{15,24} = \frac{1}{2} (\cos \theta_{25} - \cos \theta_{14}) \cos \left(\frac{\theta_{24} - \theta_{15}}{2} \right) - \frac{1}{2} (\cos \theta_{25} + \cos \theta_{14}) \sin \left(\frac{\theta_{24} + \theta_{15}}{2} \right)$	$\rho_{12,24}^{15,24} = -\frac{1}{2}(\cos\theta_{25} + \cos\theta_{14})\cos\left(\frac{\theta_{24} + \theta_{15}}{2}\right) \\ -\frac{1}{2}(\cos\theta_{25} - \cos\theta_{14})\sin\left(\frac{\theta_{24} - \theta_{15}}{2}\right)$	$\rho_{45}^{15,24} = \frac{1}{2} (\cos \theta_{25} + \cos \theta_{14}) \cos \left(\frac{\theta_{24} + \theta_{15}}{2} \right) - \frac{1}{2} (\cos \theta_{25} - \cos \theta_{14}) \sin \left(\frac{\theta_{24} - \theta_{15}}{2} \right)$	$\rho_{25}^{15,24} = -\frac{1}{2} (\cos \theta_{25} + \cos \theta_{14}) \cos \left(\frac{\theta_{24} - \theta_{15}}{2} \right) -\frac{1}{2} (\cos \theta_{25} + \cos \theta_{14}) \sin \left(\frac{\theta_{24} + \theta_{15}}{2} \right)$
	$ m TQ_{16}$ and $ m SQ_{34}$ subspace	$\rho_{14}^{16,34} = -\frac{1}{2}(\cos\theta_{14} - \cos\theta_{36})\cos\left(\frac{\theta_{34} - \theta_{16}}{2}\right) -\frac{1}{2}(\cos\theta_{14} + \cos\theta_{36})\sin\left(\frac{\theta_{34} + \theta_{16}}{2}\right)$	$\rho_{13}^{16,34} = -\frac{1}{2}(\cos\theta_{14} + \cos\theta_{36})\cos\left(\frac{\theta_{34} + \theta_{16}}{2}\right) + \frac{1}{2}(\cos\theta_{14} - \cos\theta_{36})\sin\left(\frac{\theta_{34} - \theta_{16}}{2}\right)$	$\rho_{46}^{16,34} = \frac{1}{2} (\cos \theta_{14} + \cos \theta_{36}) \cos \left(\frac{\theta_{34} + \theta_{16}}{2} \right) + \frac{1}{2} (\cos \theta_{14} - \cos \theta_{36}) \sin \left(\frac{\theta_{34} - \theta_{16}}{2} \right)$	$\rho_{36}^{16,34} = \frac{1}{2}(\cos\theta_{14} - \cos\theta_{36})\cos\left(\frac{\theta_{34} - \theta_{16}}{2}\right) - \frac{1}{2}(\cos\theta_{14} + \cos\theta_{36})\sin\left(\frac{\theta_{34} + \theta_{16}}{2}\right)$

Appendix E

E.1 Matrix representation of the basis states and spin-operators for the S=3/2 spin-system.

Table E.1: Matrix representation of Zeeman basis for the S=3/2 spin system

$$|1\rangle = |3/2\rangle_S = \begin{bmatrix} 1\\0\\0\\0\\0 \end{bmatrix}; \ |2\rangle = |1/2\rangle_S = \begin{bmatrix} 0\\1\\0\\0 \end{bmatrix}; \ |3\rangle = |-1/2\rangle_S = \begin{bmatrix} 0\\0\\1\\0 \end{bmatrix}; \ |4\rangle = |-3/2\rangle_S = \begin{bmatrix} 0\\0\\0\\1\\1 \end{bmatrix}$$

Table E.2: Matrix representation of the Cartesian spin-operators for the S=3/2 spin system.

$$\hat{S}_x = \frac{1}{2} \begin{bmatrix} 0 & \sqrt{3} & 0 & 0 \\ \sqrt{3} & 0 & 2 & 0 \\ 0 & 2 & 0 & \sqrt{3} \\ 0 & 0 & \sqrt{3} & 0 \end{bmatrix}; \hat{S}_y = \frac{i}{2} \begin{bmatrix} 0 & -\sqrt{3} & 0 & 0 \\ \sqrt{3} & 0 & -2 & 0 \\ 0 & 2 & 0 & -\sqrt{3} \\ 0 & 0 & \sqrt{3} & 0 \end{bmatrix}; \hat{S}_z = \frac{1}{2} \begin{bmatrix} 3 & 0 & 0 & 0 \\ 0 & 1 & 0 & 0 \\ 0 & 0 & -1 & 0 \\ 0 & 0 & 0 & -3 \end{bmatrix}$$

E.2 Matrix representation of the product basis states and spin-operators for the I=1/2 and S=3/2 coupled spin-system

Table E.3: Matrix representation of the single-transition operators for the S=3/2 spin system.

Table E.4: Single-transition operator representation of the spin-operators for the S=3/2 spin system.

$$\hat{S}_x = \sqrt{3}(\hat{S}_x^{12} + \hat{S}_x^{34}) + 2\hat{S}_x^{23}; \quad \hat{S}_y = \sqrt{3}(\hat{S}_y^{12} + \hat{S}_y^{34}) + 2\hat{S}_y^{23}; \quad \hat{S}_z = (3\hat{S}_z^{14} + \hat{S}_z^{23})$$

Table E.5: Matrix representation of the product basis for the I=1/2 and S=3/2 spin system.

$$|1\rangle = |1/2\rangle_I \bigotimes |3/2\rangle_S \equiv |\frac{1}{2}, \frac{3}{2}\rangle = \begin{bmatrix} 1\\0\\0\\0\\0\\0\\0 \end{bmatrix}; \ |2\rangle = |1/2\rangle_I \bigotimes |1/2\rangle_S \equiv |\frac{1}{2}, \frac{1}{2}\rangle = \begin{bmatrix} 0\\1\\0\\0\\0\\0\\0 \end{bmatrix}$$

$$|3\rangle = |1/2\rangle_I \bigotimes |-1/2\rangle_S \equiv |\frac{1}{2}, -\frac{1}{2}\rangle = \begin{bmatrix} 0 \\ 0 \\ 1 \\ 0 \\ 0 \\ 0 \\ 0 \end{bmatrix}; \ |4\rangle = |1/2\rangle_I \bigotimes |-3/2\rangle_S \equiv |\frac{1}{2}, -\frac{3}{2}\rangle = \begin{bmatrix} 0 \\ 0 \\ 0 \\ 1 \\ 0 \\ 0 \\ 0 \\ 0 \end{bmatrix}$$

$$|5\rangle = |-1/2\rangle_I \bigotimes |3/2\rangle_S \equiv |-\frac{1}{2}, \frac{3}{2}\rangle = \begin{bmatrix} 0 \\ 0 \\ 0 \\ 1 \\ 0 \\ 0 \\ 0 \end{bmatrix}; \ |6\rangle = |-1/2\rangle_I \bigotimes |1/2\rangle_S \equiv |-\frac{1}{2}, \frac{1}{2}\rangle = \begin{bmatrix} 0 \\ 0 \\ 0 \\ 0 \\ 1 \\ 0 \\ 0 \end{bmatrix}$$

$$|7\rangle = |-1/2\rangle_I \bigotimes |-1/2\rangle_S \equiv |-\frac{1}{2}, -\frac{1}{2}\rangle = \begin{bmatrix} 0 \\ 0 \\ 0 \\ 0 \\ 0 \\ 1 \\ 0 \end{bmatrix}; \ |8\rangle = |-1/2\rangle_I \bigotimes |-3/2\rangle_S \equiv |-\frac{1}{2}, -\frac{3}{2}\rangle = \begin{bmatrix} 0 \\ 0 \\ 0 \\ 0 \\ 0 \\ 1 \\ 1 \end{bmatrix}$$

Table E.6: Matrix representation of the S-spin Cartesian operators in product basis.

Table E.7: Matrix representation of the *I*-spin Cartesian operators in product basis.

List of Publications

Publications based on the Thesis

- E. Nehra and M. K. Pandey, Unravelling the mechanism of polarization transfer from spin-1/2 to spin-1 system in solids, Phys. Chem. Chem. Phys., vol. 26, pp. 2995–3007, 4 2024. doi: 10.1039/D3CP05921A.
- 2. E. Nehra and M. K. Pandey, Analytic theory of cross-polarization dynamics between spin-1/2 to spin-1 under off-resonance irradiation and second-order quadrupolar effects (To be submitted).
- 3. E. Nehra and M. K. Pandey, Analytic theory of CP transfer from I = 1/2 to S = 3/2 spin system in solids (under preparation).

Other publications

- E. Nehra†, N. Sehrawat†, T. Kobayashi, Y. Nishiyama, and M. K. Pandey, "Proton-detected ¹⁵N-¹H dipolar coupling and ¹H chemical shift correlation experiment for the measurement of NH distances in biological solids under fast MAS solid-state NMR," Journal of Magnetic Resonance Open, vol. 10-11, p. 100 028, 2022.
 - doi: https://doi.org/10.1016/j.jmro.2021.100028.
- N. Sehrawat[†], E. Nehra[†], K. K. Rohilla, T. Kobayashi, Y. Nishiyama, and M. K. Pandey, "Determination of the relative orientation between ¹⁵N-¹H dipolar coupling and ¹H chemical shift anisotropy tensors under fast MAS solid-state NMR," J. Magn. Reson., vol. 350, p. 107 428, 2023. doi: https://doi.org/10.1016/j.jmr.2023.107428. († equal contributions)